ION CHANNELLING IN DIAMOND

by

TREVOR ERNEST DERRY

a thesis submitted

to the Faculty of Science,

University of the Witwatersrand, Johannesburg,

for the degree of

DOCTOR OF PHILOSOPHY

June, 1978

A B S T R A C T

This thesis is an account of the first comprehensive ion channelling experiments to be reported for diamond single crystals. Since the discovery of ion channelling sixteen years ago, detailed investigations have been performed on many solids, mostly those crystallising in the diamond structure, but there have been few experiments on diamond itself. It is obviously useful to extend measurements to another substance with a familiar structure but diamond moreover is one of the most extreme cases from a channelling point of view, having the smallest thermal vibration amplitude and the lowest atomic number of commonly-encountered crystals. These are the two parameters most important for determining channelling behaviour. It is of consiberable interest therefore to see how well the theories which have proved quite successful in explaining and predicting the channelling properties of other substances, succeed with diamond.

Natural diamond, although the best available form for these experiments, is rather variable in its physical properties and so the first part of the project was devoted to considering and solving the problem of obtaining reproducible results representative of the ideal crystal. It is shown how this can be achieved by selecting from a sufficient number of good stones, using the channelling itself as a criterion, and by paying careful attention to a number of precautions. Techniques which were found to improve the quality of natural crystals are described.

Channelling studies were performed on several good crystals, using the Rutherford backscattering method. Critical angles for proton channelling were measured for incident energies from 0.6 to 4.5 MeV, in the three most open axes and three most open planes of the diamond structure, and for α-particle channelling at 0.7 and 1.0 MeV (He^+) in the same axes and planes. For 1.0 MeV protons, the crystal temperature was varied from 20°C to 700°C. The results are presented as curves of backscattered yield versus angle in the region of each axis or plane, and summarised in the form of tables and graphs.

Generally the critical angles are well predicted by the accepted theories, being closely represented by the semi-empirical expressions of Barrett. Agreement is best for the lowest-order axes (namely, <110> and <111>) and for equally-spaced planes (for example {110} and {100}). For higher-order axes (for example, <100>) the measured critical angles are smaller than the predictions, and for unequally-spaced planes (for example {111}) a modified theory must be used to obtain agreement with the measurements. Temperature dependence is close to that predicted, but is a slightly stronger function of temperature than expected in the axial case; it is suggested how theory might be modified to take account of this. The most valuable overall conclusion is that the mean thermal vibration amplitude of the atoms in a crystal determines the critical approach distance to the channel walls at which an ion can remain channelled, even when this distance is much smaller than the Thomas-Fermi screening distance of the atomic potential, as is the case in diamond.

Axial minimum yields and their temperature dependence are well predicted by Barrett's expression for these quantities, confirming that they are determined largely or even entirely by thermal vibrations. The smallness of the latter i diamond enables a more unambiguous conclusion to be reached than is possible with other substances.

An additional result of the minimum-yield and surface-peak investigations was to provide some corroboration for current ideas as to how the diamond structure terminates itself at a free surface.

A brief study was made of the radiation damage caused by a-particle bombardment, via its effect on the channelling phenomenon. The subject is evidently complex, but a few preliminary conclusions are reached as to the probable nature of the damage: chiefly amorphous clusters, interstitials in tetrahedral sites, and mosaic spread. It was possible to hold dar age d wn to negligible levels during the performance of a channelling experiment.

I declare that the results presented in this thesis are my own work performed under the supervision of Professor J.P.I. Sellschop.

None of the material has been submitted for a degree in any university.

To my parents

ACKNOWLEDGEMENTS

During the course of this work I have become indebted to most of my colleagues, past and present, in the Nuclear Physics Research Unit, to many members of the Physics Department proper, and to sundry other individuals and organisations for advice and assistance of one kind or another. Some specific examples are acknowledged in the text. The following deserve to receive special thanks:

- Professor J.P.F. Sellschop, my supervisor, who suggested this line of research, for his constant presence, encouragement, and guidance throughout the period of its undertaking. In a less direct way, too, he contributed towards its success by his dynamic administration of the Unit.

- Professor Donald Mingay, for much gladly-given advice, interest, and support, and for his hard work in setting up "Christine" as a thoroughly reliable and well-thought-out ion accelerator.

- Roger Fearick, whose sound grasp of the theory relating to channelling and ion penetration helped illuminate many dark corners and provided many valuable discussions. He also frequently rendered assistance with the experiments, and gave me the use of his excellent computer programmes.

- Harold Annegarn, for valuable advice on the finer points of thesis-writing, and encouragement to do it.

- All those colleagues who helped collect data, often at unpleasant hours. They include all of the above, plus Avelino and Anna Morgado and Tony Campos (of the then Lourenço Marques University), Mike Renan, John Vanstone, Professor Rex Keddy, and Mike Stemmet.

- Lieb Verga and his workshop staff for constructing the apparatus and for practical help; Mick Rebak for precision work, including diamond-polishing; the electronics workshop staff for construction and repair of electronic equipment.

- Laurie Hoare and the generations of accelerator technicians who succeeded him, for their efforts to keep the equipment in good working order.

- Professor J.H.N. Loubser and other members of the Physics Department for assistance, especially for the use of their ultra-high-vacuum equipment.

- Vacation students Sharon Wainman and Desmond Arthur for helping to extract some of the data.

- Jeannette Menasce who typed the manuscript with painstaking attention to detail, and Mrs Katherine Peach who re-drew most of the Figures. The excellent quality of their work speaks for itself.

I express my appreciation to the University of the Witwatersrand, the Gold and Diamond Mining Industries of South Africa, and the Council for Scientific and Industrial Research, for financial support.

C O N T E N T S

LIST OF FIGURES

LIST OF TABLES

CHAPTER 1

INTRODUCTION

1.1 HISTORICAL

It is one of the ironies of physics that von Laue, Friedrich and Knipping's discovery of X-ray diffraction by crystals and W.L. Bragg's explanation of it in terms of a wave picture, coincided with the publication in 1912 of the first paper [Stal2] to consider the possibility of ion channelling. Once this had been disproved as an explanation for the X-ray experiments (see Lau52), the idea was shelved for fifty years, until the observation of anomalously large penetrations of fast ions in crystalline solids led to its independent revival [Og59, Ne62].

Ion channelling was first unambiguously found in the computer simulations of Robinson and Oen [Oe62, Ro63a, Ro63b]. This stimulated a rash of penetration experiments using heavy radioactive ions, whose depth profiles were determined by stripping off crystal layers and measuring the residual radioactivity [Pie62, Lut63, Tor64, Dav64, Pie64, Lut64, Kor64, Ch64, Bal65]. At the same time, increased transmission of light ions through thin crystals was observed by Nelson and Thompson [Ne63], then by others [Tea64, Erg64, [illegible], [illegible] (heavy ions), Gi65, Anr65]. The expected reduction in nuclear reaction yields for channelled ions was soon reported [Bo64, Thr64, Bra65, Bo65], as was the inverse-channelling effect - blocking - for ions originating at lattice sites

[Do65, Tu65a, Ge65, Tu65b, Tu65c]. Even electron 'channelling' was demonstrated [As65, Be65]. Initially the emphasis was on proving the existence of channelling and blocking effects in as many substances as possible. The theory was rapidly developed [Ne63, Li64, Tu65a, Erg65, Ap65, Oe65, Li65], with the most important and enduring contribution coming from Professor Jens Lindhard in 1965 [Li65]. Detailed surveys of the work of this period are present in several review articles (for example, Dat67, Bra68, Thm68, Gi71) and in the Introduction by Thompson to the book Mo73.

Ion channelling rapidly found applications in studies of the lattice location of impurity atoms [Mat67, Eri67, Dav67, May67, May68, Cai68, Bj68, Eri69b]; fabrication of ion-implanted particle detectors [Mey67, Lae69a, Lae69b]; lattice disorder investigations [Bo68, Eri69a, Pic69b, Das69, Bo69, Ha69, Jo69, Wes69, etc]; nuclear reaction lifetime measurements (by blocking) [Brm68, Mar69, Kom69, Gi70]; and the determination of interatomic potentials [Lut66, Dat69, Ro69]. Such applied work shared the field with a continuation of more basic investigations during the next period of channelling experimentation.

Refinements to the understanding of the channelling process followed. The most important were the appreciation of 'flux-peaking' [Ale70, Ku70a, Do70, And71, Val71, Mo72] - the flux of ions is not constant across the channel space, but is greatest at the centre, with important implications for lattice-location experiments - and the investigation of dechannelling [Mor70a, Ac70, Ku70a, Fo70, Ku70b, Mor70b, Fu70, Fo71, Mor71, Cam71, and others], the group of processes by which ions pass from the 'aligned'

to the 'random' component of the beam.

Present-day investigations cover a wide field, including continuation of most of the lines of work which have been indicated above by their first few publications. The best general reviews are probably the book Mo73 and Gemmell's comprehensive review article Ge74. The latter contains references to all channelling publications up to 1973.

Although channelling has been established in a wide variety of elemental and compound crystals, a few substances have borne the brunt of investigations. By far the greatest number of experiments has been on silicon, followed by gold, tungsten, germanium, copper and various III - V compounds [Ge74, page 217]. The Group IV and III - V semiconductors are of obvious interest to industry, while W and Au have attracted investigators because of their negligible surface oxide thickness.

Ions ranging from protons to Au^{+} have been channelled, plus mesons and electrons - the latter conforming only approximately to the classical channelling theory.

1.2 MOTIVATION FOR THIS WORK

An important segment of channelling research has been the comparison of measured channelling parameters, chiefly critical angles and minimum yields, with theoretical predictions, and their intercomparison between different substances. Since the greatest volume of

work has been carried out on two elements in Group IV of the Periodic Table, both crystallizing in the diamond structure (Si and Ge), it is an obvious next step to perform measurements on the third such member of the Group, namely diamond itself, for purposes of comparison. Further, the Group III - V compound semiconductors, which have been quite well characterized by channelling (GaP, GaAs, GaSb, InSb), crystallize in the analagous zincblende structure. That few diamond channelling experiments have been reported [Pic69a, Dast9, Ga70, Das71, Se73), is probably due to the problems of procuring suitable samples in countries other than South Africa, and of obtaining consistent results with this material (see Section 5.1).

Although it is necessary to rely on natural samples, carbon tends to form large, good-quality single crystals, if impurities are absent, under natural conditions. Thus, samples which are sufficiently large, defect- and impurity- free for use in making valid channelling measurements may be obtained by a simple process of selection. (This will be considered further in Chapter 5.) There is no problem of substantial surface oxide layers, since the oxides of carbon are volatile. (But see Section 5.3).

Moreover, carbon has the lowest atomic number of those elements which can conveniently be obtained as single crystals (channelling studies on beryllium have only recently been reported [Kau75]). The channel potentials, and hence the critical angles, are therefore also low for a given ion and direction, and diamond provides an opportunity for verifying channelling theory in an extreme case.

Finally, diamond has a uniquely high Debye temperature of 1860±10 K (effective value, 0 - 800°C) [Vic62]. At room temperatures (∿300 K) the atomic vibration amplitudes are relatively small as will be the dechannelling by thermally displaced atoms. Diamond thus offers the opportunity to study channelling in an atomically 'cold' crystal, at room temperature. The situation is actually somewhat more complex, and will be discussed fully in §2.3.1.

1.3 OUTLINE OF THE THESIS

A review of theoretical channelling results is given in Chapter 2. This is not intended as an exhaustive treatise on the theory itself, but merely summarises those results of others to be used in subsequent analyses.

In Chapter 3, the apparatus is described, and the advantages of certain peculiarities of design are explained. Its mode of use to obtain the channelling measurements is outlined in the section on experimental methods.

Preliminary experiments were performed on silicon, and all information on these is encompassed in Chapter 4: target preparation, the experiments themselves and the results.

The thorny problems of the selection and preparation of the diamond specimens, so as to obtain results representative of pure diamond, are considered in Chapter 5. It is shown that ultimately the

only reliable index of crystal perfection is, for our purposes, the channelling experiments themselves. Techniques which have been developed for improving the perfection thus indicated, for regenerating beam-damaged crystals, and for surface cleaning, are described. The results of other diagnostic techniques are mentioned.

All problems related to the actual performing of the experiments, and the special techniques developed, are detailed in Chapter 6. These include problems of data-taking, of target contamination, and of the reproducibility of the data. This chapter and the previous one, on the question of ensuring the value of the data presented, take equal importance with the following chapters, on the results themselves.

Chapter 7 presents studies of the critical angles for channelling in diamond at room temperature. Measurements for different axes, planes, ion species, and ion energies were made and compared with the predictions of theory and with related results. In most cases the theory is in good agreement with experiment.

A study of the dependence of critical angles on temperature (for one ion species at one energy) is presented in Chapter 8. Theory predicts this dependence quite well, but improvements are suggested.

Measurements of the channelled minimum yields are considered in Chapter 9. Their temperature dependence appears to be well predicted by theory, and thermal vibrations appear to dominate over atomic size effects, despite the relatively small size of the former in diamond.

Some conclusions are made about the nature of the diamond surface as revealed by a channelled ion beam.

Chapter 10 is an abbreviated study of radiation damage in diamond. The main object was to ascertain that damage due to the ion beam would not interfere seriously with the channelling measurements.

Conclusions are drawn in Chapter 11 concerning the value and significance of the results, and the extracted parameters are summarised.

1.4 OUTLINE OF THE WORKING PERIOD

The period of data-taking divides roughly into three phases. Phase I was a preliminary phase, in which ion channelling effects were sought and investigated with simply constructed apparatus, taking only elementary precautions. The Mark 1 goniometer and the 1 MeV accelerator 'Phoenix' were used. All the silicon experiments, and the preliminary diamond experiments, belong to this period.

During Phase II, the special problems of obtaining good channelling results in diamond, were investigated systematically, and data-taking techniques were refined. The purpose-designed Mark 2 goniometer was used with the 1.4 MeV accelerator 'Christine' for this work.

This phase merged into Phase III, in which selected diamond channelling parameters were measured as precisely and accurately as

possible. Most of the quoted results come from this period, but it will sometimes be indicated that the earlier (and less accurate) results have been drawn upon. Apparatus modifications were slight, and Phase III continued to use the Mark 2 goniometer on the 1.4 MeV accelerator. The measurements were also extended to higher energies using a similar goniometer on the Unit's 6 MV Tandem van de Graaff accelerator.

Various aspects of the work reported herein have appeared in the form of contributions to conferences or as internal publications [Der70a, Der70b, Der71, Der74, Der75a, Der75b, Der75c, Der76a, Der76b, Der76c, Der77a, Der77b, Der78].

1.5 PROPERTIES OF DIAMOND

Well-known and well-established properties of diamond will be quoted in this thesis without reference. They can generally be found in the comprehensive book edited by Berman [Ber65], which is soon to be superseded by an updated and rewritten version [Fi78]. A useful brief summary of numerical values comprises the booklet Db73. Derived parameters which appear frequently in channelling calculations are tabulated in the Appendix.

CHAPTER 2

THEORY

2.1 NATURE OF ION CHANNELLING

If one handles a crystal model of the traditional 'ball and stick' variety, it is readily noticeable that it is very transparent in certain special directions. These are the directions of the major crystal axes, in which the atoms are arranged in rows, and to a lesser extent those of the major crystal planes, in which sheets of atoms appear. These observations point to the basic idea of ion channelling, that a beam of fast ions, directed at a crystal parallel to one of the major axes or planes, penetrates the crystal much more easily than it would in the amorphous solid or in a random direction in the crystal. That is to say, the stopping cross-section is less, the range is greater, and the nuclear encounter probability - the probability for a close interaction between an ion and a crystal atom nucleus - is drastically reduced.

The phenomenon, however, is not simply one of transparency. In that case the critical angle for channelling - the maximum misalignment between beam and chosen crystal direction - would be

$$\psi_c = \frac{\text{width of channel}}{\text{thickness of crystal}}$$

which is an almost unobservably small angle even for the thinnest obtainable crystals. Critical angles are, on the contrary, easily

observable (typically ~1°) and independent of crystal thickness. This is explained by the fact that, provided its incidence angle to a row is small, an ion can collide with a row (or plane) and be steered away from it: in fact, a typical channelled trajectory oscillates from side to side in a transverse potential well. This picture is exact for planes, but rows cannot confine the ion within a single tunnel, and it wanders laterally amongst the rows in an irregular spiral. (Illustrations depicting this can be found in Ro63b and Bra68.)

The essential part of this channelling picture is that the ion behaves as if it interacts with a smeared-out row potential or planar potential, rather than those of single atoms. This is known as the continuum model. What is happening on the level of individual atomic collisions is that the ion suffers a series of many correlated glancing binary collisions, each contributing a small deflection away from the channel wall. These ideas have led to the theory of channelling which is outlined below.

The inverse phenomenon, blocking, affects ions emitted from lattice sites, for example by nuclear reactions. Such ions are steered away from major axes and planes by a similar mechanism, and cannot emerge from the crystal in these directions. Blocking investigations of diamond are not included in this work.

The question of whether quantum-mechanical effects must be included in a description of channelling, was once a controversial one. It is now agreed that classical mechanics is adequate for all particles

heavier than electrons. Lindhard [Li65] showed that the accuracy of a classical treatment actually improves with increasing energy, in contrast to the case of single collisions.

2.2 CRITICAL ANGLES

2.2.1 The Continuum Model of Lindhard

The theory of ion-crystal interactions was developed chiefly by Lindhard circa 1964, soon after the first channelling experiments, and although modified or re-described by other workers it has in essence not been superseded. The main results are summarised in Li64 and the theory is presented in full in Li65. The contributions of many other workers are summarised and evaluated in Ge74 pp 135-140, from which the original references may be obtained.

The interaction potential between an ion of nuclear charge $Z_1 e$ and an isolated neutral atom of nuclear charge $Z_2 e$ may be written approximately as a function of their separation r in the Thomas-Fermi form

$$V(r) = (Z_1 Z_2 e^2/r)\, \phi(r/a_{TF}) \qquad (2.1a)$$

where cgs electrostatic units have been used. Several different approximate analytic forms for the screening function $\phi(r/a_{TF})$ have been proposed; the most accurate at the separations of interest in channelling theory is that of Molière [Mo47]

$$\phi(r/a_{TF}) = 0.1 \exp(-6.0r/a_{TF}) + 0.55 \exp(-1.2r/a_{TF}) + 0.35 \exp(-0.3r/a_{TF}) \quad (2.1b)$$

The Thomas-Fermi screening length a_{TF}, which effectively defines the range of the potential, is given by

$$a_{TF} = 0.4685 Z_2^{-1/3} \quad (2.2a)$$

if $Z_1 = 1$ or if the ion is fully ionised, and by

$$a_{TF} = 0.4685(\sqrt{Z_1} + \sqrt{Z_2})^{-2/3} \quad (2.2b)$$

otherwise.

In the continuum model of axial channelling, the individual ion-atom potentials may be replaced by an average along the row or 'string'; for an ion at a distance ρ from a static (that is, non-vibrating) row of atomic spacing d, the continuum potential is

$$V_{RS}(\rho) = \int_{-\infty}^{\infty} d^{-1} V(\sqrt{\rho^2 + z^2})\, dz$$

where z represents distance measured along the row. Using Eqn 2.1a,

$$V_{RS}(\rho) = (2Z_1 Z_2 e^2/d)\ f_{RS}(\rho/a_{TF}) \quad (2.3a)$$

where

$$f_{RS}(\xi) = \int_0^{\infty} \frac{\phi(\sqrt{\xi^2 + \eta^2})}{\sqrt{\xi^2 + \eta^2}}\, d\eta \quad (2.3b)$$

Lindhard [Li65] has proposed as a good analytic approximation, the 'standard potential', in which

$$f_{RS}(\xi) = \tfrac{1}{2} \log(C^2/\xi^2 + 1) \quad (2.3c)$$

with $C^2 = 3$.

In order to derive the conditions for validity of the continuum approximation, Lindhard [Li65] considered that the distance over which interaction with a string occurs should be large compared to d. For an ion approaching with velocity v at an angle ψ to a string, and interacting during a time Δt,

$$v \cos\psi \, \Delta t > d.$$

Considering the motion perpendicular to the string, with a minimum approach distance ρ_{min},

$$\Delta t = \rho_{min}/(v \sin\psi)$$

giving (for small ψ)

$$\rho_{min} > \psi d$$

The values of ρ_{min} and ψ are also connected by the requirement that energy be conserved in the transverse motion:

$$V_{RS}(\rho_{min}) = E \sin^2\psi \approx E\psi^2$$

where E is the energy of the ion on approach. The relationships may be solved simultaneously using Eqns 2.3a and 2.3c; since ρ_{min} is small if E is high enough, Eqn 2.3c is approximated to

$$f_{RS}(\rho/a_{TF}) = \log(Ca_{TF}/\rho_{min})$$

whence the solution is

$$\left(\frac{Ca_{TF}}{\psi d}\right) \exp\left(-\frac{\psi^2 dE}{2Z_1 Z_2 e^2}\right) = 1$$

As ψ increases, the inequality is first violated by the rapid decrease

of the exponential, provided that the other factor remains sufficiently large. So one must have

$$\psi < \psi_c$$

where ψ_c is a critical angle given by

$$\psi_c \approx \psi_1 \approx \left(\frac{2Z_1 Z_2 e^2}{Ed}\right)^{\frac{1}{2}} \qquad (2.4a)$$

The critical angle is ψ_1 provided that

$$\psi_1 \lesssim a_{TF}/d$$

which is equivalent to

$$E > 2Z_1 Z_2 e^2 d/a_{TF}^2$$

$\sim$ 8 keV for protons on diamond.

If the latter condition is not fulfilled, another critical angle may be defined, $\psi_c = \psi_2$, but the experiments to be reported in this thesis were well inside the high-energy region where $\psi_c = \psi_1$.

Lindhard himself referred to ψ_1 as the critical angle for applicability of the continuum approximation, rather than the critical angle for channelling (which he defined in a way different to that now current), but ψ_c has been found to be quite close to measured critical angles in the many channelling experiments which have been performed (see Section 1.1) and to give the right functional dependence on the variables contained in Eqn 2.4a.

What is normally measured experimentally is $\psi_{\frac{1}{2}}$, the half-width at

half-minimum of the channelling dip obtained by plotting the yield χ in a nuclear reaction experiment (for example, Rutherford scattering) against ψ. Although many workers have confused ψ_c and $\psi_{\frac{1}{2}}$, they differ systematically, and Lindhard proposed that

$$\psi_{\frac{1}{2}} = \alpha_R \psi_1 \qquad (2.4b)$$

where α_R is a constant, $\sim$ 1-2.

Lindhard pointed out that the existence of a critical angle results in the division of an incident beam into two quite well-defined, almost independent components:

i) The 'aligned beam', which has $\psi < \psi_{\frac{1}{2}}$. The ions move through the crystal leaving the strings at an angle equal to the angle of approach (that is, normal multiple scattering is suppressed). Thus the energy in the transverse motion (often loosely called the 'transverse energy'), given by

$$E_\perp = E\psi^2 + V_{RS}(\rho),$$

is conserved. The distance of closest approach to a string is never less than a critical value ρ_c; Lindhard suggested $\rho_c \sim a_{TF}$. Although this approximation is usually valid, ρ_c is not in fact determined by a_{TF}; it appears to be determined by the mean thermal vibration amplitude of the atoms (see §2.2.3 and §8.3.1).

ii) The 'random beam' has $\psi > \psi_{\frac{1}{2}}$. These ions interact normally with the solid, almost unaffected by the crystal lattice structure.

A continuum model for planar channelling was developed by Lindhard [Li65] and by Erginsoy [Erg65]. The continuum potential at a distance ρ from a plane of static atoms is

$$V_{PS}(\rho) = N_A \int_0^\infty 2\pi R dR \; V(\sqrt{\rho^2 + R^2})$$

where the distance R is measured in the plane from the foot of the perpendicular defining ρ, and

$$N_A = \text{areal density of atoms in plane}$$
$$= N_V d_p$$

where N_V = volume density of atoms

d_p = interplanar spacing.

Thus

$$V_{PS}(\rho) = 2\pi Z_1 Z_2 e^2 a_{TF} N_V d_p f_{PS}(\rho/a_{TF}) \qquad (2.5a)$$

where

$$f_{pc}(\xi) = \int_0^\infty \phi(\sqrt{\xi^2 + \eta^2})\, d\eta \qquad (2.5b)$$

Lindhard's treatment, considering a plane as a 'string of strings', leads to a planar critical angle

$$\left.\begin{aligned} \psi_c &= 0.93\, \psi_a \\ \psi_a &= (2\pi Z_1 Z_2 e^2 a_{TF} N_V d_p / E)^{\frac{1}{2}} \end{aligned}\right\} \qquad (2.6a)$$

One may relate this to the measured half-width of the planar channelling dip by

$$\psi_{\frac{1}{2}} = \alpha_p \psi_a \qquad (2.6b)$$

where $\alpha_p \sim 1$.

In the experimental chapters of this thesis, the half-angle $\psi_{\frac{1}{2}}$ will often loosely be referred to as the 'critical angle'. Since this is the only critical angle which will be considered there, no confusion should arise, but the relationships 2.4b and 2.6b may be borne in mind.

2.2.2 The Dip-Shape Calculations of Andersen

The above treatment does not explicitly contain a temperature dependence, which may be regarded as contained in the coefficients α_R and α_p. Their consideration is part of the broader problem of establishing the connection between a critical angle measured outside the crystal, say $\psi_{\frac{1}{2}}$, and the critical angle ψ_c defined inside the crystal by the continuum theory.

Lindhard [Li65] showed how temperature dependence and surface transmission could be included, and his expressions were evaluated numerically by Andersen [And67] to give detailed shape predictions for measured channelling dips. Lindhard had established the existence of a reversibility relationship between channelling and blocking experiments under idealised conditions, and Andersen's calculations were in fact carried out for the blocking situation, but the results should be equally applicable to channelling.

Particles of energy E were assumed to be emitted isotropically

by an atom displaced a distance ρ from its string or plane owing to thermal vibrations. A Gaussian distribution of displacements was assumed. By integrating over all displacements and emission angles, and applying conservation of transverse energy

$$E_T = E\psi^2 + V_{RS}(\rho) \quad \text{(axes)}$$

$$= E\psi^2 + V_{PS}(\rho) \quad \text{(planes)}$$

the distribution in transverse energy of the emitted particles was obtained. Lindhard [Lin65] has shown that in the axial case, transverse energy is strictly conserved only if calculated at the planes halfway between the atoms of the string, and this was done by Andersen. He assumed that the effect on the continuum potential due to adjacent rows or planes was negligible; this approximation is good for rows but not very good for planes.

Redistribution of the transverse energy during passage of the particles through the crystal was neglected. Spatial redistribution was taken into account: in the axial case the ions occupy their available channel cross-sectional area with uniform probability, but in the planar case, the probability is $(d\rho)^{-1}$.

Allowance for surface transmission was made by considering the fact that the particles are undeflected as they pass through the crystal surface. Thus the distribution in external angle is the same as the distribution in ψ just inside the crystal surface, and is obtained from the distribution in E_T by applying the transverse energy conservation relationship at this point:

$$E\psi^2 = E_T - V_{RS}(\rho) \quad \text{(axes)}$$

$$= E_T - V_{PS}(\rho) \quad \text{(planes)}$$

If only one string or plane is taken into consideration, the particles will continue to spread out from it and will pass through the crystal surface at large enough ρ that $V_{RS}(\rho)$ or $V_{PS}(\rho) \sim 0$. The distribution in external angle will then be obtained by putting

$$E\psi^2 = E_T$$

(This relationship also gives the distribution of mid-channel crossing-angles in the complete lattice, provided that the complete-lattice potential has been used and normalised to zero at mid-channel.) Andersen called this the angular distribution without allowance for surface transmission. It was found [And67, Pic69c] that inclusion of the surface transmission made little difference for axes but considerable difference for planes, reflecting the fact that $V_{RS}(\rho)$ is negligible over much of the channel space, but that $V_{PS}(\rho)$ is everywhere appreciable.

Agreement of the calculations with the shape of experimental dips was good, but the widths in these and other calculations (for example, Pic69c, And70) based on a single atomic row or plane, were generally about 25% larger than the experimental ones. Andersen and Feldman [And70] compared axial-channelling calculations based on the halfway-plane model, the simple continuum model, and a binary collision model. Agreement between the three was good; all disagreed similarly with experiment. Allowing all atoms in the string (and not just the emitter)

to vibrate, made very little difference to the results. It must be concluded that there is an intrinsic difference between isolated atomic rows and a full lattice.

2.2.3 The Analytical Expressions of Barrett

In a full lattice the continuum potential for strings becomes, in vector notation, with the i-th row positioned at $\underline{r}_i$,

$$U_{RS}(\underline{r}) = \sum_i V_{RS}(|\underline{r} - \underline{r}_i|) - U_{RS}^0$$

where U_{RS}^0 is subtracted in order to normalise the minimum value of $U_{RS}(\underline{r})$ to zero. Provided that the critical approach distance ρ_c can be defined, the energy conservation relationship for the transverse motion gives an exact expression for ψ_c:

$$E\psi_c^2 = U_{RS}(\rho_c)$$

Here ψ_c is to be measured in a field-free region, that is, either at mid-channel, or outside the crystal. Thus 'surface transmission' has been implicitly included.

Since $V_{RS}(\rho)$ is a rapidly decreasing function of distance, it is a good approximation in $U_{RS}(\rho_c)$ to neglect the contributions of neighbouring rows, and U_{RS}^0, that is, to replace $U_{RS}(\rho_c)$ by $V_{RS}(\rho_c)$. Then using Eqns 2.3a and 2.4a one obtains

$$\psi_c = [f_{RS}(\rho_c/a_{TF})]^{\frac{1}{2}}\psi_1$$

$$= F_{RS}(\rho_c/a_{TF})\psi_1$$

where

$$F_{RS}(\xi) = [f_{RS}(\xi)]^{\frac{1}{3}}$$

The function $F_{RS}(\xi)$ is tabulated for the Molière potential in Bar71 (as $R(\xi)$) and plotted in Ge74.

For a set of planes located at positions y_i (measured along the normal to the planes), the continuum potential becomes

$$U_{PS}(y) = \sum_i V_{PS}(|y - y_i|) - U_{PS}^{\infty}$$

and the critical angle is given by

$$E\psi_c^2 = U_{RS}(\rho_c)$$

provided that ρ_c can be defined. In this case at least two planes must be included in calculating $U_{PS}(y)$, and U_{PS}^{∞} cannot be neglected. For a pair of planes of identical composition, U_{PS}^{∞} is the potential at mid-channel. Then

$$U_{PS}(\rho_c) = V_{PS}(\rho_c) + V_{PS}(d_p - \rho_c) - 2V_{PS}(d_p/2)$$

giving, via Eqns 2.5a and 2.6a,

$$\psi_c = F_{PS}(\rho_c/a_{TF},\ d_p/a_{TF})\psi_a$$

where

$$F_{PS}(\xi,\eta) = [f_{PS}(\xi) + f_{PS}(\eta - \xi) - 2f_{PS}(\eta/2)]^{\frac{1}{2}}$$

The function $F_{PS}(\xi,\eta)$ is presented graphically in Bar71 and Ge74.

Analytic calculations including the full lattice are prohibitively complex, and the most fruitful approach for further refinement of channelling predictions has been the Monte Carlo technique of Barrett [Bar68, Bar71]. Barrett performed computer simulations, mainly for tungsten, and fitted the results for ψ_1 by analytic expressions based on the full-lattice treatment outlined above, using two adjustable parameters (k and m) [Bar71]. He determined optimum values for k and m, and the resulting semi-empirical relationships have been shown to describe experimental ψ_1 data for a wide variety of ion-target combinations.

Barrett warned that "although physical intuition suggested [the forms of the expressions used], it should be recognised that they have been used to provide empirical curves expressing the results of the Monte Carlo calculations. Caution should be exercised in drawing conclusions therefrom". However, their good agreement with many experiments implies that they can in fact be regarded as describing the physical situation. Barrett's approach was tantamount to defining the critical approach distance ρ_c as being directly proportional to u_1, the root-mean-square thermal vibration amplitude in one dimension of the atoms bordering the channel, and to setting ψ_1 proportional to the resulting value of ψ_c. The two proportionality constants were used as the adjustable parameters:

$$\rho_c = mu_1$$

$$\psi_1 = k\psi_c$$

Thus Barrett's expressions are:

For axes:

$$\psi_{\frac{1}{2}} = k\, F_{RS}(mu_1/a_{TF})\ \psi_1$$

$$= k\, F_{RS}\left(\frac{mu_1}{a_{TF}}\right)\left[\frac{2Z_1 Z_2 e^2}{Ed}\right]^{\frac{1}{2}} \qquad (2.7)$$

For planes:

$$\psi_{\frac{1}{2}} = k\, F_{PS}(mu_1/a_{TF},\ d_p/a_{TF})\ \psi_a$$

$$= k\, F_{PS}\left(\frac{mu_1}{a_{TF}},\ \frac{d_p}{a_{TF}}\right)\left[\frac{2Z_1 Z_2 m_u v^2 a_{TF} N_v d_p}{E}\right]^{\frac{1}{2}} \qquad (2.8)$$

The optimum values which Barrett assigned to k and m are listed in Table 2.1.

TABLE 2.1

Values of Barrett's Fitting Parameters

Channels	Dependence Fitted	k	m
Axes (Eqn 2.7)	Temperature	0.83	1.2
	Ion and energy	0.80	1.2
Planes (Eqn 2.8)	Temperature	0.76	1.6
	Ion and energy	0.72	1.6

2.2.4 Other Theoretical Treatments

Using the halfway-plane model of axial channelling, Lindhard [Li65] considered the exactness of the conservation of transverse energy, and concluded that E_T is closely conserved if

$$E \gg \frac{d^2}{8}\left(\frac{\partial^2 U}{\partial \rho^2}\right)_{\rho=\rho_c}$$

Varelas and Sizmann [Var72] showed that the analyses of several other workers could be summarised by similar formulae with the factor $\frac{1}{8}$ replaced by a different factor, that is, they differed essentially in the degree of accuracy with which E_T was required to be conserved. Varelas and Sizmann therefore performed binary-collision calculations in order to investigate fully the accuracy of the conservation under different conditions, and thereby to determine critical approach distances ρ_c and critical angles ψ_c for applicability of the continuum model. They were able to extend their calculations to rows with non-uniform spacing and mixed atomic species by the use of suitable combined parameters, obtaining slight differences from results using simple averages of d, Z_2, etc.

Their results for ρ_c and ψ_c as universal functions of a reduced energy parameter are presented graphically in Var72, together with a procedure for including the effect of thermal vibrations. Agreement between calculated values of ψ_c and a large variety of experimental values of ψ_1 is shown to be fairly good. It becomes much better if the ψ_c's are multiplied by the Barrett factor k (§2.2.3), regarding this as a generally-applicable conversion factor between ψ_c and ψ_1.

Morgan and Van Vliet have published a series of papers (for example, Mo70) based on computer simulations of protons channelling in copper, with the results interpreted in terms of the continuum model, and expressed by analytic formulae. Starting with the criterion for the conservation of E_T in axial channelling i the form

$$E = \frac{d^2}{5}\left(\frac{\partial^2 U}{\partial \rho^2}\right)_{\rho=\rho_c}$$

they found that a good approximate solution for the minimum approach distance ρ_c (in a static lattice) w

$$\rho_c/a_{TF} = (2/3)\sqrt{\alpha}(1 - \sqrt{\alpha}/19 + \alpha/700)$$

in terms of the dimensionless parameter

$$\alpha = \frac{Z_1 Z_2 e^2 d}{E\, a_{TF}^2}$$

The same procedure could be used for static planes with d replaced by an effective value $\bar{d}$. Empirical expressions were given in Mo71 for adding the effects of thermal vibration to ρ_c, which could then be inserted in the continuum potential to yield critical angles ψ_c.

The expression suggested for $\bar{d}$ is proportional to a logarithmic term whose argument depend inversely on E; for proton on diamond it becomes <1, and $\bar{d} < 0$, for E 168 keV. This is well below the energies of the present investigation, and precluded any comparison with the planar data. A comparison of axial ρ_c values with those calculated by the methods of Barrett and of Varelas and Sizmann indicated that for

axes, too, Morgan and Van Vliet's approximations are rather far from their region of validity if applied to diamond.

2.3 MINIMUM YIELDS

2.3.1 The Predictions of Lindhard

The yield of close-encounter nuclear processes never falls to zero at the bottom of a channelling dip; its minimum value, normalised to that for a non-channelled beam, is denoted by χ_{min}. The least value of χ_{min}, and the one most easily considered theoretically, is that for ions which have interacted just under the crystal surface, where dechannelling has not yet become important.

Lindhard [1165] pointed out that in the continuum approximation, the yield due to thermal vibrations never vanishes, and that its minimum value (for a beam incident parallel to axial channels) is

$$\chi_1 = N_V d\pi u_2^2$$

where u_2 is the RMS thermal vibration amplitude in two dimensions, $u_2 = \sqrt{2}\, u_1$. This gives a first estimate for χ_{min}.

A second estimate was obtained by considering the division of a beam into aligned and random parts on passing through the crystal surface. If the random beam consists of ions which passed within $\sim a_{TF}$ of the strings and were deflected by angles $\sim \psi_c$, this leads to a second contribution to χ_{min}:

$$\chi_2 \approx N_V d\pi a_{TF}^2$$

Lindhard regarded χ_2 as a more tentative proposal than χ_1.

Possible amorphous layers on the surface of the crystal might scatter the beam sufficiently to add a third contribution, χ_3. Lindhard's estimate for χ_3 is given in the form used by Barrett as Eqn 2.13.

Thus the overall estimate for χ_{min} becomes

$$\chi_{min} = \chi_1 + \chi_2 + \chi_3$$
$$= N_V d\pi u_1^2 + N_V d\pi a_{TF}^2 + \chi_3 \qquad (2.9)$$

This formula is not obeyed very well (it may be compared with the more accurate Eqn 2.10). It predicts $\chi_1 \sim \frac{1}{3}\chi_2$ for many substances, so that χ_1 was often neglected in experimental comparisons, and discrepancies blamed on χ_3.

Lindhard's prediction for planar minimum yields was the geometrical factor analagous to χ_2 for axes:

$$\chi_{min} \sim 2a_{TF}/d_p \qquad (2.9')$$

Both Eqn 2.9 and Eqn 2.9' generally produce underestimates of the measured values, often ascribed to the effect of surface layers. However, it is evident that Lindhard did not expect them to be accurate.

2.3.2 The Expressions of Barrett

Barrett's Monte Carlo calculation technique [Bar71] was able to

show that a simple geometrical interpretation of the minimum yield is untenable (see §9.4.2 for an explanation). Barrett fitted the following expression to his calculations for axial channelling:

$$\chi_{min} = N_V d\pi (Cu_2^2 + C'a_{TF}^2)\sqrt{1 + \zeta^{-2}} + \chi_3 \qquad (2.10)$$

The coefficients C and C' are functions of beam divergence, but approach constant values if this is small. The best-fit values were found to be

$$C = 3.0 \pm 0.2 \qquad C' = 0.2 \pm 0.1$$

The square-root factor takes account of the fact that the effective number of surface layers 'seen' by the beam is greater than one, and increases (weakly) with energy;

$$\zeta = \frac{2.2u_1}{\psi_1 d} \qquad (2.11)$$

was found to provide a good fit. The effective number of surface layers in this model is

$$L = \sqrt{1 + \zeta^2} \qquad (2.12)$$

Here the spacing of the layers is the same as the string spacing for the axis concerned.

Amorphous layers, however, contribute directly to χ_3:

$$\chi_3 = \sum_i n_i N_V d\pi \left[\frac{Z_1 Z_i e^2}{E\psi_1}\right]^2 \qquad (2.13)$$

where n_i is the number of layers with atomic number Z_i, and the spacing

of the layers is to be taken equal to the string spacing d. (This is a much larger value than a spacing calculated from the layer density, especially for higher-order axes.)

An expression similar to Eqn 2.10 has been derived from Lindhard's halfway-plane model by including the effects of neighbouring rows [Kb73]. Comparisons of the temperature dependence of χ_{min} with Eqn 2.10, for protons and deuterons backscattered from silicon and germanium [Kom71], have confirmed that $C \approx 3.0$ and $C' \approx 0$.

Barrett did not determine a general expression to give χ_{min} for planar channelling, but he performed some Monte Carlo calculations for protons on tungsten which showed a linear relationship between χ_{min} and u_1. If by analogy with Eqns 2.9' and 2.10 (neglecting surface effects) one assumes a relationship of the form

$$\chi_{min} = 2/d_p(Bu_1 + B'a_{TF})$$

then one can extract values of B and B' from Barrett's graph:

$$B = 2.2 \qquad B' = 0.6$$

It is not known whether they would be applicable to other substances.

2.3.3 Other Theories

Morgan and Van Vliet [Mo70, Mo71] suggested using their critical approach distance for stable channelling, r_c, determined in the manner indicated in §2.2.1, in a simple geometrical formula analagous to Eqn 2.9':

$$x_{min} = 2\rho_c/d_p$$

Barrett [Bar⁻1] showed that if one used a geometrical interpretation, the parameter ρ_c occurring in the minimum yield was not exactly equal to the ρ_c determining the critical angle. A comparison with Morgan and Van Vliet's prediction could not be made for diamond planes because of the breakdown of their approximations (see §2.2.4).

2.3.4 The Thermal Vibrations of Diamond

It was mentioned in Section 1.2 that diamond has exceptionally small thermal vibrations at room temperature (and therefore provides an interesting matrix for channelling studies). This statement needs clarification, since the absolute magnitude of the RMS vibration amplitude u_1 (calculated by the Debye theory) is quite appreciable, about half that of a typical metal such as copper (Table 2.2). The same

TABLE 2.2

Some Properties of Diamond and a Typical Metal

	u_1 (Å) @ 300K	a (Å)	a_{TF} (Å)	u_1/a_{TF}
Diamond	0.044	3.567	0.258	0.17
Copper	0.084	3.615	0.152	0.55

comment applies to u_1 relative to the lattice constant, a, which has a similar magnitude for diamond and most cubic metals.

It can be seen from Eqn 2.10 that what is important for channelling minimum yields is the value of u_1 relative to the range of the atomic potential as measured by the Thomas-Fermi screening distance a_{TF}. Diamond has one of the largest values of a_{TF} (see Table 2.2) owing to its inverse cube root dependence on Z_2 (Eqns 2.2). In Eqn 2.10, $C \gg C'$, so that in most substances at ordinary temperatures, where u_1 (and therefore u_2) is $\approx a_{TF}$ typically (see Ge74, p 217), the thermal term (χ_1) predominates greatly over χ_2. In fact Barrett suggested taking

$$C = 3.0 \pm 0.3 \qquad C' \approx 0$$

In diamond $u_1 \ll a_{TF}$ and Eqn 2.10 predicts that χ_1 and χ_2 will be about equal. So the magnitude of C' can be assessed more precisely than has hitherto been possible. It is also of interest to see whether the above value of C still holds in the extreme case of diamond.

The small value of u_1 relative to a_{TF} also has interesting implications concerning critical angles. Lindhard [Li65] originally proposed that channelling was governed by a critical approach distance to rows or planes, $\rho_c \approx a_{TF}$ (§2.2.1), but the spirit of Barrett's work [Bar71] indicates that $\rho_c \approx u_1$ (§2.2.3). The temperature dependence of critical angles supports the latter, but the question cannot be resolved directly because $a_{TF} > u_1$ for most substances. In diamond the evidence is unequivocal because of the large difference between u_1 and a_{TF}.

2.4 BACKSCATTERING ANALYSIS

2.4.1 Identification of Surface Layers

In large-angle Rutherford scattering, the energy of a scattered ion E_{scatt} is related to its incident energy E_{inc} by

$$E_{scatt}/E_{inc} = K^2$$

$$= [(M_1\cos\theta_L + \sqrt{M_2^2 - M_1^2\sin^2\theta_L})/(M_1 + M_2)]^2 \qquad (2.14a)$$

where M_1 = mass number of incident ion

M_2 = mass number of scatterer atom

θ_L = scattering angle in laboratory co-ordinates.

Thus if a solid, bearing surface layers with different values of M_2, is analysed by ion scattering, the different values of E_{scatt} observed enable identification of the atomic species present. For this purpose Eqn 2.14a may be rearranged to read

$$M_2 = M_1(\varepsilon - 2\sqrt{\varepsilon}\cos\theta_L + 1)/(1 - \varepsilon) \qquad (2.14b)$$

where $\varepsilon = E_{scatt}/E_{inc}$.

By differentiating Eqn 2.14a with respect to M_2, the condition for optimum energy resolution between adjacent mass-numbers may be found. For the present work ($\theta_L \sim 180°$ or 155°) this is

$$M_2/M_1 \sim 2.$$

Thus α-particles ($M_1 = 4$) are a reasonable choice for analysing impurity layers with similar mass-number to carbon ($M_2 = 12$).

2.4.2 Quantifying Surface Layers

The number of atoms per unit area N_A in a surface layer may be determined by comparing the number of counts in its peak in the scattered energy spectrum, with the number of counts per unit depth due to scattering by the substrate (of known density). Allowance must be made for the quadratic dependence of the Rutherford scattering cross-section on atomic number, so that the atomic species must first be determined as in §2.4.1. The method of analysis is developed in, for example, Mey70. The result for diamond is

$$N_A = \frac{P}{\Delta S} \Delta E_2 \left[\frac{dz}{dE_2}\right]\left[\frac{Z_C}{Z_i}\right]^2 \frac{\rho_{Di} N^*}{M_C} \cos\theta_L \qquad (2.15)$$

where

P = counts in surface-layer peak

ΔS = counts per channel in substrate spectrum

ΔE_2 = energy width per channel of spectrum

$\frac{dz}{dE_2}$ = energy to depth conversion factor

Z_C = atomic number of carbon

Z_i = atomic number of i-th layer

ρ_{Di} = density of diamond

N^* = Avogadro's number

M_C = mass number of carbon

This may be converted into 'number of monolayers' provided a value for the layer density is assumed. A reasonable value in typical cases seems to be

$$N_A \text{ (monolayer)} = 2 \times 10^{15} \text{ atoms cm}^{-2}.$$

2.4.3 Energy to Depth Conversion

For an extended solid rather than a layer, most ions penetrate before scattering, losing energy by ionising and exciting the target atoms on both the inward and outward journeys, and being detected at progressively lower energies as the depth of the scattering event increases. The resulting energy spectrum thus contains depth information, and may be converted to a 'depth spectrum' provided the form of the energy-depth relation can be approximated. The geometry is illustrated in Figure 2.1; the relation between emergent energy $E_2(z)$ and scattering depth z (measured along the beam trajectory) is of the form

$$E_2(z) = K^2[E_0 - \Delta E(0 \to z)] - \Delta E(z \cos\theta_1/\cos\theta_2 \to 0) \qquad (2.16)$$

where the ΔE's are the energy losses along the paths indicated, and are functions of energy.

It is usual to evaluate Eqn 2.16 by the method of Bøgh [Bo68, Bo69]. In the present work, the approximate relation between range R and energy E given by Zaidins [Za74] has been used:

$$R = \frac{0.585\, E^{\alpha/2}}{C[1 - \exp(-3/7.4)]}$$

The best-fit values of C and α have been tabulated by this author for various projectiles and targets; for protons on diamond they are

$$C = 0.08026 \qquad \alpha = 8.9$$

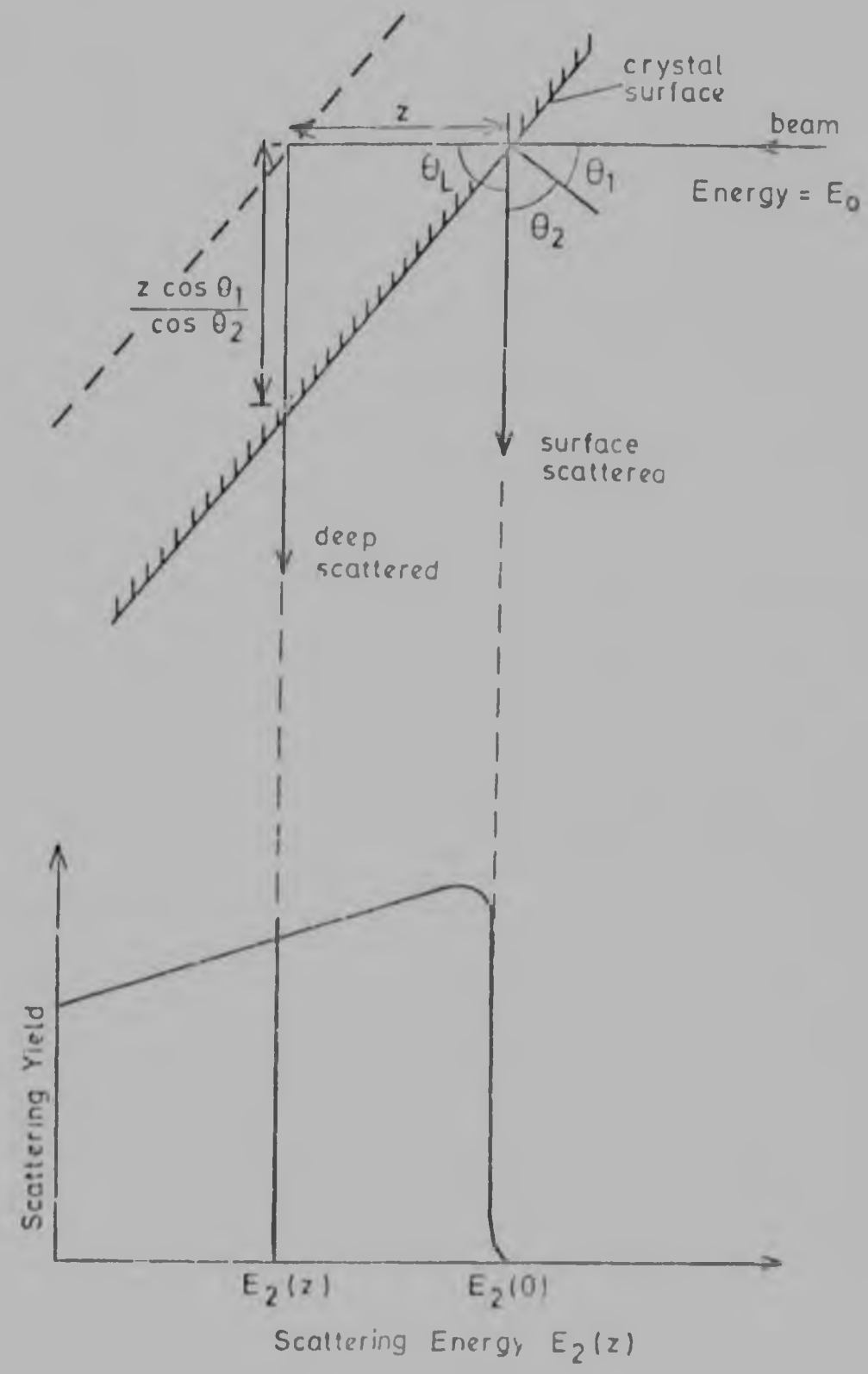

Figure 2.1: Schematic diagram showing relationship between beam penetration and backscattered energy spectrum (after Bo68).

when E is in MeV and z is in μm.

The mode of use of Eqn 2.17 was that suggested in Za74. If an ion with initial energy E_0 slows down to an energy E_1 in passing through a thickness z of a solid, then the initial range $R(E_0)$ is related to the residual range $R(E_1)$ by the equation

$$R(E_0) = R(E_1) + z \qquad (2.17b)$$

For given input parameters E_0 and z, this equation may be solved for E_1 with the aid of Eqn 2.17a, using the Newton-Raphson method to derive E_1 from $R(E_1)$.

After scattering at depth z, the energy is K^2E_1, and this is the 'initial energy' for the outgoing path (which has a length $z\cos\theta_1/\cos\theta_2$ according to Figure 2.1). A second application of Eqns 2.17a and 2.17b yields the exit energy E_2. (The procedure is equivalent to determining the values of ΔE for the ingoing and outgoing paths in Eqn 2.16.) In this way, for a series of depths z, a series of detected energies E_2 was determined, and the scattered particle spectrum divided up into a series of energy steps; the z-steps were of equal size resulting in unequal E_2-steps. The integrated spectral count in each energy interval was assigned to the corresponding value of z. The depth-conversion procedure was carried out by computer as part of the programme CHANSPEC [Rea77b] referred to in §7.2.3.

2.5 RADIATION DAMAGE EXTRACTION

2.5.1 General

The principle of the method by which crystal damage profiles may be extracted from channelling measurements was first outlined by Bøgh [Bo68]. Bøgh made approximations appropriate to a shallow, thin layer, namely a constant stopping-power and negligible dechannelling for ions traversing the layer. The theory has been expanded by many other workers (notably Ziegler [Zi72a], Schmid [Sc73], and Walker et al [Wal77] for application to deeper damage layers and to include reasonable models of the dechannelling. There seems to be no shortage of confusion in many of the treatments as to what each step in the analysis is doing.

Bøgh originally applied his analysis to amorphous surface oxide layers; Quéré [Qu76] has emphasised that it is only in the case of randomly disordered atoms that an analysis of this type gives an accurate measure of the number of atoms not on lattice sites (see Section 10.1). In other cases, although the disorder parameter appearing in the equations tales the form of a 'relative number of disordered atoms', it may not be quantitatively interpreted as such. Rather, it represents the 'degree of disorder' expressed in arbitrary units.

The major problem in extracting damage profiles is to find an appropriate model for the dechannelling due to the damage, which enters into the calculations as shown in §2.5.2. Most calculations have assumed dechannelling either by a single scattering event (which underestimates the dechannelling) or by multiple scattering (which overestimates it); scattering by a small number of events, known as plural scattering, has

sometimes been used, and is evidently the most appropriate model, but the analysis is more complicated. Ziegler [Zi72a] and Walker et al [Wal77] have shown that the extracted damage profiles are rather insensitive to the type of scattering assumed, provided than an adjustable parameter is used to force the extracted damage to zero at depths beyond those where the damage has occurred. Without this precaution, the disorder parameter continues to be positive at greater depths in the single scattering model, and becomes negative if multiple scattering is used.

2.5 2 Method

The approach taken here is based most closely on that of Ziegler [Zi72a] and Schmid [Sc73]. A backscattered spectrum for ions channelled in a crystal with a buried damage layer, is illustrated schematically in Figure 2.2; such spectra are described more fully in §10.3.1. The ordinate is assumed here to have been normalised to the random yield (§7.2.2), and the abscissa to have been converted from an energy to a depth scale (§2.4.3 and §7.2.1). The peak in the yield results from ions backscattered in the damage layer, and is due both to ions dechannelled into the random beam and then backscattered by normal interactions with the crystal, and to channelled ions backscattered directly by displaced atoms. The two contributions are assumed to be additive (an approximation), so one can write for the damaged crystal yield $\chi_d(z)$ as a function of the depth z:

$$\chi_d(z) = f(z) + g(z) \qquad (2.18)$$

The fraction of ions which is in the random beam is

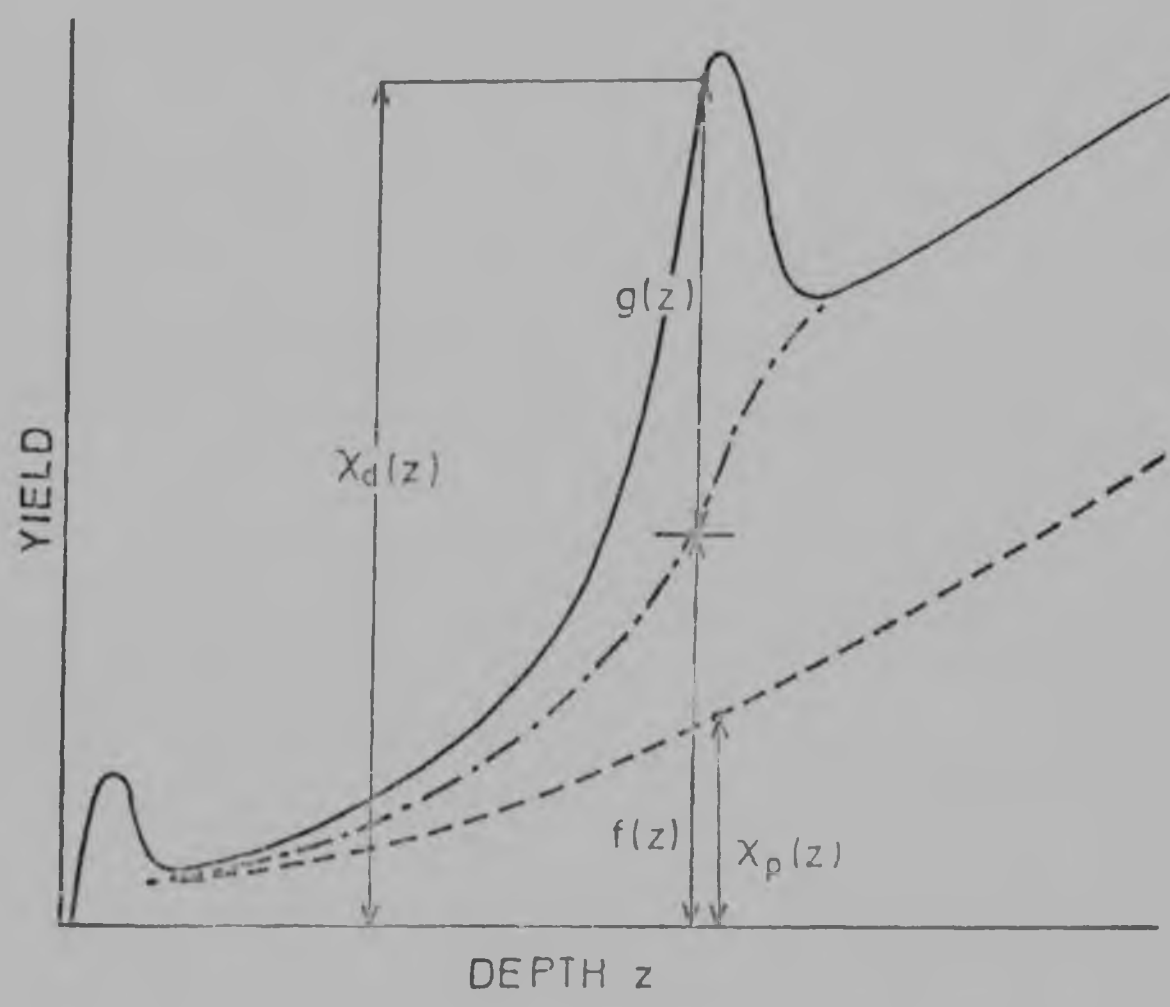

Figure 2.2: Schematic diagram showing quantities involved in extracting damage profiles from channelled spectra:

– 'damaged' spectrum (depth converted) $\chi_d(z)$

-·- dechannelling function f(z)

--- 'undamaged' spectrum $\chi_p(z)$

$$f(z) = \chi_p(z) + F(z) \tag{2.19}$$

where $\chi_p(z)$ is the dechannelled fraction which would occur even in a perfect crystal, that is, the channelled minimum yield of a perfect crystal measured at the same depth; $F(z)$ is the fraction of ions which has been dechannelled by the damage.

The fraction of ions which is backscattered directly out of the channels is

$$g(z) = [1 - f(z)]n(z) \tag{2.20}$$

where $[1 - f(z)]$ is the fraction of the beam which was still channelled, and $n(z)$ is a parameter measuring the disorder; in the special case where the atoms are randomly disordered it is equal to their volume density $N_d(z)$ relative to the atomic density of the crystal, $n(z) = N_d(z)/N_V$. Flux peaking is here neglected so $n(z)$ will be some average across the channel space.

Ziegler [Zi72a] suggested setting the dechannelled fraction $F(z)$ proportional to the cumulative damage encountered by the beam from the crystal surface up to the depth z. Schmid [Sc73] suggested a proportionality to the cumulative sum of $g(z)$ and pointed out that this (dechannelling - direct backscattering) is a result of the single scattering model. Thus

$$F(z) = \kappa \sum_{z'=0}^{z} g(z') \tag{2.21}$$

where κ is to be adjusted to ensure that $\eta(z)$ becomes zero beyond the damage peak.

The functions $f(z)$ and $g(z)$ each depend on the other; if the depth range is divided up into small increments, and the value of $f(z)$ is determined from $\Sigma g(z)$ accumulated up to the previous depth interval, then they may be evaluated step-wise with respect to depth. The use of computer iteration to optimise κ is described in §10.5.1. In each depth interval, the disorder parameter is calculated:

$$\eta(z) = \frac{\chi_{\parallel}(z) - f(z)}{1 - f(z)} \qquad (2.22)$$

It may be integrated with respect to depth to provide an indicator of the total damage in the crystal.

It is generally necessary to apply a correction for the different energy loss rates of channelled and non-channelled ions, which lead to their having different Rutherford cross-sections ($\propto 1/E^2$) at the same depth. This was not necessary for the present work because the two energy loss rates could be taken as equal, to a good approximation (§7.2.1).

CHAPTER 3

APPARATUS AND METHODS

3.1 GENERAL CONSIDERATIONS

Any ion channelling experiment has two essential requirements, in addition to the requirements of a normal scattering experiment (viz. vacuum apparatus, detectors, etc):

i) a parallel beam of ions, that is, with a divergence substantially less than the expected critical angles for the ion-target combinations to be investigated.

ii) a means of orientating the crystal over the entire solid angular range of interest, with an angular accuracy substantially less than the expected critical angles. Two perpendicular rotation axes are the minimum requirement for any orientation to be attainable.

The first requirement is satisfied by passing the beam through a collimation system having two small apertures separated by a long flight-tube, so that only ions with less than the required path divergence are transmitted. The second requirement may be met by a suitable goniometer, which must be capable of operating in vacuum.

Two such sets of apparatus were used, described in Sections 3.2 and 3.3. The basic procedures for obtaining channelling data are

outlined in Section 3.4.

3.2 GONIOMETER MARK 1 AND ACCESSORIES

3.2.1 Goniometer

Apparatus for the preliminary channelling experiments of Phase I (see Section 1.4) was built around a conventional X-ray goniometer (Pye Unicam S34). This has two perpendicular rotation axes of ±30° range, with vernier readout having a least count of 10' of arc (0.17°). A third rotation axis of 360° range was provided by making the entire goniometer mounting-plug rotatable by means of a worm-and-wheel arrangement. This could be set and read to 0.02° although the accuracy was probably less over long distances.

The Unicam goniometer also has two perpendicular translation axes, which were supplemented by a home-made third axis and used for centring the target in the beam.

The four movements provided by the manufacturer were operated manually from outside the vacuum via flexible cables rotated by shafts passing through the vacuum wall by means of well-lubricated O-ring seals. The arrangement is shown in Figure 3.1.

A clip was added to the goniometer to accept standard microscope cover-slips, which were used as target-holders. These had a hole etched in the middle, over which the silicon or diamond sample was fixed with Apiezon wax. A thin wire was attached for measuring the target current.

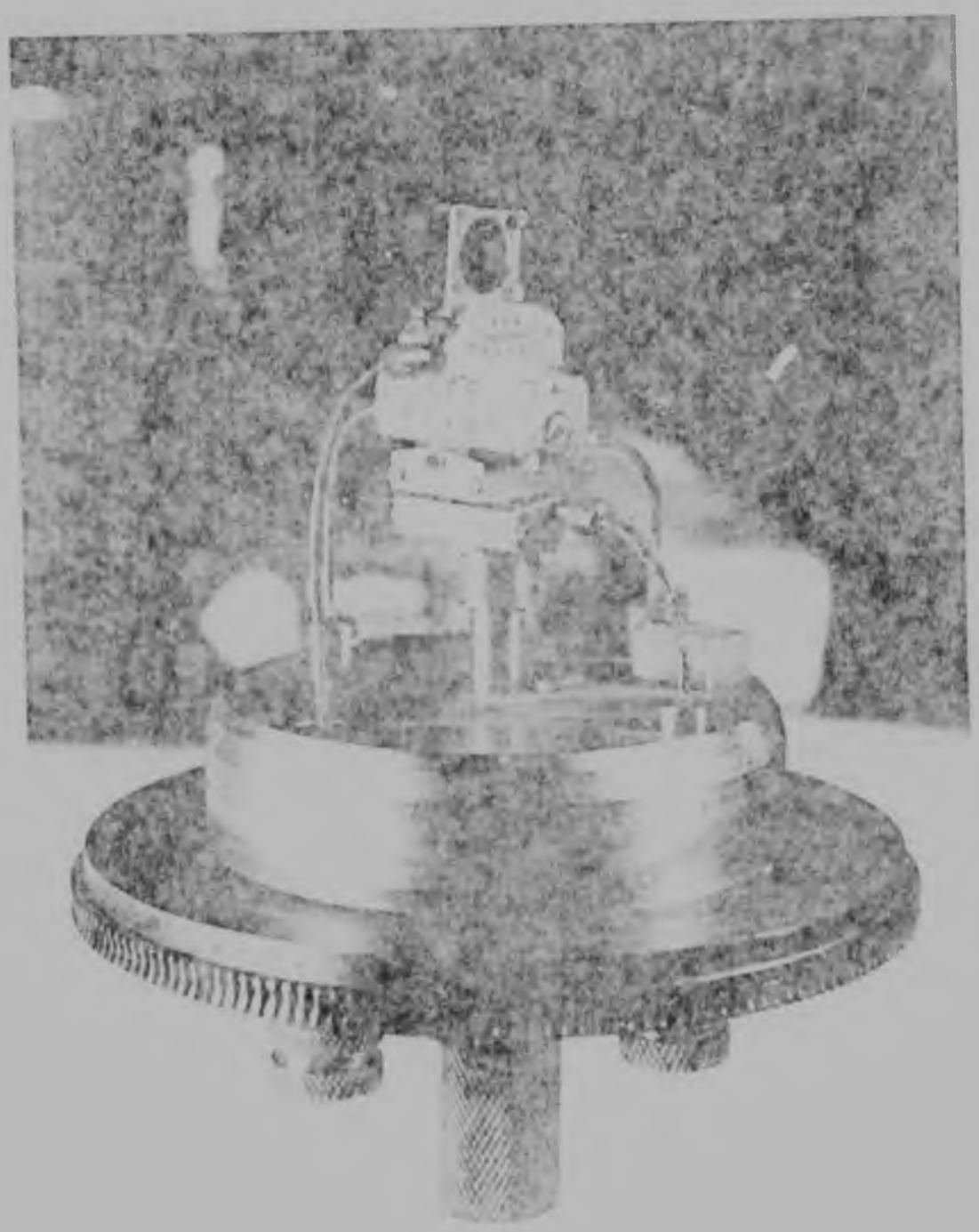

Figure 3.1: Pyranometer

3.2.2 Beam-line Hardware

The plug carrying the goniometer and drives fitted into the top of a scattering-chamber which was substantially the one used with the second goniometer, and is described thereunder (§3.3.2).

The beam-line was somewhat different to that subsequently adopted, and is shown diagrammatically in Figure 3.2. The focused beam from the accelerator was collimated by two variable tantalum collimators placed 2.0 m apart, and then struck a thin carbon or nickel foil. This was used after the manner of the Harwell/Sussex group (see, for example, Dea63) to attenuate the beam and also to spread it (by electron multiple scattering) so as to reduce the sensitivity of the alignment to slight accidental shifts of the beam-line components. A third tantalum collimator 2.0 m downstream, at the chamber entrance, served to define the divergence of the beam at the crystal (in combination with the diameter of the beam-spot on the foil). With all three apertures set at 1 mm in diameter, the half-angle of divergence was 0.029°.

A small surface-barrier detector was placed to count particles scattered through 90° by the foil, and served to normalise the runs to a fixed number of particles incident on the crystal. This indirect monitoring arrangement was not entirely satisfactory because of contamination build-up on the foil and the presence of pinholes, and the foil was eventually dispensed with. The beam-current on the target was then monitored directly using a current integrator.

A vacuum of $\sim 2 \times 10^{-6}$ torr was maintained in the beam-lines by

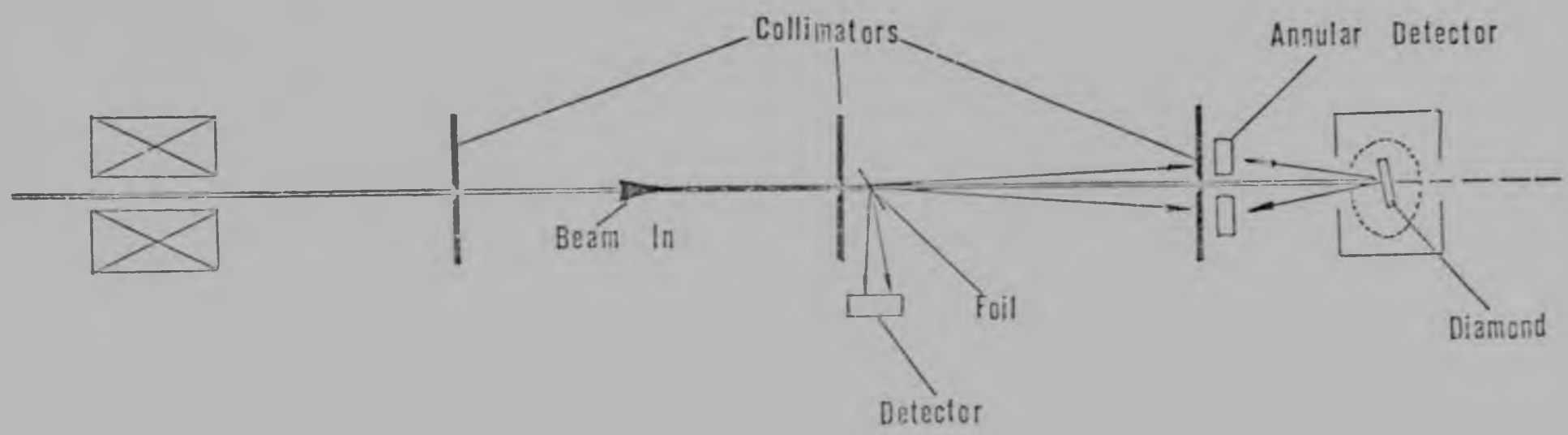

Figure 3.2: Schematic diagram of beam-line used for the Phase I experiments.

two trapped oil-vapour diffusion pumps. In an effort to reduce contamination, a copper cylinder was placed round the target and attached to a cold-finger.

3.2.3 Detector and Electronics

Particles backscattered from the target crystal were detected by a 150 mm² annular surface-barrier detector, Ortec Model 150-300, through which the incident beam passed. A special mask prevented particles from being detected at the edges of the active area, where resolution might be poorer. The measured resolution was 30 ± 2 keV (FWHM) for 5.477 MeV α-particles, and the scattering angle was 170 - 175°. The detector fed a similar electronic set-up to that described in §3.3.3.

3.2.4 Accelerator

Beams of protons and singly-ionised helium for the Phase I experiments were obtained from the Nuclear Physics Research Unit's 1 MeV Cockcroft-Walton accelerator 'Phoenix'. Manufactured by Philips, it has been described by Renan [Ren72], and is now retired.

3.3 GONIOMETER MARK 2 AND ACCESSORIES

3.3.1 Goniometer

In order better to fulfil the experimental requirements, a new goniometer was designed, based on the one developed by Bell Telephone Laboratories [Au71] for their channelling experiments. It is shown diagrammatically in Figure 3.3. Two perpendicular rotations of the

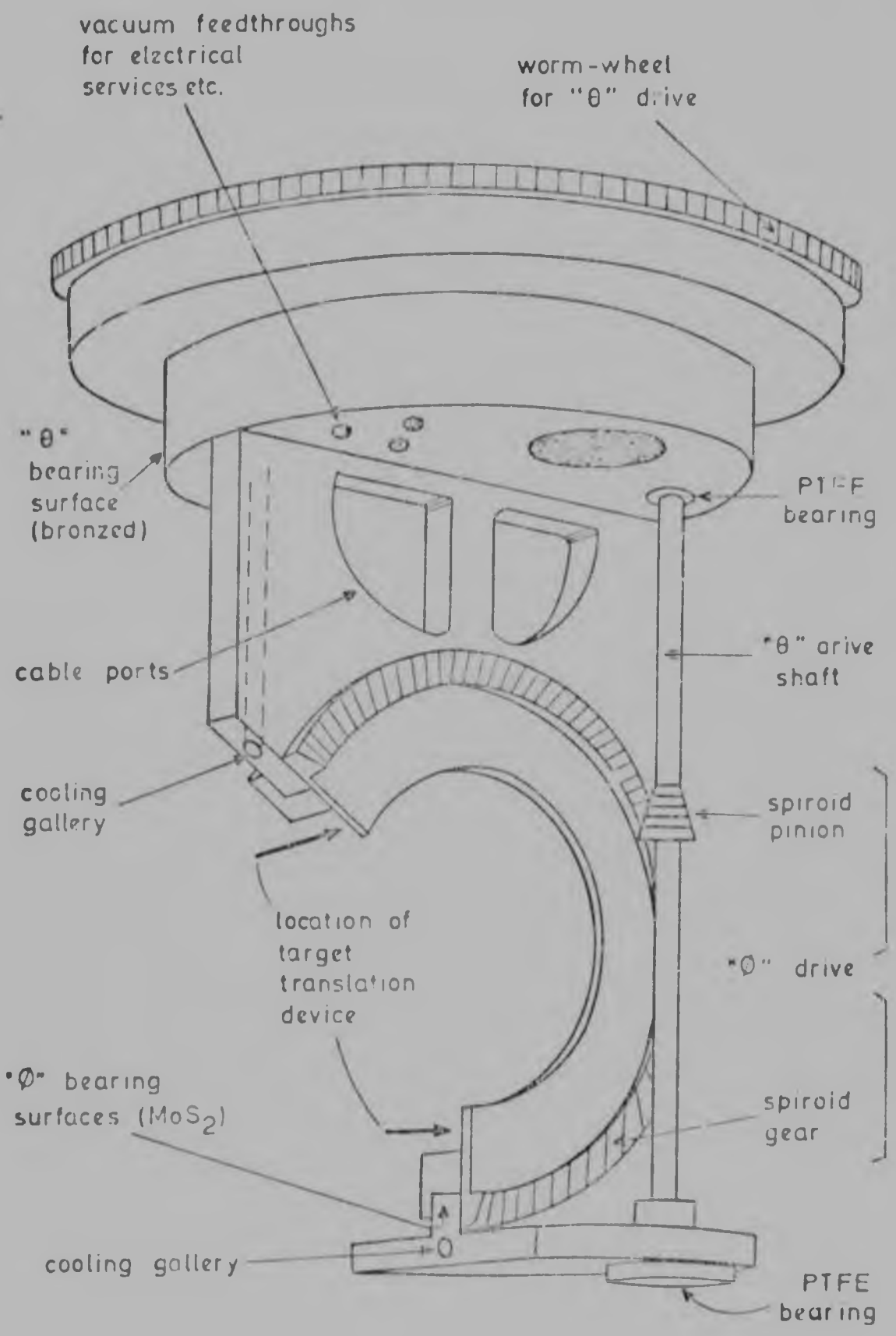

Figure 3.3: Cutaway view of Mark 2 goniometer

target are produced by precision gears driven by stepping-motors located outside the vacuum. The step size is equivalent to 0.01° at the target for both rotations, both of which have a range of 360°. Lubrication under vacuum is achieved by the use of PTFE bushings or vacuum greases and, in addition, the large precision metal-to-metal bearings for the crystal tilt movements are coated with bronze (polar angle 'θ') or molybdenum disulphide (azimuthal angle 'ϕ'). Drives through the vacuum wall pass through O-rings lubricated with Apiezon 'L' grease. The main structural framework or 'spool' was machined from stainless steel in one piece for accuracy and rigidity, and the two rotation axes, the beam axis, and the crystal surface, all intersect at one point to within 0.05 mm. The goniometer is compatible with a vacuum of 10^{-7} torr.

A feature is the large aperture available for mounting the target (7.50 cm), achieved by the use of a large spiroid gear for the ϕ drive. This not only provides plenty of room for the services described below, but also results in an outstandingly wide angular aperture, giving the beam access to the crystal up to ~70° from the normal. The flat profile of the design provides the same access angle to both front and rear of the crystal, to facilitate transmission experiments on the same apparatus by colleagues.

Selection of different spots on the crystal for analysis is commonly achieved by deflecting the beam, an inconvenient procedure which results in the beam not intersecting the rotation axes and therefore moving across the crystal as the angles are changed. A special feature of the present design is that the target may be translated in its own plane by up to ±2.0 mm in two perpendicular directions, without breaking

vacuum, and with the beam axis continuing to intersect the rotation axes at the crystal surface.

This is achieved as follows. The target-holder fits into a pyrophyllite (lava) square with grooved edges, which is held within four steel sliders (see Figure 3.4). The pyrophyllite provides both thermal and electrical insulation. Two of the sliders are driven radially by screws, while their opposite numbers are spring-loaded. Turning a screw in provides a 'positive' translation, compressing the opposite spring; while turning it out allows the spring to expand providing a 'negative' translation. Meanwhile, spring-tension holds the other movement steady, and the two translations are completely independent. All forces are applied in the same plane and intersect at a common point; because of this, the shape of the grooves, and the spring-tension, the design is kinematically stable and self-centring (provided that the lead-screws and spring-pistons are accurately machined). There is no back-lash. The thin flat profile does not inhibit beam access to the crystal up to 70° from the normal, front and rear.

A condition for operation of the device is that the coefficient of friction (μ) between sliders and pyrophyllite be low enough, in order that the springs can produce negative translations. For the dimensions used,

$$\mu < 0.1 \quad \text{approximately}$$

(neglecting the weight of the target). Accordingly, the pyrophyllite

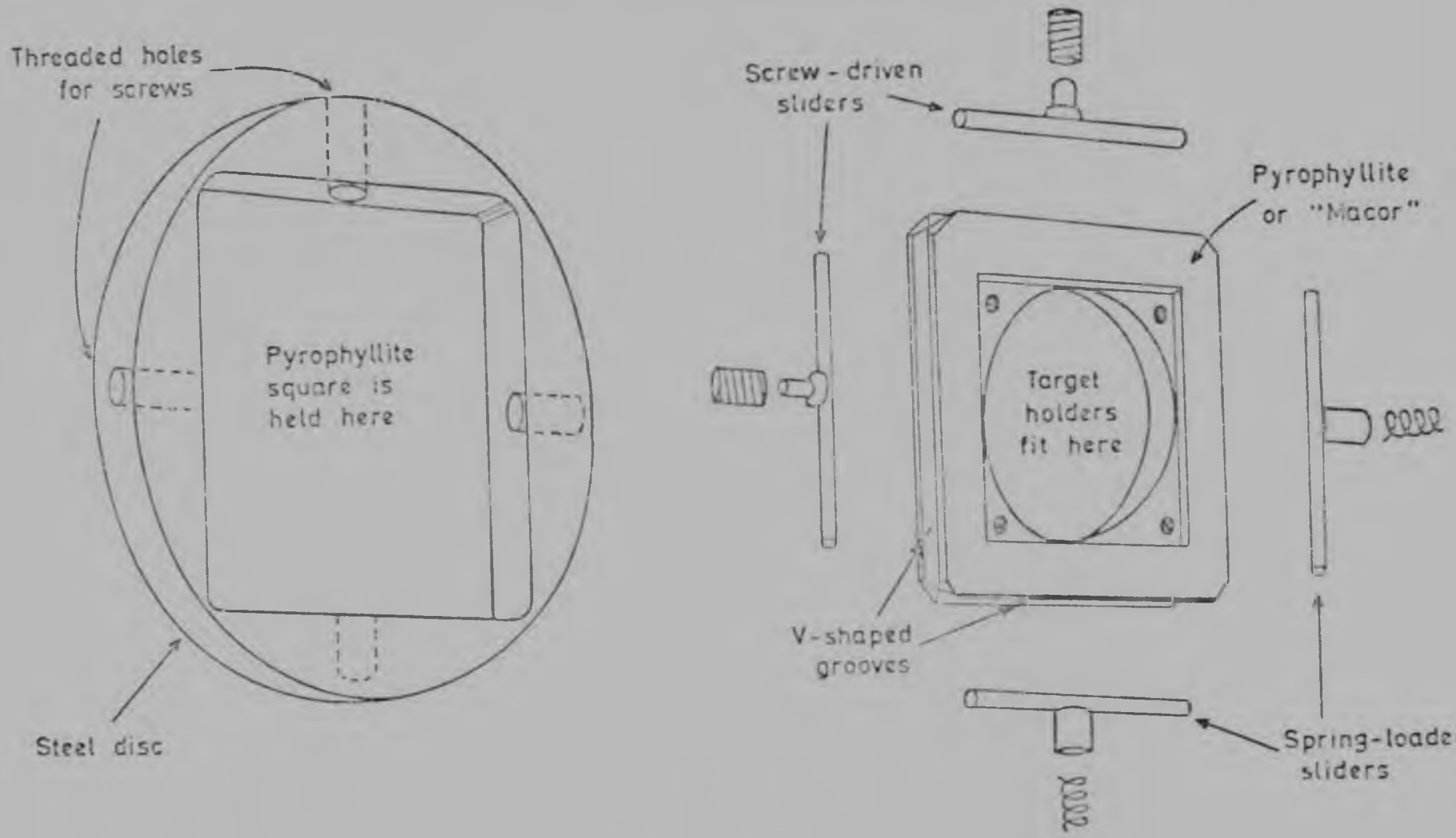

Figure 3.4: Exploded view of target translation device.

grooves were coated with 0.1 mm thickness self-adhesive PTFE sheet (μ = 0.04).

To translate the crystal, a long shaft, passing through a vacuum-seal, was inserted down the centre of the goniometer spool, through the ϕ-bearing, to engage with one of the lead-screws. The angle ϕ had first to be set to the correct position (0° for a 'y' movement, and +90° for 'x'). The x or y value was read off on a micrometer head outside the vacuum. On releasing the shaft, it was withdrawn by a spring, far enough to avoid fouling the ϕ-bearing.

Two designs of stainless-steel target-holder were used, referred to as 'thin' and 'thick' (Figure 3.5). In both, the diamond was clamped between a front and back part, the front part having a hole to allow beam access. The thin holders were suited to tabular specimens (<1.5 mm thick), and could be adapted for transmission by making a hole in the back part also. The thick holders allowed firm holding of rounded specimens in a recess machined in the back part or 'slug' to the exact specimen size.

A resistive heater could be screwed on to the back of the target-holder for runs at elevated temperatures. It consisted of a molybdenum bobbin wound with 'Thermocoax' insulated coaxial heating-wire (Amperex Electronic Corporation, Long Island). The windings had a large enough diameter to allow a 60° bevelled hole to be bored through the heater if transmission experiments were to be undertaken. The mating faces of target-holder and heater had matching grooves between which a Thermocoax

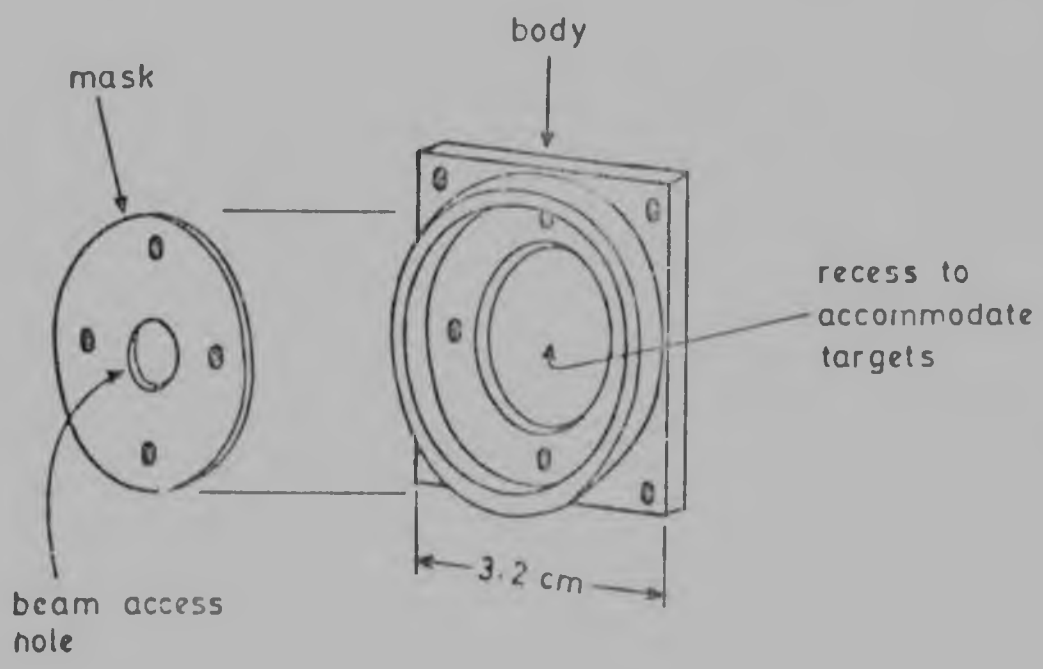

Figure 3.5(a): Target-holder, 'thin' type.

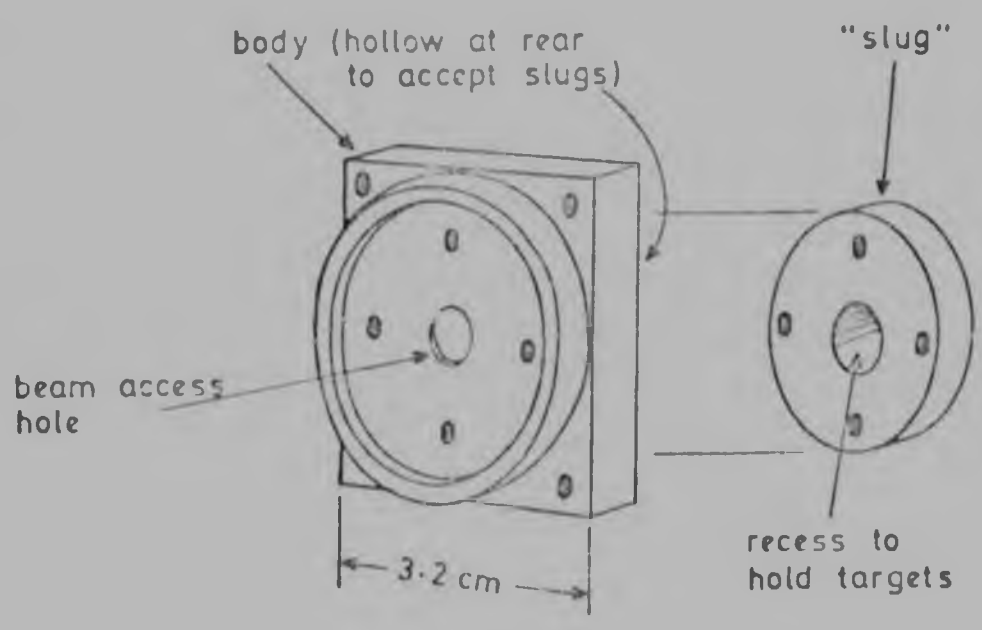

Figure 3.5(b): Target-holder, 'thick' type.

insulated sheathed thermocouple (chromel-alumel) was clamped for measuring the temperature. The temperature at this point was found to be a good approximation to that of the diamond, provided that with the thick holders, copper slugs were used to improve heat transfer. The heater was designed for a maximum working temperature of 700°C, at which it dissipated about 100W by conduction to the spool and by radiation.

Overheating of the spool was anticipated, and a U-shaped cooling gallery was drilled right round the ϕ-bearing as close to it as possible, through which a cooling fluid could be circulated (see Figure 3.3). The bearing temperature was monitored by a second Thermocoax thermocouple. In fact, this temperature only rose to about 100°C and cooling was not often used.

3.3.2 Beam-line Hardware

The goniometer fitted into the roof of a 25cm diameter steel vacuum-chamber (Figure 3.6) whose floor communicated directly with a 15 cm diameter turbomolecular pump. Ports in the chamber wall contained viewing windows and an argon-ion milling gun. A cryopump in the form of a copper can almost completely surrounded the target, so that cold (and therefore, 'clean') surfaces were 'seen' by the target in almost all directions. The cryoshield was cooled by a thick copper rod dipping into a closed liquid nitrogen reservoir suspended in the pumping port. This arrangement resulted in efficient heat transfer with minimal losses, and caused only a slight reduction in the speed of the main pump. Vacuum was in the region of 5 x 10^{-7} torr.

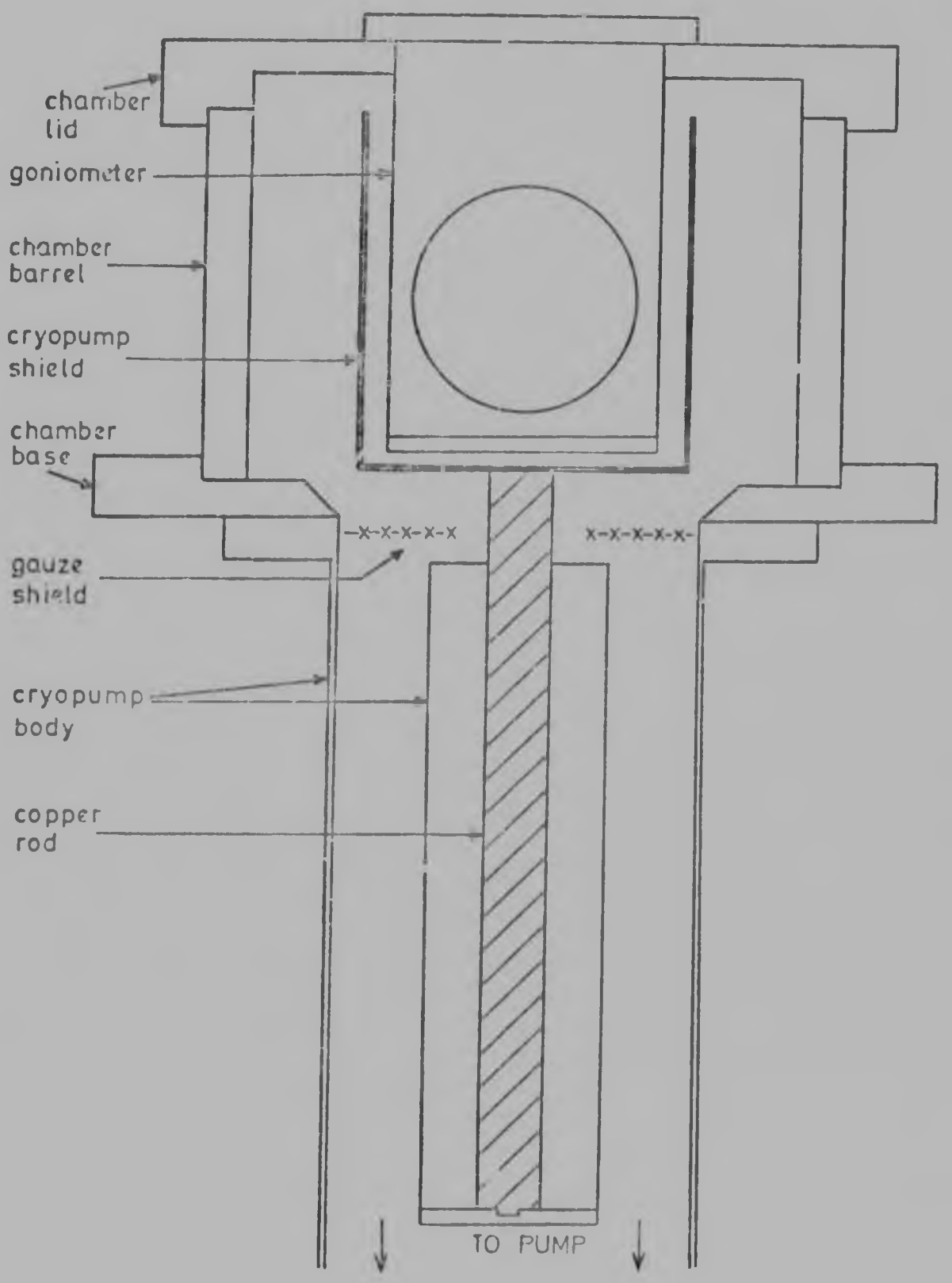

Figure 3.6: Vacuum chamber and pumping arrangement.

The beam was collimated by two apertures in tantalum, spaced 2.47 m apart, the upstream one variable and the downstream one fixed (but replaceable). The usual sizes were, upstream: 1.0 mm square, downstream: 0.75 mm diameter, giving a maximum beam divergence of 0.025° (half-angle). The downstream collimator, at the chamber entrance, had an antiscatter baffle to intercept slit-edge scattered particles, but it was found to be much more important to polish the bore of the primary aperture with a fine abrasive to a microscopically high finish. This reduced the observed background by a factor of 20.

The collimation line and the chamber were bolted rigidly to a single firm girder frame supported at its ends only. The two apertures and the goniometer centre were optically aligned with one another, once and for all; small misalignments with the accelerator at the beginning of each new run were then taken up by moving the frame and its contents as a whole, by means of screw adjustments at the end supports. Realignment was very rapid with this system.

A vacuum of about 5×10^{-6} torr was maintained between the collimators by a trapped oil-vapour diffusion pump, and an additional in-line trap reduced migration of pump-oil into the chamber. The whole layout is shown diagrammatically in Figure 3.7.

3.3.3 Detectors and Electronics

Two surface-barrier detectors were installed in the chamber: the annular one described in §3.2.3, whose large area allowed rapid location of channels, and a small plain detector of higher resolution, for taking

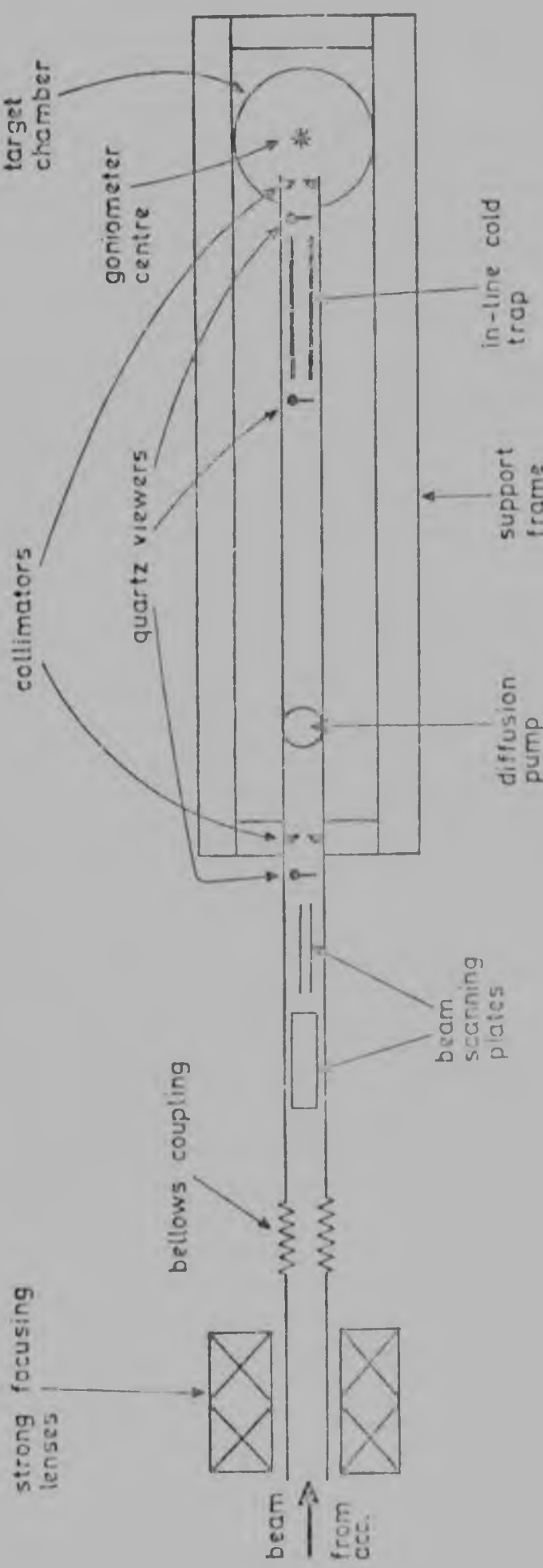

Figure 3.7: Schematic diagram of beam-line used for the Phase II and III experiments.

data. This was either an Ortec Premium Series BE-014-050-100 (resolution 14 keV, FWHM) or an Ortec Ruggedised BR-016-05 -100 (resolution 16 keV). The latter was essential for high-temperature data-taking owing to its insensitivity to infrared radiation.

The small detector was placed at a scattering angle of 155°, at a distance from the target determined by the condition that the energy spread of the detected particles due to the variation of backscatter energy with angle across the detector face, should make a negligible addition to the detector resolution. The ingoing and outgoing ion trajectories lay in a plane which included the axis, so that the exit path length in the crystal was independent of .

Typical nuclear pulse electronics were used: a block diagram is given in Figure 3.8. The components were commercially manufactured except for the normalising rateneter, which was built to the Aarhus design (private communication). The overall linearity of the system was checked (a) with a test-pulser, and (b) by backscattering off various materials of known mass numbers, and was found linear to about 2 KeV, or much less than the detector resolution.

3.3.4 Accelerators

The Phase II and III experiments performed with the apparatus just described, used beams of protons and singly-ionised helium provided by the Nuclear Physics Research Unit's 1.4 MeV pressurised Cockcroft-Walton accelerator 'Christine'. This machine, converted from a Philips electron accelerator Type PW5121, has been described by Annegarn [Ann76]. The

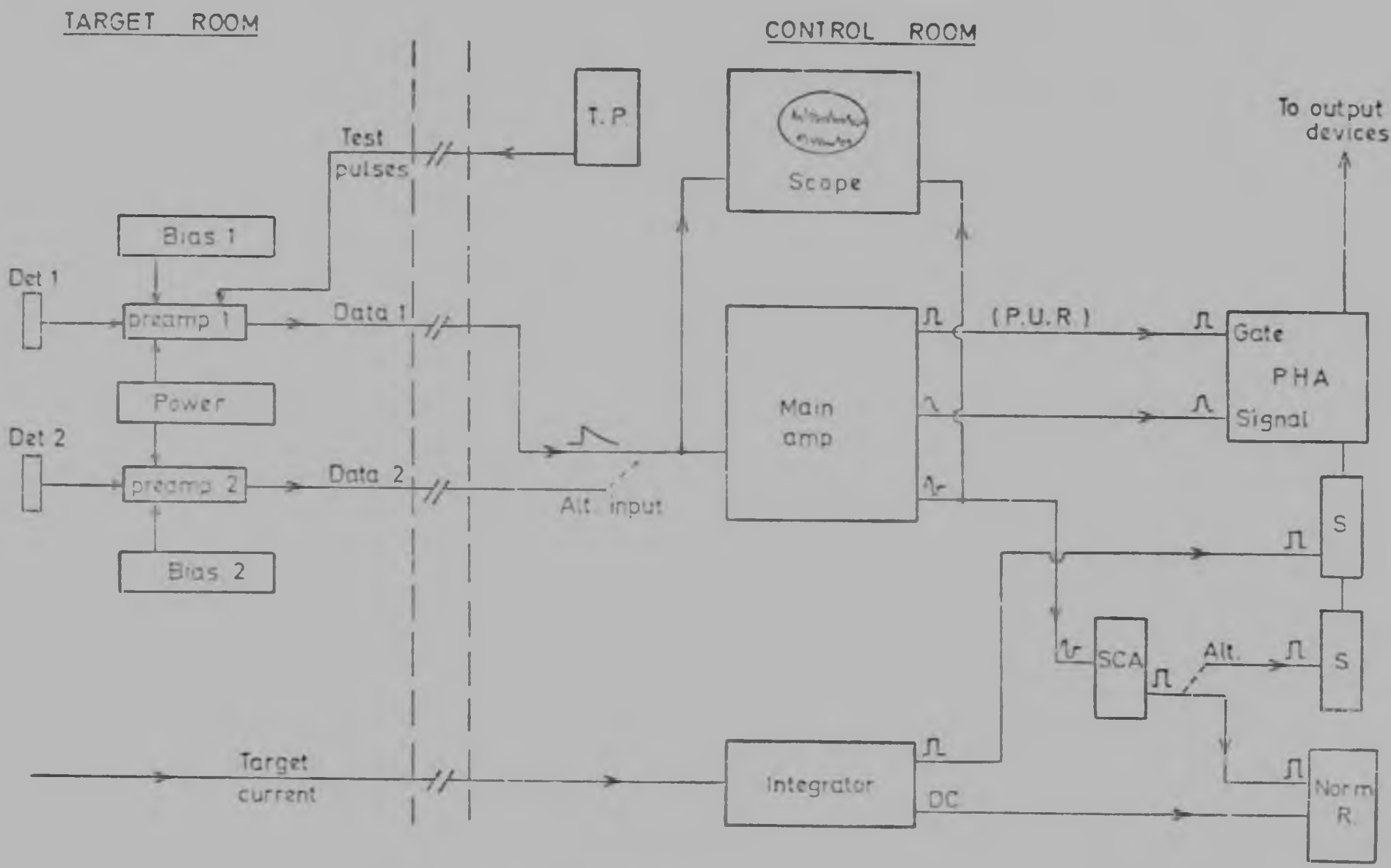

Figure 3.8: Block diagram of electronics.

energy calibration was rechecked against $^{27}Al(p,\gamma)^{28}Si$ resonances during the course of these experiments, and found correct to within ±4 keV. The beam energy spread, due to the analysing slit width was also ±4 keV.

With the collimators at their usual settings, a beam of 4nA could easily be obtained on target. The problems of target-current integration are considered in Sections 2 - 4 of Chapter 6.

During Phase III, the proton experiments were carried to higher energies, up to 4.5 MeV, on the Unit's 6 MV Tandem van de Graaff accelerator. This machine is a standard High Voltage Engineering Corporation EN Tandem with the usual beam-handling equipment. The energy calibration is accurate to 6 parts in 10^3 and the energy spread for protons is also 6 parts in 10^4. The experiments were performed with a second Mark 2 goniometer installed on one of the Tandem beam-lines, with similar accessories and electronics to those already described.

Amongst many small differences in detail between the two sets of apparatus, the only important ones were in the beam collimation. Since channelling critical angles are inversely proportional to the square root of the ion energy (Eqn 2.4a), the beam divergence had to be reduced appropriately at the higher energies. The collimators were separated by a greater distance (5.1 m) and the upstream aperture set according to the energy being used. Typically, this was 2.0 mm square at 2.5 MeV (giving a divergence half-angle of 0.020°) and 1.0 mm square at 4.5 MeV (divergence 0.012°). The half-angle of divergence was about 1/20 of the major axial critical angles at each proton energy.

Beam-currents on target were rather smaller on the Tandem, typically 1 nA.

3.4 EXPERIMENTAL METHODS

3.4.1 Location of Channels

A backscattered Laue X-ray photograph was taken of each crystal after it had been secured in its holder with the desired face exposed. From the symmetry of the pattern, the crystal orientation was deduced (if this was not already obvious from its morphology). The most easily-accessible axis of each type to be investigated was identified, and with the aid of a Greninger net the angular coordinates of each axis could be read off to about 1°.

The holder was attached to the goniometer, vacuum established, and protons backscattered from the crystal while the two goniometer angles were varied slowly in the region of the predetermined values. A deep minimum in the backscattered count rate gave the position of the axis sought, to about 0.1°.

This procedure was greatly facilitated by the use of the normalising rateмeter, which divided the backscattered count rate by a signal representing the target current. Beam fluctuations were thus prevented from confusing the channel identification. For greatest sensitivity, a single channel analyser selected only the counts of the highest-energy protons, that is, those backscattered just under the surface. The location usually took only a few minutes.

Finally, the output of the single channel analyser was connected to a scaler, and the angles scanned stepwise, one at a time, through the axis, with proton counts being accumulated at each point for a fixed incident dose. Thus the axis was located with an accuracy of up to 0.01°. Planes could be located in the same way.

Sometimes difficulty was experienced in finding an axis, for example, the narrow <100> dip at high energies. In these cases, the wider <110> and <111> axes were located first and the elusive axis predicted by spherical trigonometry, then located exactly, as above.

3.4.2 Data

Data were taken in two forms:

i) energy spectra of the backscattered particles, as accumulated by a multichannel analyser, and

ii) scans through an axis or plane, that is plots of count versus angle.

The scans could be obtained with a single channel analyser or, for finer depth resolution, from a series of spectra. The spectra could be printed out, plotted, or recorded on magnetic tape. Runs were normalised to the same number of incident ions by means of a current integrator (of 0.05% accuracy).

3.4.3 Coordinate Conversion

In order to measure critical angles, it is necessary to scan

through each crystal axis in a plane passing through the axis. One of the goniometer movements may coincide with a suitable plane, but complete freedom of choice of the scan-plane is preferable, for reasons elaborated in Section 6.8.

For this purpose, it was found convenient to write a programme which could be run on either an HP25 or HP65 pocket calculator. The programme, dubbed GCS, performed a true planar scan through the given axis, with any given orientation and step size, in terms of spherical polar coordinates centred about the axis, converting the results into the spherical polar coordinates used by the goniometer. Thus the output was a series of pairs of (θ,ϕ) values to be set on the goniometer to produce the desired scan.

A second programme (CRYP-2) calculated scans around the surface of a cone, whose axis was a crystal axis, in given azimuthal steps. Its use is referred to in §6.8.2. The programmes, based on standard spherical trigonometry, are listed in the Appendix.

CHAPTER 4

PRELIMINARY EXPERIMENTS ON SILICON

4.1 MOTIVATION

Silicon was chosen for the initial channelling experiments because it had already been well investigated by other workers using light ions (see Ge⁻4, p21⁻) and was known to display the phenomenon clearly. The aim was to test and establish experimental technique by reproducing the results of others, using elementary apparatus (Section 4.2). In keeping with previous work at that date, transmission experiments were planned, and considerable time was devoted to preparing thin targets (Section 4.3). However, the work was eventually done in the backscattering mode; the results are presented in Section 4.4.

4.2 APPARATUS

All the silicon work belongs to Phase I (see Section 1.4) and was carried out on the 1 MeV accelerator 'Phoenix', using goniometer Mark 1 and the accessories described in §3.2.1.

4.3 SILICON TARGET PREPARATION

4.3.1 Thickness Requirement for Transmission

The low maximum beam energy available from 'Phoenix' (600 keV if long-term stability were required) placed a stringent requirement on

crystal thickness if the beam were to penetrate, even assuming a lower stopping-power under channelling. The range of 0.6 MeV protons in silicon (calculated using the Bragg-Kleeman range relation and data from reference Kay57) is

$$R \sim 7\ \mu m.$$

Using the relative mass stopping-powers tabulated in reference Kay57, the thickness δx for an energy loss of $\sim$0.1 MeV is

$$\delta x \sim 2\ \mu m.$$

A maximum thickness of about 5 μm was thus indicated, with a desirable thickness of ∿2 μm. In addition, if accurate energy-loss measurements were to be made, the thickness ought to be constant over the usable area to perhaps 10%.

4.3.2 Techniques: Lapping

Other workers have prepared thin silicon wafers by lapping followed by etching [In62, Dea64, Ma64]. Lapping (abrasive polishing) is capable of producing a parallel-sided wafer, satisfying the requirement of uniform thickness, but cannot normally be used below about 100 μm because the resulting crystal damage (chiefly dislocations) penetrates well below the surface. Therefore, a chemical etching procedure is used in the final stages, to remove lapping damage and to produce the required thickness. Inskeep et al [In62] found it necessary to remove ∿50 μm in this way. Etching is confined to the final stage because it is slower

and less uniform than lapping.

More recent workers have used specialised mechanical thinning for the entire process [Wh65, Mas70]. A review of techniques is given by Whitton [Wh69].

Although thin silicon was not used in the final experiments, it was essential to apply the same etching techniques to the thick samples used for obtaining the backscattering data. As-cut silicon slices would be surfaced with a damage layer and would be expected to show poor channelling effects unless thus prepared.

4.3.3 Lapping

Transistor-grade silicon was supplied by Standard Telephones and Cables in 1 - 2 cm diameter slices, and lapped by them on a Lapmaster machine from ~ 1 mm to ~ 100 μm thickness. No specification of electrical type or resistivity was made, since these should have little effect on a basic experiment. Thickness uniformity was sought by lapping the silicon in the midst of many identical quartz slices, all waxed down to a large (~10 cm) flat glass plate.

A sample supplied and lapped by Bell Telephone Laboratories, Murray Hill, New Jersey, was also used.

4.3.4 Cutting

Small discs (7 mm diameter) were cut using an ultrasonic drill fitted with a brass 'cookie-cutter', which was flooded with a

carborundum slurry to produce a cutting action.

4.3.5 Planar Etching

The techniques of references In62, Ma64 and Ma70 were followed, using the 7-stage cleaning-procedure of Madden [Ma64, Ma70], including ultrasonic cleaning and copper-plating. The samples were handled only with PTFE-coated tweezers or dipped using a PVC-mesh basket.

The etchant was the standard nitric/hydrofluoric acid mixture with some added acetic acid to promote etch uniformity, the proportions being

nitric : hydrofluoric : acetic :: 20 : 1 : 1.

This was swirled slowly in a PTFE ('Teflon') beaker using a PTFE-coated magnetic stirrer and the sample held on the end of a PTFE rod so that the sample plane was parallel to the flow streamlines. It was slowly rotated in its own plane to ensure symmetric etching. After half the planned etching, it was turned over and etched on the other side. At this stage, samples intended for transmission experiments were strengthened by fusing them on to a waxed (50% Apiezon, 50% paraffin) glass cover-slip (with a hole in the middle) which functioned as a target-holder in the Mark I goniometer. The etch-rate was about 2 $\mu m\ min^{-1}$, in agreement with the data of Klein and d'Stefan [Kl62].

The samples were checked for surface uniformity before and after etching, using a Talysurf stylus-type surface analyser, by the

University's Metrology Workshop. The surface was quite rough on a ~1 μm-scale, and the etch technique would evidently have needed improving if transmission experiments had been undertaken in earnest.

A visual monitoring of the surface revealed a transition from a satin grey to a bright mirror-finish in the region of 20 - 30 μm removal. This was tentatively identified with removal of the damaged layer to expose good-quality underlying crystal.

4.3.6 Thickness Measurement

The initial thickness of all slices was determined roughly with a micrometer reading to 10 μm. From measurement of the final thickness, or by taking an unwanted portion to disappearance, the etch-rate was determined, and the amount of silicon removed from other samples could be calculated from the elapsed time.

This method proved rather inaccurate because the etch-rate slowed down as the etchant aged, presumably due to evaporation of the hydrofluoric acid. For thick samples, however, it was sufficient to know that about 50 μm had been removed.

For thin samples, very large errors in the final thickness could result. The problem was overcome by first etching a scrap piece of the same slice for a time calculated to remove a thickness equal to the required final thickness of the sample to be used. Both pieces were then etched side by side, with periodic inspections, and when the scrap piece disappeared, the experimental sample was at the required thickness.

By this differential etch technique the absolute error was made proportional to the final thickness (a small quantity) rather than to the total removal (a large quantity).

Finally, the thickness of very thin crystals was checked by the onset of a brown translucence, occurring at ~1 μm [Ma70].

4.4 CHANNELLING EXPERIMENTS WITH SILICON

4.4.1 Experimental Technique

In the first experiments, channels were located 'blind' without benefit of an X-ray photograph. It was known that the slices had been cut almost parallel to a ⟨111⟩ plane, and a ⟨111⟩ axis could, therefore, be expected almost perpendicular to the surface. The crystal angles were varied in 1° steps in the region of zero, backscattered counts accumulated at each position for fixed incident proton fluence and the numbers represented on a grid-like angular plot by drawing circles with radius proportional to the number of counts observed at that angle. Eventually, the positions of the ⟨111⟩ axis and the major planes intersecting it, were clearly revealed as a pattern of smaller circles (Figure 4.1). A discriminator was used to count only particles scattered from just under the crystal surface, where channelling produces the greatest reduction.

This method was refined by off-setting one angle by a couple of degrees and scanning the other very finely to pick up the planar minima exactly. These were then joined by straight lines (an approximation)

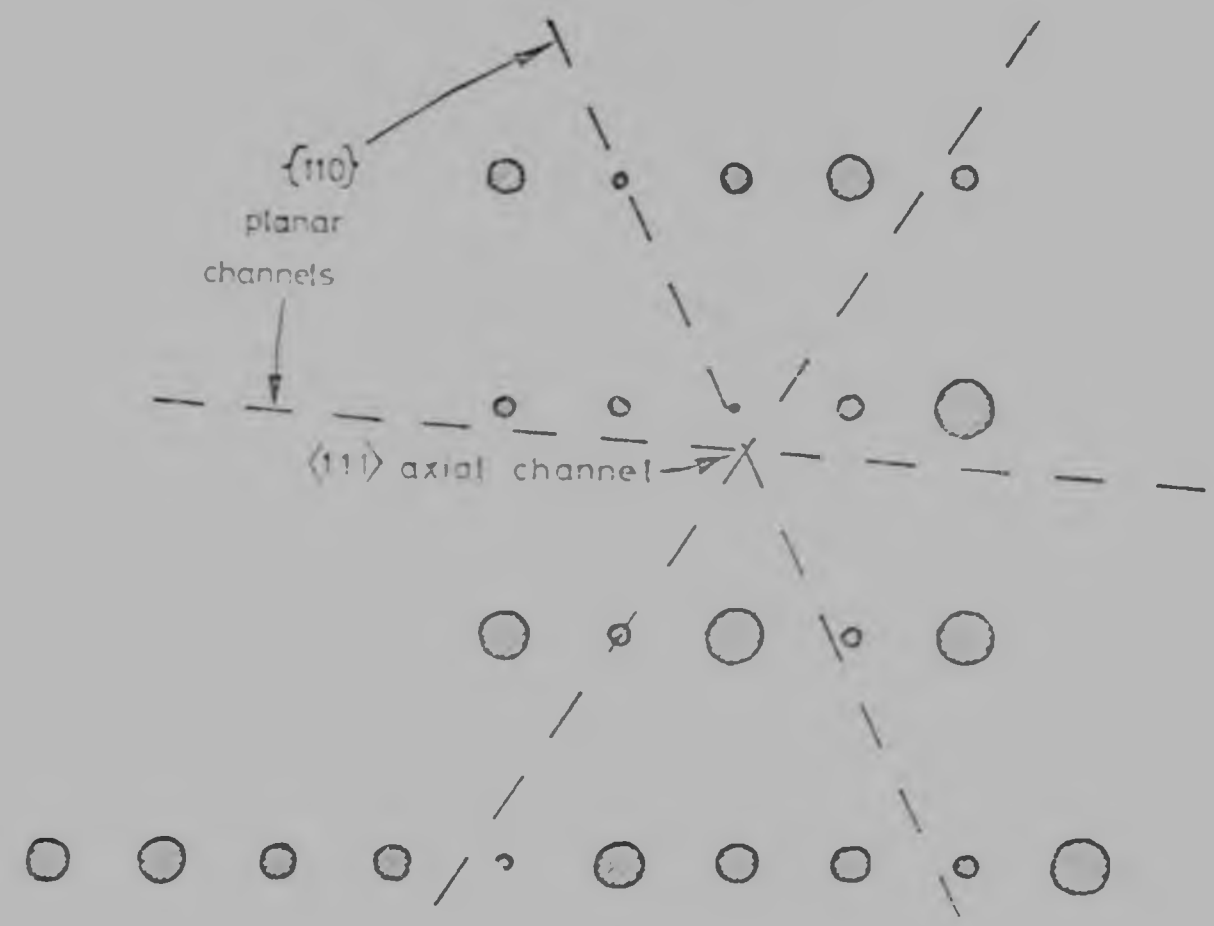

Figure 4.1: Location of channels in silicon: first method.

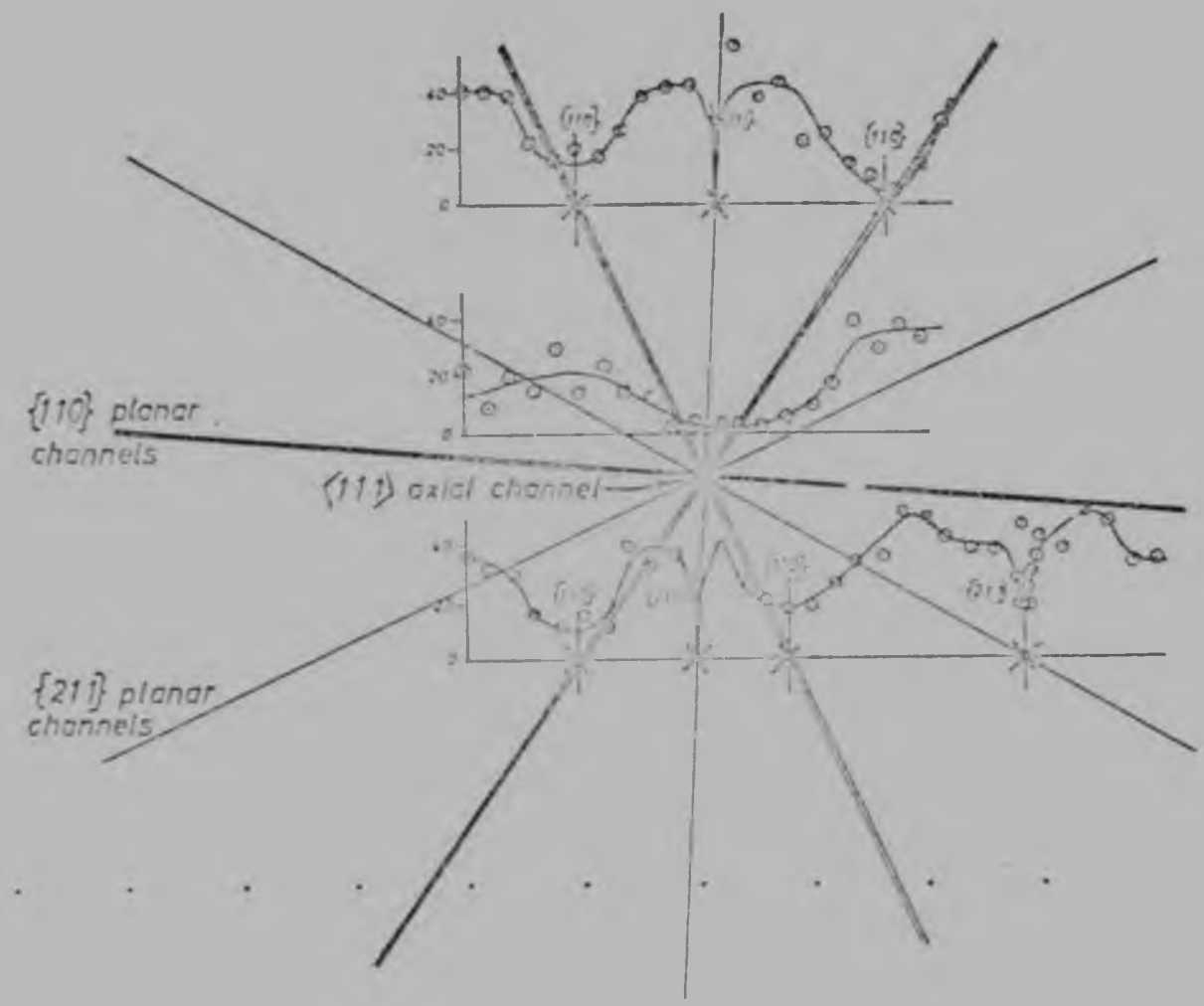

Figure 4.2: Location of channels in silicon: second method.

TABLE 4.1

Critical Angles for Silicon

Measured on sample Si7.
Typical errors ±0.1° (axes); ±0.05° (planes).

Ion	Channel	$\psi_{\frac{1}{2}}^{\circ}$ (exptl)	$\psi_{\frac{1}{2}}^{\circ}$ (theor)
0.6 MeV H^+	<110>	0.9	0.66
	<111>	0.6	0.60
	{110}	0.2	0.22
	{111}	0.3	0.18
	{100}	0.15	0.16
	{211}	0.15	0.13
0.8 MeV H^+	<110>	0.5	0.58
	<111>	0.45	0.52
	<100>	0.45	0.48
	{110}	0.15	0.19
	{111}	0.25	0.16
	{100}	0.1	0.14
0.5 MeV He^+	<111>	1.0	0.89
	{110}	0.35	0.33

to locate the <111> axis (Figure 4.2). Other axes were subsequently located in a similar fashion.

Although slow, this method had the advantage of revealing the symmetry of the planar channels, which could be seen to agree with theory (for example, the <111> axes in the cubic system are required to have three {110} planes intersecting there at 120°, with three {211} planes bisecting these angles). For such exploratory measurements as these, this was an important check.

4.4.2 Results

Final data on silicon consisted of energy spectra (not shown) of backscattered protons at two energies (600 keV and 800 keV) and singly-ionised helium at 500 keV, with the beam incident in the three lowest-index axes (<110>, <111>, and <100>) and the three lowest-index planes ({110}, {111}, and {100}). In addition, the beam was scanned through the axis or plane with the particles backscattered from just under the surface (that is, above a discriminator level) being counted in a scaler. Plots of these scans enabled rough values of the critical angles and minimum yields to be obtained.

The minimum yield values contained a large contribution from surface contamination, and are not shown here. The critical angles ψ_2 are presented in Table 4.1, together with theoretical values calculated according to Barrett's modification of Lindhard's formulae [Bar71], and are also presented graphically in Figure 4.3. It can be seen that a reasonable agreement with theory is obtained, considering the rather

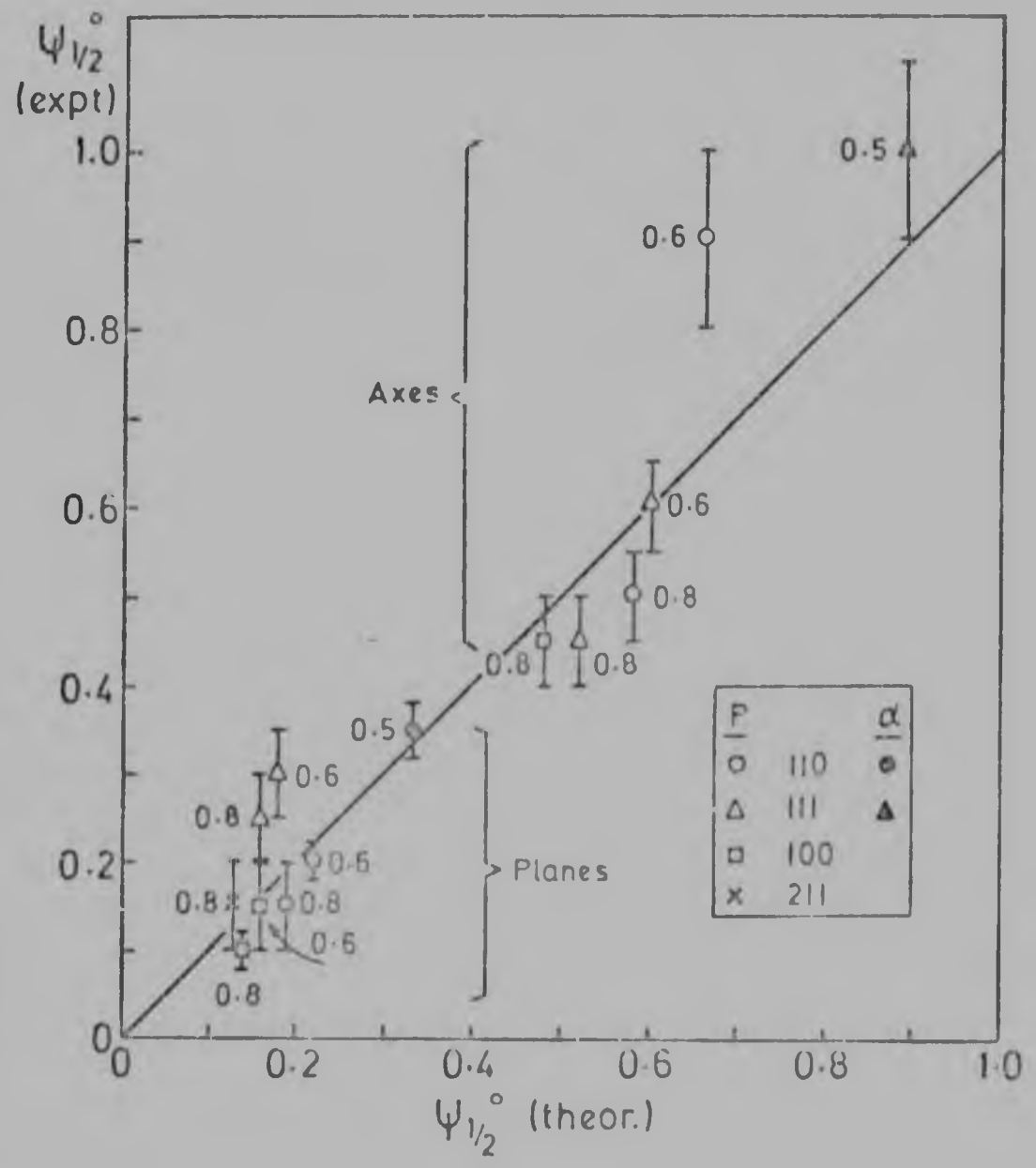

Figure 4.3: Comparison of experimental values of $\psi_{\frac{1}{2}}$ for silicon axes and planes, with theoretical values calculated from Eqns 2.7 and 2.8 respectively.

large depth range over which the yields have been averaged, and the fact that no particular care was taken with the orientation of the transaxial scan planes (see Section 6.8); the latter point is responsible for the very large ψ_1 measured for <110> at 0.6 MeV. It will be noticed also that {111} planar values are anomalously high. This appears to be a general phenomenon for diamond-structure crystals and will be considered in the appropriate section of the diamond results (§7.5.2).

CHAPTER 5

DIAMONDS FOR ION CHANNELLING

5.1 INTRODUCTION

Experiments on diamond suffer from the inherent problem that the material cannot be prepared to specification, for example by refining to a high purity or recrystallising to a high degree of crystal perfection (contrast, for example, the zone refining of silicon). Results therefore tend to be variable, and ion channelling is no exception, as shown in the next section. Synthetic diamond can indeed be made, but with difficulty, and the crystals tend to be poor, full of metal inclusions, small, and unpredictable with respect to these properties. It is necessary therefore to experiment on naturally-occurring samples, and to consider the problem of how representative of pure diamond the results are. Furthermore, the maximum size of crystals which may be acquired readily is limited (and the largest crystals tend to be the less perfect ones), which increases the awkwardness of performing experiments such as those described here.

Several other laboratories have embarked on diamond channelling experiments: Aarhus University, Bell Telephone [Se73], Brookhaven, Chalk River [Pic69a], and Stanford University [Das69, Das71]. They found diamond to display the phenomenon clearly, but (with the exception of Stanford, where the interest was concentrated on radiation damage) did not carry the experiments beyond the initial stages, since they were

TABLE 5.1

The Di-Stones

Batch	Serial Number	Description
A	Di1, Di2	Polished slices, ~3 mm square.
B	Di3 + Di13	Eleven natural platelets, about half macles*, typically ~6 mm on a side and ~1 mm thick.
C	Di14 + Di17	Four more macles. Small (~3 mm), poor quality, not used for channelling.
D	Di18	Large polished cuboid, ~7 x 5 x 2 mm.

*A macle is an octahedral diamond twinned on a {111} plane. The twin law is a 60° rotation about <111>, producing triangular plates. Only one twin is penetrated by the ion beam.

confronted with the problems indicated above (private communications).

The question of how closely individual samples represent 'intrinsic' diamond is considered in Section 5.2, which contains a brief description of the stones used and how they were selected. It is shown that, with care, representative results could be obtained. Cleaning procedures are described in section 5.3, and ways of improving the crystal perfection, in Section 5.4.

Diamond is classified into two types (I and II) on the basis of optical properties, and four subtypes (Ia, Ib, IIa and IIb) according to electron spin resonance properties and semiconducting features. The outcome of many diamond experiments has been found to depend on the type used. There was no reason to expect that this would be true for channelling, with its dependence on long-range crystal order rather than the point phenomena which determine the diamond type. It could be safely assumed that all the stones used were of Type Ia (~98% abundance), and this was confirmed by electron spin resonance and infrared absorption measurements on many of them.

5.2 SELECTION

5.2.1 The Di-stones

The first diamonds for channelling were chosen with no special requirements, other than freedom from inclusions and a good appearance. They were acquired through Dr I.A. Raal of the Diamond Research Laboratories, in four batches, and numbered as in Table 5.1. The most studied group was batch B, the eleven natural platelet diamonds. The

TABLE 5.2

The K-Stones

Serial Number	Origin	Description
KC1 - KC11	Consolidated Diamond Mines	Industrial yellow dodecahedra and octahedra, including some macles. (KF4 is a strained brown octahedron.) Weights ~ 0.2 - 0.4 g, diameters ~6 mm.
KF1 - KF4	Finsch Mine	
KK1 - KK7	Kleinzee Mine	
KP1 KP2	Premier Mine	Industrial chips ~6 mm across. (KP2 is a Premier Overblue.)
KT1	De Beers' collection	Large tabular hexagon ('portrait stone') 12 x 10 x 2.0 mm.
KT2	De Beers' collection	Large tabular trapezium 8 x 10 x 1.3 mm.

numbering in the group, from Di3 to Di13, is in decreasing order of perfection as estimated visually both with the naked eye and under a surface microscope.

5.2.2 The K-stones

Defects such as inclusions, dislocations and microcracks set up strain fields in a crystal, so it was argued that strain-free diamonds would be the most perfect and would provide the best channelling results. The presence of strain causes birefringence, detected by observing the crystal between crossed polars [Wi71, Wi76]. Accordingly, the second major group of diamonds was selected under a polarising microscope from several thousand near-gem industrial stones.

The selection was carried out at the main De Beers sorting offices in Kimberley. The firm kindly provided employees to pick out the better stones visually, and these were screened further, with K.W. Tearick, under a polarising microscope. Preference was given to well-shaped crystals with smooth faces.

Twenty-four of the best stones were chosen. Most were yellow stones, both octahedra and dodecahedra, including a few macles. In addition, De Beers lent two large flat clear stones from their special collection, making 26 in all. The numbering (in order of decreasing mass within each group) and the mines of origin are indicated in Table 5.2.

5.2.3 Assessment

Initial determinations on all the Di-stones, of the backscattered energy spectra of 0.7 MeV He^+ ions, gave a wide variety of channelled yields, emphasising the problem of determining values for comparison with theory. For ions incident in the close-packed <110> directions, and backscattered from just under the surface, minimum yields ranged from 5% to 31%.

It was presumed that low dechannelling, that is, a low channelled yield, would be the hallmark of a good crystal. The ideal crystal would be one consisting only of carbon atoms arranged on their proper sites, and it has been shown (see Qu76 and references therein) that foreign interstitials, self-interstitials, stacking-faults, dislocations, and other defects, all increase dechannelling above the basic value due to electron multiple scattering in the channels. The critical angles might also be affected, but less directly and therefore probably less sensitively.

An X-ray topograph of one used crystal (Figure 5.1), taken by Dr A. Lang of Bristol University, revealed heavy distortion in the region struck by the ion beam, with misorientations ~1-2 minutes of arc, although it was still clearly displaying channelling. This indicated that other conventional indices of crystal perfection might not correlate well with channelling. The major evidence was the carefully selected K-stones, which showed higher dechannelling than the best of the Di-stones (except for KT1 and KT2).

FIGURE 5.2

Channelled Yields of Various Diamonds (1 MeVp, <110>)

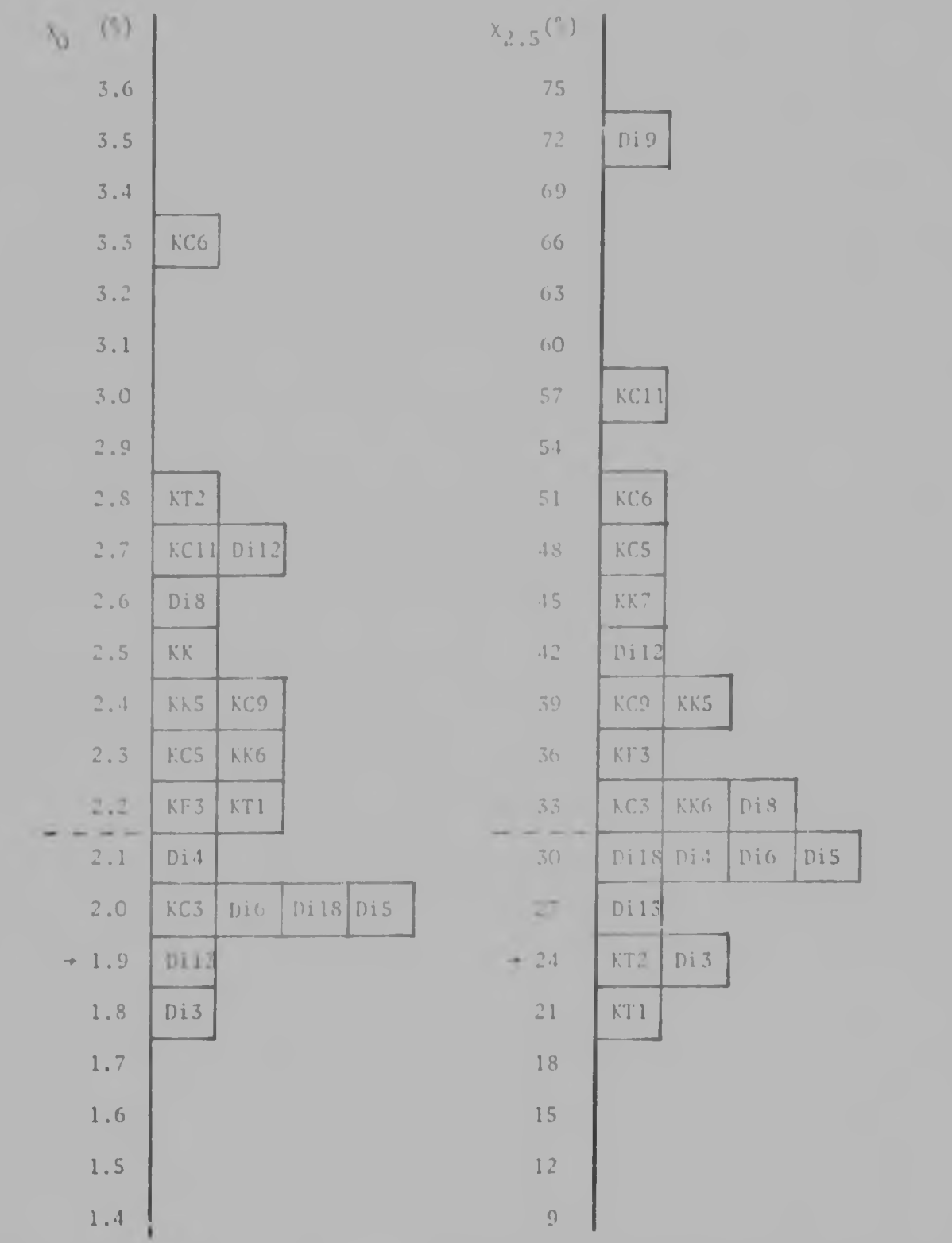

Evidently, the most reliable criterion for selecting good crystals for channelling would be the channelling results themselves.

Of course it was not known what minimum channelled yield to expect from a perfect diamond (the Lindhard prediction was already known to be an overestimate). But it seemed reasonable to assume that if many diamonds were examined, giving a distribution of channelled yields, and if the distribution showed a cutoff at some low value, then this could be taken as the yield for a perfect diamond.

Such a cutoff was found to occur. Figure 5.2 shows histograms of the yields of 1 MeV protons channelled down <110>, measured at two different depths: χ_0 is the sub-surface minimum yield, measured just below the surface peak, and $\chi_{2.5}$ is the yield from 2.5 μm (approximately the greatest depth from which the protons can be scattered out of the crystal). The measurements were taken after the improvement techniques of Section 5.4 had been tried, and the lowest values attained by each crystal were selected. Errors were approximately equal to the plotting intervals.

The cutoff can be clearly seen on both histograms. It was defined at $\chi_0 = (1.9 \pm 0.1)\%$ and $\chi_{2.5} = (24 \pm 3)\%$ (arrowed). Moreover, there was a clustering of results just above this value. It can be seen that the same samples tended to give results in this region on both plots. Since many of these were also the samples which on morphological grounds appeared to be the best crystals, it could be asserted fairly confidently that the intrinsic <110> yield for diamond is represented by

TABLE 5.3

Diamonds Selected for Channelling Studies

Serial Number	Shape	Faces	Treatment	x_0 [%]	$x_{2.5}$[%]
KT1	hexagon	{111}	anneal	2.2	21
Di3	macle	{111}	gas-etch	1.8	23
KT2	trapezium	{111}	none	2.8	24
Di13	macle	{111}	polish, anneal	1.9	27
Di6	chip	random	gas-etch (later polished)	2.0	29
Di18	pol. cuboid	random	polish, anneal	2.0	29
Di5	macle	{111}	gas-etch	2.0	30
Di4	macle	{111}	polish, anneal	2.1	31

the above figures, and that samples with yields close to these values can be regarded as perfect crystals as far as channelling is concerned.

As an arbitrary criterion, diamonds with $\chi_0 < 2.2\%$ and $\chi_{2.5} < 32\%$ (indicated by the broken lines) were regarded as satisfactory. The correlation between the two indices was close but not exact, and greater weight was given to $\chi_{2.5}$ as representing a sampling of a greater thickness of crystal.

5.2.4 Selection

In this way eight first-class diamonds were selected: they are listed in Table 5.3. It was interesting to reflect that these were just the stones which would have been selected on a visual examination alone (note the preponderance of the low Di-numbers). All were clear (probably of gem quality) with no obvious colouration; all exhibited a good morphology with well-defined flat faces. The only exception was Di18, brownish and already polished. Six had {111} planes as the major faces; half were macles.

The final selection was made after the techniques of Section 5.4 had been applied.

5.3 CLEANING

5.3.1 Contamination

The use of helium-ion backscattering to reveal the presence of foreign atoms on the diamond surface and to enable their mass-numbers

to be determined, was described in §2.4.1. Application of this technique showed that all the diamond samples had more or less dirt on the surface, despite a clean appearance and despite having been ultrasonically cleaned in various solvents (usually water, trichloroethylene, alcohol and acetone). This was also observed by Sellschop and Gibson [Se73]. There were three obvious possible sources:

i) The matrix in which the diamond was found. This would be expected to contribute a variety of different elements, which would appear as a 'mass continuum' in the backscattered spectra (owing to the finite detector resolution), with peaks due to those more abundant. Such impurities will be referred to as 'earthy'.

ii) Processing, including separation and recovery, and possible polishing. Some processes might add specific elements, for example, the heavy media separation.

iii) The vacuum environment of samples already experimented on. The silicone diffusion-pump oil, which backstreams at an appreciable rate [Pow54] if cold-traps are allowed to warm up, contains silicon, oxygen, carbon, hydrogen and possibly sulphur. (The carbon would not be visible on a diamond substrate, and the hydrogen cannot scatter ions at backward angles.)

The disadvantage of surface impurity layers is that they increase the beam divergence (by electron multiple scattering) and therefore the

TABLE 5.4

Cleaning

Summary of Results on Many Diamonds

Process	Effect on	
	Pump oil	'earth'
1) Acid Process		
Boil in HF/H_2SO_4 and HNO_3 Time taken: approximately 5 hours	cleaned	cleaned
2) Solvents		
1 hour with ultrasonic agitation		
Acetone	none	none
Diethyl ether	some	none
Benzine	cleaned	none
Ethylene diamine + dimethyl formamide*	cleaned	none
3) 'Contrad'		
With ultrasonic agitation		
4 minutes	none	some
8 minutes	some	some
15 minutes	some	cleaned
30 minutes	cleaned	cleaned
60 minutes	cleaned	cleaned

*Reference: [Vo73].

dechannelling in the crystal. They proved difficult to remove, especially contamination due to source (iii). Ultrasonic cleaning with conventional solvents (for example acetone, trichloroethylene) made little difference to the silicone oil (silicon and oxygen) backscatter peaks. It was thought possible that a chemical rather than a physical adsorption mechanism was at work, due perhaps to the chemical similarity between Si and C.

5.3.2 Systematic Approach

Tests of different cleaning procedures were made on the eleven platelets Di3 - Di13, all of which showed both an earthy mass continuum and prominent pump-oil (silicon and oxygen) peaks. Rutherford backscattering of He^+ ions was used to inspect the surfaces before and after cleaning. Three general types of cleaning were tried:

i) A hot hydrofluoric and sulphuric acid process, used successfully in this laboratory by Fesq et al on diamonds for neutron activation analysis [Fes73].

ii) Ultrasonic cleaning for one hour in various organic solvents (chosen after testing a wide variety of solvents for miscibility with silicone oil).

iii) Ultrasonic cleaning with the commercial detergent 'Contrad' (Decon Laboratories Limited, Brighton, England).

The results are summarised in Table 5.1, and some examples of spectra are shown in Figure 5.3. The detergent process is evidently the most efficient. The HF process is successful but slow; some of

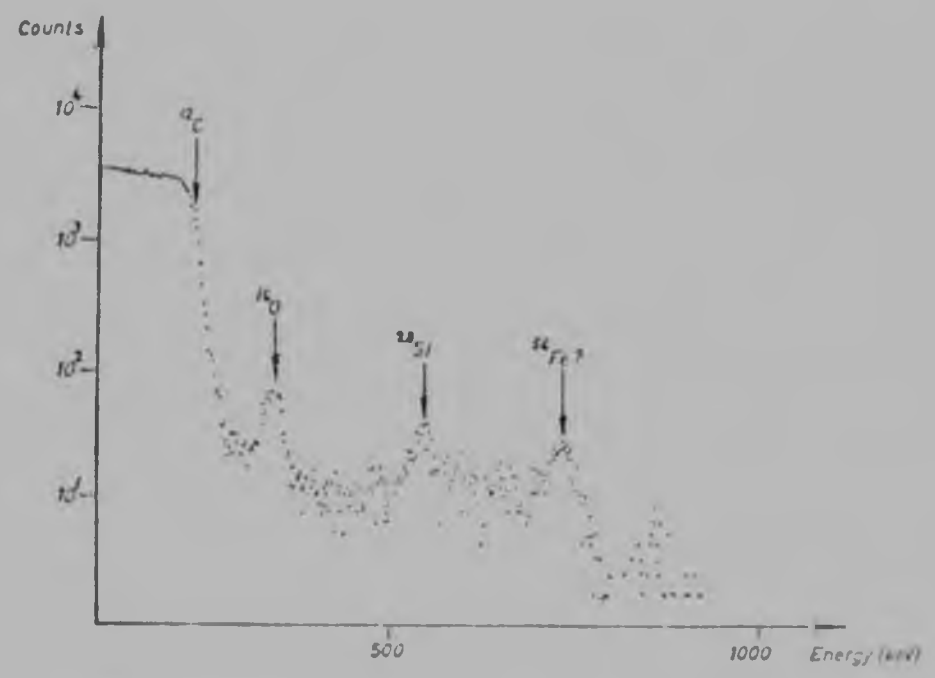

a) cleaned in conventional solvents (Di9)

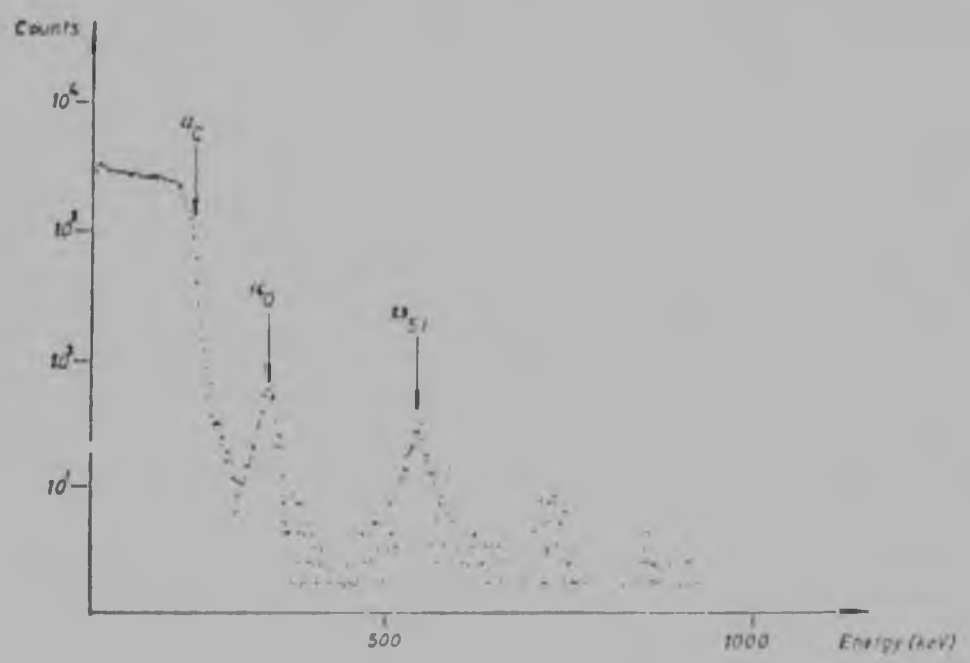

b) cleaned in Contrad 1 mins (Di9)

Figure 5.3: Examples of impurity spectra taken with 1.0 MeV He^+ ions (continued on next page).

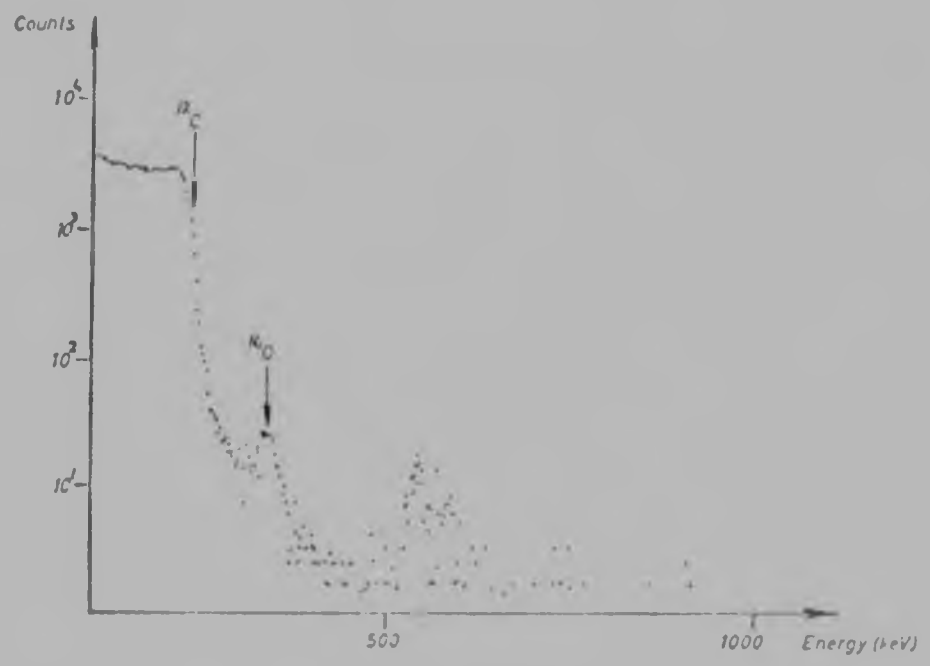

c) cleaned in Contrad 8 mins (Di13)

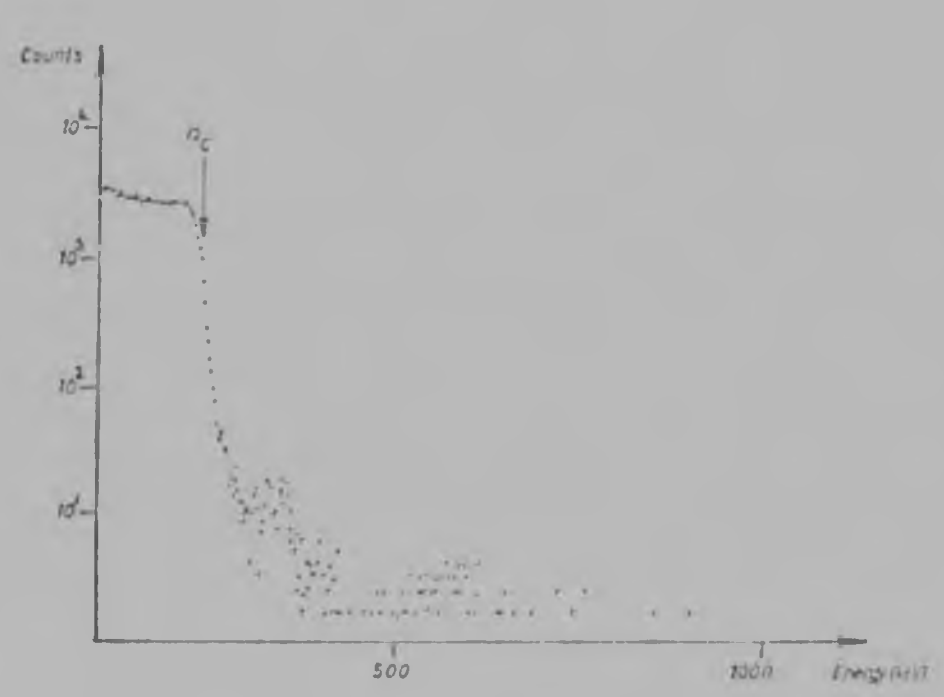

d) cleaned in Contrad 30 mins (Di11)

Figure 5.3: (continued from previous page).

the organic solvents attack the pump-oil quite vigorously, but are ineffective against th earthy impurities; whereas 'Contrad' removes everything, and is fast.

'Contrad' (sold under the name of 'Decon 90' in some countries) is designed for radiochemical decont ination and other demanding cleaning jobs. It is believed to contain a surfactant and a chelating agent. The concentration used was 20%, in deionised water. Tests showed that ultrasonic agitation for 30 minutes was more than sufficient in all cases.

A small oxygen peak always remained after cleaning, equivalent to about a monolayer. It is thought to be intrinsic to some diamond surfaces, and will be considered again in Section 9.5.

As an independent test of the method, some cleaning experiments were carried out in collaboration with Professor R.W. Ditchburn and the Diamond Research Laboratories. Packets of diamonds of concealed history, some of which had been cleaned by conventional gemstone methods, were cleaned in Contrad and the results analysed using Rutherford backscattering. The Contrad method showed itself superior [Per77a].

5.3.3 Routine

Ultrasonic cleaning in 20% Contrad for 20 - 30 minutes was adopted as the standard procedure applied to all diamonds before experimentation, and before processes such as annealing (§5.4.4). Each specimen was cleaned in an individual 10 ml PTFE beaker. The cleaning was finished

with several ultrasonic rinses in deionised water, and the diamond allowed to dry by evaporation. It was handled by the edges using only 'Fluoroware' plastic tweezers or a plastic-tipped vacuum pencil. Clean diamonds were stored in clean 'Fluoroware' boxes, but were preferably mounted and used immediately.

Contamination from the vacuum environment was minimised by always using the cryopump and keeping the other traps cold (see Section 6.6).

5.4 IMPROVEMENT

5.4.1 General

The first diamond channelling experiments (in Phase I) were performed on natural faces of the platelet diamonds Di3 - Di13. Many these untreated stones exhibited quite low channelling yields. Because the yields were eventually degraded by radiation damage and beam-related deposition of vacuum contaminants, methods of regenerating the stones were sought, and the usefulness of applying the same techniques to improve virgin crystals became apparent. Several techniques were investigated during Phase II, and the effective ones were applied to all stones prior to taking good-quality data in Phase III.

Most of these techniques involved removing material from the diamond surface to expose fresh crystal. This was expected to make an improvement in the following cases:

i) The surface had been abraded or microcracked in the earth or during recovery. The fact that improvements to natural surfaces

TABLE 5.5

Effect of Surface Treatment on Minimum Yield

<110> axis, 1 MeV protons (except * = 0.7 MeV alphas)

Stone	Treatment	Minimum Yield χ_0 (%)	
		Before	After
Di3	Gas-etch	5	1.8
Di4	Polish and gas-etch	5.3	2.0
	Polish near {111}		37
	Repolish		2.7
	Ion mill @ 0° incidence		3.2
	Ion mill @ 45° incidence		2.9
	Heat in hydrogen		2.2
	Anneal		2.1
Di13	Gas-etch	9*	2.9
	Polish		2.3
	Anneal		1.9
KC11	Polish	5.2	3.0
	Anneal (polished surface)	3.0	2.7
	Anneal (unpolished surface)	5.2	3.5
KF3	Polish and gas-etch	5	2.3
	Anneal		2.2
KK6	Polish	5.0	2.7
	Anneal (polished surface)	2.7	2.3
	Anneal (unpolished surface)	5.0	3.5
	Anneal @ 1100° (pol. surf.)	2.3	3.1
	Anneal @ 1400° (unpol. surf.)	3.5	3.6
KK7	Polish and gas-etch	26	2.6
	Anneal		2.5
KT1	Anneal	3.5	2.2

were always observed, indicated that diamonds, as found, usually have a slightly damaged surface region. The exact nature of the damage could not be deduced from these experiments.

ii) Radiation damage had occurred owing to beam exposure (see Chapter 10). The penetration and therefore the damage depth were only a few microns in the energy range used.

iii) Beam stimulated adsorption of contaminants had occurred; this phenomenon is dealt with in Section 6.6. Such adsorbates could not be removed by cleaning.

Some typical results are presented in Table 5.5, including at least one example of each process.

5.4.2 Gas-etching

When diamond is raised to a high enough temperature in an oxidising atmosphere (for example, oxygen, carbon dioxide, water vapour) it gradually burns away, forming carbon monoxide or possibly dioxide. Such reactions have been thoroughly investigated by Phaal and Evans [Ev61, Ph62a, Ph62b] who found that very smooth etched surfaces were produced in completely dry fast-flowing pure carbon dioxide at 1350°C [Ph62b].

An apparatus was set up in which fairly pure carbon dioxide from a cylinder or from warming dry-ice was dried by passing it through a coil cooled in a acetone/dry-ice freezing-mixture, and through a tube of indicating silica-gel. After passing over red-hot steel wool to getter

oxygen and other reactive gases, and to preheat it, the CO_2 stream passed at about 200 cm s^{-1} over the hot diamond. The latter was in a fused quartz tube heated by an oxyacetylene torch to 1000 ± 50°C. A lower temperature was used at first (~750 ± 50°C) but produced very slow etching with much pitting.

Afterwards the diamond was boiled in a mixture of equal parts of perchloric, nitric and sulphuric acids, to remove the black layer of amorphous carbon which forms on the surface. (The original workers used acid proportions of 3:1:1 respectively [Iv~6], but the proportions do not seem to be critical.) The diamond was washed, dried, and the weight loss determined; from an estimate of the surface area, the rate of recession of the surface could be calculated. This was about 2 μm min^{-1} at 1000°C.

The disadvantage of this method was that it often left the diamond surface deeply pitted (see also Ve 1); possibly the CO_2 was not dry enough. The pits tended to be in areas struck by the ion beam, probably owing to the preferential etching of dislocations comprising part of the beam damage. Etching out of dislocations is a familiar phenomenon with other crystals, and has been suggested as a mechanism (under different conditions) for pyramidal trigon development on natural diamond faces (the topic is outlined in Wi~1).

However, channelled yields obtained from smooth areas of gas-etched samples were amongst the lowest recorded.

It is possible in the light of §5.4.4 below, that some at least of the improvement found was due to annealing at the temperature used.

5.4.3 Polishing

Diamond may be polished to a very high finish by means of a spinning cast-iron disc (scaife) impregnated with diamond powder. The process is highly anisotropic [Wi72]; the most resistant directions are parallel to the {111} planes.

It was expected that channelling effects would be weak with polished surfaces, because of crystal damage (by analogy with silicon, see §4.3.2). In fact, surfaces polished in 'easy' directions with 4 - 8 μm diamond grit gave yields almost as low as those of the best gas-etched faces. This is in accordance with the brittle fracture model of the polishing process used by the Oxford group (for example Wi72, Cas72, Cas73, Thr76).

It seems that some damage, however, is associated with polished surfaces. Since they were removed by annealing (see following section). The question is considered in more detail in Section 9.5. Surfaces polished within a few degrees of the 'difficult' {111} planes showed considerable disturbance (very high channelled yields).

5.4.4 Annealing

Diamond may be annealed without graphitising at temperatures up to about 1400°C, if oxidising agents are rigorously excluded. At higher temperatures spontaneous graphitisation occurs. The temperature of the

onset of graphitisation appears not to be sharply defined, quoted values depending probably on the sensitivity with which the graphite was detected.

Stones were annealed in quartz tubes wound with resistive heating-coils, placed in a stainless-steel ultra-high vacuum chamber which was pumped to about 1 x 10^{-9} torr by 'Vacion' and titanium sublimation pumps. (Some workers prefer to anneal in flowing pure argon [Hor75, Hor76], but it is difficult to exclude traces of oxygen.) Annealing times and temperatures were varied, but were generally one hour at 1150 ± 50°C (measured with an optical pyrometer).

Diamonds always gave lower channelled yields after annealing. The total improvement was greater for polished faces than for natural faces on the same stone. Longer annealing times (up to 28 hours) and higher temperatures (up to 1300°C) appeared to make no consistent improvement on the above conditions. This is in accordance with the evidence that the vacancy in diamond is mobile above 900°C [C177], the interstitial already being mobile at room temperature [Vad75], if it is assumed that annealing depended on the motion of these defects. The best annealed stones were among the best of all those investigated by channelling.

It may be noted that annealing was the only one of the improvement techniques used which operated throughout the bulk of the stone; the others aimed simply at replacing or modifying the surface.

Essentially the same process has been used by workers in low energy electron diffraction (LEED) to obtain the best results from polished diamond surfaces [Lantt, Lur77]. However, in those studies it was regarded solely as a cleaning technique. The present work indicates a second possible reason why it produces optimum LEED contrast: the annealing out of polishing damage at the surface.

5.4.5 Ion Milling

Sputter milling with 800 eV argon ions was performed in the chamber at a background pressure of 10^{-4} torr. The rate of recession of the surface was about 1 nm min^{-1}.

Ion milling was the least successful of the methods tried. It produced considerable disorder at the crystal surface, as shown by the size of the channelled surface peak, equivalent to about 20 extra disordered layers. The peak was not appreciably reduced by heating in situ to 700°C. Similar results have been observed by LEED methods [Mah64, Lantt, Lur76, Lur77].

Ion milling was therefore rejected as a means of preparing the best possible crystals for channelling.

5.4.6 Heating in Hydrogen

Marsh and Farnsworth have reported the production of apparently clean and ordered diamond surfaces, as monitored by LEED, by heating in hydrogen either with or without prior argon ion milling [Mah64]. They found the optimum conditions to be a temperature of 700°C at a

hydrogen pressure of 10^{-3} torr for two hours

These conditions were duplicated on two stones, exhibiting polished, unpolished, and ion-milled surfaces. Channelling analysis showed a slight improvement (except for the polished surface) and the stones appeared cleaner. However, the improvement was not outstanding - in particular, ion-milling damage as revealed by the surface peak was reduced but not removed - and the technique was not pursued further.

5.4.7 Assessment

The best techniques appeared to be either

i) gas-etching, or

ii) polishing followed by annealing.

Both procedures were able to give ·110 proton minimum yields χ_0 in the region of 2.0°.

But to obtain such low yields, it was necessary to take a diamond which already had a fairly low yield before treatment. In other words it was not possible to make an excellent crystal out of a poor one by any of the above techniques.

The problem was further investigated by applying gas-etching, polishing, or annealing, in different sequences in all possible permutations, to 19 of the Di- and K-stones. It was hoped to establish an optimum procedure by which any given stone could best be improved.

TABLE 5.6

Summary of Results of Improvement Techniques

NB: The quoted values are representative only; actual values were scattered.

1.	Minimum Yield (χ_0)	
	Typical virgin crystal value (good stone)	5 %
	After polishing	2.5 ± 0.5 %
	After etching	2.5 ± 0.5 %
	Anneal for one hour ..... improvement by	0.2 % typically
	Anneal for longer ..... improvement by	0.1 % sometimes (behaviour often anomalous)
2.	Deeper Yield ($\chi_{2.5}$)	
	Typical virgin crystal value (poor stone)	50 %
	Typical virgin crystal value (good stone)	30 %
	After polishing ..... improvement by	25 %
	Anneal for one hour ..... improvement by	2 % typically
	Anneal for longer	may improve or worsen

The results (in the form of x_0 and $x_{2.5}$ values) were tabulated and plotted in various ways to try to bring out their interrelationships. However, no definite trends were found. Usually, whatever technique was first applied made a distinct improvement; subsequent ones might or might not make further improvement, or might even worsen the stone, but the differences were small and probably statistical. This can be seen in Table 5.5; an attempt at a summary is made in Table 5.6.

Thus the choice of techniques appeared to be somewhat open. Polishing with annealing conferred the advantage of flat surfaces for experimenting on, but could not be used for tabular specimens oriented on {111} planes (see §5.4.3), unless they could be polished several degrees off their natural faces. For the thinnest {111} macles, gas-etching was deemed the most suitable. Annealing on its own was successful if the stone already had very good {111} faces. The techniques used on each of the diamonds finally selected are indicated in Table 5.3.

The best systematic procedure seemed to be

i) to choose those stones with the best appearance, in terms of morphology, absence of colour, and freedom from inclusions;

ii) to apply whichever improvement technique was judged the most suitable, according to the previous paragraph; and

iii) to select for use, any stones which produced low channelled yields, and to apply no further effort to those which did not.

CHAPTER 6

EXPERIMENTAL PROBLEMS AND TECHNIQUES

6.1 INTRODUCTION

This chapter deals with problems which became apparent during the performance of the experiments, and the special techniques evolved to overcome them and to ensure reliable data. Some are peculiar to ion-beam experiments on diamond, whilst others are more generally encountered. They are chiefly concerned with beam current integration, electronics, and the status of the target. These investigations comprised the main work of Phase II.

6.2 ELECTRON SUPPRESSION

6.2.1 Background

In any experiment where data is being normalised to the same total number of incident ions via a measurement of target current, it is necessary to suppress the emission of secondary electrons. This is particularly important if the beam incidence angle is to be varied, since the electron emission coefficient is proportional to its secant [Ste57]; recently, crystallographic variations have also been seen [Bru74].

The means of suppression is often the application of a negative potential of a few hundred volts to a ring or screen in front of the

target-holder. It seems traditional to take a rather cavalier attitude towards this: a sketch of the electric field lines in some reported configurations shows them to be largely ineffective in returning all electrons to the target.

6.2.2 Design

The large flat target-holders being used (§3.3.1) suggested that the negative bias be applied to a disc of similar diameter, the two facing one another to form a parallel-plate capacitor, and the suppressor plate having a hole to allow passage of the beam. To avoid escape of electrons round the edges, their maximum range in a radial direction must be less than the radius r of the target-holder. If the target-to-plate separation is s, it can be shown that this condition gives

$$s < \tfrac{1}{2}r$$

assuming sufficient bias for no electrons to reach the plate. Tests indicated that -400V was more than adequate for 1 MeV He^+ ions on metals.

6.2.3 Self-suppression

Measured beam-currents on diamond did not change when the suppression voltage was switched off and on. Diamond appears to suppress its own secondary electrons; it was assumed that this was due to its being a good insulator and therefore charging up positively in the region of the beam-spot. Further evidence for this was seen (Section 7.3).

However, there were exceptions, for example, ion-milled diamonds showed no self-suppression. To be on the safe side, electron suppression bias was always used (until the modifications of §6.3.2).

6.3 TARGET CHARGING

6.3.1 Evidence

The problem of performing ion-beam experiments on insulating targets whose surfaces charge up under the incident beam, has been considered in a recent paper by Ahlberg et al [Ah75]. Diamond is an extremely good insulator (resistivity >10^{11} Ω-cm in the dark); the lack of any problem in collecting target currents was presumably due to surface breakdown being the predominant conduction mechanism. In fact, frequent surface 'flashovers' could easily be seen.

In some experiments, the angular position of a channel (but not the width) showed a small but distinct dependence on beam current. The effect was most noticeable at large incidence angles, for example a <100> axis at ~55° shifted by ~0.1° when the target current was changed from 1 nA to 5 nA. This could be explained if the target were charging and deflecting the beam, the equilibrium potential reached (and hence the deflection) being proportional to the rate of arrival of charge. For the above example, application of the energy conservation principle to the incident particles gives a potential of ~1 kV in the beam-spot region.

The channel-shift effect was completely suppressed by the

evaporation of a thin conducting layer of aluminium on to the diamond surface, and restored by removing the layer with acid. It was also suppressed by the use of an electron flood filament (see §6.3.2 below). Together with the self-suppression effect (§6.2.3), the evidence indicated that charging was indeed occurring on clean diamond surfaces, and was responsible for the channel shift.

6.3.2 Remedies

Conductive layers on the diamond surface could of course not be used because of their enhancement of the dechannelling. Instead, care was taken to keep the target-current, and hence the beam deflection, constant.

The problem was later eliminated by using a heated filament to flood the target with electrons and thus neutralise any positive charge build-up. Secondary electron suppression was then pointless, and the suppressor plate was removed. The target current was collected from the chamber as a whole, which was floated with respect to ground. The filament was powered by an isolated battery and grounded to the chamber.

A plain tungsten filament was found to evaporate significant quantities of tungsten on to the diamond at the temperatures required for thermionic emission. Instead, the filament assembly from an old radio valve was used; its lower operating temperature (due to its emissive coating) resulted in no target contamination. Electrons were drawn away from the filament by applying a bias of +200 V to the valve grid. The development was due to R.W. Fearick.

This configuration was found to be essential when running the high-temperature experiments. The hot target-holder apparently produced considerable thermionic emission of its own, and measurements of beam-current at the target only, became meaningless.

The old configuration was retained on the Tandem because of difficulties in insulating the target chamber. The higher energies and steadier beam-currents resulted in no detectable effects of target-charging.

6.4 TARGET CURRENT LEAKAGE

6.4.1 Heater

Although the target heater was insulated from the target by the use of 'Thermocoax', significant leakage between the two was found to occur when the heater was connected to a mains power-supply. It was therefore powered from isolated lead accumulators.

6.4.2 Other Source

Pickup of stray currents by the external battery leads and by the target current lead was reduced by careful insulation, and neutralised by periodically balancing the current integrator input bias.

6.5 ELECTRONICS

6.5.1 Noise

Pickup of 50 Hz and other electronic 'garbage' by the detectors

and their leads was reduced by systematically eliminating ground-loops, insulating all detector-lead sheaths where they passed into the chamber, and earthing to a single point on one of the preamplifiers. The annular detector was particularly subject to pickup by capacitative coupling, because of its exposed live electrode.

The noise problem is significant with diamond because of the low relative energies of backscattered ions, consequent on the low atomic mass (for example $k = 0.25$ for He^+).

6.5.2 Pulse Pileup

Several different pulse-height analysers, with different time resolutions, were used during the course of the experiments. Analyser dead-times were generally negligible (1%). In some cases, dead-times for 'random' spectra rose to 5%, and a correction factor was then applied to the data.

The analyser generally used with the low energy accelerator 'Christine' (an ND2400) had integral pileup rejection circuitry. However, it was found to reject more low-energy than high-energy pulses, resulting in a distortion of the spectral shape, and was therefore left out of circuit.

6.6 TARGET CONTAMINATION

6.6.1 Sources

The deposition, in the early experiments, of silicon and oxygen

and its attribution to diffusion-pump backstreaming, has been referred to in Section 5.3. This inference was further investigated by obtaining backscattered spectra of all oils used in the vacuum system, for comparison.

Very thin layers of oil were deposited on clean beryllium discs by dissolving a small drop of oil in 25 ml ether and spreading one drop of the ethereal solution on the disc. Backscattered spectra of 1.0 MeV He^+ ions were recorded. The use of a beryllium substrate (M = 9) rendered carbon (M = 12) visible. The following were investigated:

i) turbomolecular-pump oil (Pfeiffer T12);
ii) diffusion-pump oil (DC704 silicone);
iii) backing-pump oil (Edwards number 18);
iv) O-ring grease (Dow Corning silicone); and
v) lubricant grease (Apiezon 'L').

Only the diffusion pump oil and the O-ring grease were found to contain ^{28}Si (the peak was rather broad, and ^{32}S was probably also present). The other oils appeared to be pure hydrocarbons. A test in which a washer, smeared with O-ring grease, was held in front of the beryllium disc, produced no deposition, and all the visible contamination appeared to originate from the diffusion-pump. It was borne in mind that hydrocarbon oil contamination on diamond would be seen only with difficulty, as an increase in the channelled surface peak; there is evidence for this in Section 9.3.

It may be worth noting that silicon channelling workers often

mention observing excessive amorphous surface layers of silicon and oxygen, usually characterised as 'surface oxide'. Some of this may well originate from diffusion pumps.

6.6.2 Mechanism

It was formerly believed that contaminant molecules become entrained in the beam during its passage through the vacuum, and arrive at the target either as part of the beam, or as a concentric 'halo'. That this is not the case, was indicated by the observation that with the cryoshield cold, very little target contamination occurred. Moreover, the characteristic black surface bear-spot indicative of contamination, developed quickest on those beryllium discs which had already been smeared with oil. It appeared that target contamination must be deposited directly from the surrounding vacuum.

On the other hand, when the cryopump was not used, a rapid buildup of contamination occurred only during the periods when the beam was on target. Thus a two-stage mechanism is implied. Contamination is deposited from the vacuum, perhaps as a condensed monolayer, but is 'fixed' by beam-induced decomposition. More vapour then condenses to restore the liquid/vapour equilibrium and contamination steadily increases.

Such beam-stimulated adsorption is well-known in electron beam analysis (for example, see Co70, Lam73, Ki74 and Jur77); in view of the findings of Lam73, the secondary electrons emitted through the target surface, rather than the incident ions, may be responsible. An analysis

of the dynamics of carbonaceous film growth has recently been published [Hi77].

A second mechanism was considered: that of recoil implantation of the atoms of a condensed surface layer, under the impacts of the beam ions [Ne69]. However, the fraction of atoms implanted was calculated to be quite negligible, $\sim 10^{-7}$ [Fea77d].

With a hot target, direct baking on of contaminants seemed to be implicated (see Section 9.3).

6.6.3 Prevention

The rate of contamination was reduced to a negligible level by always chilling the cryopump before putting beam on target. In addition, migration of pump oil vapour to the target-chamber was minimised by the use of the diffusion-pump trap and in-line trap (§3.3.2).

During a run, spectral evidence of contamination was monitored, and a new beam-spot selected if necessary.

6.7 RADIATION DAMAGE

Radiation damage by the analysing beam causes an increase in dechannelling, and it was therefore necessary to ensure that it was negligible at the doses used. The topic is treated in more detail in Chapter 10.

No effects of proton damage were seen in the longest runs used.

Helium damage was obvious in very long runs, and was investigated systematically as described in Chapter 10. Damage effects on χ_{min} first became evident for a dose $D \sim 3\times10^{17}$ ions cm^{-2}.

The taking of a channelled spectrum resulted typically in a $D \sim 1\times10^{16}$ ions cm^{-2}, and a full scan with spectra gave $D \sim 3\times10^{15}$. Thus it was feasible to obtain results free of observable radiation damage effects.

The integrated charge per spectrum was chosen as the minimum compatible with good statistics. Unnecessary exposure was avoided by placing a shutter in the beam whenever data were not being taken.

6.8 AXIAL SCAN-PLANE ANALYSIS

6.8.1 Nature of the Problem

Major axial channels are intersected by a number of systems of planar channels, comprising all those planes for which the axis is zone axis. An ion beam scanned through the axis in a plane parallel to one of these crystal planes will pass directly from axial to planar channelling, rather than from axial channelling to random incidence (Figure 6.1, and Reference Dav68, p 348).

If the planar yield is $\leq 50\%$ in the saddle region between planar and axial channels, it will not be possible to measure $\psi_{\frac{1}{2}}$ for the axis. Even if the yield there is $>50\%$, it would be expected that the dip is wider and gives larger $\psi_{\frac{1}{2}}$ values than a scan in a non-channelling plane.

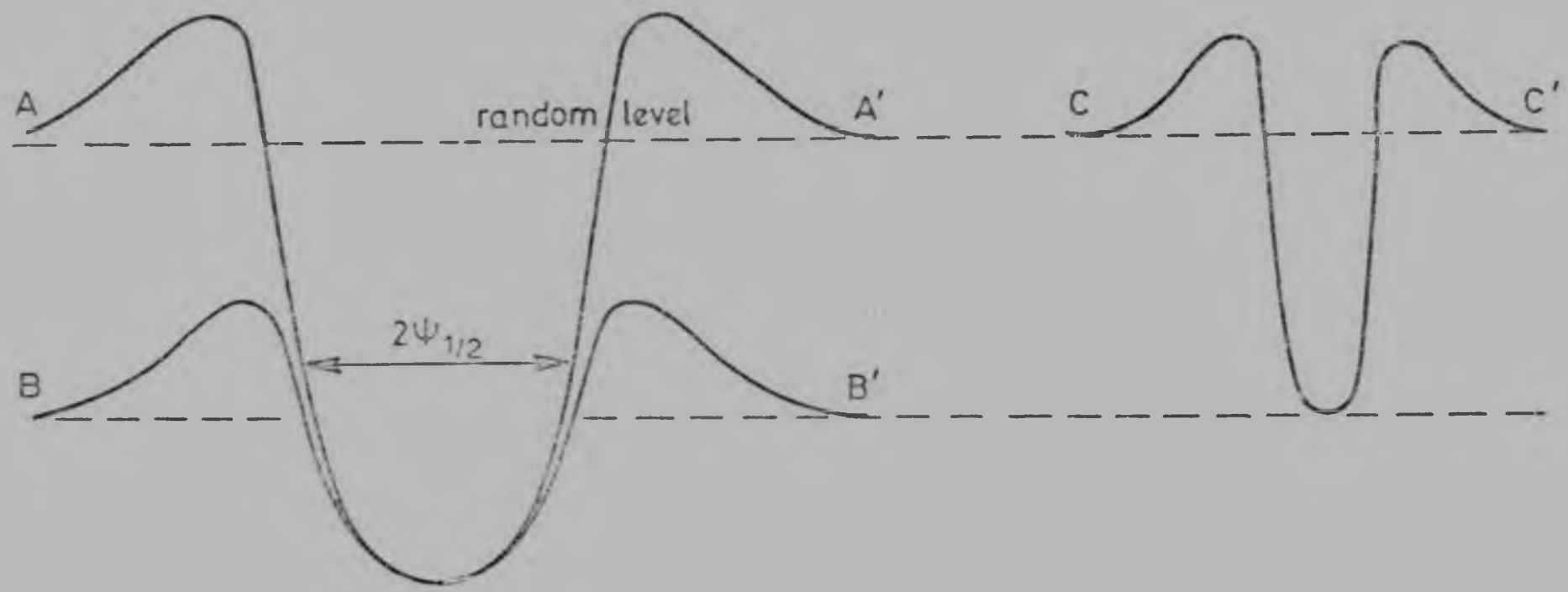

Figure 6.1: Schematic diagram of scans (backscattered counts versus angle) taken through a major axial channel for different scan-planes:

AA', scan-plane randomly orientated;

BB', scan-plane coinciding with a major crystal plane;

CC', scan across the same crystal plane, far from the axis, for comparison.

This was confirmed by these experiments and those of others (for example, see And68).

For an accurate comparison with theory, axial critical angles must clearly be measured by scans which do not coincide with major crystal planes. The axial theories of Lindhard and others consider the rows in isolation, and do not take account of any planar channelling component.

Many published critical angle studies have taken no account of the scan-planes used - or at least have not reported them. Some workers have reported a deliberate choice of major crystal planes. This could be the source of some of the observed discrepancies with theory.

6.8.2 Investigation

The magnitude of the planar effect was investigated experimentally, using 1.0 MeV protons incident near <110>, <111>, and <100> axes. Two types of experiment were carried out:

i) Scans through an axis were made at different orientations and the derived critical angles compared.

ii) The beam was precessed around the surface of a cone whose axis was the crystal axis.

Scans (i) clearly revealed the variations in critical angle (Figures 6.2, 6.3). Repetition in fine azimuthal steps would have been too time-consuming, so the detailed structure was revealed by method (ii).

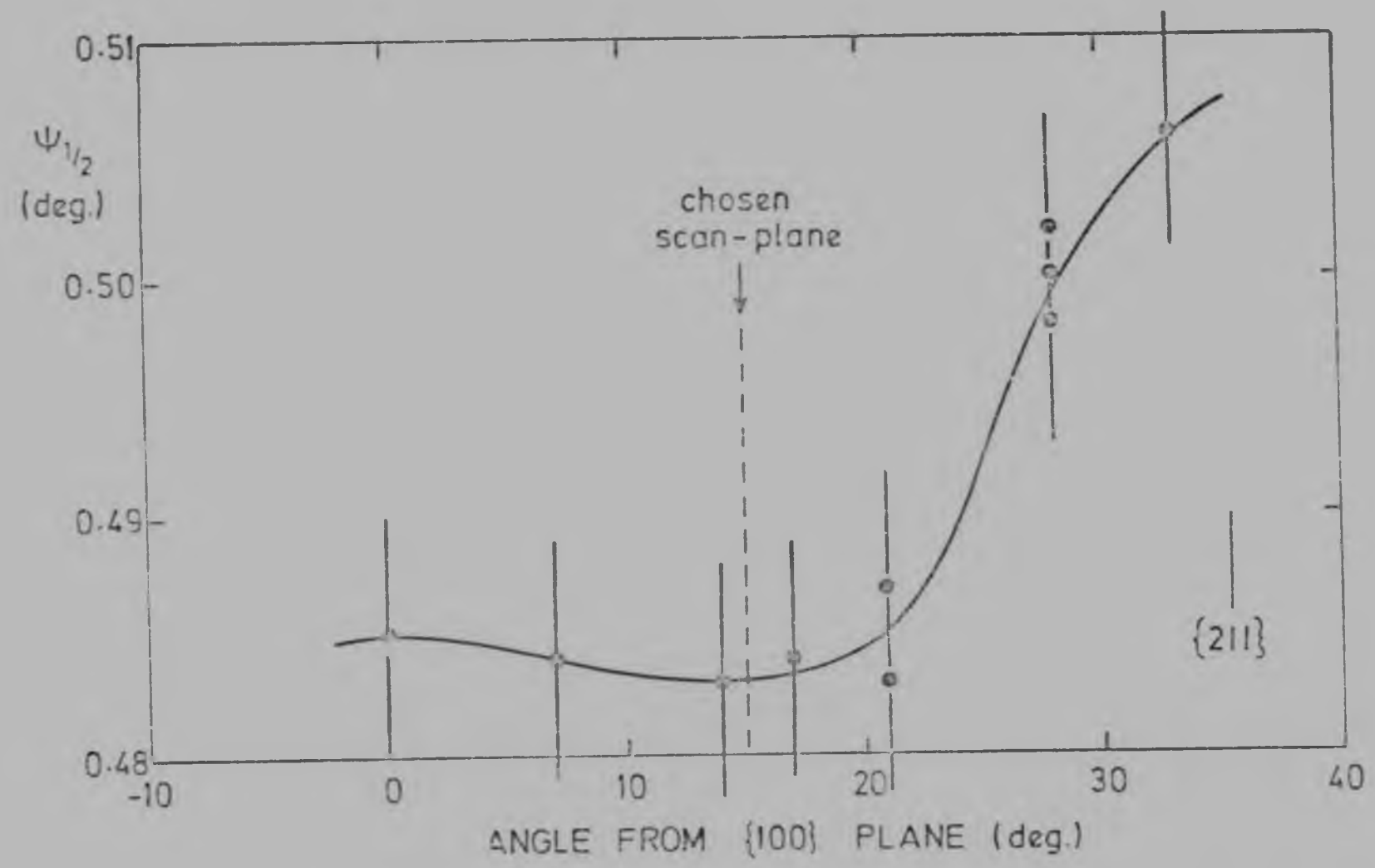

Figure 6.2: Variation of $\psi_{\frac{1}{2}}$ with scan-plane azimuth for a <110> axis (1.0 MeV p, Di4).
NB: Absolute values of $\psi_{\frac{1}{2}}$ are here incorrect.

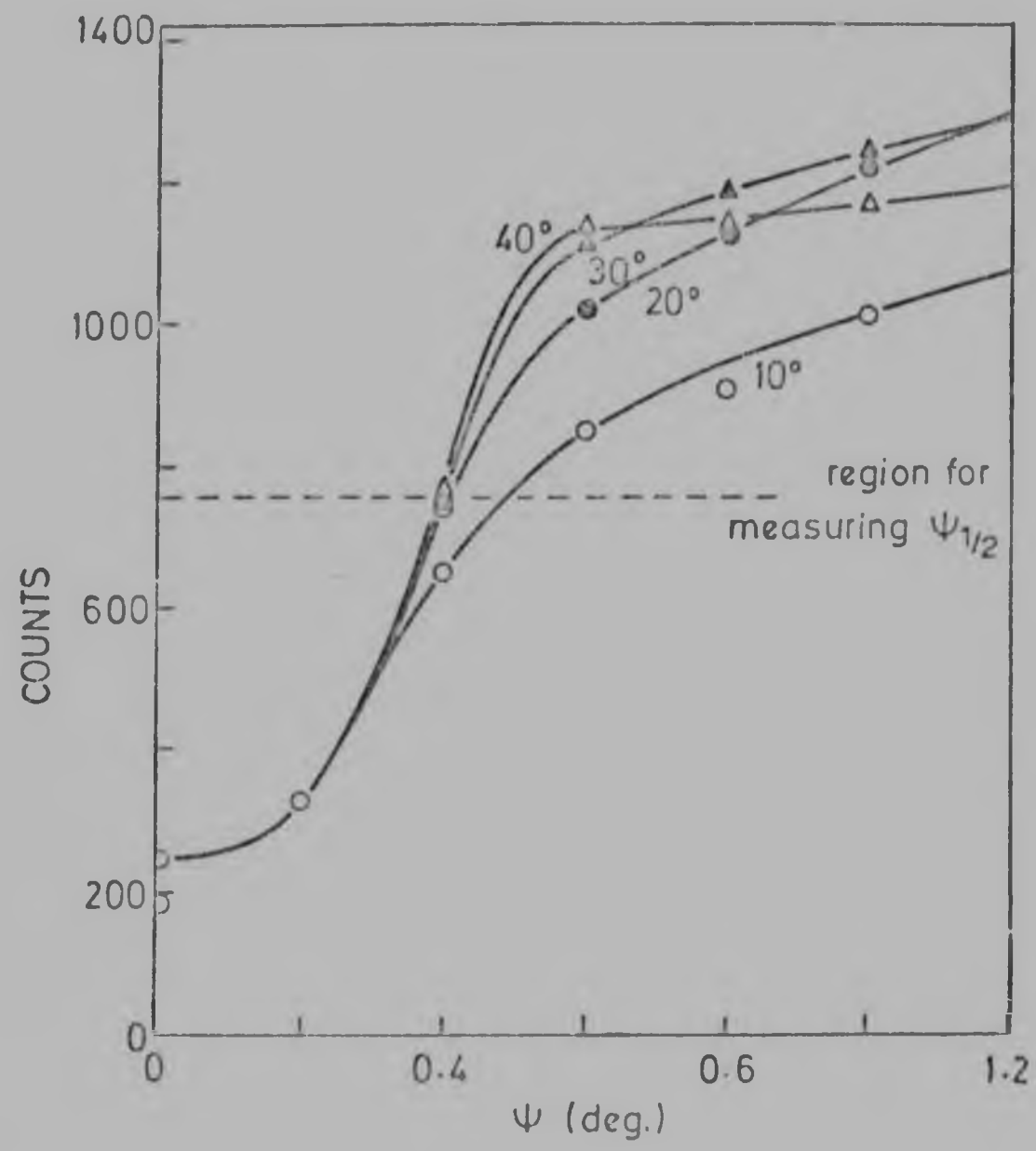

Figure 6.3: Scans through a <100> axis at different azimuths (1.0 MeV p, Di3). Angles between scan-planes and {110} plane are marked on curves.

Conical scans were performed for several different cone half-angles in the region $0<\psi<\sim 2\psi_1$, producing a contour plot of the yield in the region of the axis. The θ and ϕ coordinates for these scans were calculated with the aid of the pocket calculator programme CRAP-2 (Appendix). It was not necessary to scan through 360° in azimuth, but through 180/n degrees, where n was the order of the axis, because of symmetry (including mirror planes). The azimuthal ranges of the scans are indicated in Figure 6.1.

Results for the three axes are shown in Figures 6.5, 6.6 and 6.7, and the <111> data are re-presented as a three-dimensional contour plot in Figure 6.8.

The influence of low-index planes is clearly seen. However, they do not produce sharply-etched 'canyons' but a gradual yield variation, and their effect is evidently felt over most of the axial region. The best choice of scan-plane is presumably that which samples the highest off-axis yields. The planar effects are evidently small within ψ_1 of the axis, which is why a careless choice of scan-plane does not have an immediately noticeable effect on the measured value of ψ_1. For example, in Dav68 the effects were judged indistinguishable.

6.8.3 Scan-plane Choice

Optimum scan-planes were chosen and adhered to for all the critical angle measurements of Phase III; they are listed in Table 6.1. The permissible errors (chosen as the maximum deviation which made a negligible difference to the yield in the conical scans) are quite small

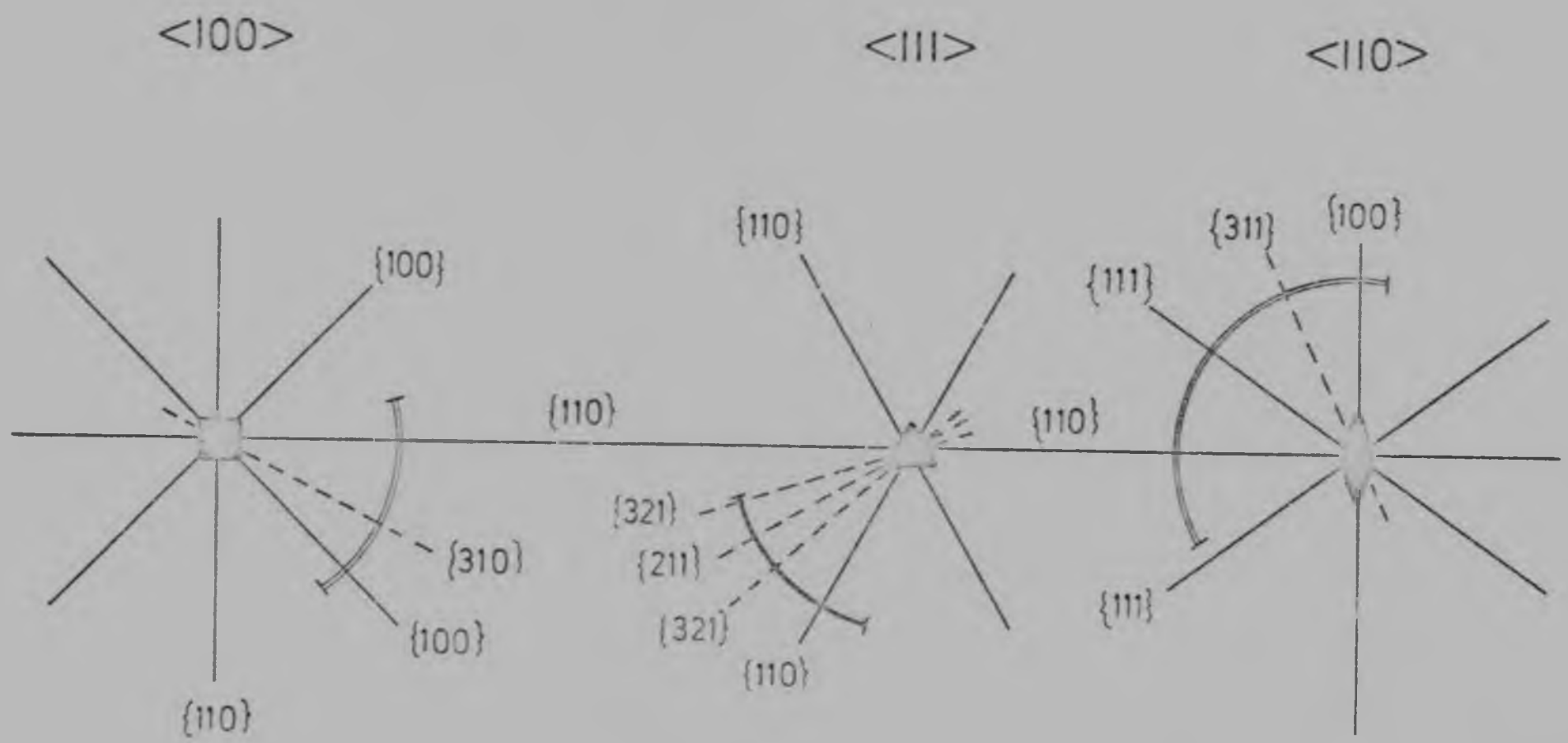

Figure 6.4: Schematic illustration of the azimuthal ranges of the conical scans reported in §6.8.2 (not to scale).

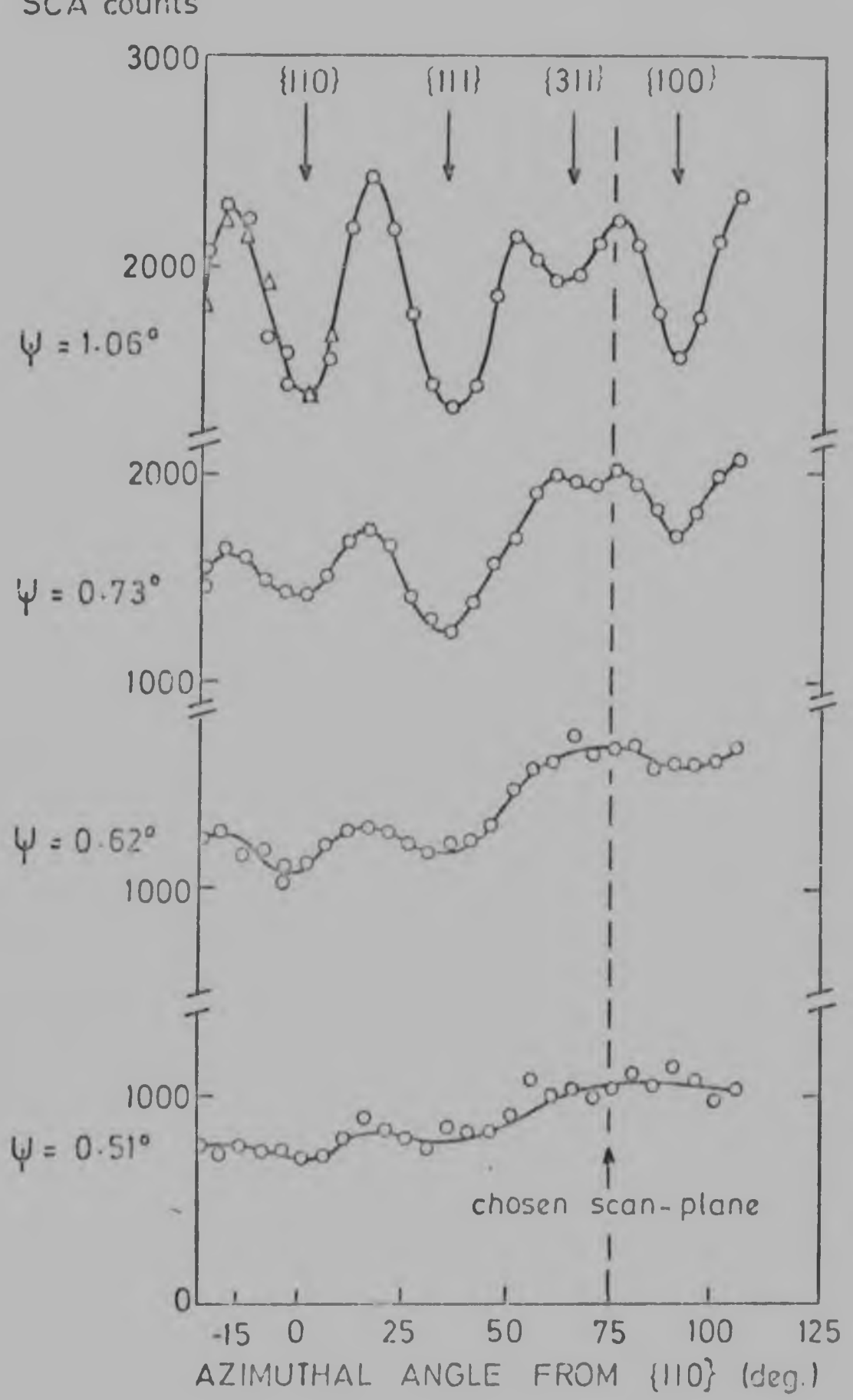

Figure 6.5: Conical scans about a ⟨110⟩ axis (1.0 MeV p, Di4; $\psi_{\frac{1}{2}}$=0.55°).

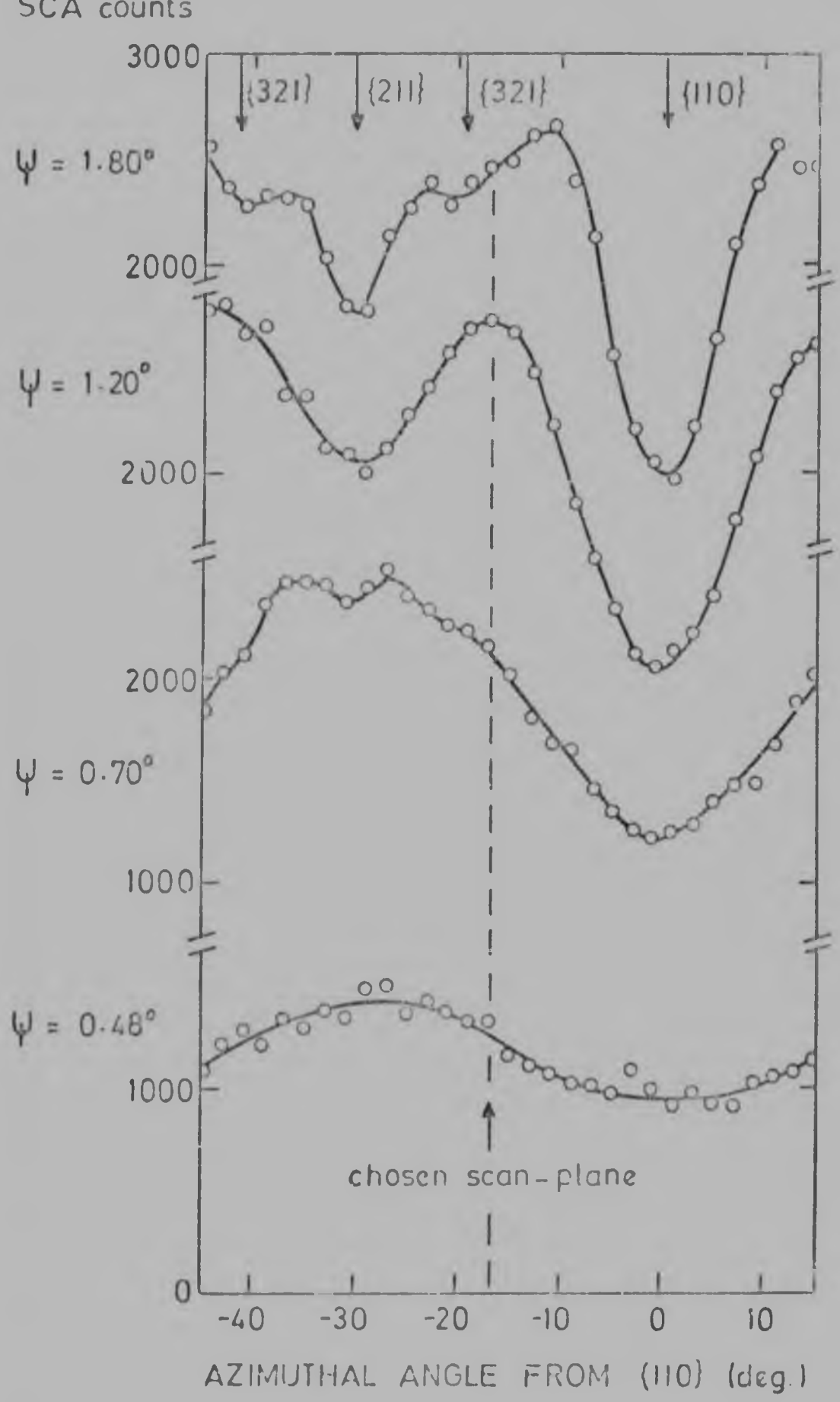

Figure 6.6: Conical scans about a <111> axis (1.0 MeV p, Di1; ψ_β=0.49°).

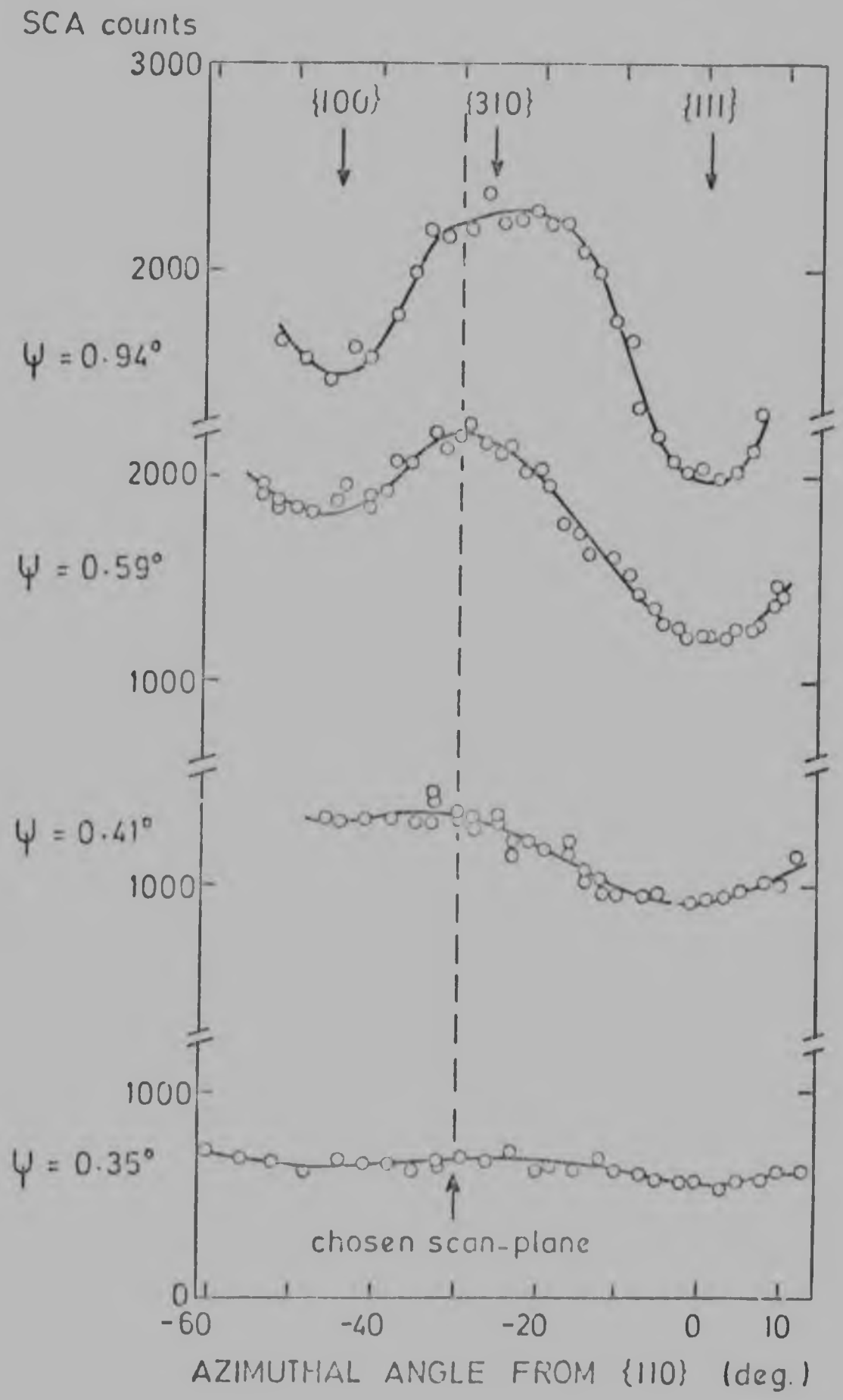

Figure 6.7: Conical scans about a <100> axis (1.0 MeV p, Di4; $\psi_{\frac{1}{2}}$=0.42°).

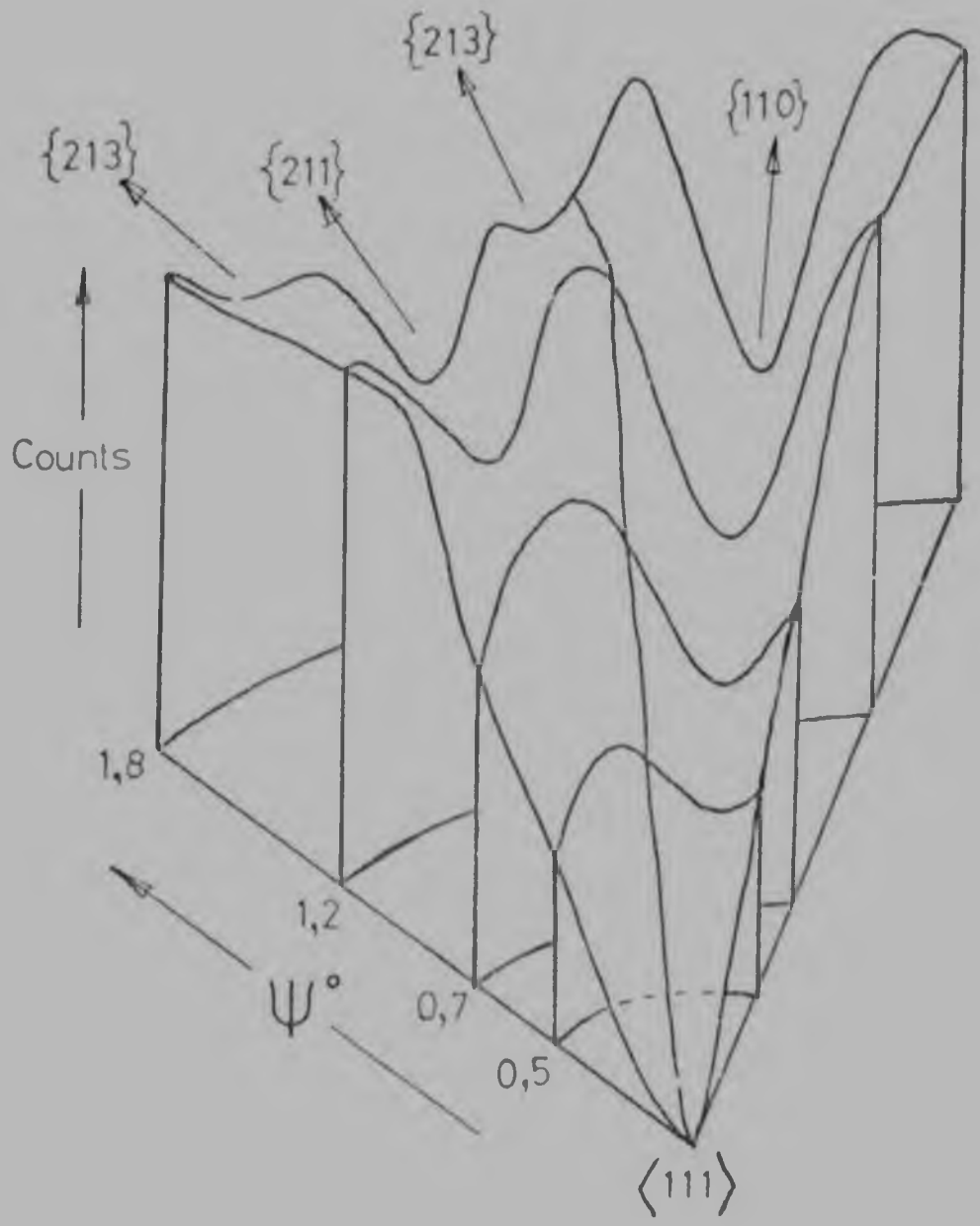

Figure 6.8: Three-dimensional plot of conical scans about ⟨111⟩ (1.0 MeV p, Di4; ψ_1 = 0.49°).

if the reproducible values of ψ_1 are to be determined. In the case of <111>, it may be seen that the scan-plane chosen according to the previous paragraph varies with ψ, and here a compromise was made.

TABLE 6.1

Optimum Transaxial Scan-planes

Azimuthal angles are measured between the scan-plane and a {110} crystal plane

Axis	Azimuth (degrees)
<110>	75 ± 5
<111>	17 $^{+1}_{-2}$
<100>	30 ± 1

6.9 PLANAR SCAN LOCATION

6.9.1 Nature of the Problem

A kindred problem to the above is encountered when performing a trans-planar scan: that of selecting a region of the plane free of the more close-packed minor axes, which would inflate the measured planar critical angles. Many of these are visible with heavier targets (for example, see Dav68, p 348).

6.9.2 Investigation

The problem was approached by

i) Calculating the positions of the minor axes with relatively low indices, and avoiding them.

ii) Scanning down the plane looking for evidence of minor axes.

The planes of interest ({110}, {111}, and {100}) were investigated in the region of the <110> axis (where it was found convenient to take scans). The results are presented in Figures 6.9, 6.10 and 6.11 respectively, together with the calculated positions of those minor axes having critical angles of similar magnitude to that of the plane in question. Some minor axes are visible, in the calculated positions. Apparent evidence for others is probably counting-statistics; only those which were repeatable are shown.

6.9.3 Scan-plane Choice

Optimum trans-planar scan positions were selected, avoiding the calculated positions of undetected minor axes as well as the detected ones, since the scans of 6.9.2 are probably not very sensitive. They are listed in Table 6.2. As in the axial case, the maximum permissible errors are quite small for reliable results.

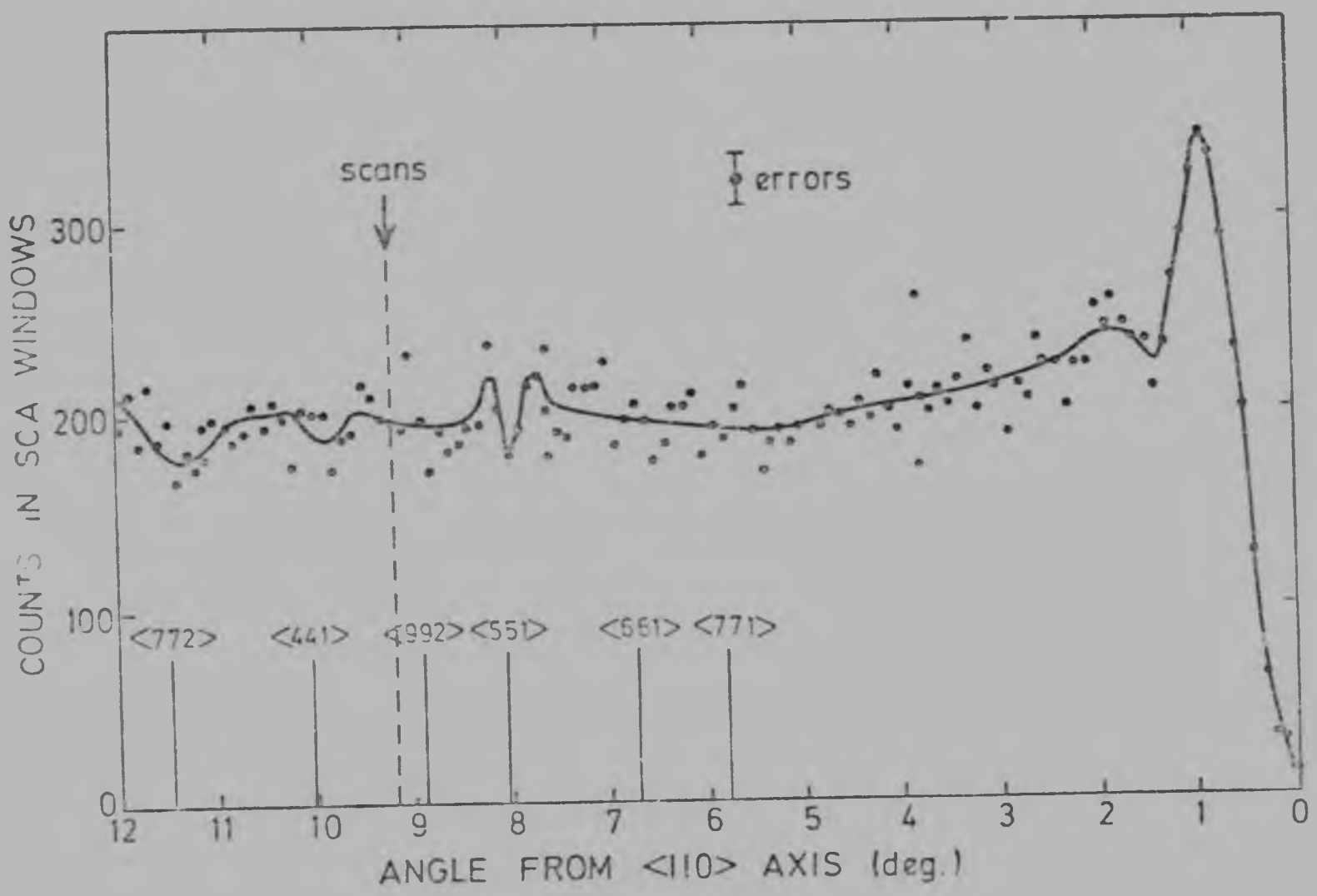

Figure 6.9: Scan down a {110} plane near <110> (1.0 MeVp, KT1).

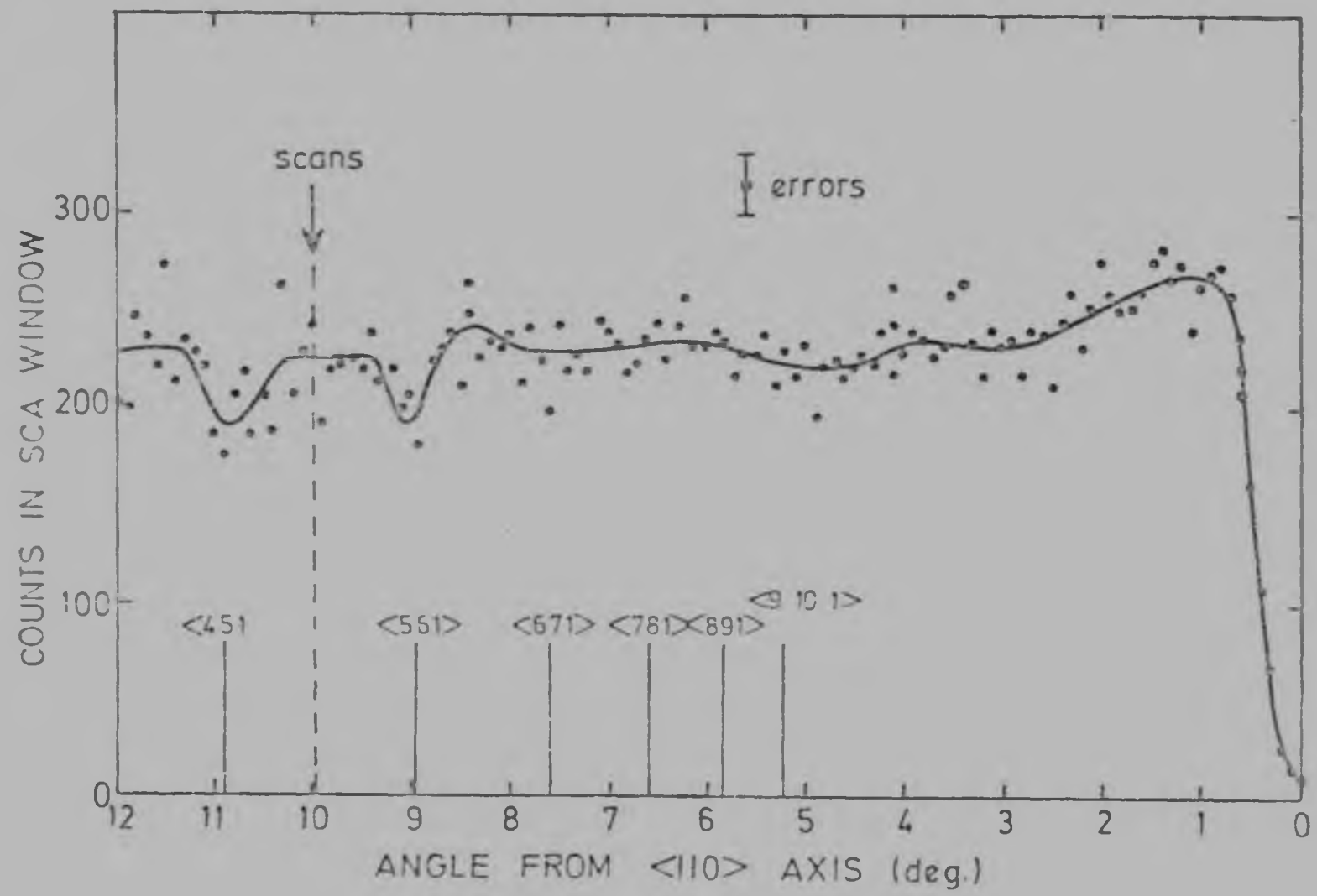

Figure 6.10: Scan down a {111} plane near <110> (1.0 MeV p, KT1).

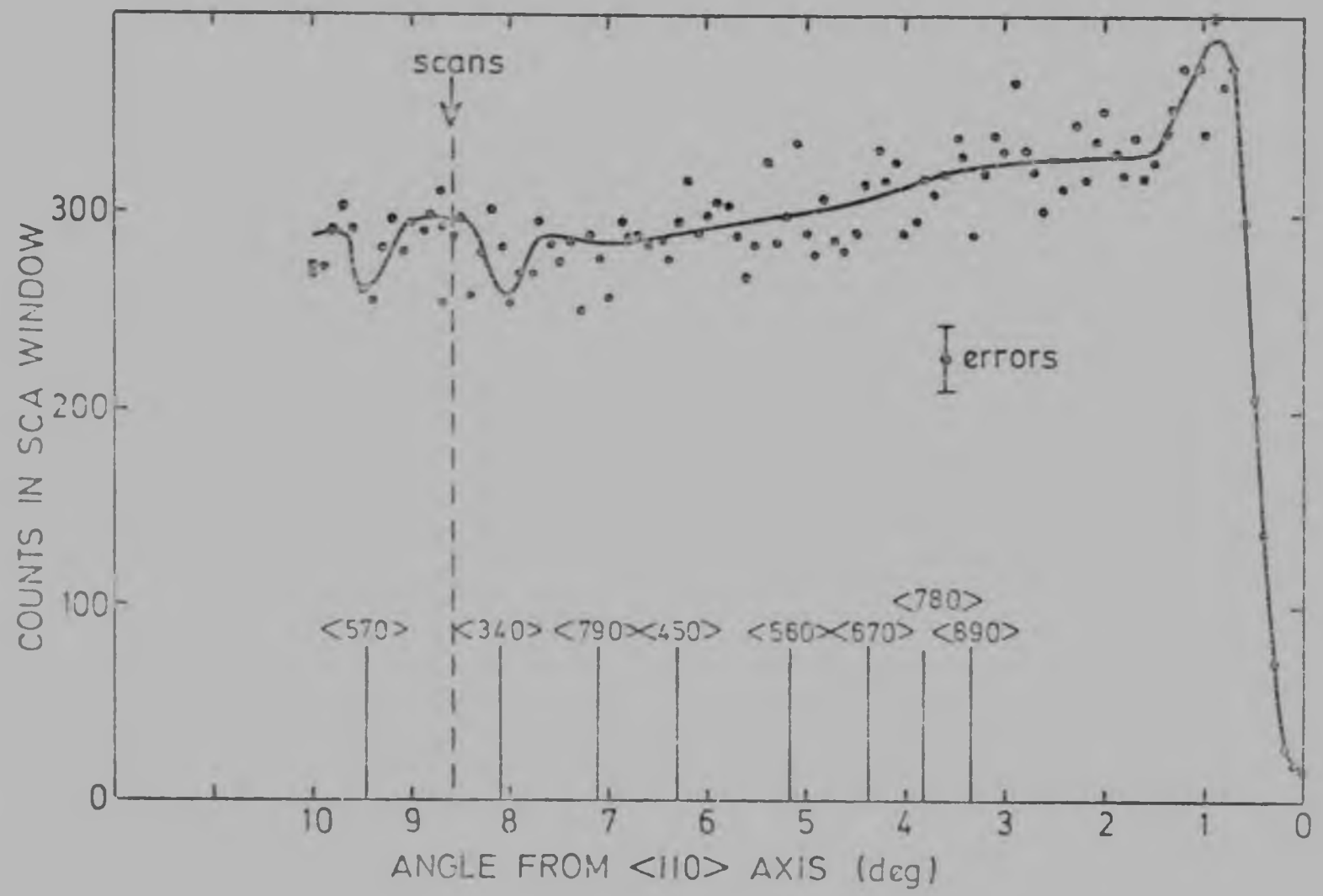

Figure 6.11: Scan down a {100} plane near <110> (1.0 MeV p, KT1).

TABLE 6.2

Optimum Trans-planar Scan-planes

Region of <110> axis. Angles are measured along the crystal plane in question, from the <110> axis.

Plane	Angle (degrees)
{110}	9.2 ± 0.2
{111}	10.0 ± 0.3
{100}	8.6 ± 0.2

CHAPTER 7

CRITICAL ANGLE STUDIES AT ROOM TEMPERATURE

7.1 INTRODUCTION

Measurements of critical angles of channelled ions backscattered from good diamond crystals, are presented in this chapter. Measurements of the same type were generally made on more than one stone to reveal any specimen dependence.

For each set of conditions, the channelling half-angles ψ_1 were measured for the three most open axes of the diamond structure, namely <110>, <111>, and <100>, and for the three most open planes, namely {110}, {111}, and {100}. A few measurements were made for higher axes and planes. The methods of processing and analysing the raw data are outlined in Sections 7.2 and 7.3 respectively.

The results are set out in Section 7.4. Data for 1.0 MeV protons at room-temperature were regarded as standard; measurements were extended to higher energies, to other ion species, and to higher temperatures, keeping the other parameters unchanged in each case. The high-temperature data are considered separately in Chapter 8. Comparisons with theory are made in Section 7.5, and with other results in Section 7.6.

7.2 DATA PROCESSING

7.2.1 Depth Conversion

It was pointed out in §2.4.3 that an energy spectrum of back-scattered ions could be converted to a 'depth spectrum' via Eqn 2.16 or, as used in the present work, Eqns 2.17. It was assumed that the channelled stopping-power is equal to the random, the so-called 'Aarhus convention' [Bot73]; this is a good average approximation for ions which are backscattered [Ed70, Bot73]. In any case theory predicts a stopping-power in diamond for well-channelled particles of about 85% of random [Det75].

7.2.2 Normalisation

Channelled spectra were normalised by dividing them point-by-point by a spectrum for random incidence of the same ions. Here the question arises as to how one ought to define 'random': ideally the target itself should be random, that is, amorphous. Many workers carefully choose an incidence direction which does not coincide with major axes or planes, and set the crystal to this orientation for each random spectrum; although it ensures consistency, the randomness of this procedure is at best doubtful.

This problem is often the major source of systematic error in channelling experiments, and deserves some consideration.

It might be expected that an amorphous target would provide the most accurate random spectra. This was the approach taken by Ziegler and Crowder [Zi73], who reported a difference of ~2% between random

spectra (of alpha-particles backscattered from silicon) taken with crystalline targets as described below, and those taken with fully amorphised targets. They attributed the difference to an artifact of the data-collection in the crystalline case, and concluded that a 2% correction should be applied to random spectra taken with crystals.

However, the difference was more likely due to chemical effects on the stopping-powers of crystalline and amorphous forms of silicon. Such effects were clearly demonstrated eleven years earlier in the different allotropes of carbon by Softky [Sof61], who reported a 6% difference in the stopping-powers (and therefore approximately in the heights of backscattered spectra) of diamond and graphite for 1.1 MeV protons. A cursory experiment was found to confirm his result. Similar observations have been made by others (for example, Matt[?]). Clearly the random spectra must be taken on diamond.

(It is of interest to note that Softky suggested further that "..... since a large effect due to crystal structure was observed it is possible that the stopping power may depend somewhat on crystal orientation. Further experiments should investigate this point ....." - a year before the first report of the discovery of ion channelling [Oe62]!)

In the present work, random spectra were taken while continuously rotating the crystal. There was often a major axis almost perpendicular to the surface, at $\theta \approx 0°$; in these cases θ was offset by $\sim 10.^{\circ}_{5}$, as suggested by Ziegler and Crowder [Zi[?]], and ϕ was scanned through

360/2n degrees, where n is the order of the axis (which always included mirror-planes). Apart from these deliberate precautions, aimed at avoiding excessive influence from major axes, the beam sampled the crystal randomly.

7.2.3 CHANSPEC

Depth conversion and normalisation for many of the spectra were carried out using the Fortran programme CHANSPEC [Fea77b], run on the in-house Interdata 7/32 computer. The programme also smoothed the spectra by fitting cubic spline functions [Rei67].

7.3 DATA ANALYSIS

7.3.1 Plotting

For each combination of conditions, the normalised yield was plotted against incidence angle ψ (with respect to the channel direction) for ions backscattered at a series of chosen depths z. The width $\psi_{\frac{1}{2}}$ of the resulting channelling dip (half width at half minimum) was read off from the graph. The curves were carefully drawn freehand through the points.

7.3.2 Curve Fitting

With a view to putting the data extraction on a more rigorous footing, the fitting of reasonable functions to the data points was investigated. For the U-shaped portion of the curve only, that is, $|\psi| < \psi_{\frac{1}{2}}$, the dips for shallow depths were fitted quite accurately by the function

$$\chi - \chi_{min} = \lambda(\psi-\delta)^k \qquad (7.1)$$

where (δ,χ_{min}) are the coordinates of the dip minimum, λ is a constant, and $k = 4$ for axes and 2 for planes. The kth root of both sides of Eqn 7.1 was taken, and λ and δ fitted by linear regression. Then

$$\psi_{\frac{1}{2}} = \left[\frac{100 \cdot \chi_{min}}{2\lambda}\right]^{1/k} \qquad (7.2)$$

The values of $\psi_{\frac{1}{2}}$ obtained from Eqn 7.2 agreed with the graphically extracted ones to within 0.01° in all cases tested. This corresponds to the angular resolution of the goniometer. Since there seemed to be nothing to choose between the two methods as regards accuracy, the purely graphical one was preferred on the grounds that any interesting behaviour of the curves would be immediately obvious, whereas it might be concealed by a curve-fitting procedure.

7.3.3 Depth Plots

The dependences of critical angles on depth were of interest not only for their own sake, but also to enable the measured values to be extrapolated to zero depth for comparison with theory. It must be borne in mind that the critical angle itself is not being measured at a specific depth - it is always measured outside the crystal - but the value obtained depends on the depth from which the scattered ions originated.

When $\psi_{\frac{1}{2}}$ was plotted against the depth z, it could be extrapolated to $z = 0$ by drawing a curve through the points (as in And72). The surface value was quite insensitive at the 0.01° level to the exact shape of the curve, since the extrapolation distance was rather small.

TABLE 7.1

Transaxial Scans: Incrementing Values of . for Spectra

Values in degrees for 1.0 MeV protons.
Both + and - values (opposite sides of axis) were taken.

<110>	<111>	<100>
0.0	0.0	0.0
0.2	0.2	0.2
0.4	0.3	0.3
0.5	0.4	0.4
0.6	0.5	0.5
0.8	0.7	0.7
1.2	1.2	1.0
2.0	2.0	1.6

TABLE 7.2

Transplanar Scans: Incrementing Values of . for Spectra

Values in degrees for 1.0 MeV protons.
Both + and - values (opposite sides of plane) were taken.

{110}	{111}	{100}
0.00	0.00	0.00
0.06	0.05	0.05
0.14	0.15	0.10
0.18	0.20	0.15
0.26	0.25	0.30
0.44	0.45	0.50
0.84	0.75	0.70

The corrections determined from spectral scans were applied to convert single-channel-analyser (SCA) scan data from Phase I to zero depth. This procedure was somewhat dubious since the dependence of ψ_1 on z is specimen dependent (see Section 7.4). However, the corrections were only a few hundredths of a degree, and the residual error from this source could not have been more than ~0.02°.

7.4 THE DATA

7.4.1 General

In order to delineate the channelling dip accurately, while minimising the beam time on target, the ψ intervals were made smallest in the region of $\psi \sim \psi_1$, and widest in the shoulder region, which was not under particular investigation in this study. A fixed set of ψ values was chosen and adhered to, scaling them according to the projectile and energy; they are listed (for 1.0 MeV protons) in Tables 7.1 (axes) and 7.2 (planes).

Except at the greatest depths, where statistical fluctuations became important, there was generally no difficulty in passing a smooth curve through all the data points, and they have not been reproduced on the plots presented here. Some typical curves including the data-points are shown in Figure 7.1.

7.4.2 1.0 MeV Protons at Room Temperature

Typical backscattered energy spectra for 1.0 MeV protons incident on diamond in major channelling, and random, directions are shown

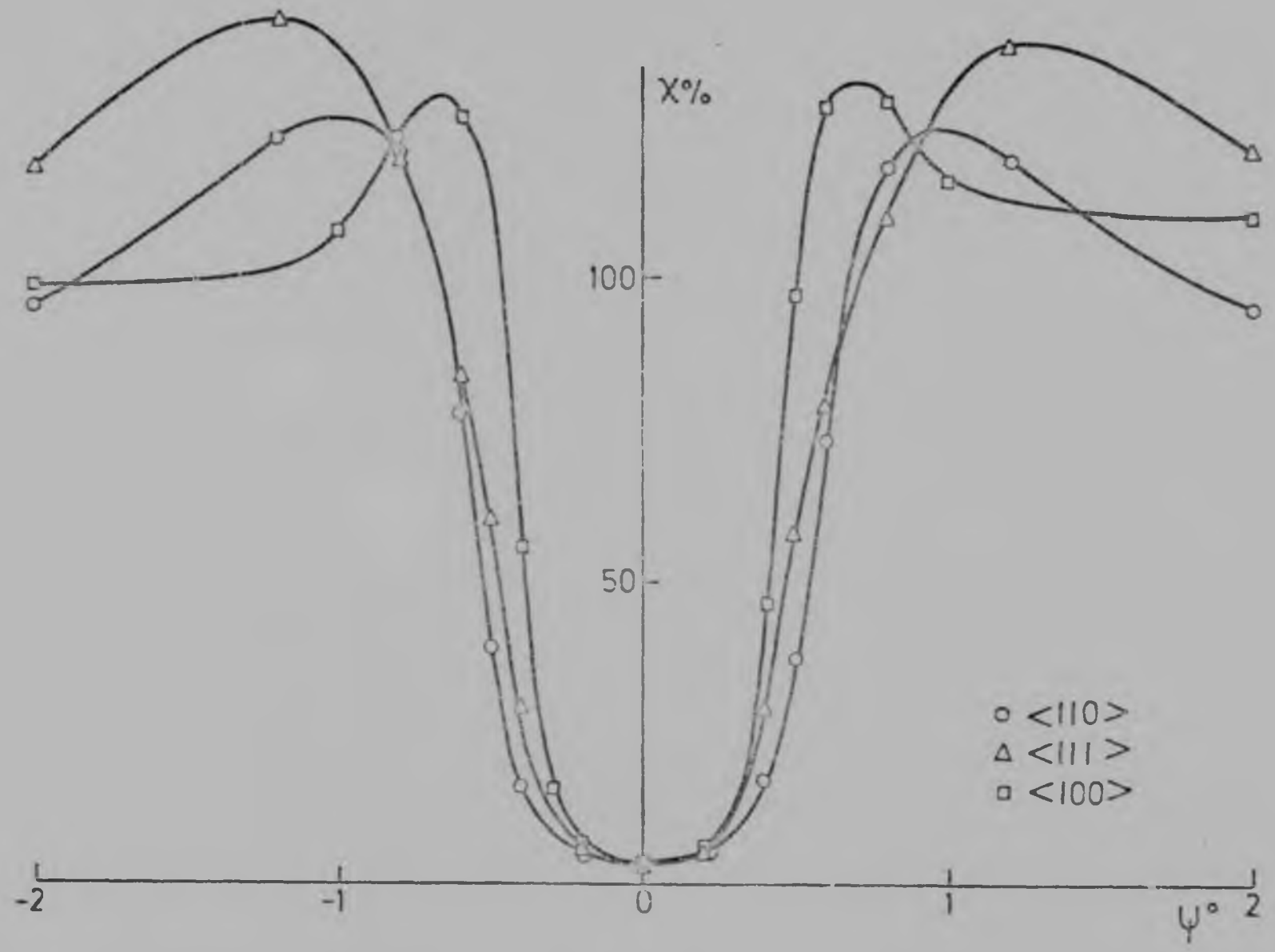

Figure 7.1: Transaxial scans including data-points (1.0 MeV p, z = 0.1 μm, KTl)

superimposed in Figure 7.2. The qualitative differences between different channels and between channelled and random incidence, and the presence of a surface peak, can all be seen.

Angular scans of the three major axes and three major planes of a typical good diamond crystal, for backscattered 1.0 MeV protons, are presented in Figures 7.3, 7.4, 7.5, 7.6, 7.7 and 7.8 respectively, in the form of families of curves for different depths. The shapes of the curves and their trends with depth are similar to those which have been reported for many other substances. The gradual disappearance of the shoulders with increasing depth is attributable to the rapid scattering out of the aligned beam, of ions which sample a higher-than-average atomic density in penetrating the walls of the channels. This corresponds to changes in the spectral shape very similar to those observed by Sone and Fukuzawa [Son72] for protons on silicon.

It is interesting that all the curves of each family intersect at (or very close to) two common points, having $\chi \sim 80\%$. This is observed in all the data, irrespective of energy or ion. The explanation may be speculated upon as follows:

i) In between stable channelled trajectories, having $\psi \sim \psi_1$ with a normalised nuclear encounter probability [Bar71] $P \sim 1$, and semi stable trajectories penetrating deeply into the rows, having $\psi \sim 1.5\psi_1$, with $P > 1$, there may be stable trajectories having $P \sim 1$ (or, in this case, $P \sim 0.8$). They would produce a depth-independent yield for their particular value of ψ. The assumption of stability with depth is perhaps rather unlikely to be fulfilled for such

Figure 7.2: Backscattered 1.0 MeV H^+ spectra, random and channelled incidence (0118).

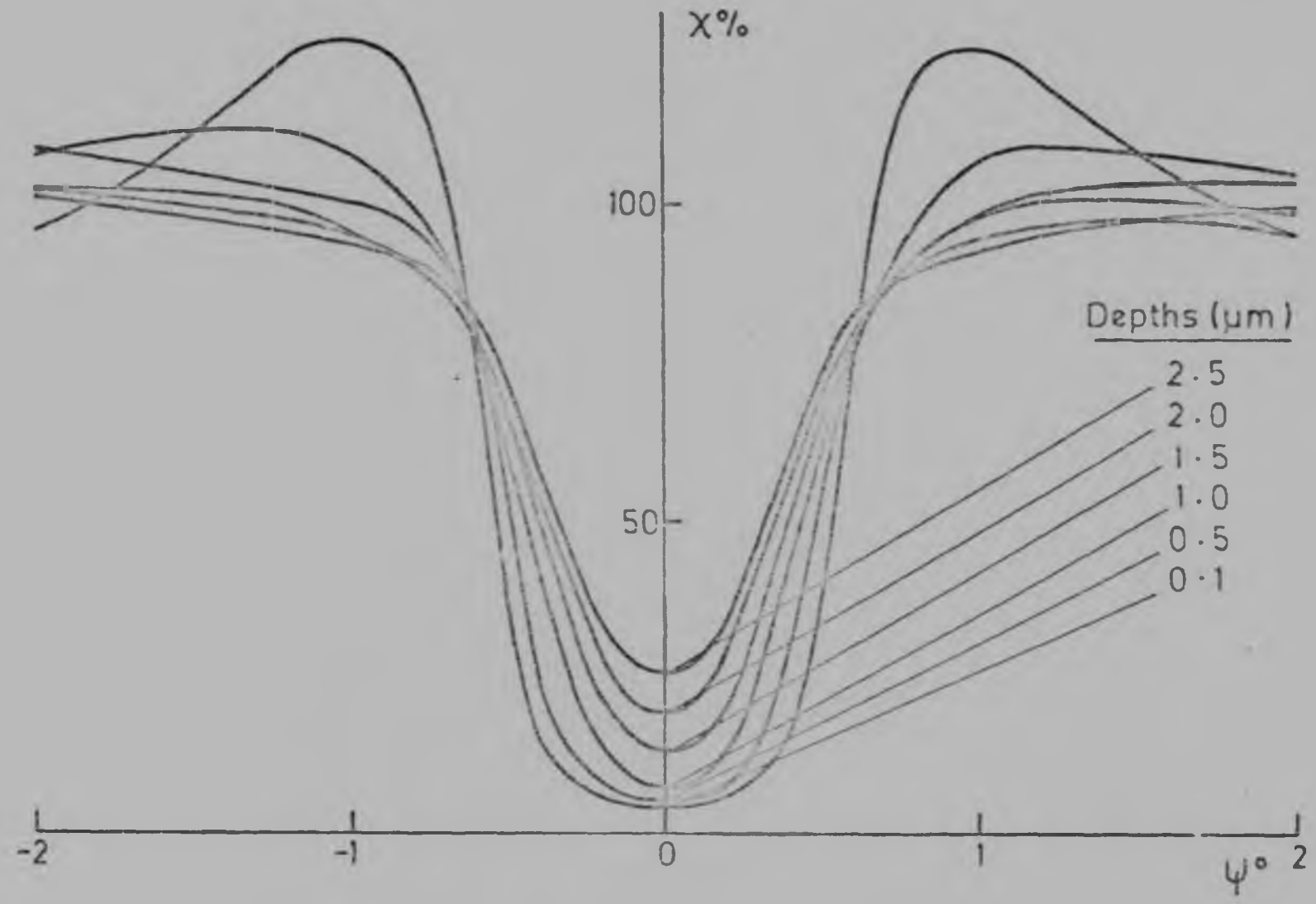

Figure 7.3: Scans through ·110·: 1.0 MeV protons (KT1).

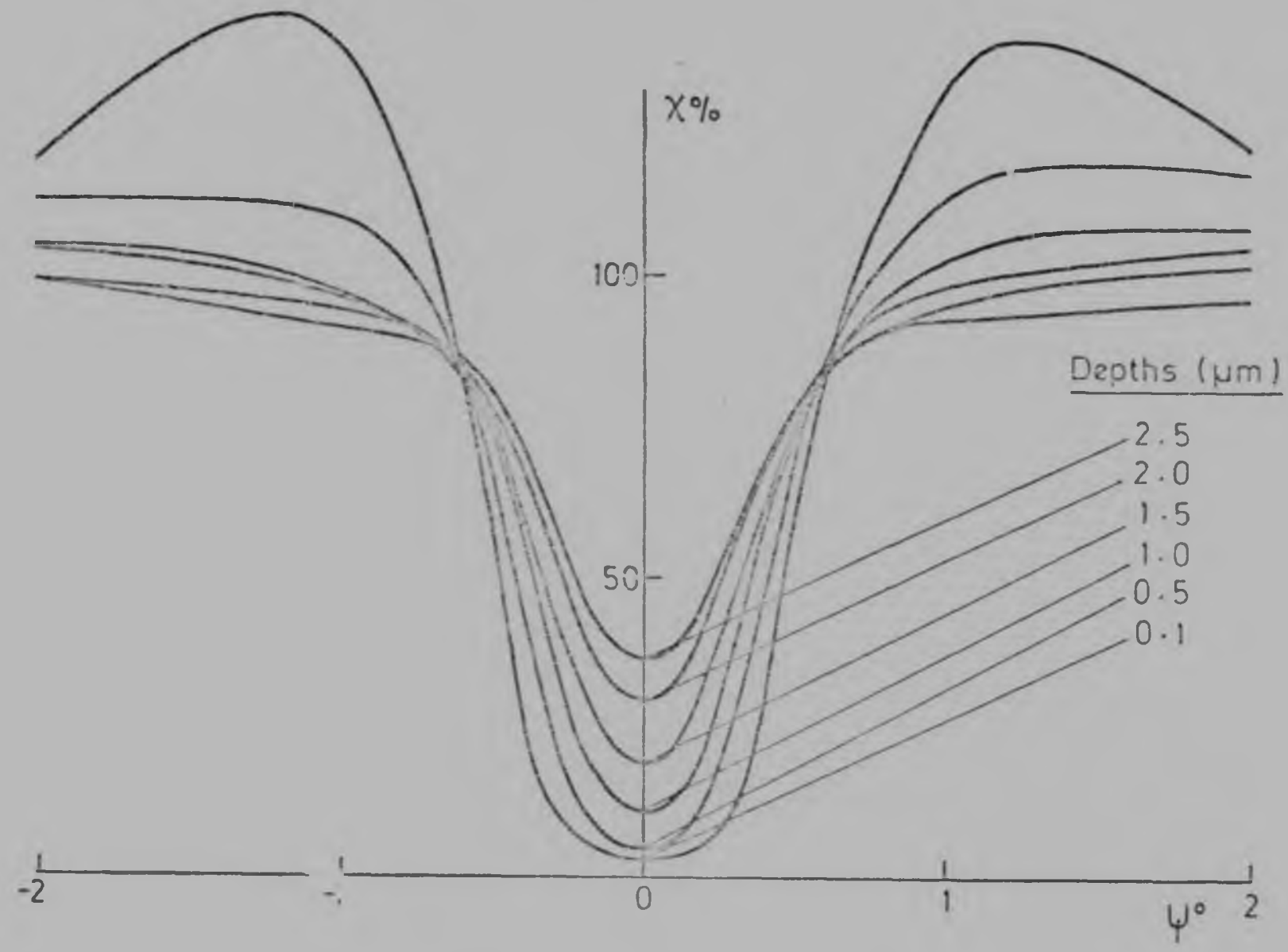

Figure 7.4: Scans through <111>: 1.0 MeV protons (KTI).

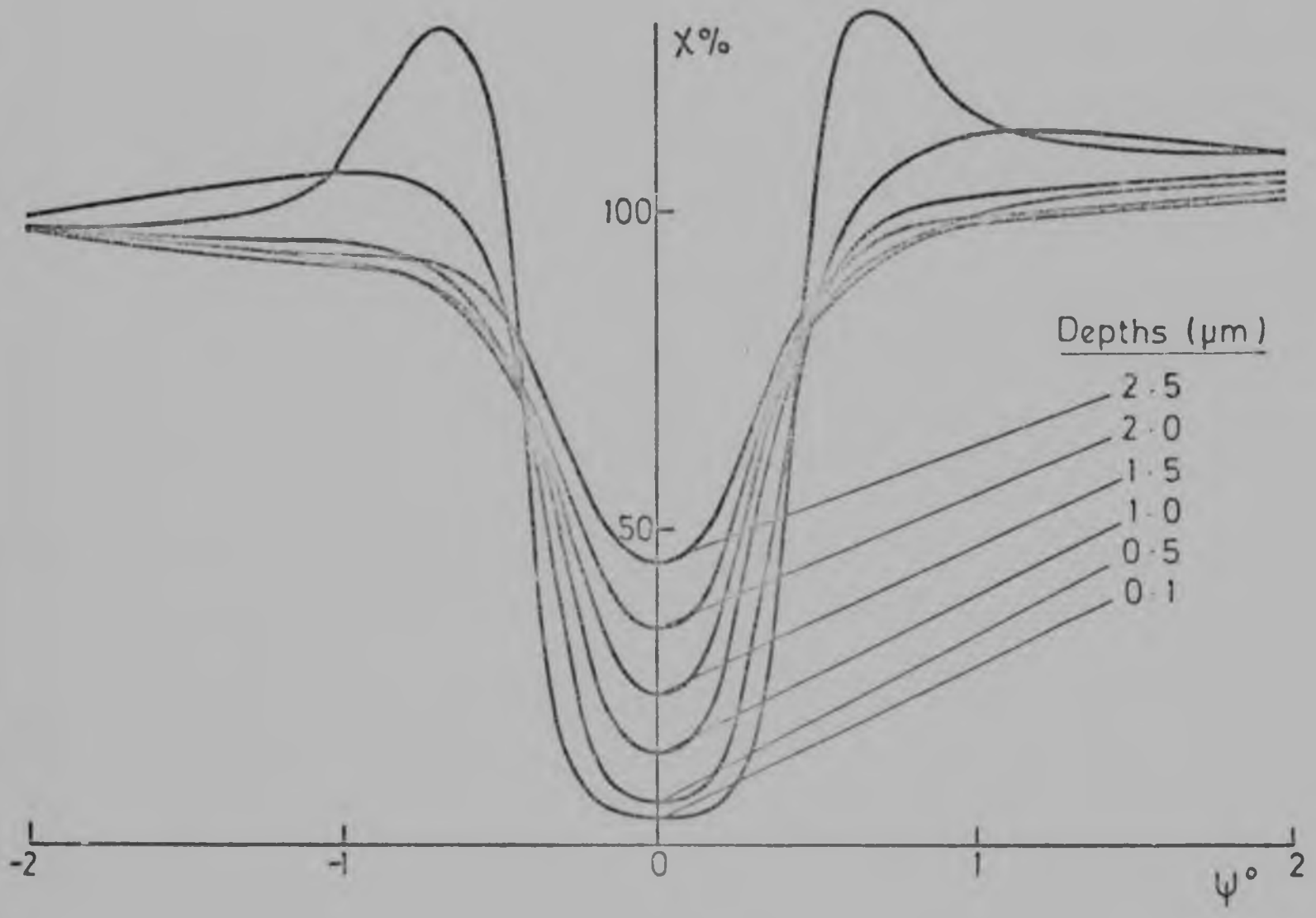

Figure 7.5: Scans through <100>: 1.0 MeV protons (KT1).

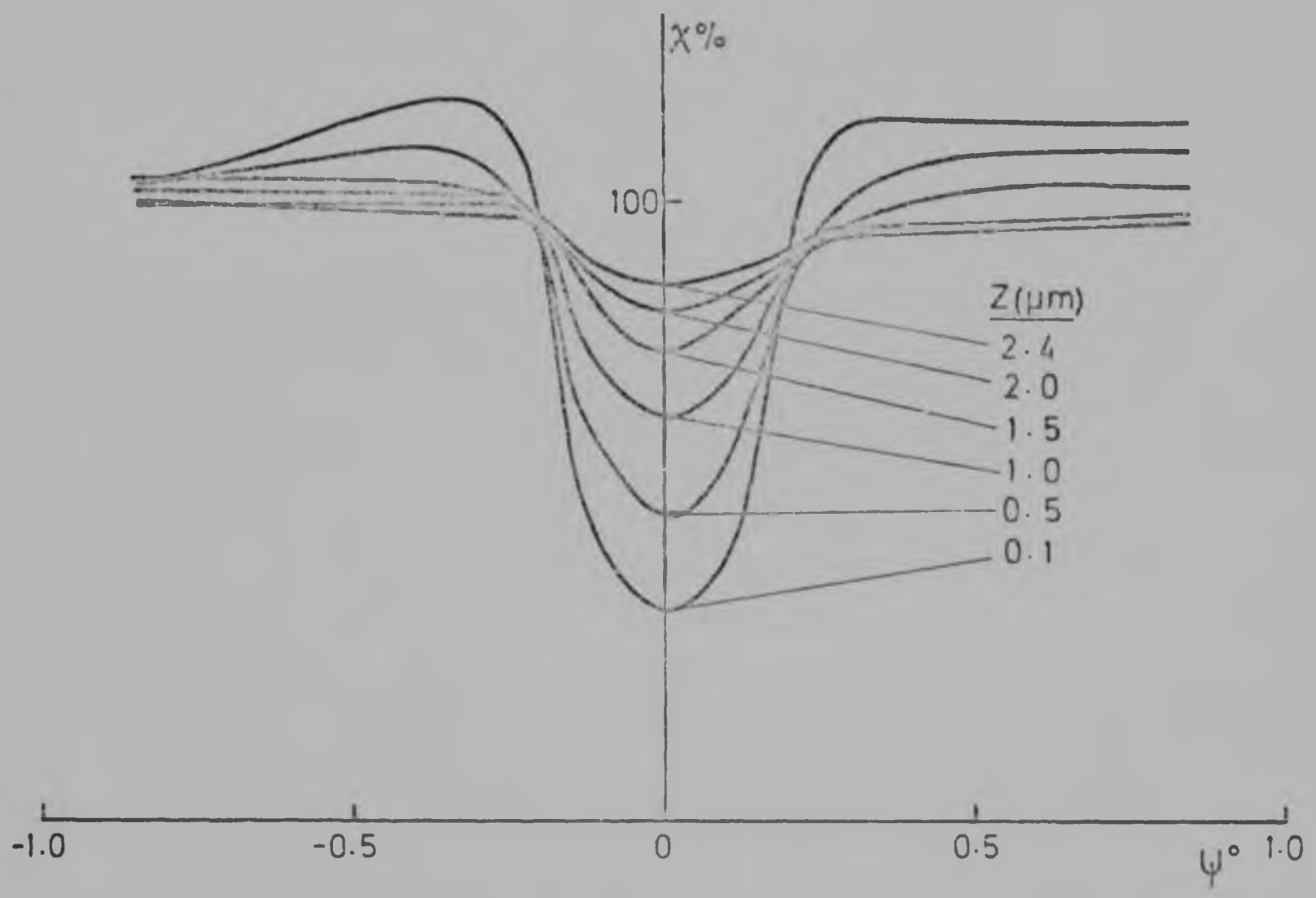

Figure 7.6: Scans across {110}: 1.0 MeV protons (Di18).

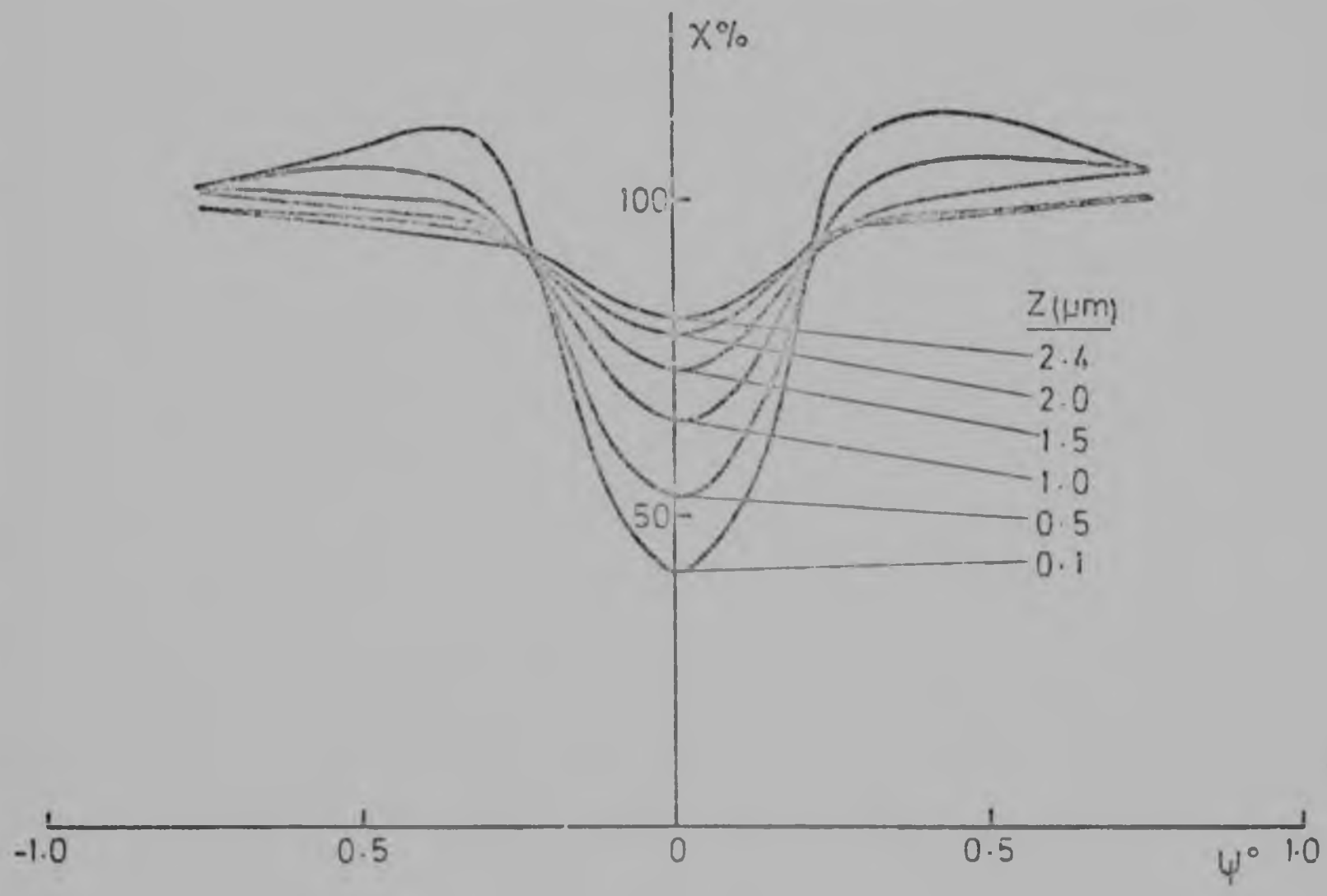

Figure 7.7: Scans across {111}: 1.0 MeV protons (Di18).

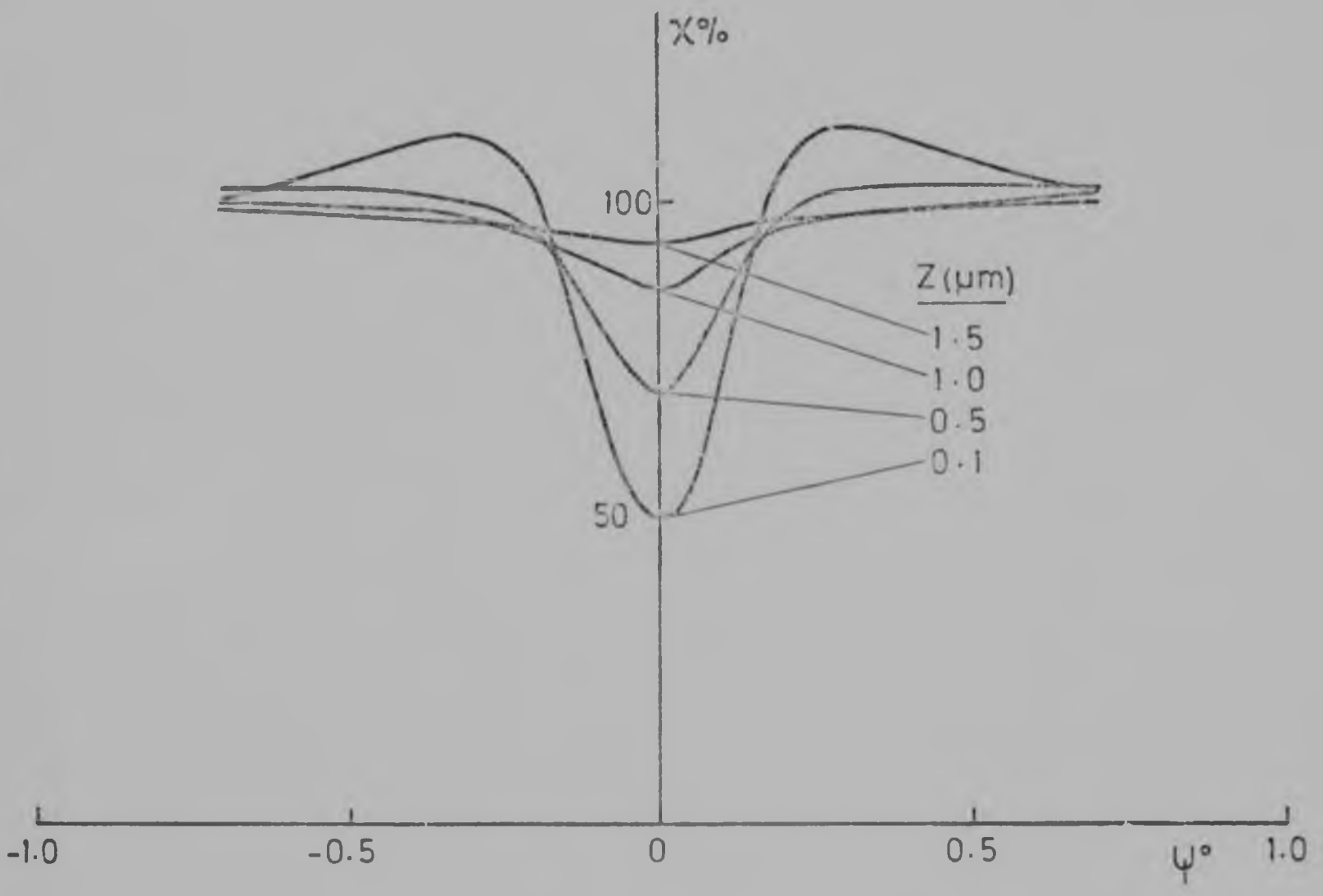

Figure 7.8: Scans across {100}: 1.0 MeV protons (Di18).

strongly interacting trajectories.

ii) A better proposal is perhaps that of a dynamic equilibrium. Trajectories with $\psi < \psi_{\frac{1}{2}}$ have a high dechannelling probability, whereas those with $\psi > 1.5\psi_{\frac{1}{2}}$, say, although mostly in the random beam, have a high probability for 'feeding-in' to channels, as is proved by the spread of the dips at larger depths to $\psi > 1.5\psi_{\frac{1}{2}}$. At some intermediate angle one might expect a balance between the two processes, and a constant yield with depth, the average ion spending about 80% of its trajectory (or the visible portion thereof) in the random beam.

iii) It may further be noted that the crossover angle ψ_x bears a constant relation to $\psi_{\frac{1}{2}}$. This is:

For axes: $\psi_{\frac{1}{2}} = (0.81 \pm 0.02)\psi_x$

For planes: $\psi_{\frac{1}{2}} = (0.73 \pm 0.03)\psi_x$

Barrett [Bar⁻1] introduced a factor k into his expressions for $\psi_{\frac{1}{2}}$ (Eqn 2.7 and Eqn 2.8) in order to fit them to experimentally and computationally determined values of $\psi_{\frac{1}{2}}$ for axes and planes respectively. The values of k are:

Axes: $k = 0.80$ (or 0.83)

Planes: $k = 0.72$ (or 0.76)

It is interesting to speculate that the 'critical angles' determined by these expressions, before application of the factor k, may be identified with ψ_x. In that case, ψ_x may represent the incidence angle of those trajectories which attain the critical approach distance with respect to the axis or plane in question

(see §2.2.3). However, Barrett has advised caution [Bar71] in drawing conclusions from these Monte Carlo based expressions; and it is not clear why such trajectories should have a depth independent yield.

The data of other workers was searched for the above phenomenon, re-plotting it if necessary. In references Dav68 (p→W) and How71 (p→Au), families of nested curves occur with no crossover (and no shoulders). In And72 (p→PbS) the data is indistinct in the shoulder region; but in the p→W data of Anderson and Uggerhøj [And68] a crossover does appear to occur, with

$$\psi_1 \approx 0.8\ \psi_x .$$

Other data presented in How71 (p→Zn) indicates a crossover with $\psi_1/\psi_x \approx 0.6$ or 0.9 depending on the axis.

This effect should evidently be sought in other materials also.

The dependence of ψ_1 on the depth z is plotted in Figure 7.9 for axes, showing the extrapolation to z=0. For planes, ψ_1 is independent of z to within the accuracy of the apparatus (0.01°) and has not been plotted here.

The depth dependence of $\psi_{\frac{1}{2}}$ for axes is seen to differ with the specimen. However, the curves all extrapolate to the same point at z = 0, to within 0.01°.

In fact, this specimen dependence is to some extent an artifact of the definition of $\psi_{\frac{1}{2}}$ as the half width at half minimum. A specimen

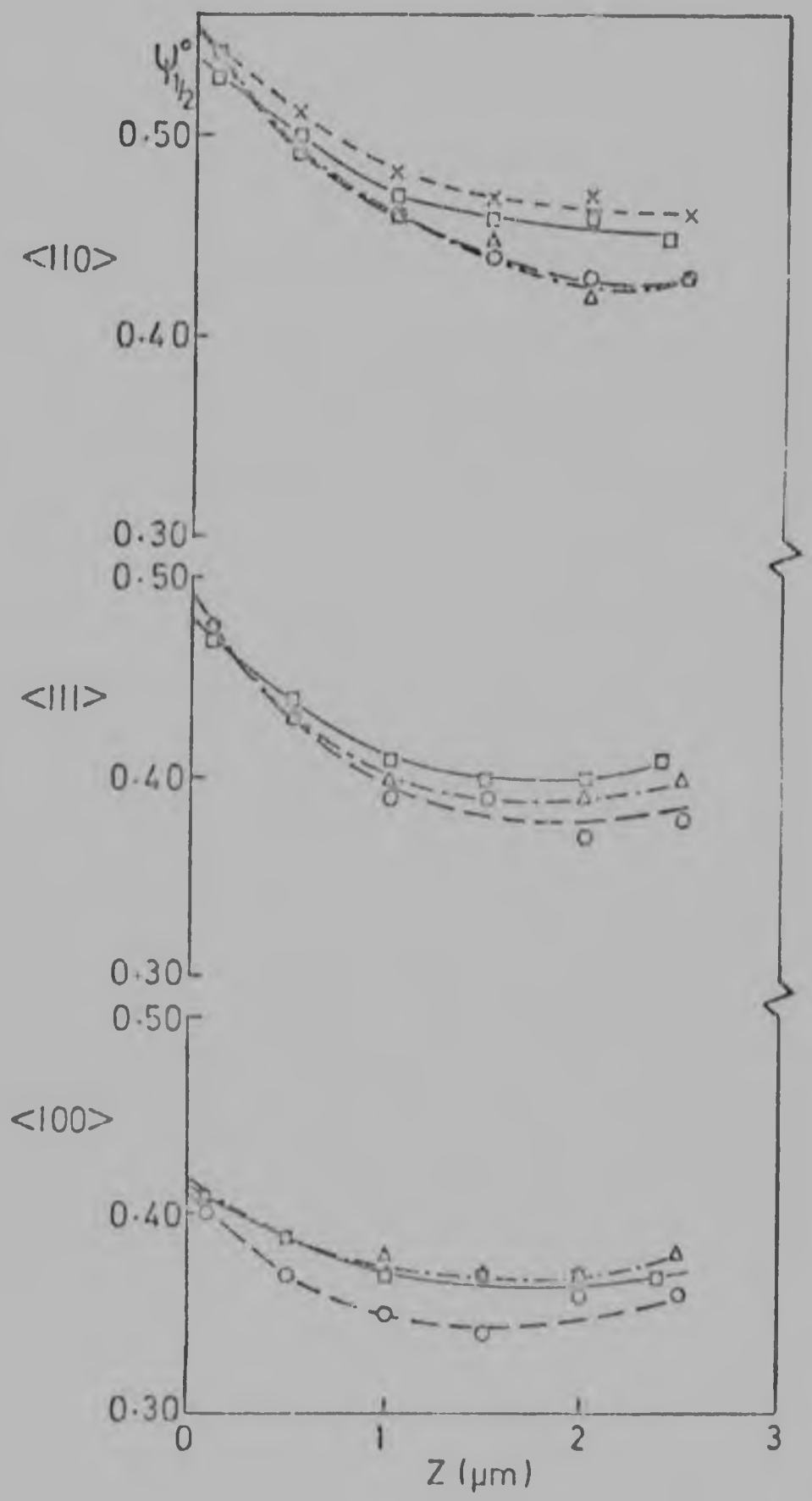

Figure 7.9: Dependence of critical angle on depth for 1.0 MeV protons.

o KT1; Δ Di3; □ Di18; x Di1.

TABLE 7.3

Critical Angles for 1.0 MeV Protons

Channel	Diamond	ψ_1° (exptl)	ψ_1° (theor)
<110>	Di4	0.55	0.54
	Di3	0.55	
	KT1	0.55	
	Di18	0.54	
<111>	Di3	0.49	0.49
	KT1	0.49	
	Di18	0.48	
<100>	Di3	0.42	0.46
	KT1	0.41	
	Di18	0.42	
<211>	Di18	0.38	0.41
{110}	KT1	0.17	0.18
	Di18	0.16	
{111}	KT1	0.16	0.15
	Di18	0.17	
{100}	KT1	0.11	0.12
	Di18	0.11	

with a larger χ_{min} will give a larger $\chi_{\frac{1}{2}}$ than one with a smaller χ_{min}, although their channelling dips may elsewhere be identical. Measurement of $\psi_{\frac{1}{2}}$ at the same value of χ, was indeed found to bring the $\psi_{\frac{1}{2}}$ vs z curves for different specimens much closer together.

There currently appears to be no analytic theory with which to compare the dependence of $\psi_{\frac{1}{2}}$ on z, and numerical calculations must be used. The results of calculations [Fea77c] using the University's IBM 370/158 computer, by means of the programme MECHANIL, are compared in Figure 7.10 with data from a good diamond. Agreement is very satisfactory. The programme is based on a diffusion model for the spreading of the transverse energy distribution, and will be fully described in a future publication [Fea79].

All the critical angle measurements for 1.0 MeV protons at room-temperature (20°C), corrected to zero depth, are tabulated in Table 7.3. Values calculated from Eqn 2.7 or Eqn 2.8 are included for comparison.

7.4.3 Higher Proton Energies

Similar measurements were made with protons at 2.5 and 4.5 MeV on the EN Tandem van de Graaff accelerator; the results are presented in Figures 7.11 to 7.17 and Table 7.4 (2.5 MeV) and in Figure 7.18 to 7.23 and Table 7.5 (4.5 MeV). The {100} plane at 4.5 MeV was too narrow for accurate data-taking and has been omitted. Some results at a lower energy, 0.6 MeV, from Phase I are listed in Table 7.6.

The same comments about depth dependence and extrapolation to the

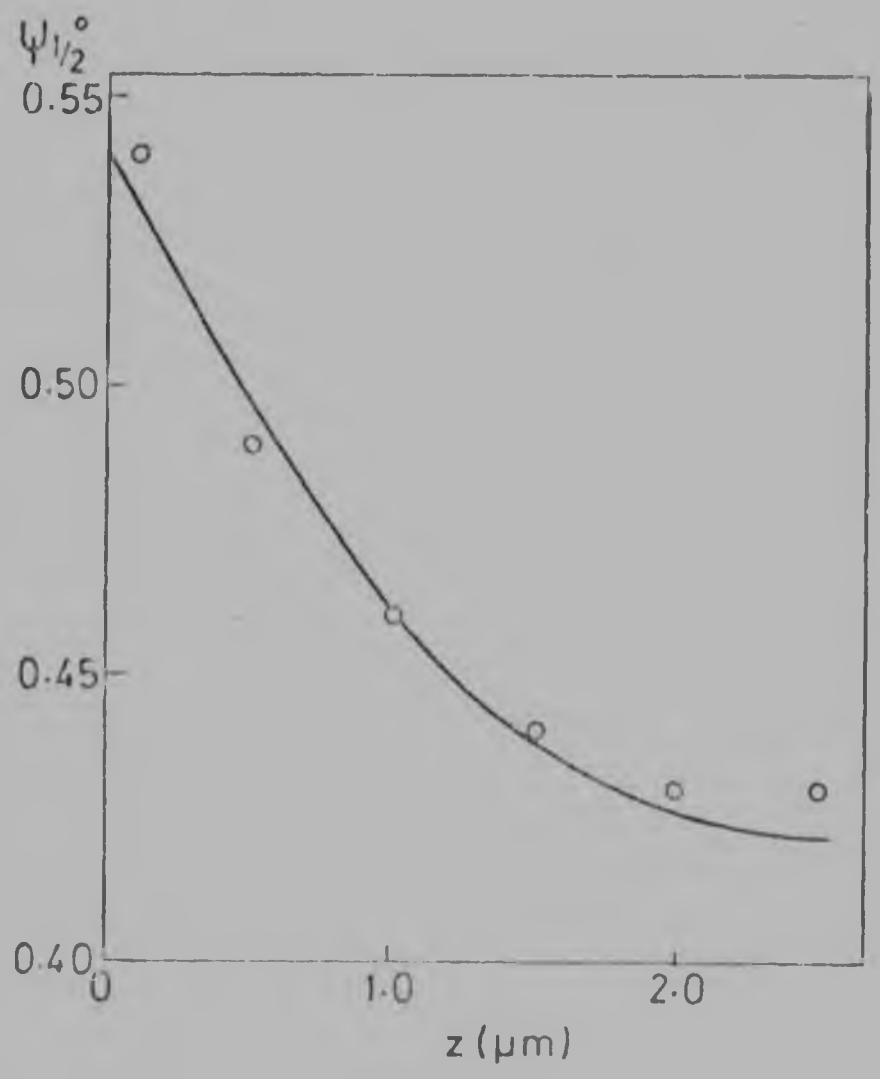

Figure 7.10: Comparison of the depth dependence of $\psi_{1/2}$ (110) with computer calculation [Hea77e], for 1.0 MeV protons. o data from KTI; — calculation.

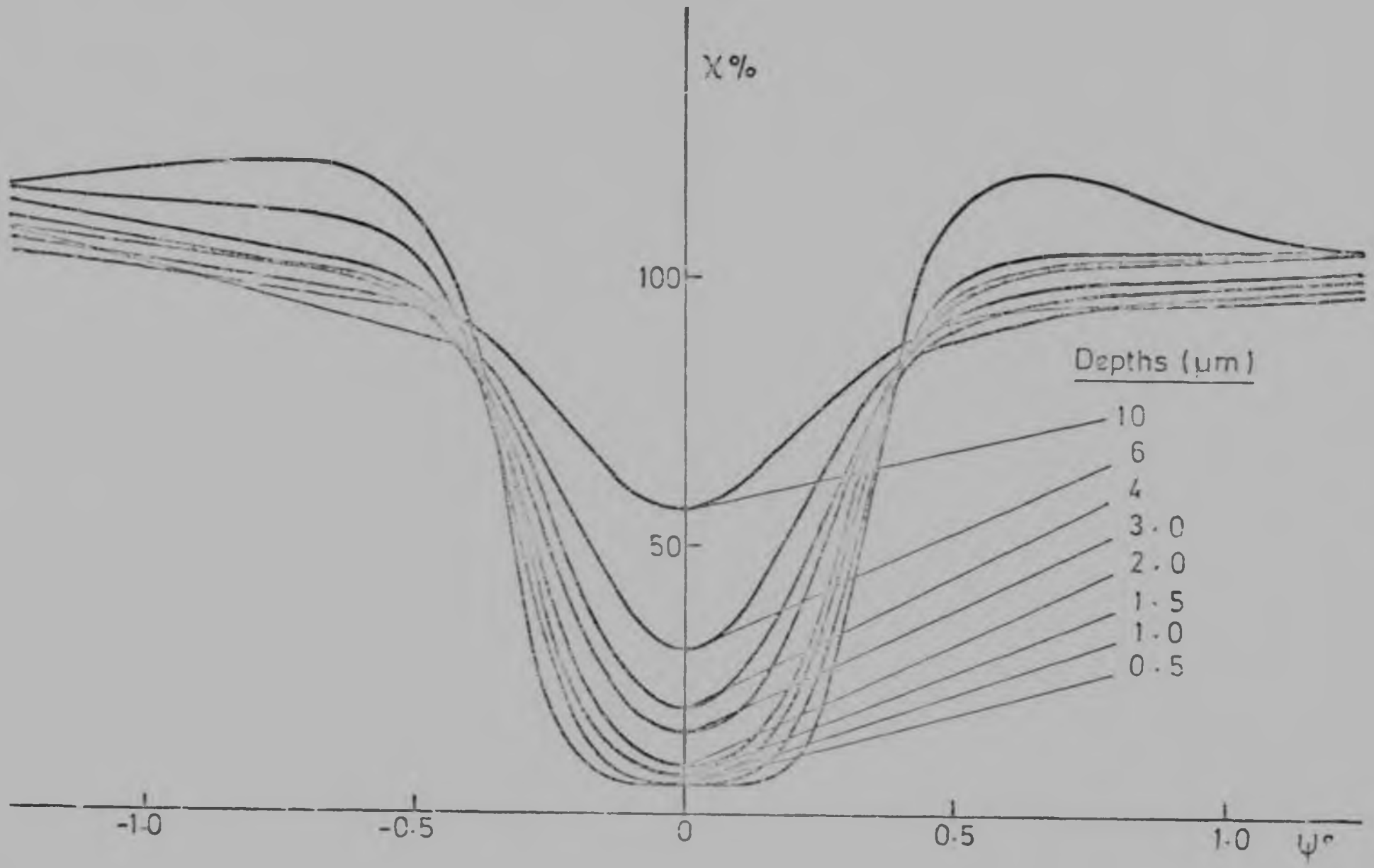

Figure 7.11: Scans through <110>: 2.5 MeV protons (KTI).

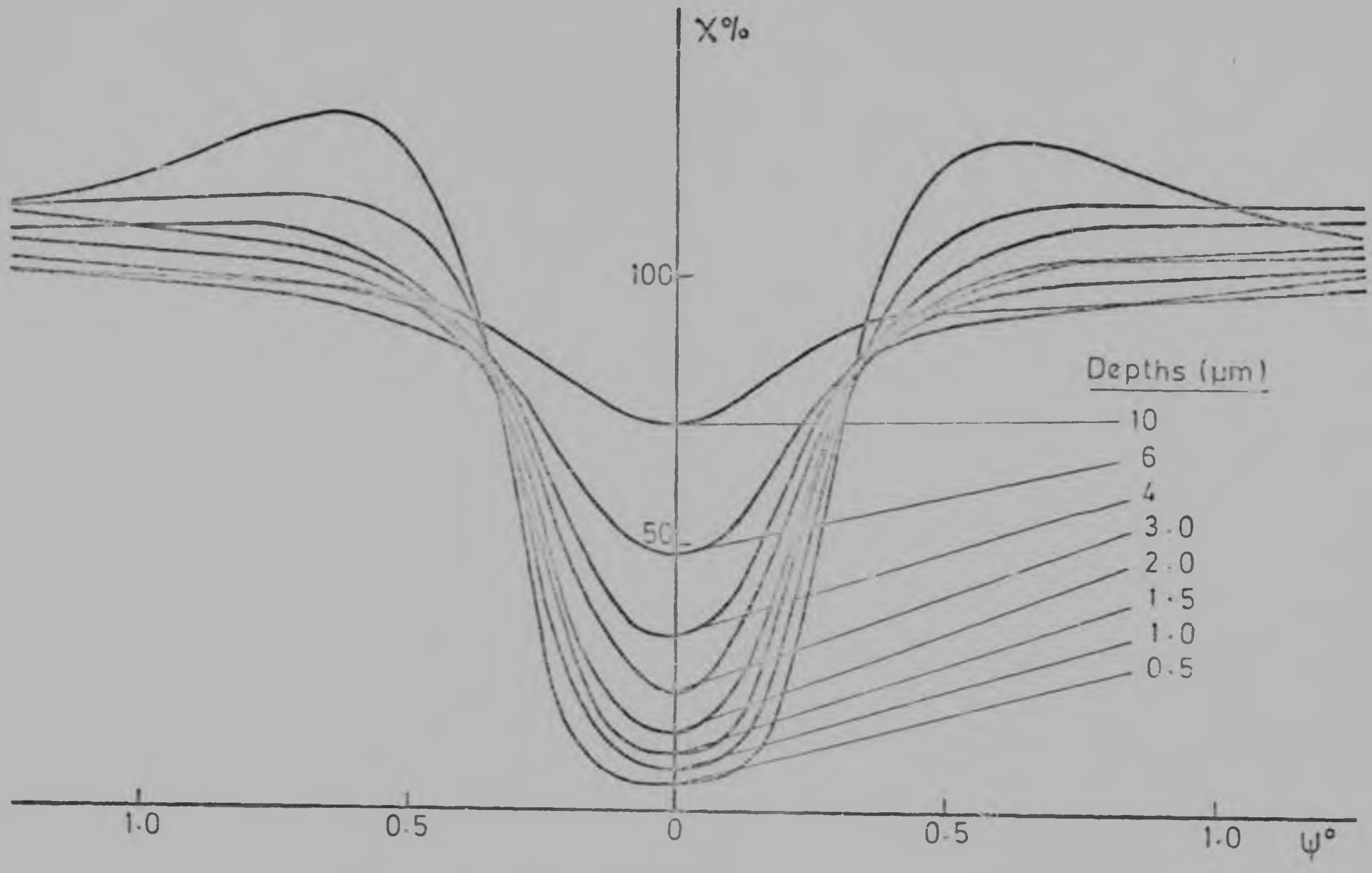

Figure 7.12: Scans through <111>: 2.5 MeV protons (KTI)

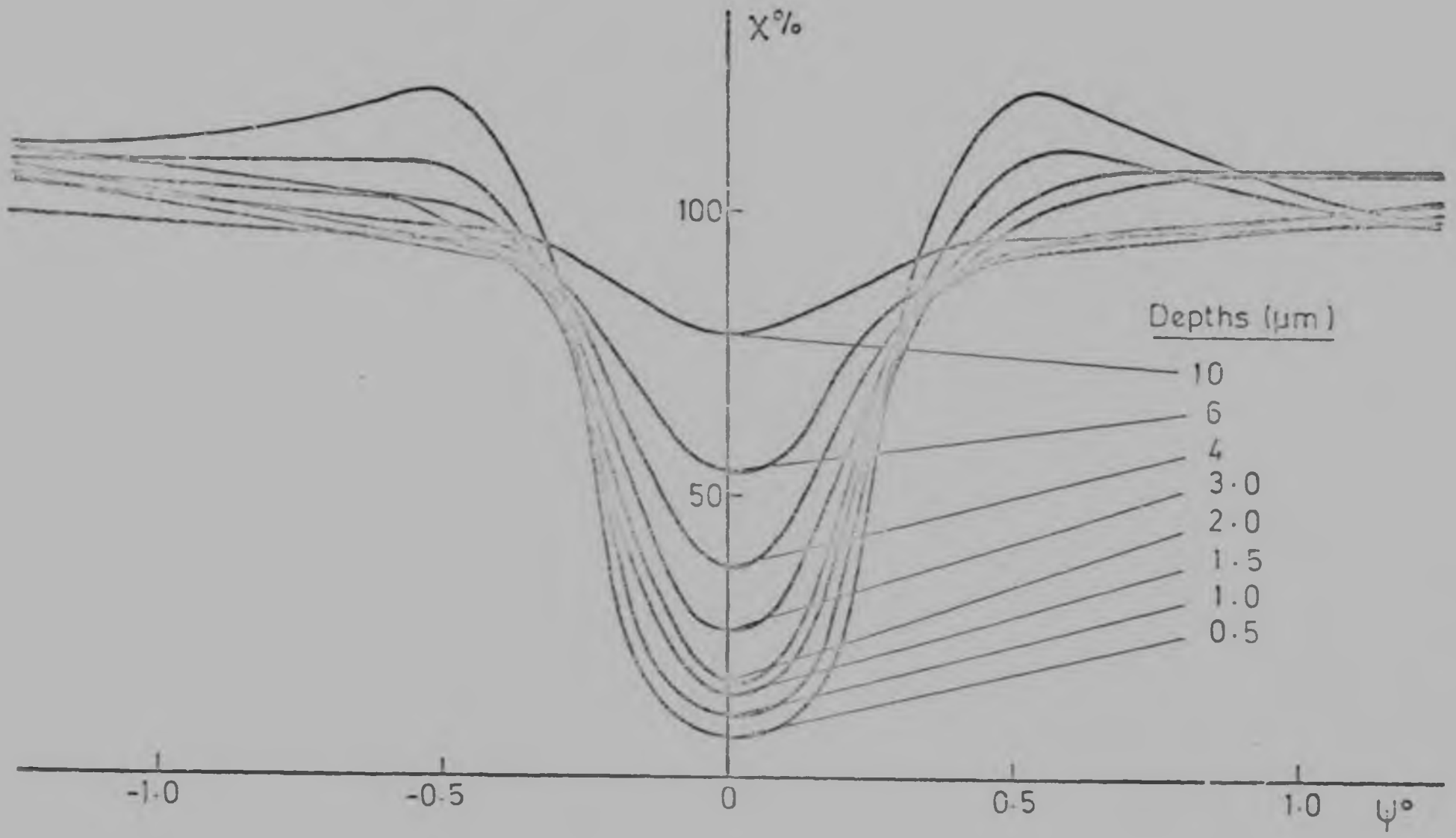

Figure 7.13: Scans through <100>: 2.5 MeV protons (KTI)

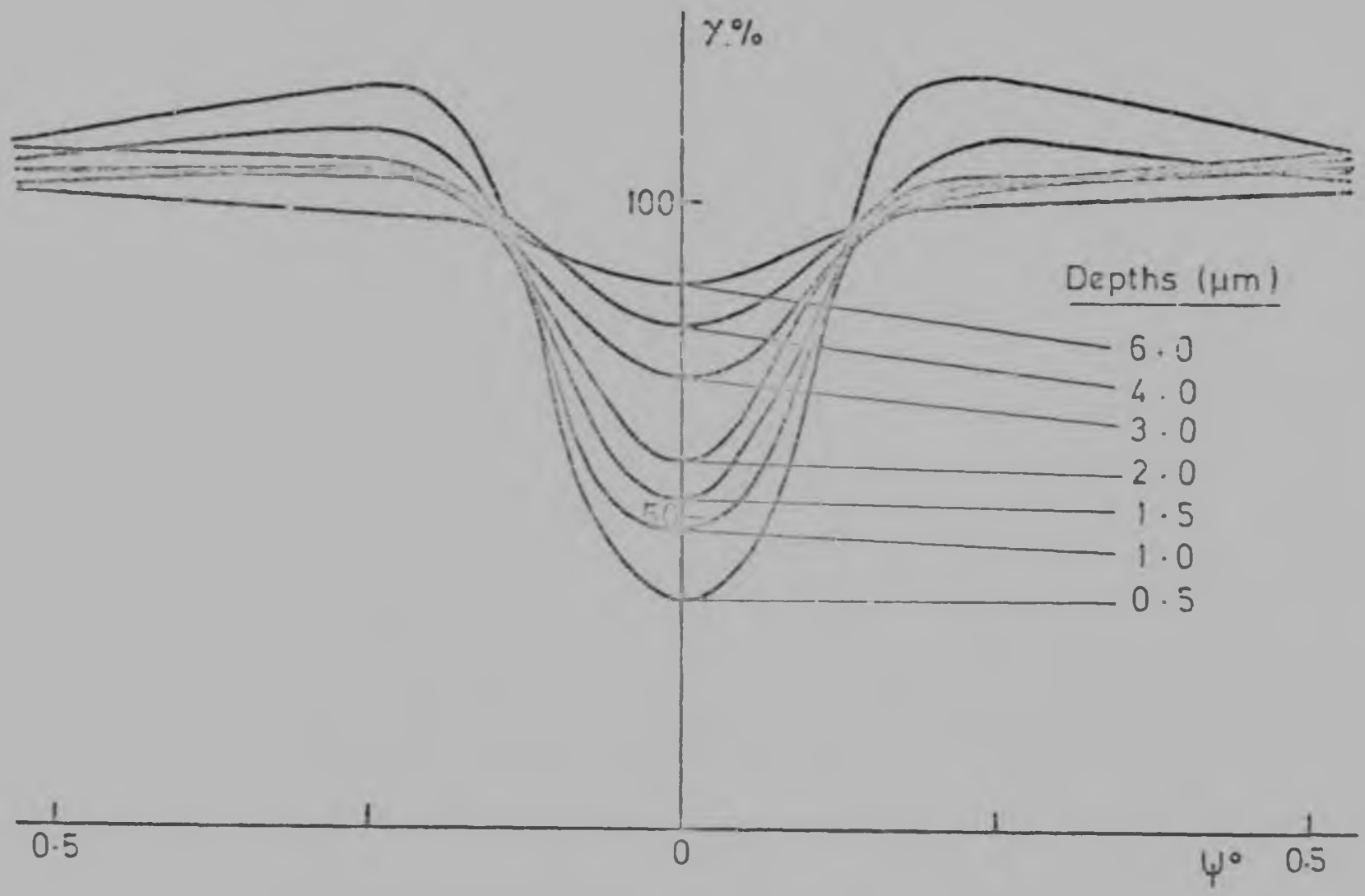

Figure 7.14: Scans across [110]: 2.5 MeV protons (KTI)

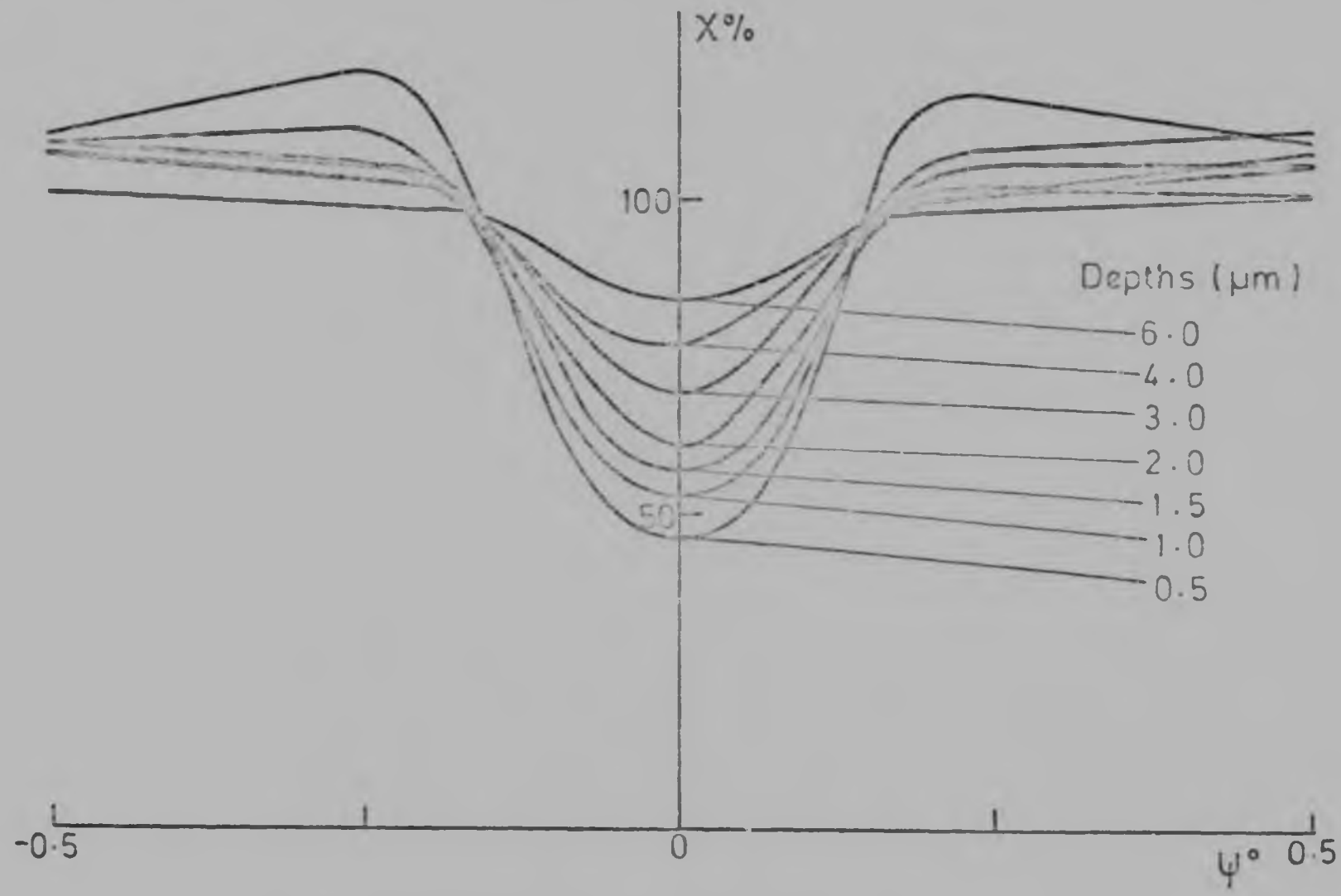

Figure 7.15: Scans across {111}: 2.5 MeV protons (KT1)

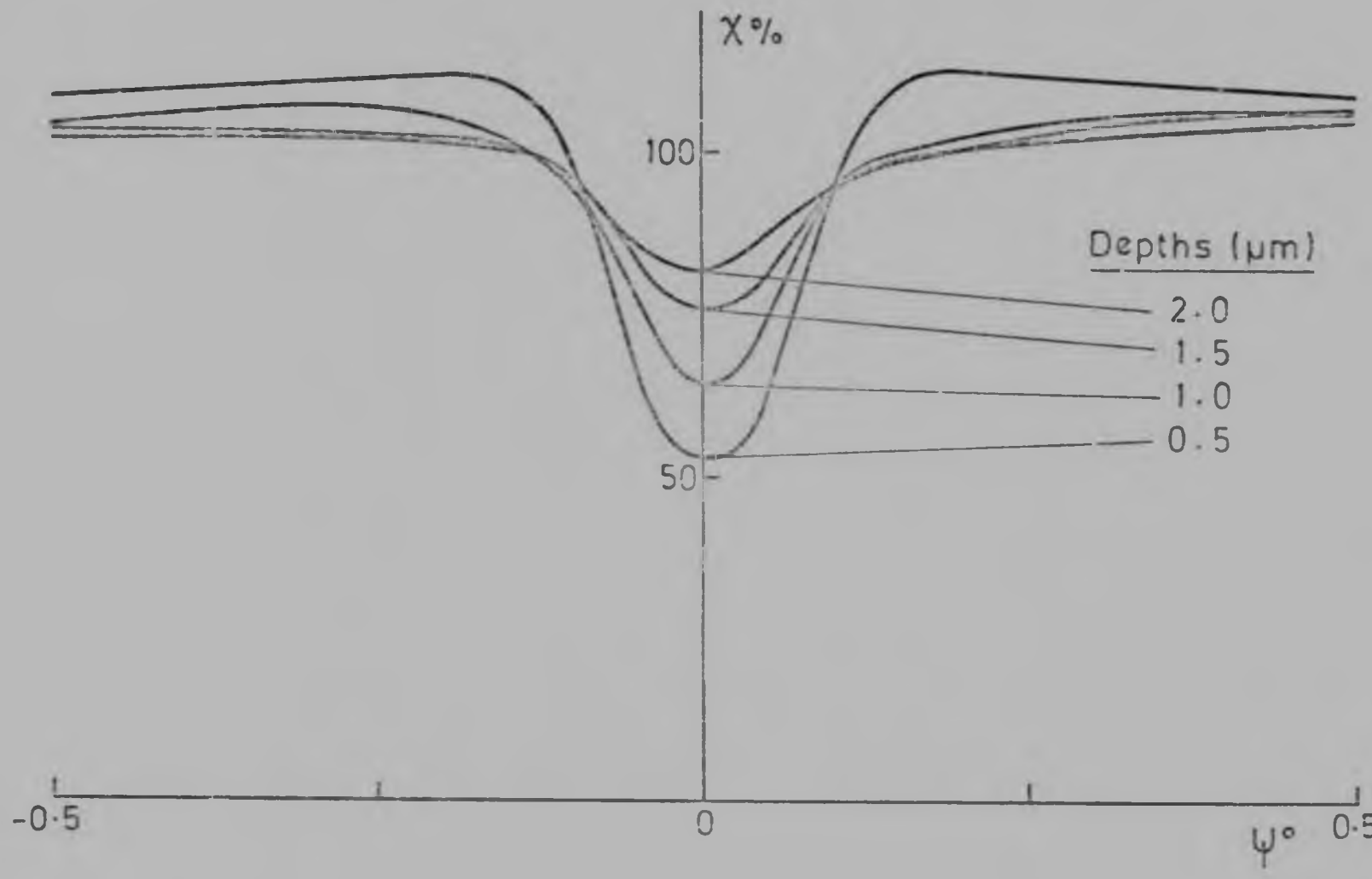

Figure 7.16: Scans across [100]: 2.5 MeV protons (KT1)

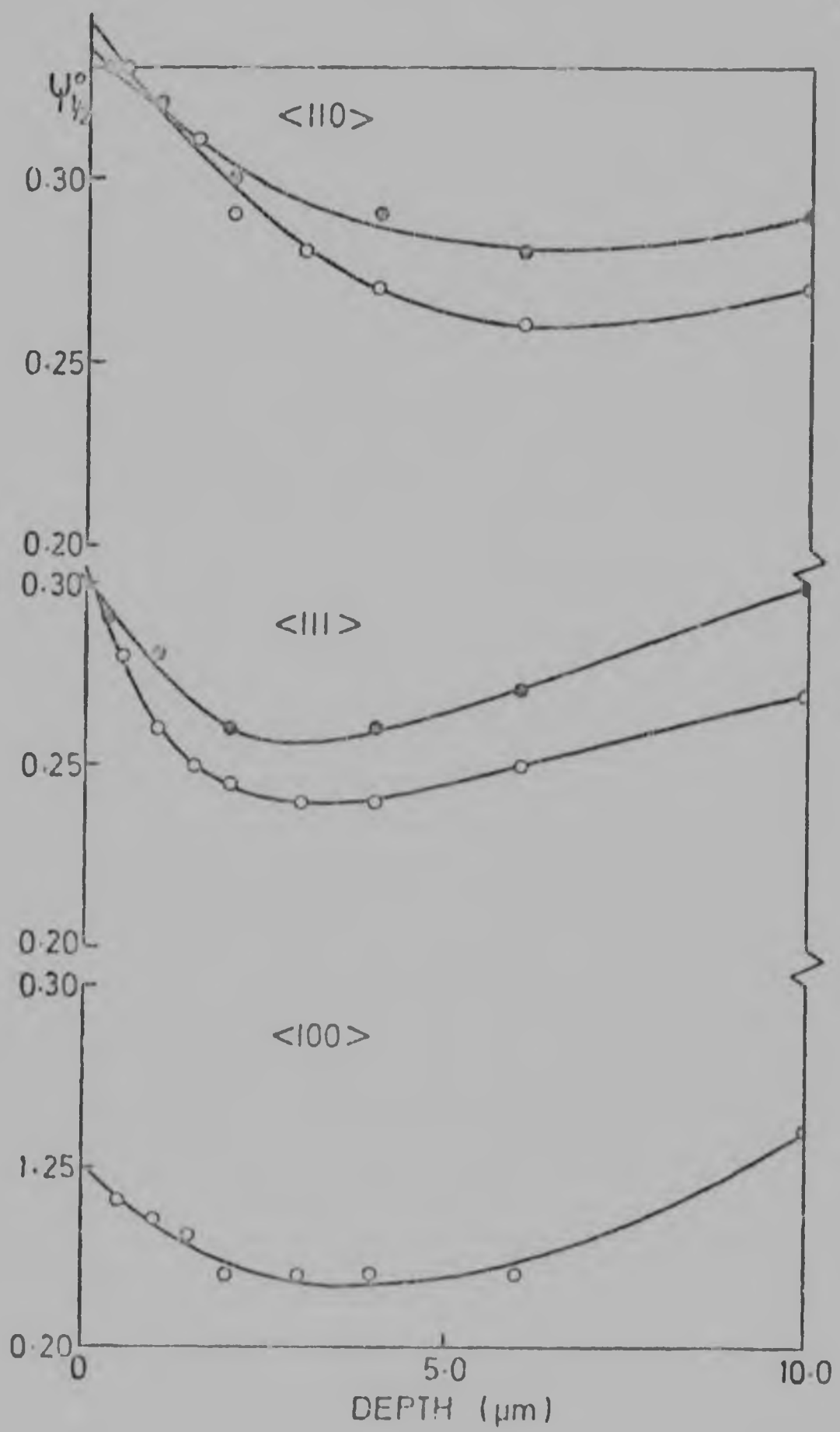

Figure 7.17: Dependence of critical angle on depth for 2.5 MeV protons: o KT1; • D113.

TABLE 7.4

Critical Angles for 2.5 MeV Protons

Channel	Diamond	ψ_1° (exptl)	ψ_1° (theor)
<110>	Di13	0.34	0.34
	KT1	0.34	
<111>	Di13	0.30	0.31
	KT1	0.30	
<100>	KT1	0.25	0.29
{110}	Di13	0.10	0.11
	KT1	0.10	
{111}	Di13	0.11	0.09
	KT1	0.11	
{100}	Di13	0.09	0.08
	KT1	0.07	

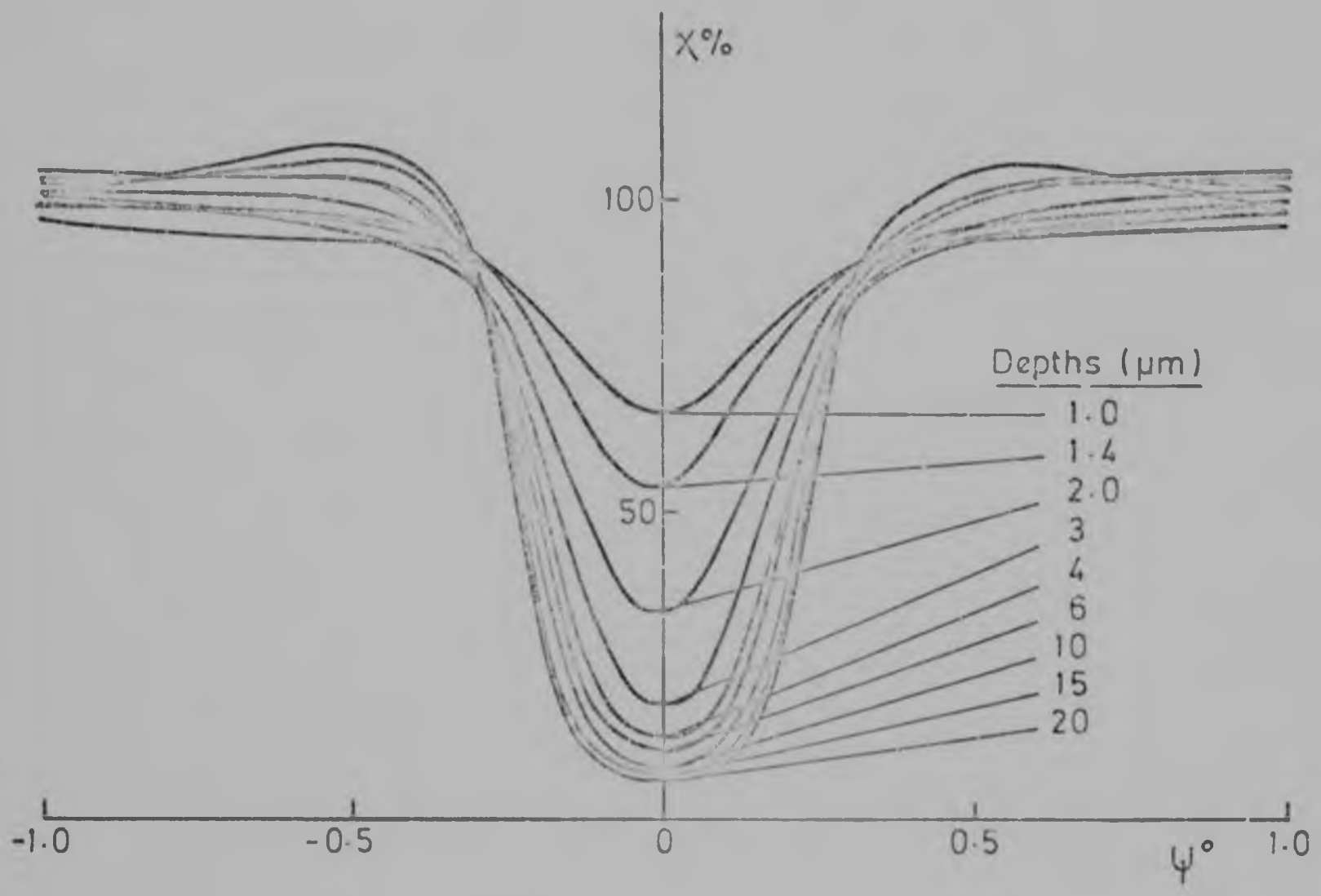

Figure 7.18: Scans through <110>: 4.5 MeV protons (KT1)

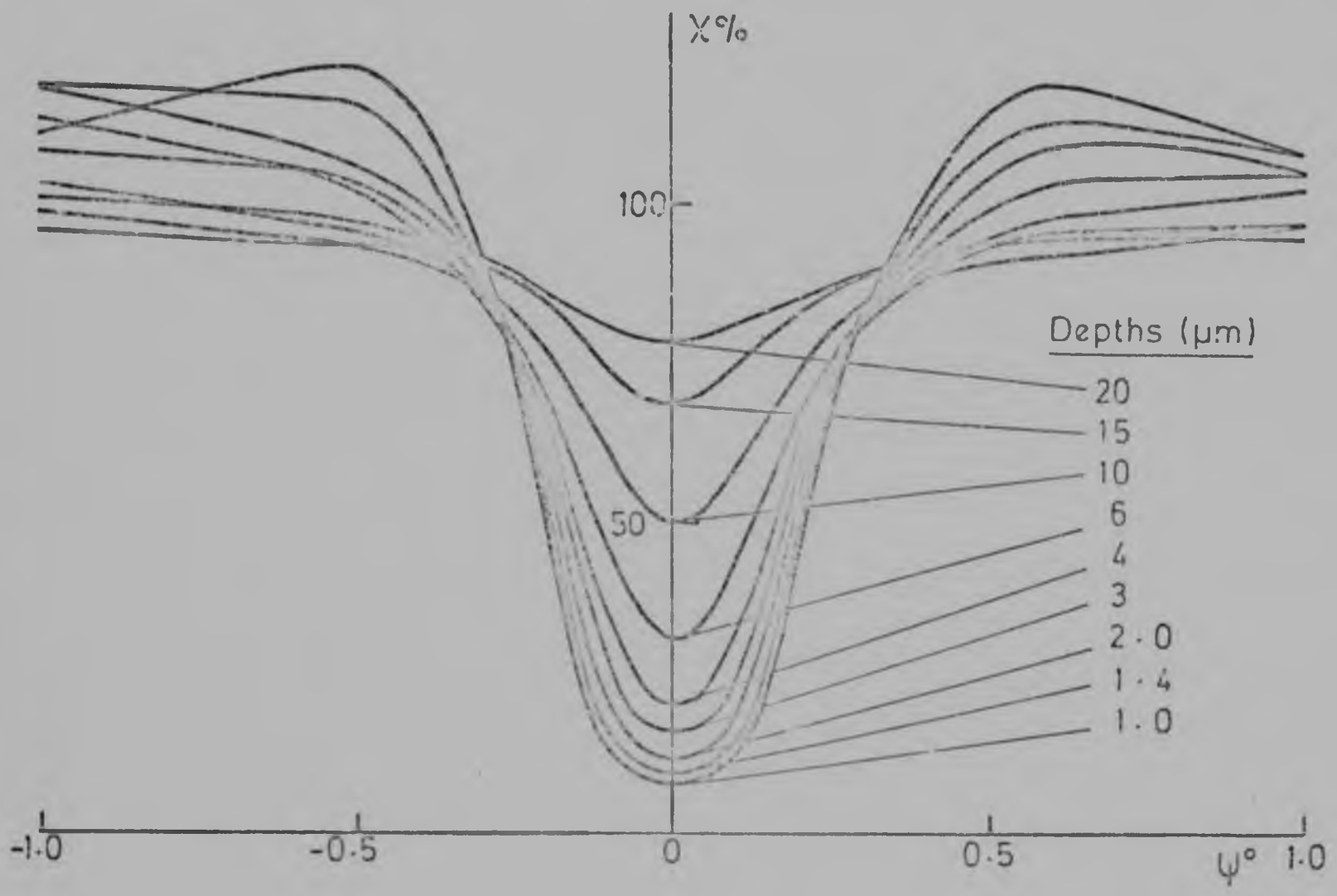

Figure 7.19: Scans through <111>: 4.5 MeV protons (KT1)

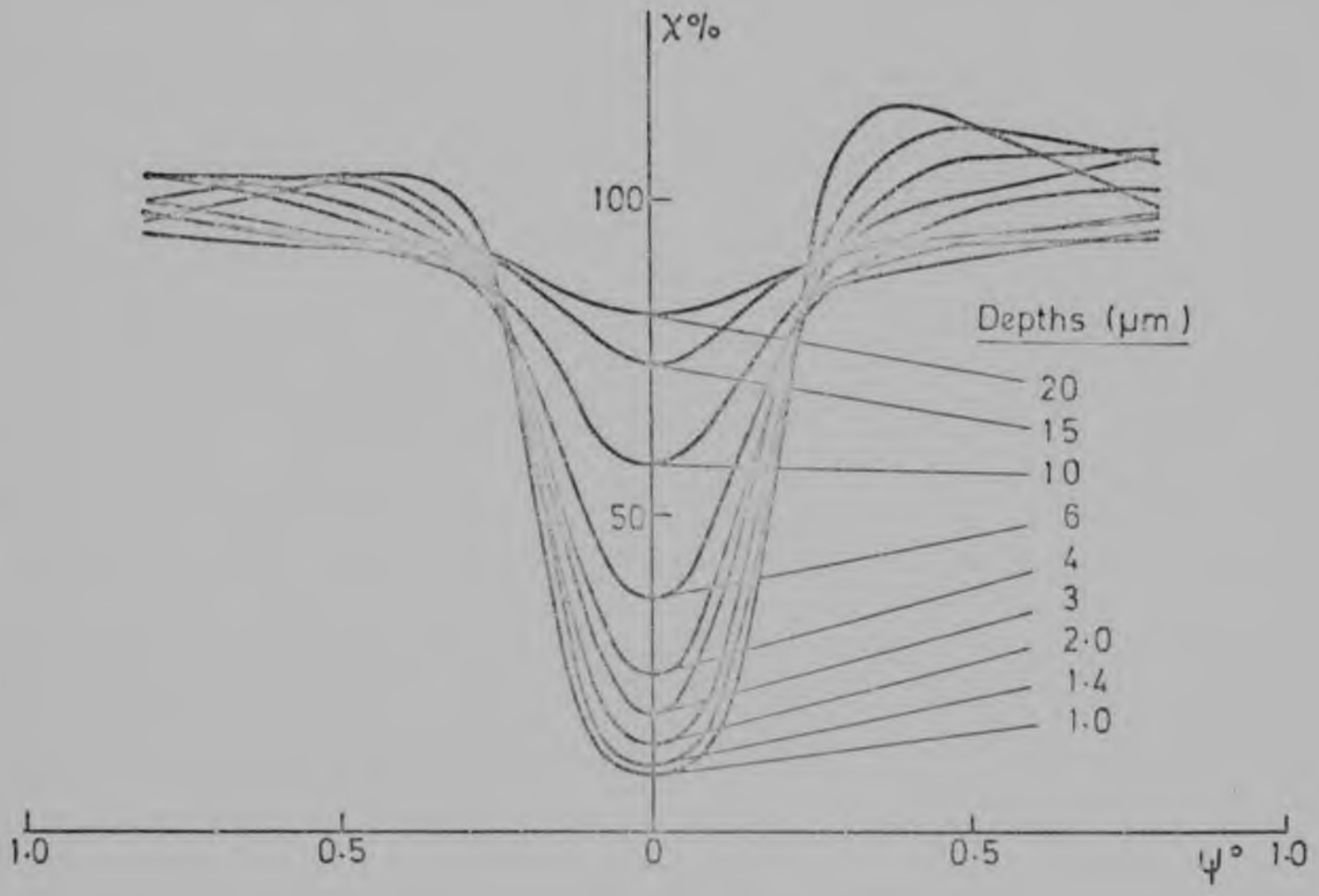

Figure 7.20: Scans through <100>: 4.5 MeV protons (KTI).

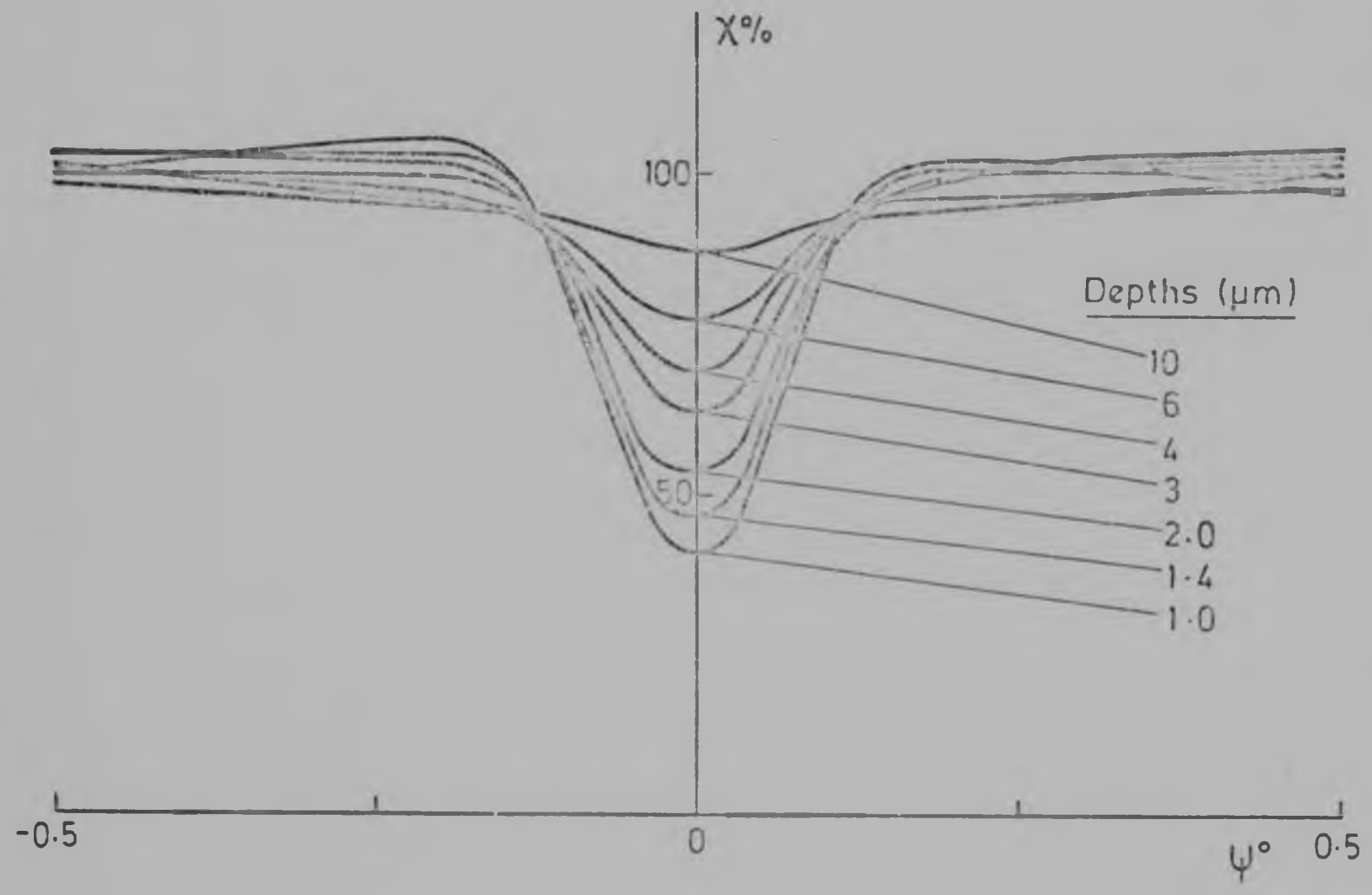

Figure 7.21: Scans across {110}: 4.5 MeV protons (KT1).

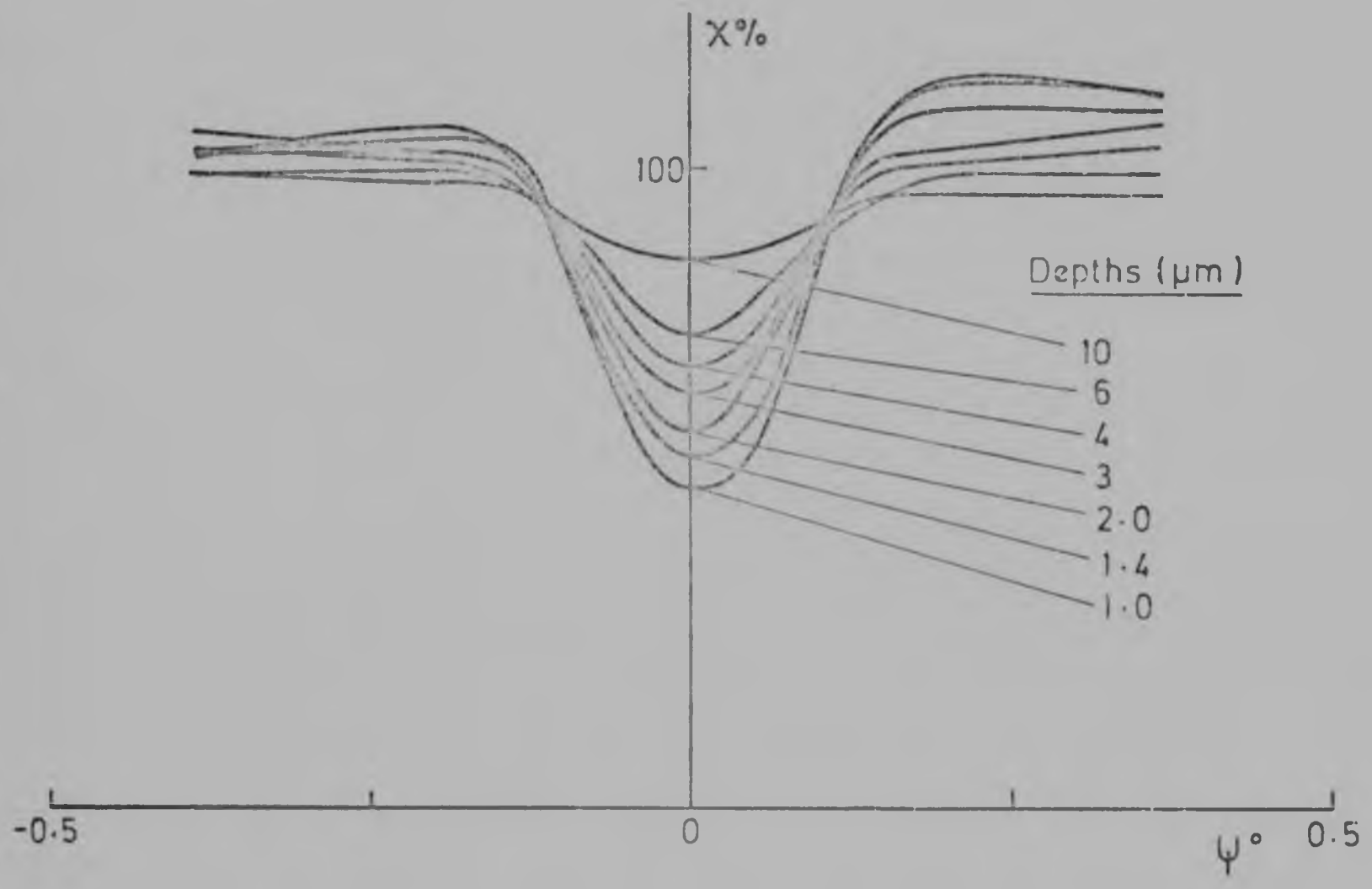

Figure 7.22: Scans across {111}: 4.5 MeV protons (KTI).

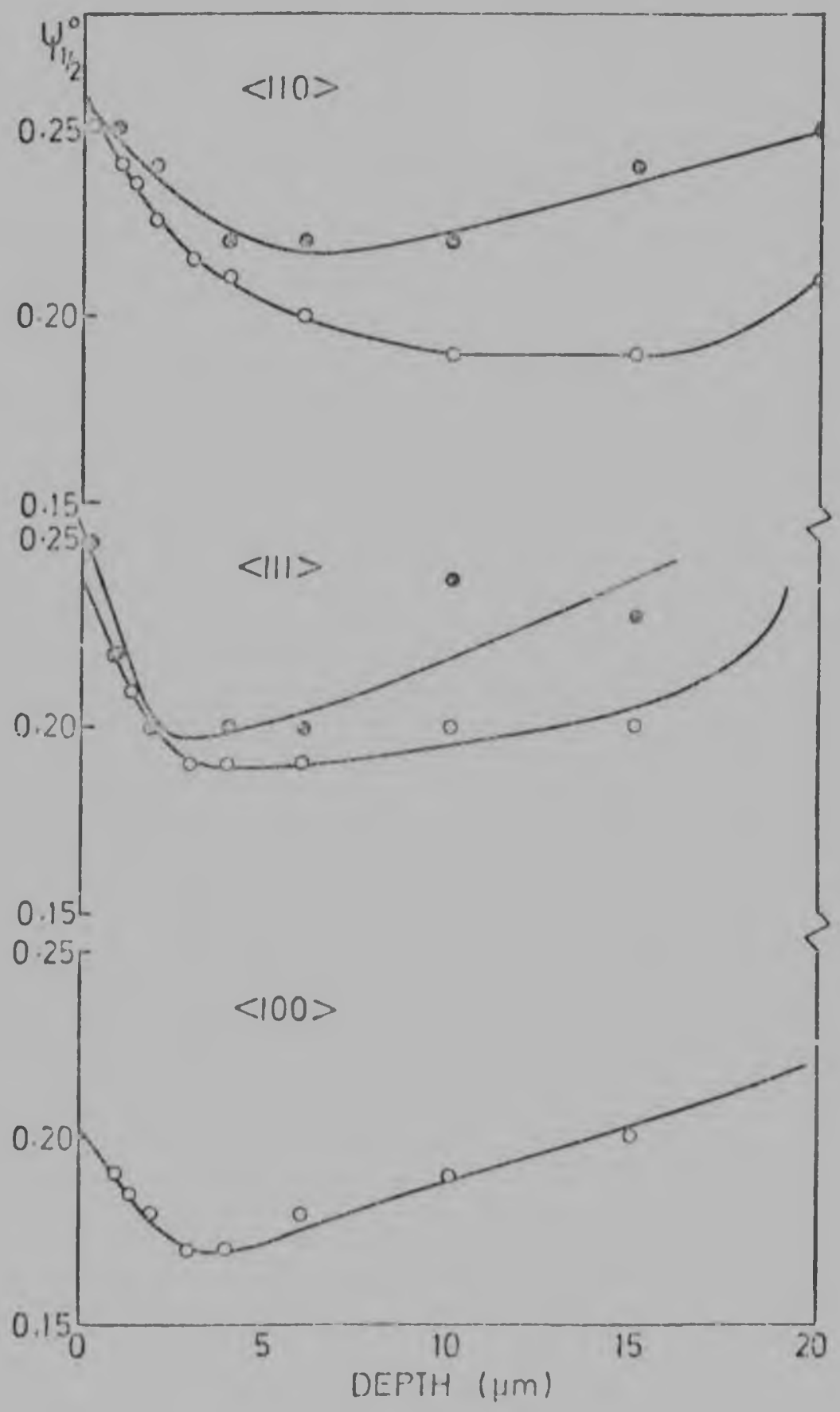

Figure 7.23: Dependence of critical angle on depth for 1.5 MeV protons: o KT1; • Di13.

TABLE 7.5

Critical Angles for 4.5 MeV Protons

Channel	Diamond	ψ_1° (exptl)	ψ_1° (theor)
<110>	Di13	0.26	0.26
	KT1	0.26	
<111>	Di13	0.24	0.23
	KT1	0.25	
<100>	KT1	0.20	0.21
{110}	KT1	0.08	0.08
{111}	KT1	0.08	0.07

TABLE 7.6

Critical Angles for 0.6 MeV Protons

Data taken using an SCA. Estimated statistical errors: ±0.01° (axes), ±0.01° (planes). Planar values are mean of ~5 scans.

Channel	Diamond	$\psi_{\frac{1}{2}}$° (exptl)	$\psi_{\frac{1}{2}}$° (theor)
<110>	Di4	0.74	0.70
<111>	Di4	0.62	0.63
<100>	Di4	0.62	0.59
<211>	Di4	0.56	0.53
<311>	Di4	0.46	0.46
<411>	Di4	0.46	0.40
{110}	Di4	0.23	0.23
{111}	Di4	0.24	0.19
{100}	Di4	0.16	0.16
{211}	Di4	0.14	0.12

surface, clearly apply here. The depth dependence decreases with increasing energy, as observed by Picraux et al [Pic69a] in germanium.

7.4.4 Alpha Channelling

Alpha-particles produce radiation damage in diamond at an appreciable rate, as mentioned in Section 6.7 and investigated in Chapter 10. In order to keep below the visible damage threshold when taking channelling measurements, it was necessary to select a new beam-spot after each full spectral scan. A further precaution was to locate the channels with protons, switching to alphas only to record spectra.

Some typical alpha-particle spectra are shown in Figure 7.24.

Axial channelling dips for 1.0 MeV He^+ ions are presented graphically in Figures 7.25 to 7.27, and critical angle vs depth plots in Figure 7.28. The depth dependences of ψ_1 are about ten times greater than those observed for protons. Because of the very shallow depths sampled, straight lines have been fitted through the data points for extrapolation to the surface.

The extracted surface critical angles are listed in Table 7.7. Some results at 0.7 MeV from Phase I are added in Table 7.8, but these probably contain significant radiation damage effects.

7.4.5 Errors

The ultimate check on the errors inherent in these experiments is the extent of agreement between similar data taken on different samples,

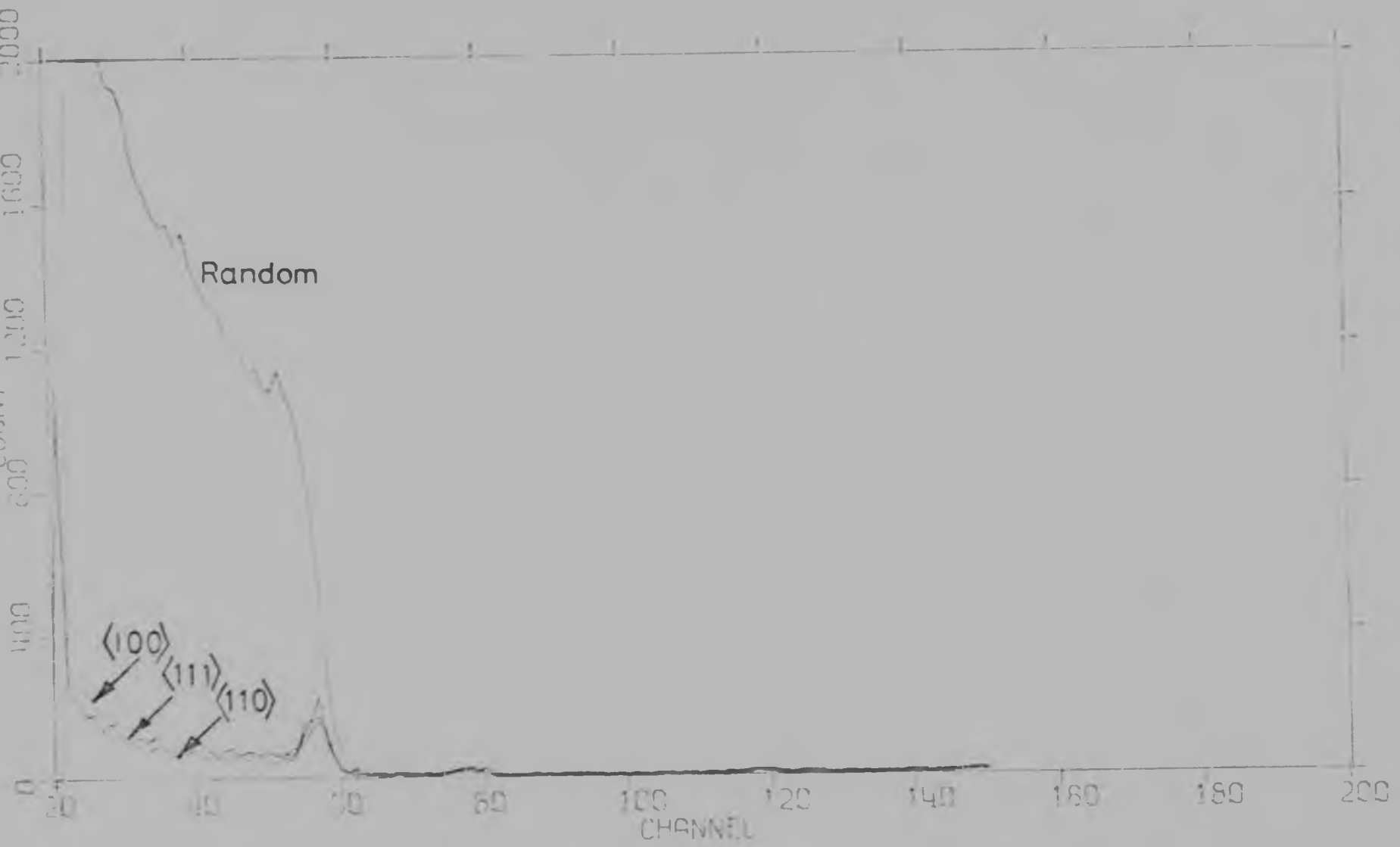

Figure 7.24: Backscattered 1.0 MeV He^+ spectra, same horizontal scale as Figure 7.2, random and channelled incidence.

Bottom curve <110>; 2nd curve <111>; 3rd curve <100>. (KTI).

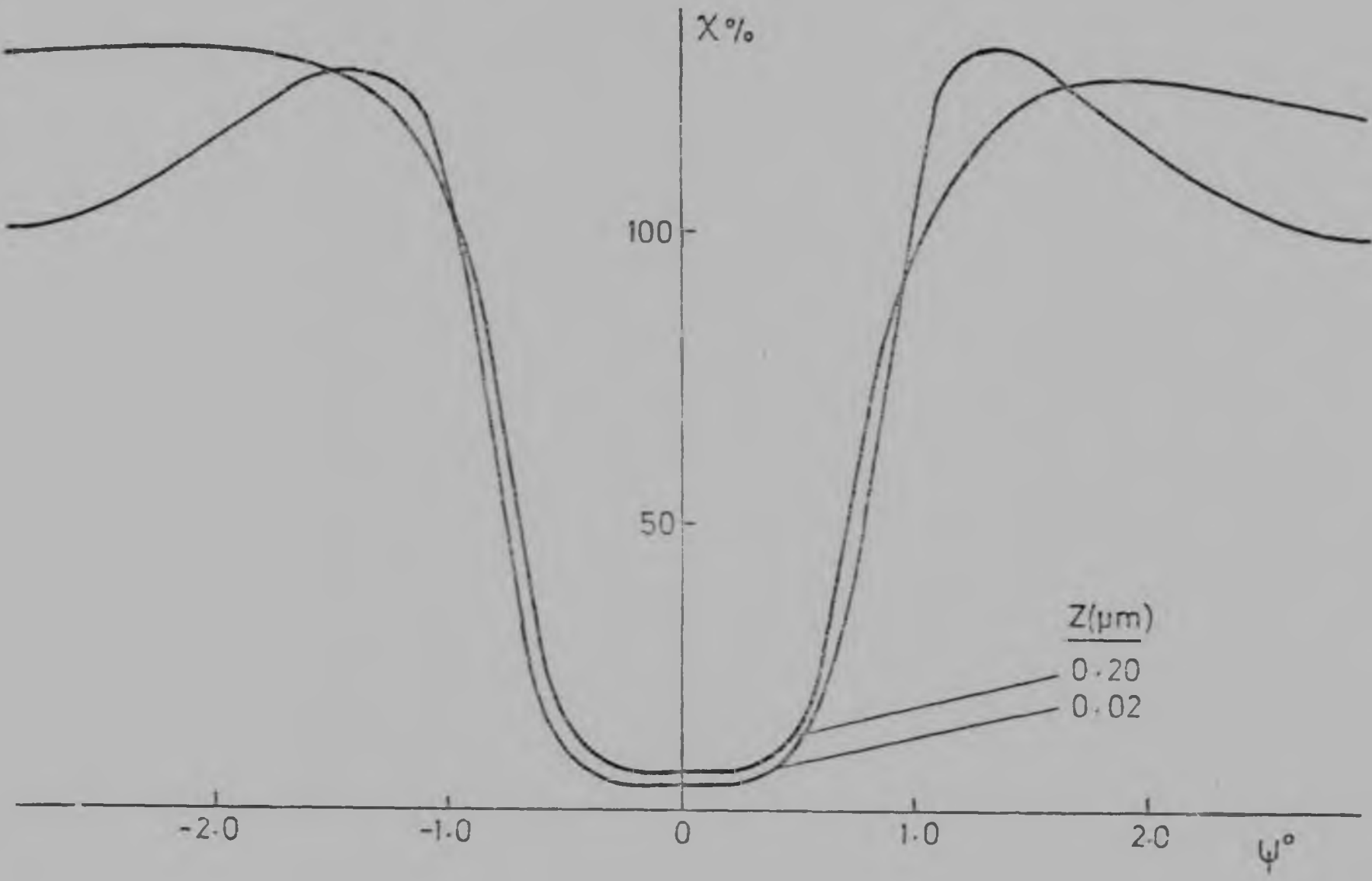

Figure 7.25: Scans through <110>: 1.0 MeV He^+ ions (KTI).

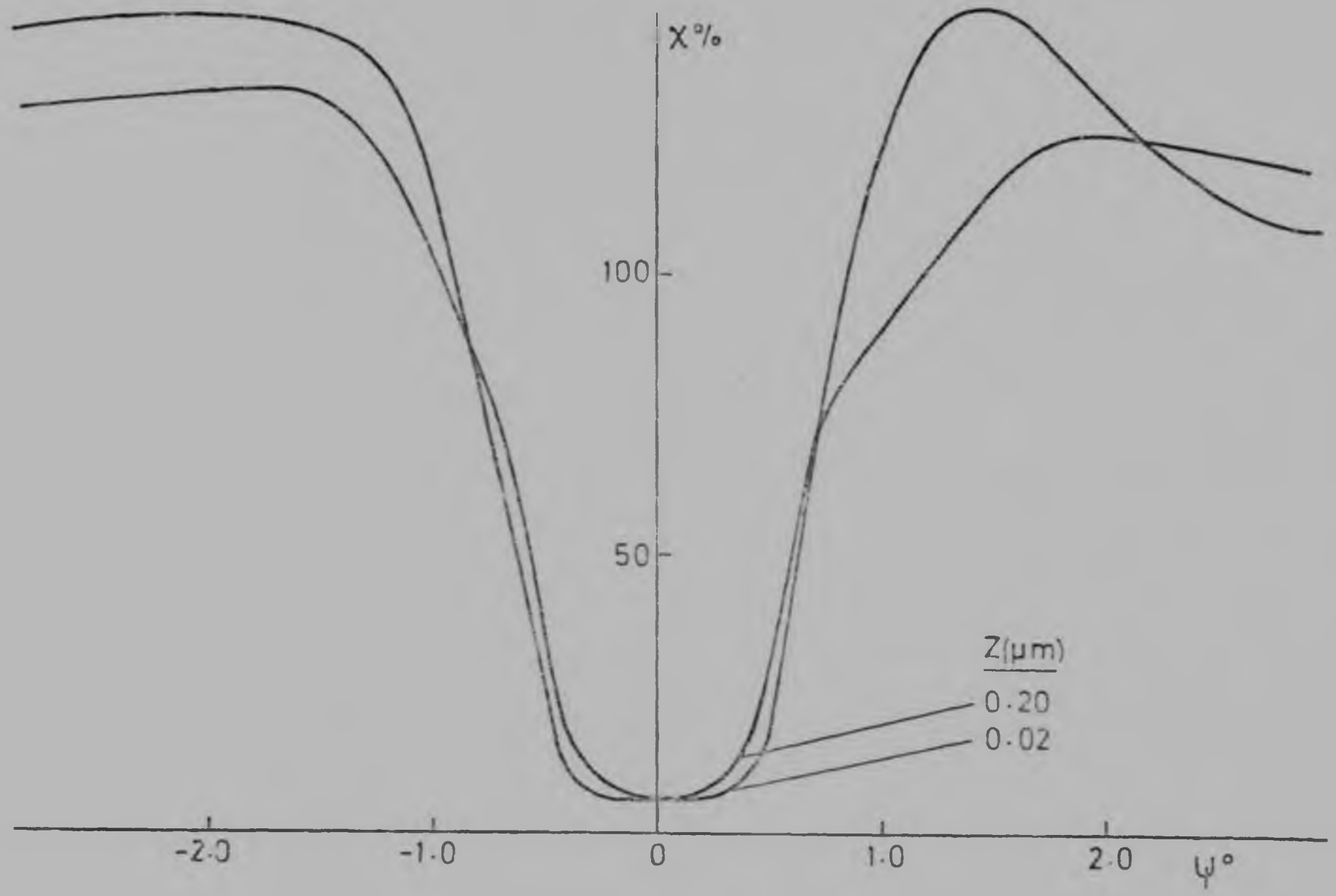

Figure 7.26: Scans through <111>: 1.0 MeV He^+ ions (KTI)

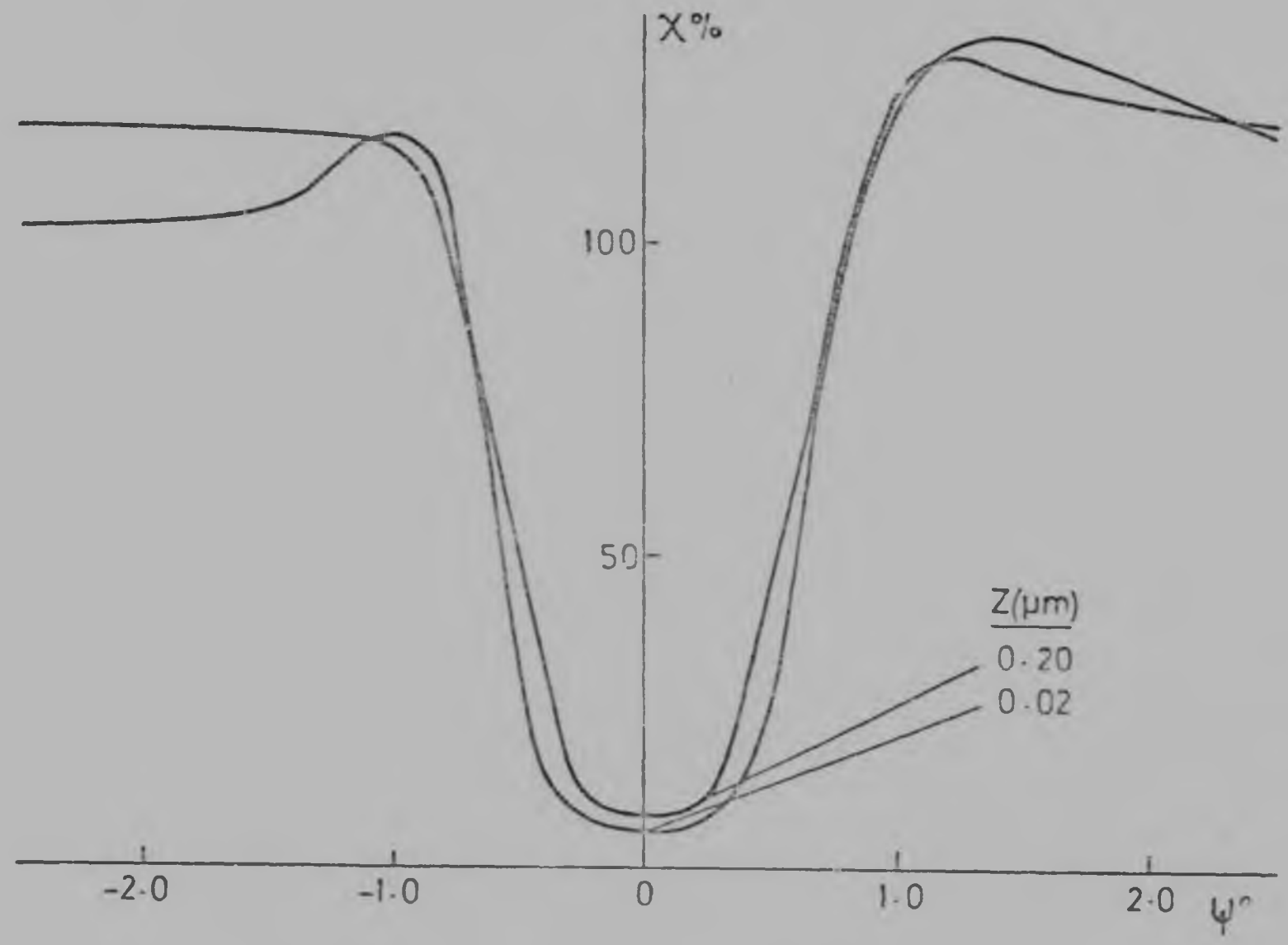

Figure 7.27: Scans through <100>: 1.0 MeV He^+ ions (XTI)

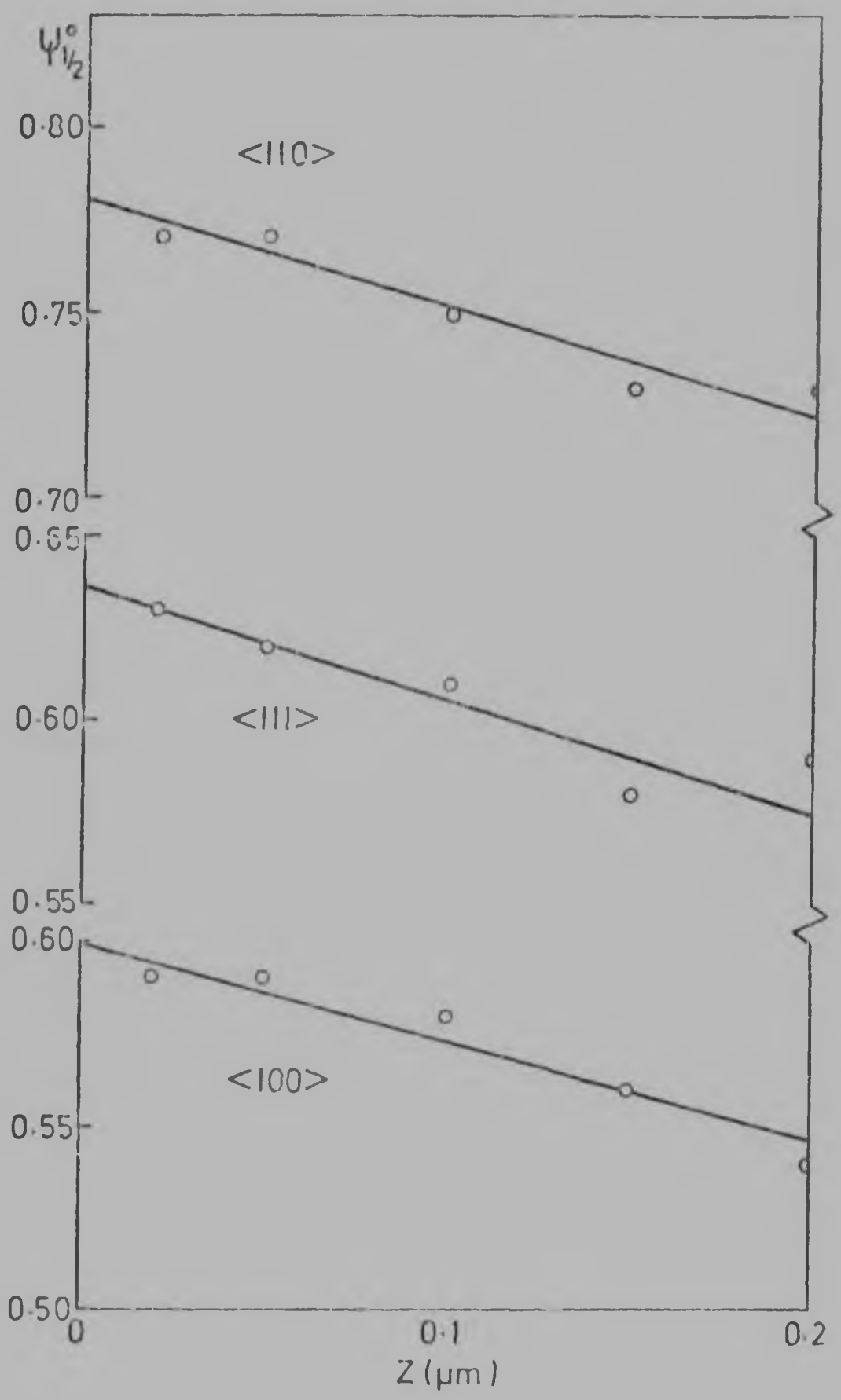

Figure 7.28: Dependence of critical angle on depth for 1.0 MeV He^{+} ions. o KTl.

TABLE 7.7

Critical Angles for 1.0 MeV He^+ Ions

Data for Di5 taken using an SCA. Estimated statistical errors ±0.02°.

Channel	Diamond	$\psi_{\frac{1}{2}}$° (exptl)	$\psi_{\frac{1}{2}}$° (theor)
<110>	Di5	0.74	0.74
	KT1	0.78	
<111>	Di5	0.64	0.66
	KT1	0.64	
<100>	KT1	0.60	0.62
{111}	KT1	0.20	0.19
{100}	KT1	0.14	0.15

TABLE 7.8

Critical Angles for 0.7 MeV He^+ Ions

Data taken using an SCA. Estimated statistical errors: ±0.04° (axes), ±0.02° (planes). Planar values are mean of ~3 scans.

Channel	Diamond	$\psi_{\frac{1}{2}}$° (exptl)	$\psi_{\frac{1}{2}}$° (theor)
<110>	Di3	0.87	0.88
<111>	Di3	0.86	0.79
<100>	Di3	0.77	0.74
{110}	Di3	0.29	0.27
{111}	Di3	0.32	0.23
{100}	Di3	0.20	0.19
{211}	Di3	0.17	0.15

at different times, and in some cases, with different apparatus; and between dissimilar data when intercompared via the Lindhard or Barrett formulae (Eqns 2.4, 2.6, 2.7 or 2.8). However, some considerations of the errors were made during analysis.

The smoothness of the angular plots and their good mirror-symmetry indicated that yield errors were less than ±2 percentage points for plots derived from spectra, in agreement with counting statistics. This was equivalent to an error in $\psi_{\frac{1}{2}}$ of $\lesssim 0.01°$ at shallow depths.

Repeat determinations of random spectra indicated a standard error in the mean of ±1% after smoothing. This contributes an error in $\psi_{\frac{1}{2}}$ of $<0.01°$ at shallow depths (rising to large values for weak channels at the greatest depths).

As mentioned in §7.3.3 and §7.4.2, the error involved in extrapolating $\psi_{\frac{1}{2}}$ to $z = 0$ was no more than 0.01°. The precision of the goniometer itself was of the same order, if this is assumed to be defined by the step size.

Different determinations of the same critical angles agree to within 0.02°, which is the value obtained by adding the abovementioned errors in quadrature. In most cases the error can be taken as ±0.01°. Data taken with Goniometer Mark 1 has a much larger spread, in keeping with its poorer accuracy of 0.1°, and with the accompanying use of SCA's (averaging over a significant depth of the crystal) to collect data.

The excellent consistency of the results and their errors needs

some explanation, however, because the largest source of possible error has not been included in the above discussion: the beam-spread of ±0.025° (at 1.0 MeV) as defined by the collimators (§3.3.2). The spread was evidently much less than this, presumably due to very good parallelism and transverse stability of the beam delivered by the accelerator. In fact in some very fine scans, it was found possible to measure their widths with a reproducibility of ±0.004°. This implies that the apparatus was capable of adding an extra significant digit to the numbers presented, but it would probably not have been justified because of other uncertainties, particularly in the height of the random spectra.

7.5 COMPARISON WITH THEORY

7.5.1 Axes

All the axial results are compared graphically with Barrett's semi-empirical relationship (Eqn 2.7), which incorporates Lindhard's predictions for the dependence on ion charge and energy and row spacing, in Figure 7.29. For unequally spaced rows (for example, <111>), the average spacing was used, as justified by the work of Picraux et al [Pic69a]. The straight line at 45° to the axes represents perfect agreement between the measurements and Eqn 2.7, which has been taken with $k = 0.83$ (which Barrett found to be the best fit to the dependence on temperature) rather than $k = 0.80$ (his value for ion and energy dependence). The agreement between measurements and Eqn 2.7 is evidently very good indeed for the two most open axes (<110> and <111>) and for the Phase III data ($E \geq 1.0$ MeV), with the modified value for k.

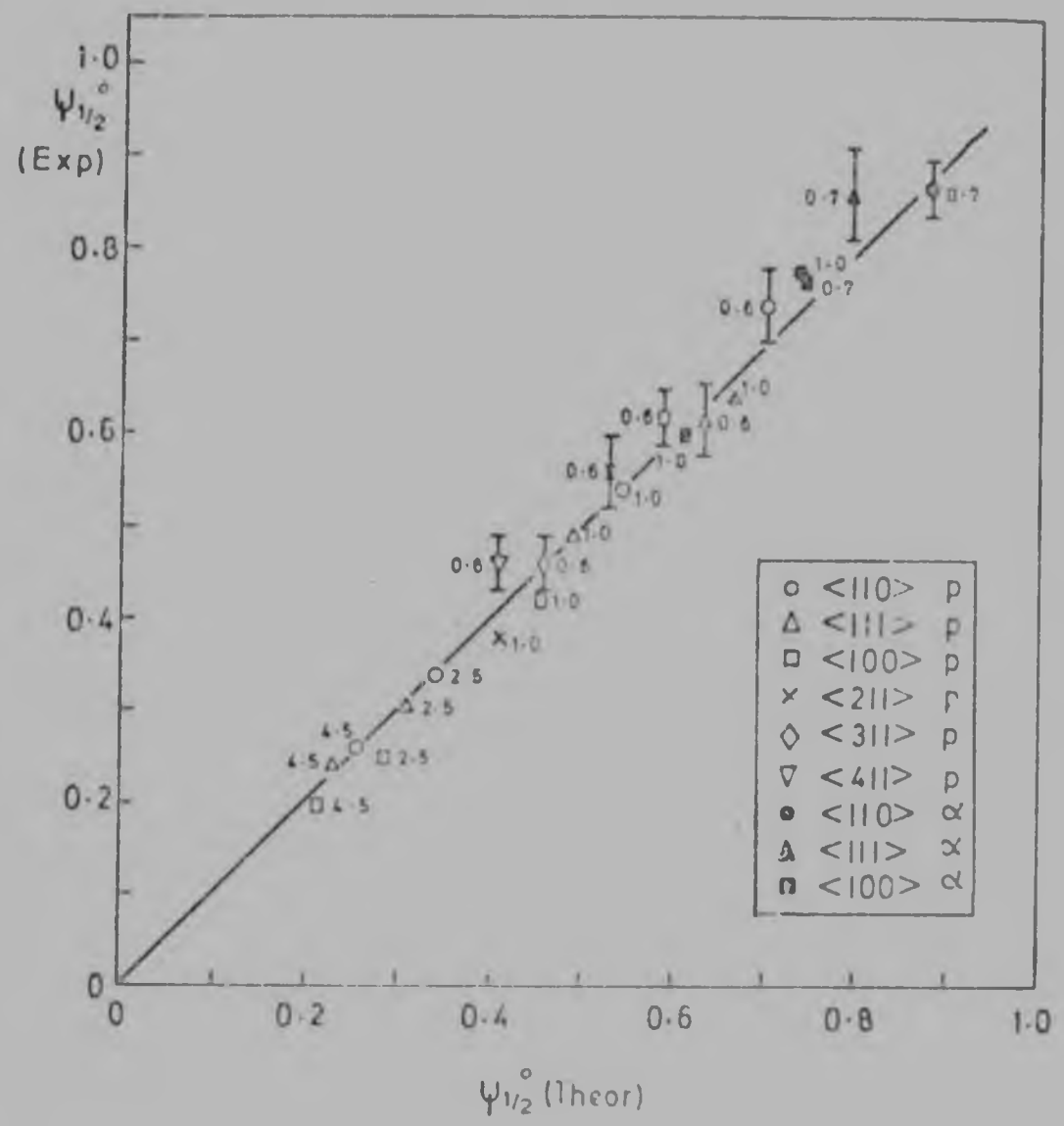

Figure 7.29: Comparison of experimental values of $\psi_{\frac{1}{2}}$ for axes with theoretical values calculated from Eqn 2.7.

The Phase I data (E < 1.0 MeV) generally give high values for ψ_1. In the proton case this is attributable to scans having been made in a {110} plane (see Section 6.8). The greater scatter corresponds to the cruder nature of the experiments.

The narrower axes (<100> and <211>) consistently have ψ_1 values smaller than those predicted by Eqn 2.7, even with k = 0.80. Most workers have tested this expression for the one or two most open axes in each crystal, finding good agreement; it appears that for more minor axes, a smaller value of k (about 0.76) is required. In other words, the ratio of ψ_1 to ψ_c is not strictly constant, but decreases for the less close-packed axes. The physical reason for this is not known. It cannot be accounted for by including the potential of nearest-neighbour rows in deriving an expression such as Eqn 2.7.

Instead of k, m could be varied, but much larger changes would be necessary (see §8.3.2).

7.5.2 Planes

In a similar way, the planar results are compared with Barrett's expression (Eqn 2.8) in Figure 7.30. Once again, the value of k appropriate to temperature dependence rather than ion and energy dependence has been preferred. The agreement here is almost as good as for axes (note the difference in scale between the two graphs), with the marked exception of the {111} plane. Not only are the measured ψ_1 values high, but they equal or exceed those for the {110} plane, although the {111} has the smaller mean planar spacing.

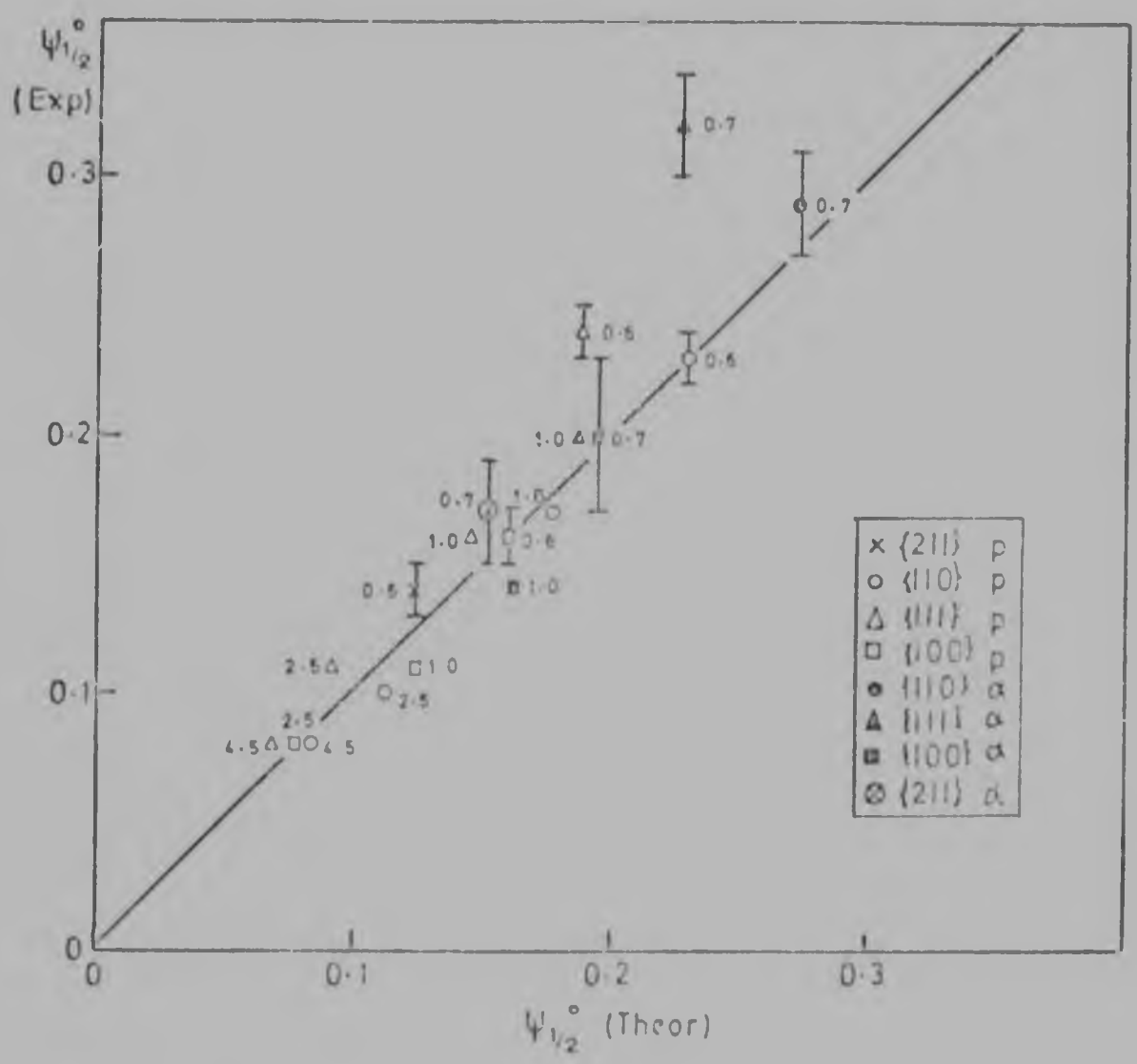

Figure 7.30: Comparison of experimental values of $\psi_{\frac{1}{2}}$ for planes with theoretical values calculated from Eqn 2.8.

The explanation in this case is readily apparent. The {111} planes in diamond have two sets of spacings (see Figure 7.31), which were averaged to produce the value of d_p inserted in Eqn 2.8. This procedure is evidently inappropriate. In order to determine accurately the effective value of $d_p\{111\}$, one may note that $\psi_1\{111\}$ is slightly greater than $\psi_1\{110\}$ (by about 5°), and therefore

$$d_p\{111\} - d_p\{110\} \sim 10^{\circ}$$

(since $d_p \propto (\psi_1)^2$), giving

$$d_p\{111\} \approx 1.4\ \text{Å}$$

Using Figure 7.31 and Table 7.9, it can be seen that this corresponds most closely to the larger of the two planar spacings (and not to their mean). Most ions are evidently channelled in this space, with only a small effect from the closely adjacent second plane of each pair.

TABLE 7.9

Spacings of {111} Planes in Diamond

Refer to Figure 7.31. Lattice parameter = a = 3.567 Å.

i) Small gap (d_1) = $\sqrt{3}a/12$ = 0.515 Å

ii) Large gap (d_2) = $\sqrt{3}a/4$ = 1.545 Å

iii) Mean (d_p) = $\sqrt{3}a/6$ = 1.030 Å

iv) $d_2 + 2\times\frac{1}{2}d_1$ = $\sqrt{3}a/3$ = 2.059 Å

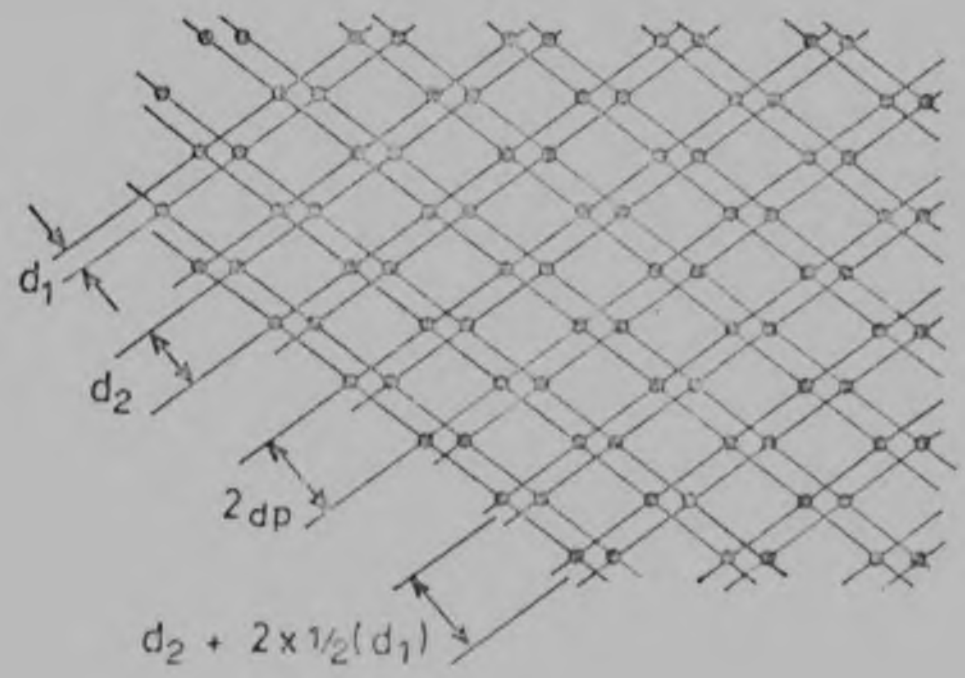

Figure 7.31: Spacings of {111} planes in the diamond lattice. Values are listed in Table 7.9.

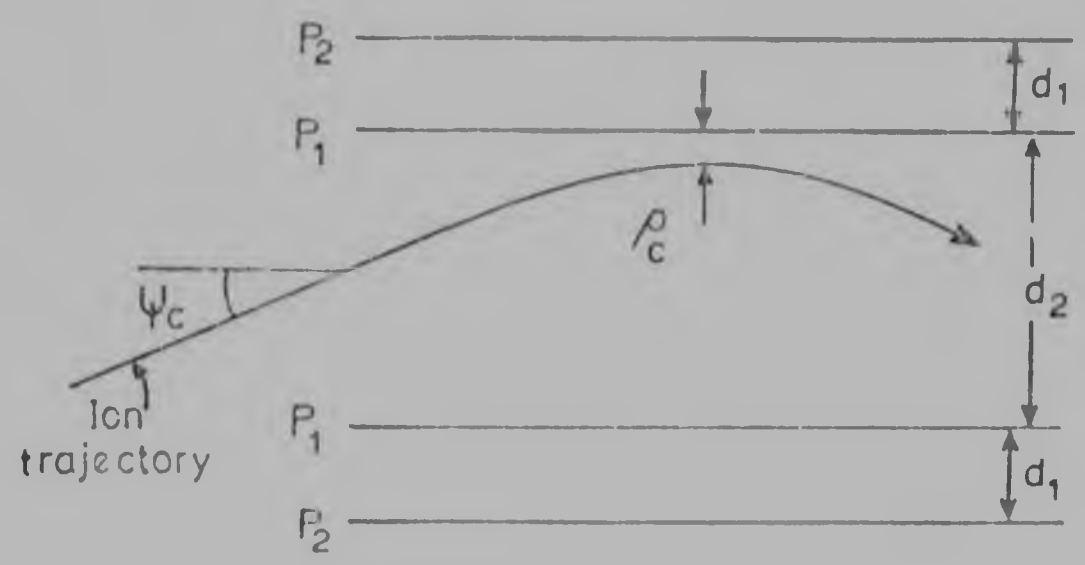

Figure 7.32: Model of {111} planar channelling in the diamond lattice, as developed in §7.5.3.

7.5.3 Re-calculation of [111] Critical Angles

The above observation may be put on a more rigorous footing in terms of the considerations outlined in §2.2.3. It is assumed that ions are confined to the wider interplanar gap (spacing d_2) with the critical angle governed by the distance of closest approach ρ_c to the two planes P_1 forming its walls (Figure 7.32); ρ_c is set equal to mu_1, where u_1 is the RMS thermal vibration amplitude and m is taken to have the same value as for single planes (= 1.6). Then in calculating the critical angle ψ_c by equating the initial transverse kinetic energy $E\psi_c^2$ to the change in potential energy between mid-channel and ρ_c, the potentials due to all four planes (P_1 and P_2) are taken into account.

In the notation of Reference Ge71 and §2.2.3,

$$\psi_c = \psi_a \{\Sigma f_{PS}\}^{\frac{1}{2}}$$

where the sum is evaluated for both pairs of planes P_1 and P_2, that is,

$$\psi_c = \psi_a \left\{ f_{PS}\left(\frac{\rho_c}{a_{TF}}\right) + f_{PS}\left(\frac{d_2-\rho_c}{a_{TF}}\right) - 2f_{PS}\left(\frac{d_2}{2a_{TF}}\right) \right.$$

$$\left. + f_{PS}\left(\frac{\rho_c+d_1}{a_{TF}}\right) + f_{PS}\left(\frac{d_1+d_2-\rho_c}{a_{TF}}\right) - 2f_{PS}\left(\frac{2d_1+d_2}{2a_{TF}}\right) \right\}^{\frac{1}{2}}$$

$$= \psi_a I_{PS}^{(4)} \qquad (7.3)$$

where

$$F_{PS}^{(4)} = \left\{ \left[F_{PS}\left(\frac{\rho_c}{a_{TF}} , \frac{d_2}{a_{TF}} \right) \right]^2 + \left[F_{PS}\left(\frac{\rho_c + d_1}{a_{TF}} , \frac{2d_1 + d_2}{a_{TF}} \right) \right]^2 \right\}^{\frac{1}{2}}$$

$$= \{ [F_{PS}(\xi,\eta)]^2 + [F_{PS}(\xi',\eta')]^2 \}^{\frac{1}{2}} \qquad (7.4)$$

with $\xi = \rho_c / a_{TF}$

$\eta = d_2 / a_{TF}$

$\xi' = (\rho_c + d_1) / a_{TF}$

$\eta' = (2d_1 + d_2) / a_{TF}$

The values of $F_{PS}(\xi,\eta)$ and $F_{PS}(\xi',\eta')$ were evaluated from the curves in Bar71, giving

$$F_{PS}^{(4)} = 0.92$$

Then, by analogy with Eqn 2.8,

$$\psi_{\frac{1}{2}} = k \left[F_{PS}^{(4)} \right] \psi_a \qquad (7.5)$$

where the value of d_p to be used in calculating ψ_a is the mean value, since d_p enters the expression via the atomic density in the plane, which is determined by the mean planar spacing. The resulting values of $\psi_{\frac{1}{2}}\{111\}$ for protons are compared with the experimental ones in Table 7.10. The agreement is good, indicating the validity of the model of {111} channelling used.

Most workers seem to have avoided the problems of unequally spaced, homogeneous planes by confining measurements to other planes in each crystal. (An exception was Davies et al [Dav68].) The present

TABLE 7.10

Calculated Values of /111/ Critical Angles

E (MeV)	ψ_1^c (Eqn 7.5)	ψ_1^c (exptal)
0.6	0.246	0.24
1.0	0.191	0.17
2.5	0.121	0.11
4.5	0.090	0.08

work shows that channelling between such planes admits of a simple description, at least when the spacings are very different (in this case, $d_2 = 3d_1$). There was no sign of a separate channelling component in the narrow spaces of width d_1, in the form of inflexions in the sides of the channelling dip; any ions initially so channelled must be rapidly dechannelled into the wider spaces or into the random beam.

7.5.4 Other Theories

Some of the proton critical angles for axes were compared with values calculated by the method of Varelas and Sizmann [Var72] as outlined in §2.2.1. This produces critical angles ψ_c rather than half-angles $\psi_{\frac{1}{2}}$ (see §2.2.1). Taking Barrett's factor k [Bar71] as being a conversion factor between ψ_c and ψ_1, the same factor k was applied in

TABLE 7.11

Critical Angles ψ_c Calculated after Reference Var72

Axis	E (MeV)	ρ_c (Å)	ψ_c°	$\frac{1}{2}\psi_c$°	$\psi_{\frac{1}{2}}$° (Eqn 2.7)	$\psi_{\frac{1}{2}}$° (Expt)
<110>	1.0	0.065	0.66	0.33	0.54	0.55
<111>	0.6	0.075	0.73	0.62	0.63	0.62
	1.0	0.071	0.58	0.48	0.49	0.49
	2.5	0.066	0.38	0.31	0.31	0.30
	4.5	0.065	0.28	0.23	0.23	0.24
<100>	1.0	0.066	0.55	0.46	0.46	0.42

this case. The resulting values were in excellent agreement both with the measurements and with the Barrett estimate, Eqn 2.7, as can be seen from Table 7.11, with the exception once again of the <100> axis, where both theoretical estimates agreed with one another but not with the measurement.

7.6 COMPARISON WITH OTHER MEASUREMENTS

The only other critical-angle measurements for channelling in diamond which have been reported in the literature are those of Picraux et al [Pic69a] and of Sellschop and Gilson [Se73]. Their values are compared with corresponding ones taken from the present work, in Table 7.12. Theoretical values calculated by means of Eqn 2.7 (axes) or Eqn 2.8 (planes) are included.

There is reasonable agreement between the measurements of the different experimental groups, taking errors into account. The values found in the present work are generally slighly higher, and tend to agree more consistently with the theoretical estimates. This is in keeping with the larger experimental errors reported by the others.

TABLE 7.12

Comparison of Diamond Critical Angles ψ_1 Measured by Different Workers

Axis	Ion	E (MeV)	ψ_1 (degrees)			
			*This Work	Ref †Fic69a	Ref Se73	Theory
<110>	H^+	1.0	0.55	0.58	$0.48^{+.02}_{-.01}$	0.54
	H^+	.5	-	-	0.39±.02	0.44
	He^+	1.0	0.76±.02	0.75	-	0.74
	He^+	2.0	-	-	0.53±.05	0.52
<111>	H^+	1.0	0.49	0.46	-	0.49
	He^+	1.0	0.64	0.58	-	0.66
{110}	H^+	1.0	0.16	0.16	-	0.18

*Errors: ±0.01° except where specified.

†Errors: ±0.06° (axes), ±0.03° (planes).

CHAPTER 8

TEMPERATURE DEPENDENCE OF CRITICAL ANGLES

8.1 INTRODUCTION

Barrett's [Bar71] semi-empirical relationships for axial and planar half-angles, Eqns 2.7 and 2.8, predict a reduction therein with increasing thermal vibration amplitude. The effect for planes is very much weaker than that for axes, in agreement with calculations (for example, Erg65, Ando7 in Lin71] and with the experimental observations of many workers (for example, Dav68, Ando8, and Lu69). It has been suggested that this is because

i) channelled ions are already sampling a pseudo-random distribution of collisions within the plane [Dav68], or

ii) the planar potential varies more slowly than the axial one in the region of a_{TF} [Pic69a].

Ordinary temperatures are so far below the Debye temperature of diamond that the mean thermal vibration amplitude changes little with temperature. The critical angle changes are therefore expected to be rather small, especially below room temperature. No cryogenic measurements were attempted for this reason.

An account of the measurement of critical angles at elevated

temperatures is given in Section 8.2. In Section 8.3 they are compared with Eqns 2.7 and 2.8, and modifications to Eqn 2.7 are considered which would bring it more closely in agreement with the axial measurements.

8.2 MEASUREMENTS AT ELEVATED TEMPERATURES

8.2.1 Experimental

Critical angles ψ_1, were measured for 1.0 MeV protons incident near the usual three major axes and three major planes, on one good specimen (KT1) while it was held at a series of temperatures up to 700°C (the limit of the apparatus). Temperatures were monitored thermoelectrically and kept to within ±10°C of the nominal value.

Other details of the experimental technique and data extraction were the same as for Chapter 7.

8.2.2 Results

A small but significant reduction of ψ_1 for increasing temperature was seen for axes; the effect observed for planes was of the order of the experimental sensitivity of 0.01°, as predicted by Eqn 2.8. Some of the axial dips are plotted in Figures 8.1, 8.2 and 8.3 for different depths. Critical angles are plotted against depth at three of the temperatures in Figure 8.4; the reduction in ψ_1 is approximately constant with depth, since the curves are almost parallel.

Surface-extrapolated values of ψ_1 are summarised in Table 8.1

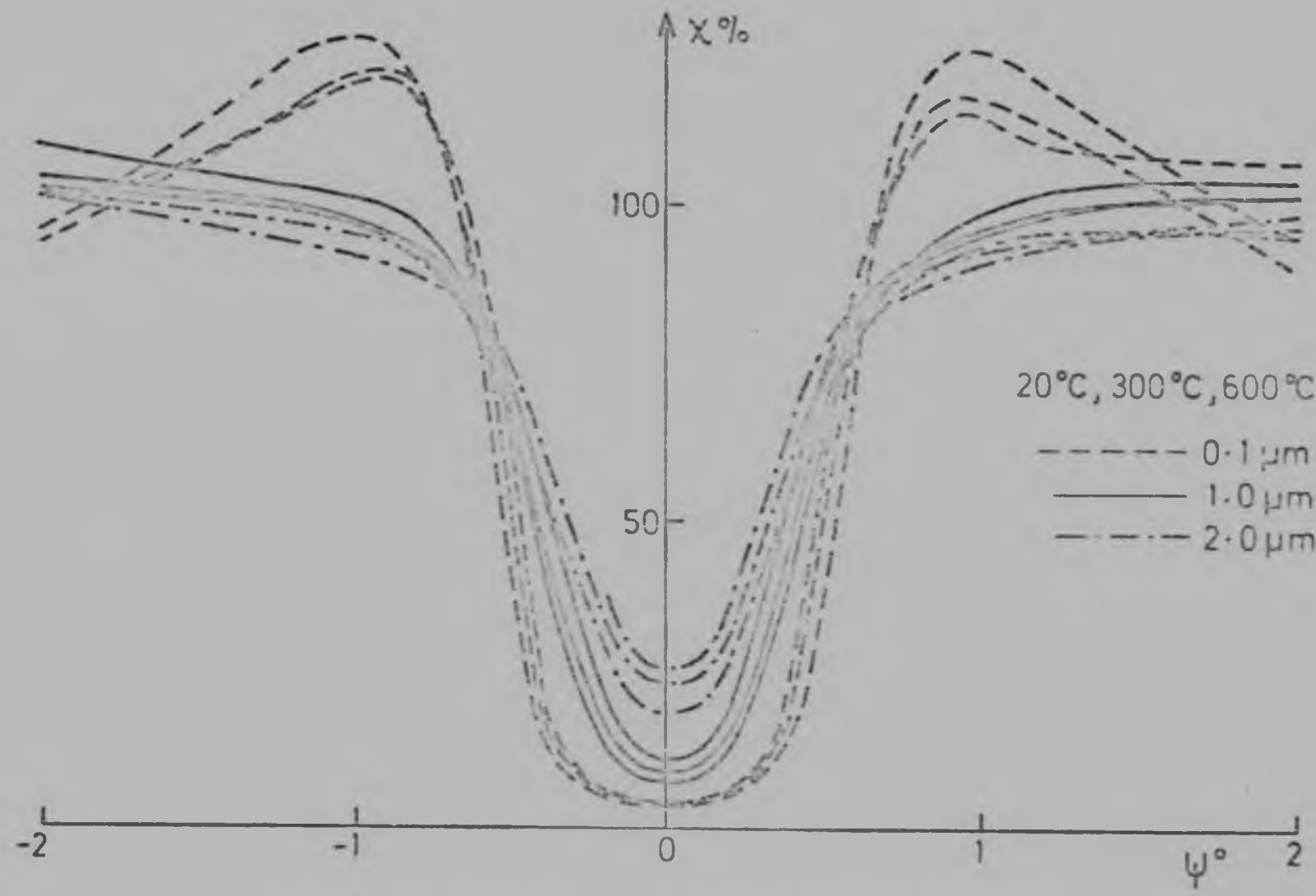

Figure 8.1: Scans through <110> at different temperatures: 1.0 MeV protons. Narrowest dip at each depth is for highest temperature. (KII).

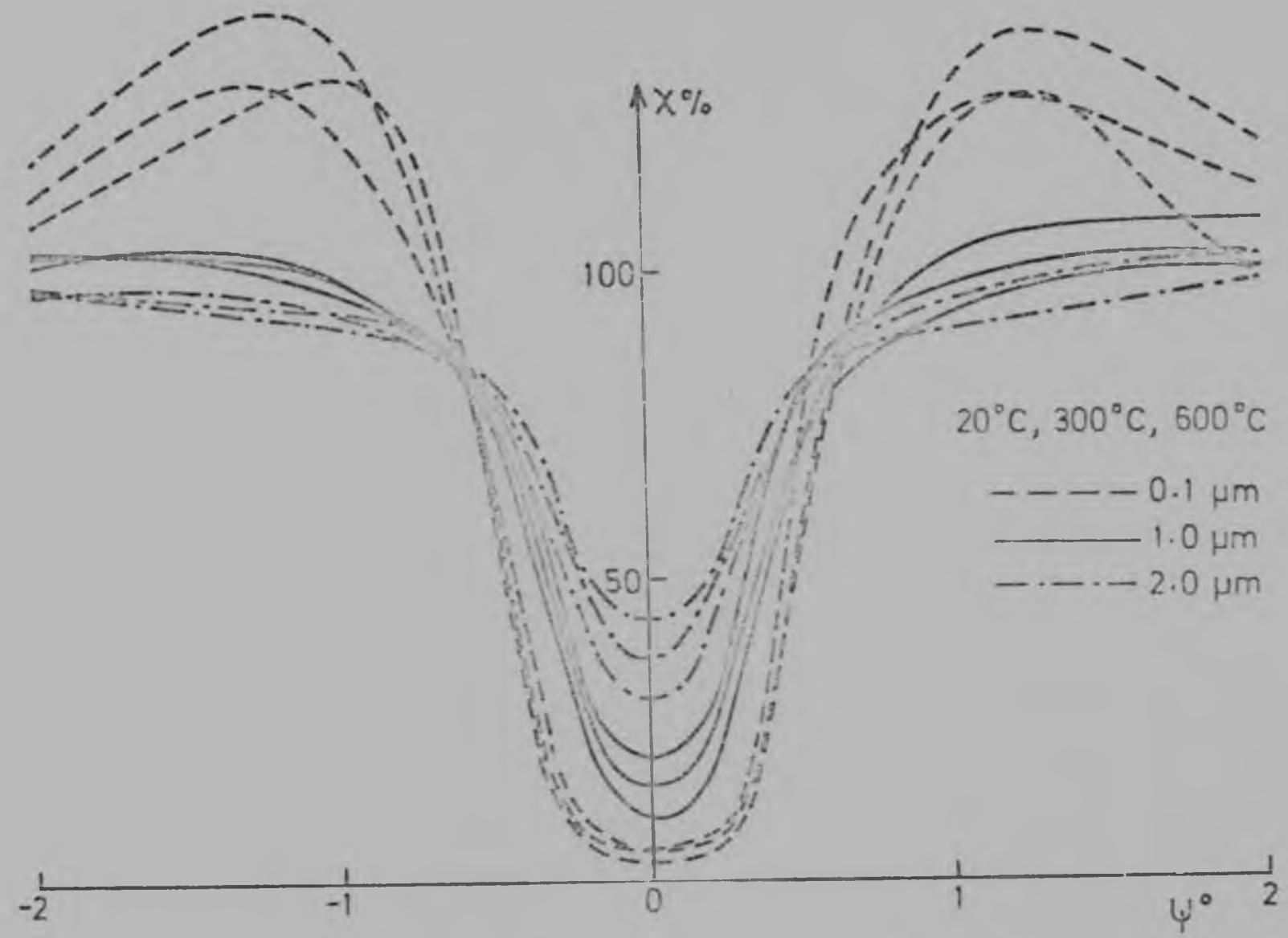

Figure 8.2: Scans through <111> at different temperatures: 1.0 MeV protons. Narrowest dip at each depth is for highest temperature. (KT1).

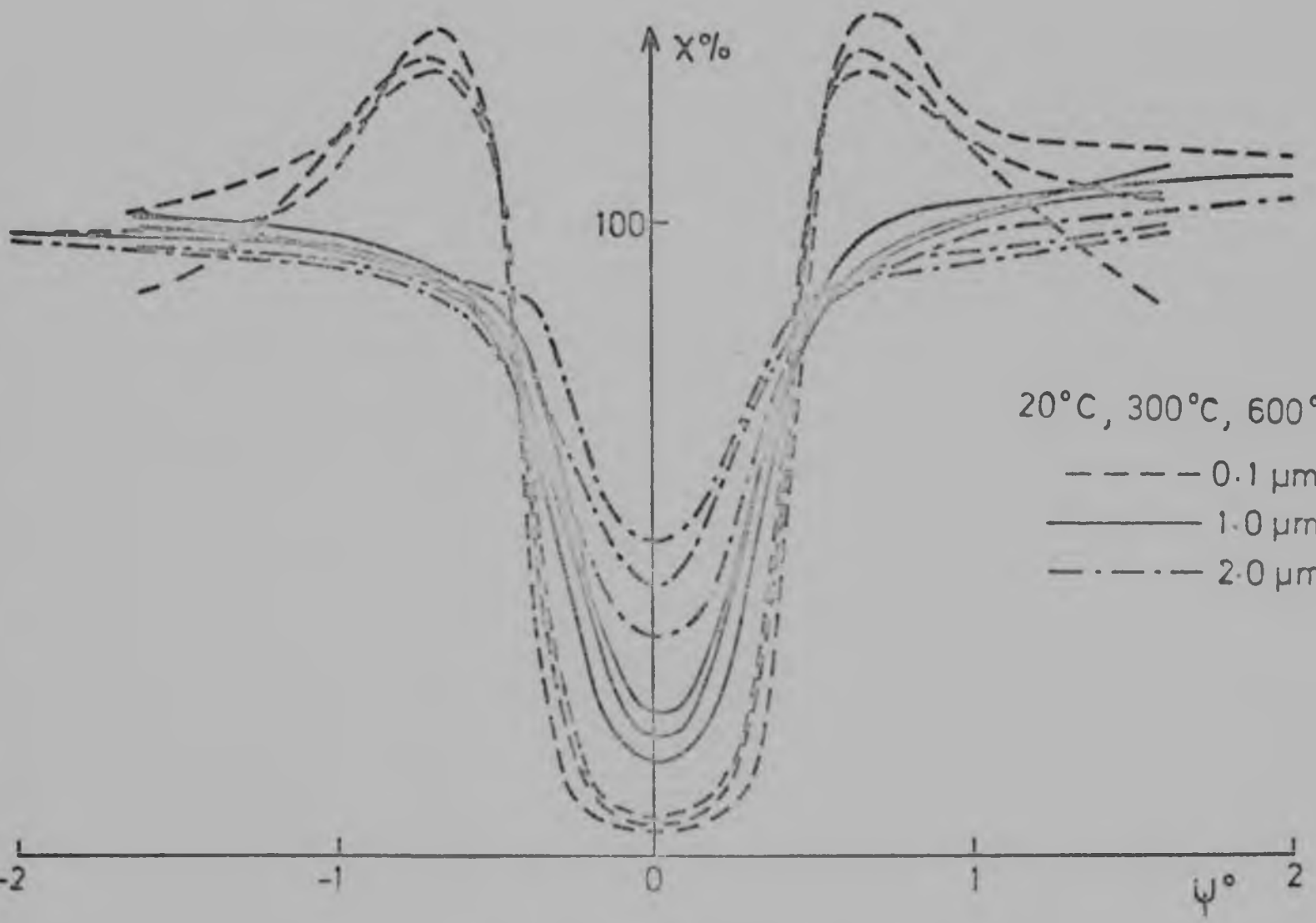

Figure 8.3: Scans through 100 at different temperatures: 1.0 MeV protons. Narrowest dip at each depth is for highest temperature. (KT1).

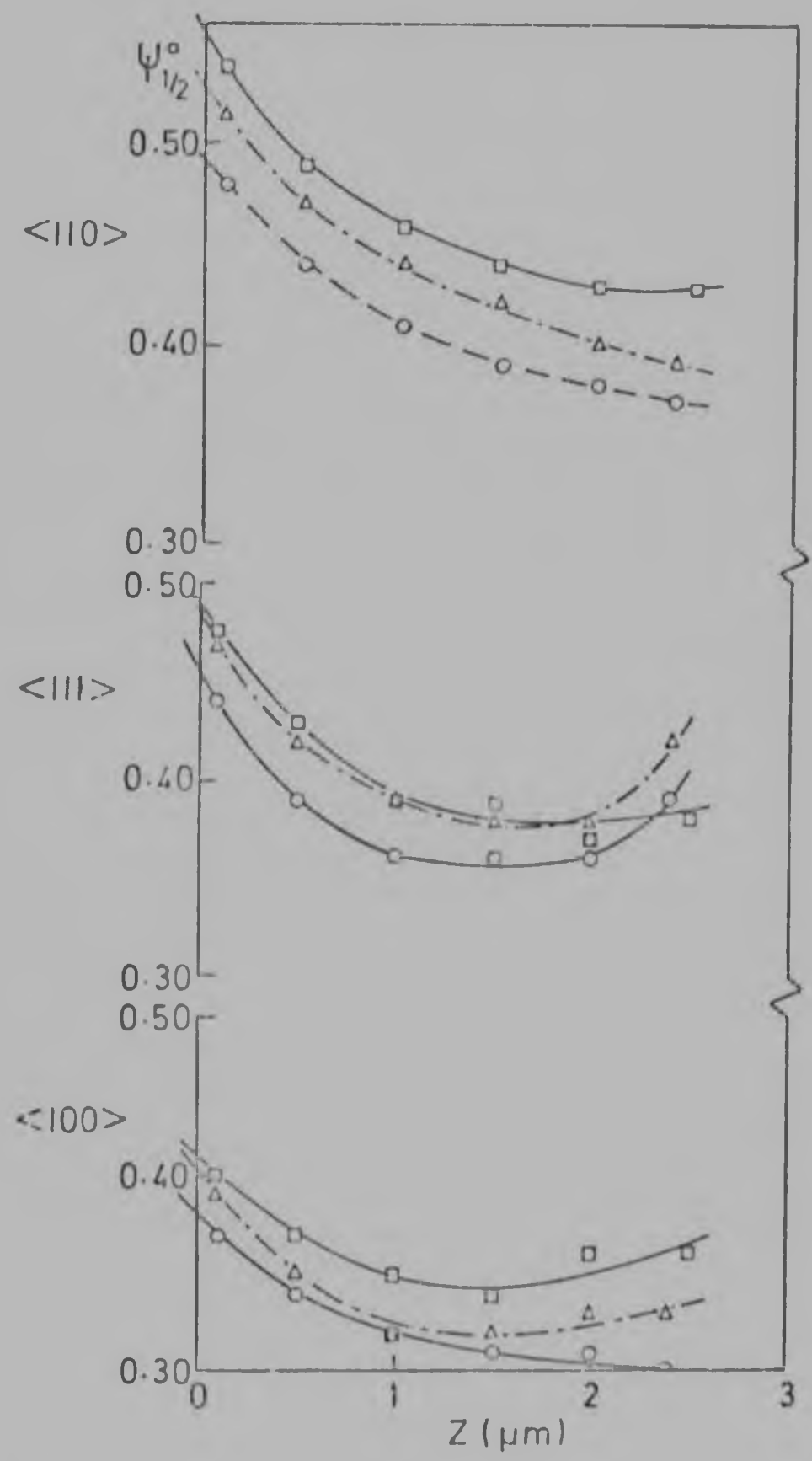

Figure 8.4: Dependence of critical angle on depth at different temperatures for 1.0 MeV protons. (KTI).

□ 20°C; △ 300°C; o 600°C.

TABLE 8.1

Temperature Dependence of Axial Critical Angles

Axis	Temp (°C)	u_1 (Å)	ψ_1° (exptl)	ψ_1° (theor) [Bar71]	ψ_1° (theor) [Var72]
<110>	20	0.044	0.55	0.54	0.55
	300	0.051	0.53	0.52	0.53
	500	0.056	0.49	0.51	0.52
	600	0.058	0.49	0.51	0.51
	700	0.061	0.50	0.50	0.51
<111>	20	0.044	0.49	0.49	0.48
	300	0.051	0.48	0.47	0.47
	500	0.056	0.46	0.46	0.46
	600	0.058	0.46	0.46	0.45
	700	0.061	0.45	0.45	0.45
<100>	20	0.044	0.11	0.46	0.46
	300	0.051	0.10	0.44	0.44
	500	0.056	0.37	0.43	0.43
	600	0.058	0.38	0.43	0.43
	700	0.061	0.37	0.42	0.42

TABLE 8.2

Temperature Dependence of Planar Critical Angles

Plane	Temp (°C)	u_1 (Å)	ψ_1° (exptl)	ψ_1° (theor) [Bar71]
{110}	20	0.044	0.17	0.18
	500	0.056	0.17	0.17
	700	0.061	0.17	0.17
{111}	20	0.044	0.16	0.15
	500	0.056	0.17	0.14
	700	0.061	0.17	0.13
{100}	20	0.044	0.11	0.12
	500	0.056	0.10	0.12
	700	0.061	0.11	0.11

for axes and 8.2 for planes, and plotted against thermal vibration amplitude (u_1) in Figure 8.5. The values of u_1 were calculated after Lonsdale [Lon48], using a value of the Debye temperature of 1860 K [Vic62].

8.3 COMPARISON WITH THEORY

8.3.1 Comparison

Values of ψ_2 calculated from Eqns 2.7 and 2.8 are included in Tables 8.1 and 8.2 respectively. In the axial case (Table 8.1) values calculated according to Varelas and Sizmann's procedure [Var72] are added (with the factor applied as described in §7.5.4); they are very similar to those of Eqn. 2.7. Curves calculated from Eqns 2.7 and 2.8 are included in Figure 8.5. For the <100> axis, discrepancies in the room-temperature measurements have already been mentioned (§7.5.1), amounting to this axis requiring a smaller value of k in Eqn 2.7. Accordingly, a second <100> curve has been plotted in Figure 8.5, with k scaled to fit the room-temperature result. For the {111} plane, which showed the discrepancies discussed in §7.5.2 and §7.5.3, the {110} curve is a good approximation. The error-bars represent ±0.01°, the overall error deduced in §7.4.5.

The planar results are consistent with Eqn 2.8, ψ_2 being constant to 0.01° over the temperature range examined. This confirms that the temperature effect is indeed very small for planes in diamond.

The axial results follow Eqn 2.7 quite well within experimental error, the maximum deviation being ±0.02°. It is of interest that this

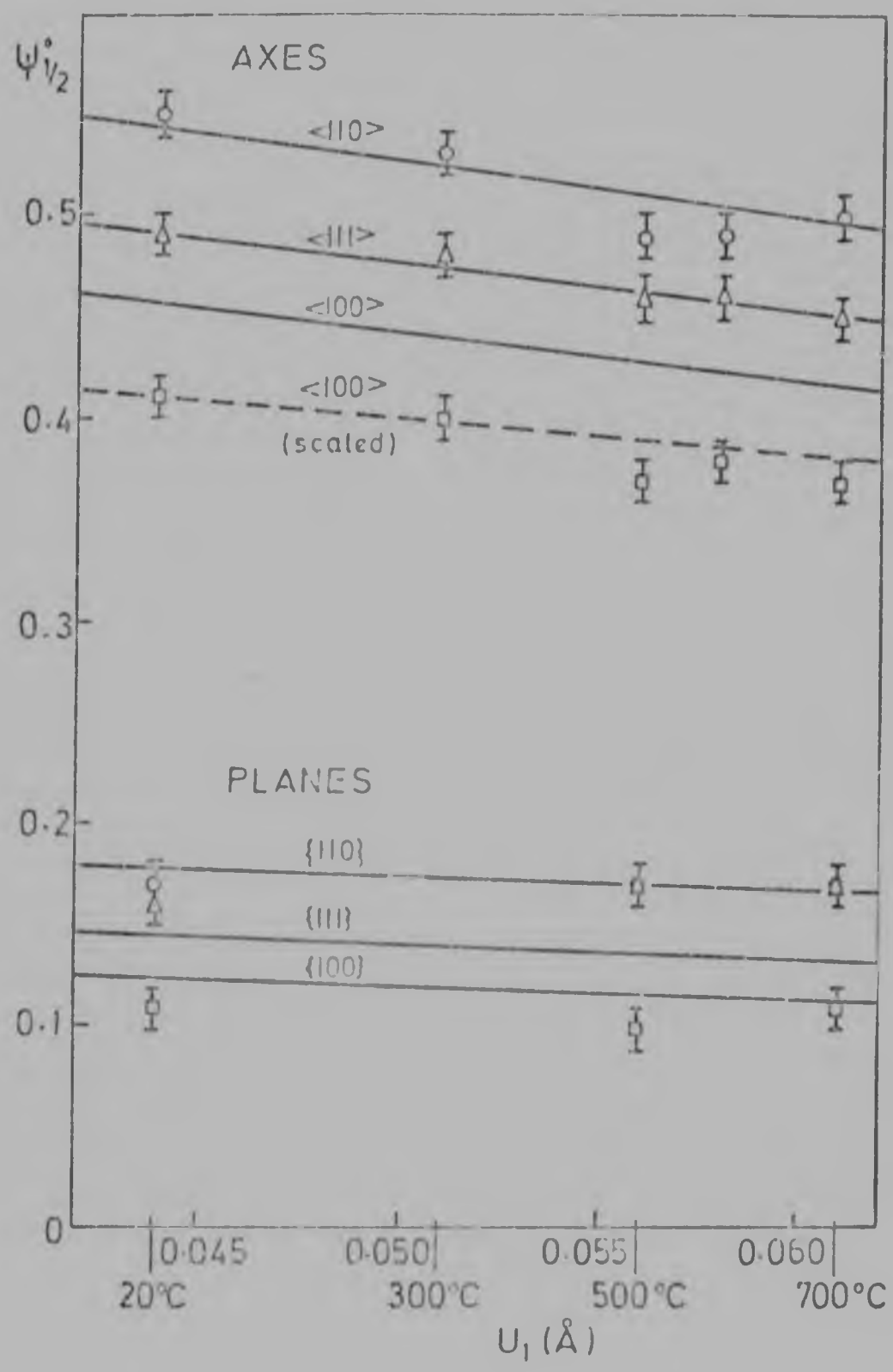

Figure 8.5: Dependence of surface critical angles on thermal vibration amplitude. (Data from KTI)

o ‹110›, {110}; Δ <111>, {111};

□ ‹100› {100} — theory.

equation is still valid for $u_1 \ll a_{TF}$ (in diamond $u_1/a_{TF} \sim 0.2$ compared with $u_1/a_{TF} \sim 0.5$ in most substances - see Table 2.2). In terms of the considerations of §2.2.3, this confirms that the critical approach distance to a string, ρ_c, is determined by u_1 rather than a_{TF}, even in so nearly static a lattice as diamond. This was also deduced by Altman et al [Alt70] from different evidence (transmission energy loss distribution of protons channelled in silicon).

There is, however, a systematic indication in the <110> and <100> results of a somewhat stronger dependence on u_1 than Eqn 2.7 suggests. This was also noted by Andersen and Lægsgård [And72] for protons channelled in ten different substances. The <111> curve here does not show this behaviour, and predicts the measurements accurately.

The theoretical treatment of Varelas and Sizmann [Var72] contains inherent differences between the behaviour of rows in which two different atomic spacings alternate, such as <111>, and those with uniform spacing such as <110> and <100>. If values of ψ_1 are calculated by their method to one more significant digit than has been included in Table 8.1, it can be seen that whereas their curves for <110> and <100> are parallel to those of Eqn 2.7 to within .001°, that for the <111> is shallower to the extent of an increment of .005° over the range 0°C to 700°C. Although this is too small to account for the difference fully, it indicates that the different behaviour observed for <111> in Figure 8.5 is likely to be a real effect, and that if the unequal string spacing were taken into account in Eqn 2.7, the same observation is probably true for all three axes, namely that the temperature dependence of ψ_1

is stronger than that predicted by the equation.

8.3.2 Modifications

The possibility of fitting the <110> and <100> results using slightly different values of k and m was investigated. The parameter k acts only as a scaling factor, and the necessary change in the slope of the ψ_1 versus u_1 curves must come from changing m.

In his paper [Bar71] Barrett presented such fits for experimental data [And68] of protons on tungsten, and it is evident that quite appreciable variations of m produce very little change in the slopes of the curves. The changes were found to be even smaller with diamond: the <110> and <100> curves required values of m = 2.5 (with k = 1.02) for the best fit to the measured points, compared to Barrett's m = 1.2 and k = 0.83. To suggest doubling the value of m appears unjustified in view of the good agreement which has been found between Eqn 2.7 and the measurements in many different experiments.

An alternative is to allow m to vary with temperature (keeping k constant). This was found to require much smaller changes; a value of m = 1.3(5) reproduced the diamond data at 600 - 700°C quite well.

Using the considerations of §2.2.3, these results may be interpreted as follows. The form of Eqn 2.7 is that obtained from the continuum model of channelling (§2.2.1) by equating the 'transverse kinetic energy' E_{1c} of an ion far from the strings to its potential energy at the critical approach distance ρ_c. The latter is assumed to

be determined only by the mean thermal vibration amplitudes u_2 of individual atoms perpendicular to the string ($u_2 = \sqrt{2}u_1$); the relationship between ρ_c and u_2 (and therefore u_1) is assumed to be linear, $\rho_c = mu_1$ where m is a constant chosen to fit the data. The resulting value of the critical angle ψ_c is converted to the half-angle ψ_1 by multiplying by the fitting parameter k.

Choosing a larger value of m implies a stronger linear relationship between ρ_c and u_2, whereas allowing m to vary implies that the relationship is not linear beyond a first approximation. This seems reasonable, as there is no a priori reason to expect a linear relationship. In fact, both Varelas and Sizmann [Var72], and Morgan and Van Vliet [Mo70], assumed a quadratic relationship and found it gave a good fit to measurements in the first case, and computer simulations in the second. However, their relationships give an m which is a decreasing function of u_1, rather than an increasing one as required here. It may be concluded therefore that ρ_c is not strictly a linear function of u_1, but that the form of the function is still to be determined.

Barrett [Bar71] advised caution in basing conclusions on Eqn 2.7, because it is a fit to Monte Carlo calculations rather than a theoretical relationship; moreover his directly determined values of ρ_c did not bear a linear (or quadratic) dependence on u_1. However, the equation has a form in keeping with the physics of the channelling situation in terms of the well-tried continuum model, and has already shown itself amenable to a physical interpretation by Gemmell and Mikkelson [Ge72], and in §7.5.3 of the present work to clarify the measurements of critical angles

for the diamond {111} planes. The non-linearity of ρ_e on u_1 is in agreement with the implications of the diamond measurements.

CHAPTER 9

MINIMUM YIELD AND SURFACE PEAK

9.1 INTRODUCTION

The characterisation of diamonds by their (very varied) values of channelled minimum yield ($\chi_{\parallel}$) has been described in §5.2.3. In the present chapter the surface minimum yields of good crystals (measured mostly for 1.0 MeV protons undergoing axial channelling) are compared with theory as regards magnitude and functional dependence. The surface peak, closely connected with χ_{min}, was also evaluated.

Data processing methods are summarised in Section 9.2. The surface peak is considered in Section 9.3 and the surface minimum yield in Section 9.4. A few conclusions about the nature of the diamond surface are brought together in Section 9.5.

The depth dependence of χ_{min} is of considerable interest, since it measures the rate of dechannelling of initially well-channelled particles. This is not treated at all in the present work, as it will form the subject of a separate thesis [Fea79].

9.2 DATA PROCESSING

In-channel spectra accumulated for larger ion fluences than those used for the critical-angle determinations of Chapter 7 (×2 for protons,

x5 for alphas) were used for the extraction of accurate minimum yields.

The extractions were performed by the Fortran programme PEAKFIT [Fea77a], which stripped the surface peak and extrapolated the underlying channelled spectrum to zero depth. This was achieved by fitting functions to the spectral points using the fitting programme MINUIT [Ja75].

Two estimates of χ_{min} at the surface were thus obtained: the yield χ_0 just behind the surface peak (similar to the χ_0 of §5.2.3, and corresponding to $z \sim 0.1$ um) and the yield χ_s extrapolated to zero depth. For accurate comparison with theory, χ_s was used.

Several workers [Bar71, Bo72, Ab72, Vae73] have reported depth oscillations of the minimum yield just behind the surface peak. They are attributed to ions deflected into the random beam close to the surface by strongly forward-peaked scattering off planes or rows; these ions must cross the channel space before they can interact again, during which time they penetrate a distance s. Van der Weg et al [Vae73] have shown that for planes

$$s \sim d_p/(1.5\psi_c) \qquad (9.1)$$

Putting $d_p \sim 1$ Å and $\psi_c \sim 0.1°$ for diamond planes gives

$$s \sim 400 \text{ Å}$$

The analysis is more complex for rows, but s is expected to be somewhat smaller. The detector resolution in the present experiments corresponded

to ∿800 Å in depth resolution; thus any depth oscillations would be smeared out, and indeed none was seen.

9.3 THE SURFACE PEAK

From the number of counts P in the surface peak, the number of atoms per unit area N_A contributing to it was calculated in each case using Eqn 2.15. For these experiments the equation became

$$N_A = Px(1.7x10^{14})\cos\theta \qquad (9.2)$$

The expected values of N_A were calculated from Barrett's suggested formula for the effective number of surface layers L (Eqn 2.12) combined with the known atomic density N_V and string spacings d:

$$N_A = LN_V d\cos\theta \qquad (9.3)$$

The measured values of N_A were generally at least twice the expected values; moreover, they showed a correlation with total proton dose, indicating that either surface radiation damage or amorphous carbon deposition were occurring. A plot of P versus approximate dose D (with due allowance for different incidence angles) is shown in Figure 9.1, for two good diamonds at different temperatures. The dashed line suggests the trend of the correlation.

A closer examination of Figure 9.1 indicates some segregation of the points according to temperature. It was assumed that the relation might be of the form

$$P = bD + c \qquad (9.4)$$

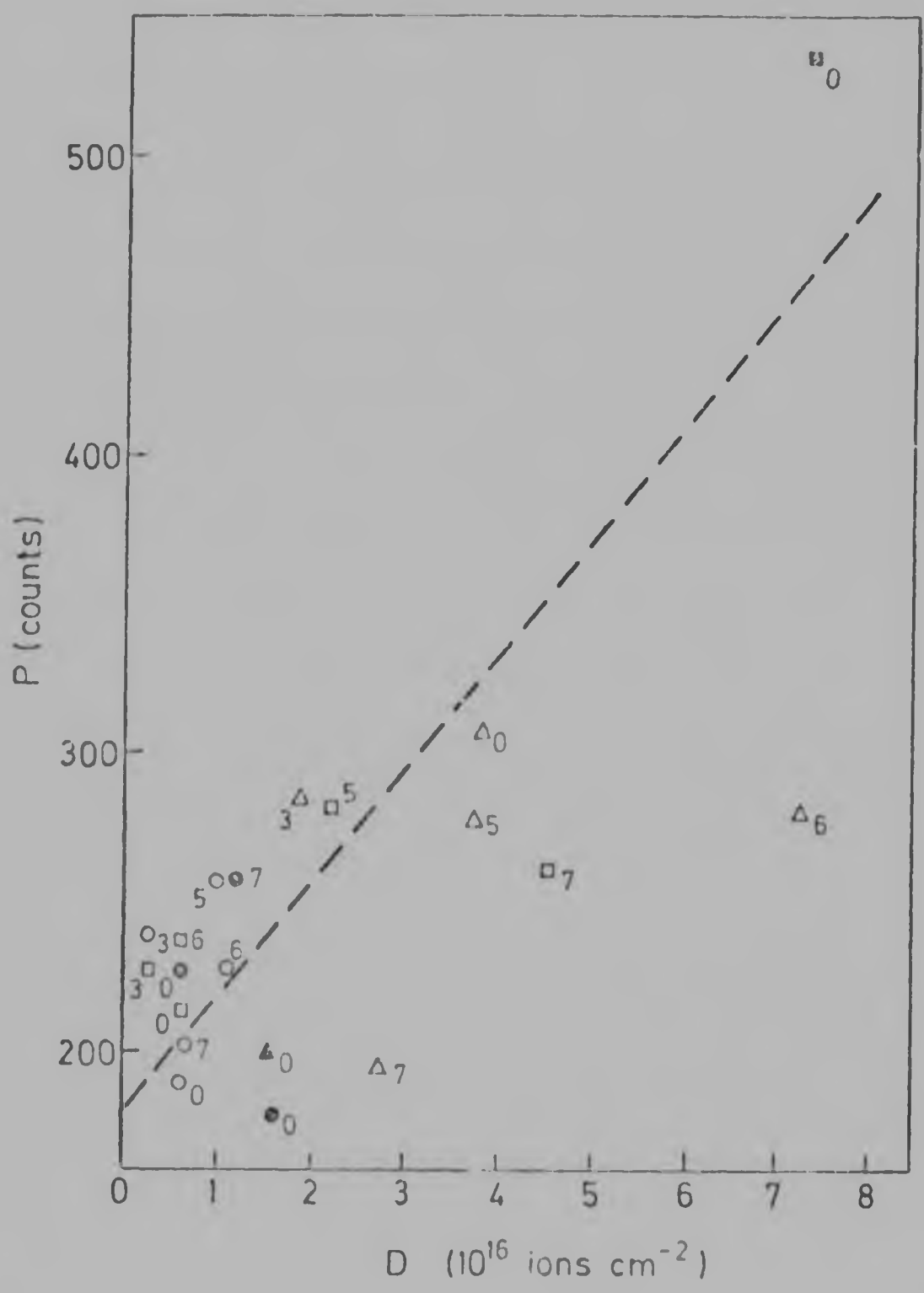

Figure 9.1: Integrated surface peak as a function of proton dose.
o <110>; Δ <111>; □ <100> (KT1);
● <110>; ▲ <111>; ■ <100> (Di3);
numbers are temperatures in units of 100°C.

where b is temperature dependent, and c = 180±20 in the units used. A plot of b = (P-c)/D is shown in Figure 9.2, with c = 180; the trend is again suggested by a dashed line. The fastest increase in the surface peak is at intermediate temperatures, which would not be expected for either radiation damage or beam-stimulated adsorption. It is surmised that direct baking-on of the hydrocarbon turbomolecular oil had occurred at these temperatures, with a burning-off process at higher temperatures.

Conversion of the number of atoms/cm² to the number of extra atomic layers is complicated by the fact that the density of the amorphous layer is unknown. Taking the density of graphite as an estimate gives about 10 - 20 amorphous surface layers in most cases (corresponding to the bottom third of Figure 9.1).

The value of c represents the number of counts in the surface peak due to the crystal alone; putting P - c = 180±20 into Eqns 9.2 and 9.3 gives an effective number of surface atoms per row

$$L = 6 \pm 1$$

(using an average value of 3 Å for the row spacings). The expected number according to Eqn 2.12 is

$$L = \sqrt{1 + \quad} = 4 \text{ to } 6$$

depending on temperature. The agreement is quite good, indicating that the crystal remains perfect almost to the surface, with the possibility of one or two disordered layers.

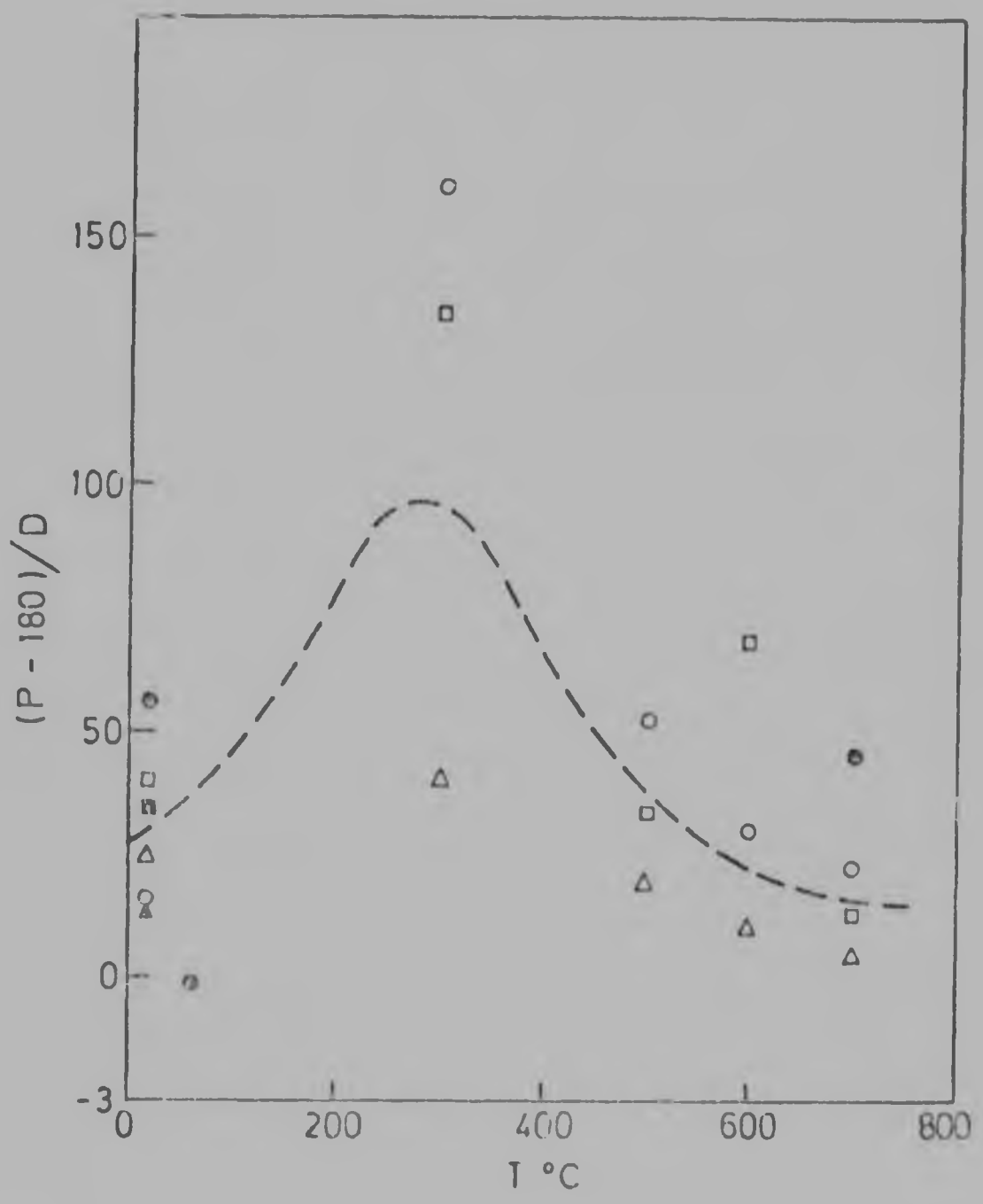

Figure 9.2: Rate of increase of surface peak versus temperature.
o <110>; Δ <111>; □ 100> (KT1);
• <110>; ▲ <111>; ■ 100> (Di3).

9.4 THE MINIMUM YIELD

9.4.1 Data Analysis

The observations of the previous section indicated that it would not be possible to extract the relative contributions to χ_{min} and P from amorphous layers and from the underlying crystal as suggested by Barrett [Bar71] nor to check his equations (listed in §2.3.2 as Eqns 2.10 to 2.13) by varying the energy and temperature, since the deposition amounted to random additions to the data, and the expected effects were much smaller. Instead, the equations were assumed to be valid for diamond, so that they could be used to correct χ_{min} for the effect of the amorphous layer. It will be shown that this correction is small, so that the exactness of the equations for diamond will negligibly affect the results.

Consider Eqn 2.10:

$$\chi_{min} = \chi_1 + \chi_2 + \chi_3$$

$$= N_V d\pi (Cu_1 + C' a_{TF}^2) \cdot \overline{1 + \xi^2} + \chi_3$$

with the symbols as defined in Chapter 2. As pointed out in §2.3.4, it is of some interest to see whether the values which Barrett assigned to C and C' still apply in the case of diamond.

Values for $\overline{1 + \xi^2}$ were calculated for the energies, temperatures, and axes to be used; they range from 1.01 to 1.04. It is therefore a good approximation and a considerable simplification to take this factor as 1.00 throughout.

Values for χ_3, the term due to surface amorphous layers, may be estimated in two ways:

i) By Eqn 2.13, which will be taken in the form

$$\chi_3 = N_A \pi \left(\frac{Z_1 Z_2 e^2}{E w_{\frac{1}{2}}} \right)^2 \sec\theta \qquad (9.5)$$

with N_A determined from P by Eqn 9.2.

ii) From work on the effects of evaporated surface layers on diamond [Lea75], which determined the value of f in

$$\chi_3 = P/\Delta S \times f \times (w_{\frac{1}{2}})^{-2} \qquad (9.6)$$

for the particular experimental conditions used.

Methods (i) and (ii) gave the same result to ~3%: a presumably fortuitous agreement, since Eqn 9.5 was not intended to be exact. Method (ii) was chosen, using Eqn 9.6 with

$$f = 6.0 \times 10^{-7} \text{ rad}^2.$$

In these equations it is necessary to correct P for those counts attributable to the crystal surface; one must use

$$P_{amorph} = P - P_{crys} \qquad (9.7)$$

where P_{crys} is calculated by substituting Eqn 2.12 into Eqn 9.3 and the result into Eqn 9.2.

TABLE 9.1

Temperature Dependence of Axial Minimum Yields

Temp [°C]	u_1 (Å)	$u_2^2 = 2u_1^2$ ($Å^2 \times 10^{-3}$)	Axis	d (Å)	χ_{min} (%)	χ_3 [calc] (%)	$\frac{\chi_{min} - \chi_3}{d}$
20	0.044	3.9	<110> <111> <100>	2.522 3.089 3.567	2.0 2.8 3.4	0.1 0.2 0.1	0.8 0.7 0.9
300	0.051	5.2	<110> <111> <100>	2.522 3.089 3.567	2.9 3.4 4.9	0.1 0.1 0.1	1.1 1.1 1.3
500	0.056	6.3	<110> <111> <100>	2.522 3.089 3.567	3.2 4.1 5.5	0.1 0.1 0.1	1.2 1.3 1.5
600	0.058	6.7	<110> <111> <100>	2.522 3.089 3.567	2.7 4.6 5.2	0.1 0.1 0.0	1.0 1.5 1.5
700	0.061	7.4	<110> <111> <100>	2.522 3.089 3.567	4.1 4.5 4.9	0.0 0.0 0.1	1.6 1.5 1.3

The value of χ_3 thus obtained is ~0.001 (0.1%) in most cases. (Without the crystal surface correction it would be ~0.002.) This is a small term compared with the expected values of χ_1 and χ_2 of ~0.01 each.

Data analysis proceeded as follows. The connection between χ_3 and P was used to subtract off χ_3 from χ_{min} and thus eliminate the variable effect of surface layers. Eqn 2.10 had now become

$$(\chi_{min} - \chi_3) = N_V d\pi(Cu_2^2 + C'a_{TF}^2) \qquad (9.8)$$

It could therefore be divided through by d, to scale the results for all axes on to one graph. (The validity of this is checked in §9.4.3.) The values of $(\chi_{min} - \chi_3)/d$ were plotted against u_2^2, enabling C to be determined from the slope (= $N_V\pi C$) and C' from the intercept (= $N_V\pi C'a_{TF}^2$).

9.4.2 Temperature Dependence

Raw data are presented in Table 9.1, and $(\chi_{min} - \chi_3)/d$ is plotted against u_2^2 in Figure 9.7. Although there is considerable scatter, the trend is clear, with no systematic deviations for any of the three axes. The line drawn through the points is a least-squares regression. The values of the two constants are (with those of Barrett [Bar71] in brackets):

$$C = 3.2 \pm 0.6 \qquad (3.0 \pm 0.2)$$

$$C' = 0.05 \pm 0.05 \qquad (0.2 \pm 0.1)$$

These results are quite interesting. The value of C is very similar to Barrett's, while C' is rather less, and may even be zero.

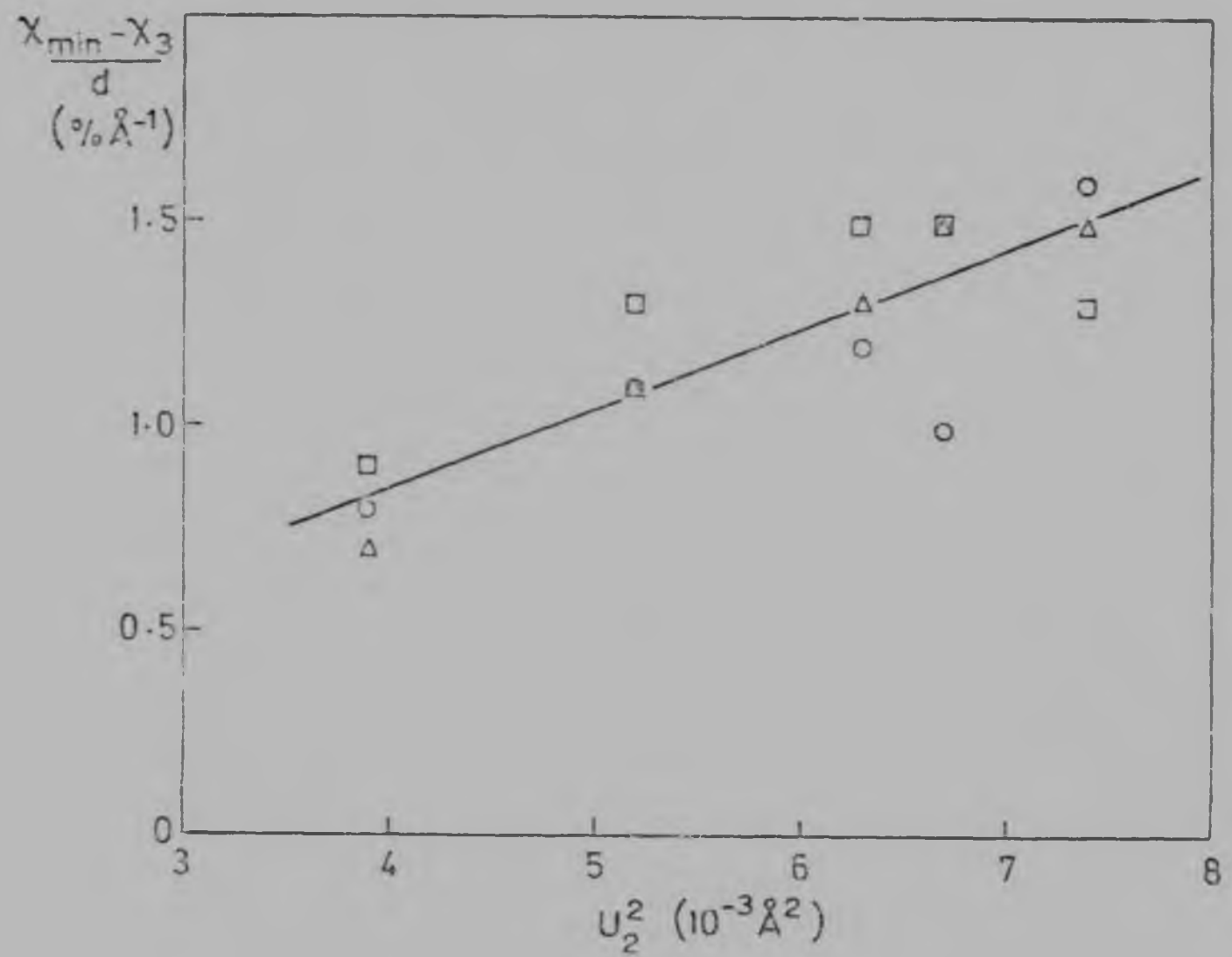

Figure 9.3: Graph giving temperature dependence of axial minimum yield (see 59.4.1). (KT1).

o <110>; Δ <111>; □ <100>;

The errors in this small number are large, but it is almost certain that $C' < 0.1$.

Similar values have been obtained by, for example, Komaki et al [Kom71] with protons in silicon. It is of particular interest that even in diamond, where the thermal vibration amplitudes are much smaller in comparison with a_{TF}, so that χ_1 does not dominate so completely over χ_2 as it does in other solids, the thermal term χ_1 plays the major rôle in determining minimum yield; the 'atomic size' term χ_2 is of little importance.

This appears to be in agreement with the critical approach distance r_c being determined by u_1 rather than a_{TF}, as was emphasised in 8.3.1, since χ_{min} can be regarded as being determined by the size of the forbidden regions surrounding the atomic strings, and written in terms of a function r_c:

$$\chi_{min} = N_V d\pi r_c^2 \qquad (9.9a)$$

where

$$r_c^2 = Cu_1^2 + C'a_{TF}^2 \qquad (9.9b)$$

However, this is not the same r_c as the one which determines $\psi_{1/2}$, as may be verified by a numerical comparison with Table 7.11. In fact, Barrett has shown [Bar71] that the simple geometrical model for χ_{min} is incorrect, and that a significant contribution to χ_{min} comes from those trajectories which do not have sufficient transverse energy to approach the rows. Such trajectories still have a finite nuclear encounter

probability, and are very numerous. The temperature dependence of χ_{min}, and its dominance, come from the temperature dependence of the density-of-trajectories function defined in Bar71 and derived from the potential for a vibrating row. Thus ρ_c as defined by Eqns 9.9 does not have a direct geometrical interpretation, and the results confirm rather that Barrett's findings apply also in the case where u_1 is small. The same conclusion about ρ_c has been deduced from experimental evidence [Alt70].

9.4.3 Row-spacing Dependence

It is clear from §9.4.1 that χ_1 is almost negligible compared with χ_2 and therefore that χ_{min} ought to be quite accurately proportional to d. Some Phase I 0.6 MeV proton data, which were not corrected for χ_1 but which include higher axes up to <111>, are appropriately plotted in Figure 9.4; the linearity of χ_{min} (represented in this case by χ_2) with d is quite accurate.

It may be noted that the slope is about three times larger than the value of $N_V\pi(Cu_1^2 + C'a_{TF}^2)$ calculated from the results in the previous section. This is because the Phase I values of χ_2 were averaged over a relatively large depth using a single channel analyser.

9.4.4 Planar Minimum Yields

No general relationship analagous to Eqn 2.10 has been found for the minimum yields in planar channelling, other than Lindhard's rough estimate, Eqn 2.9':

$$\chi_{min} \sim 2u_{TF}/d_p$$

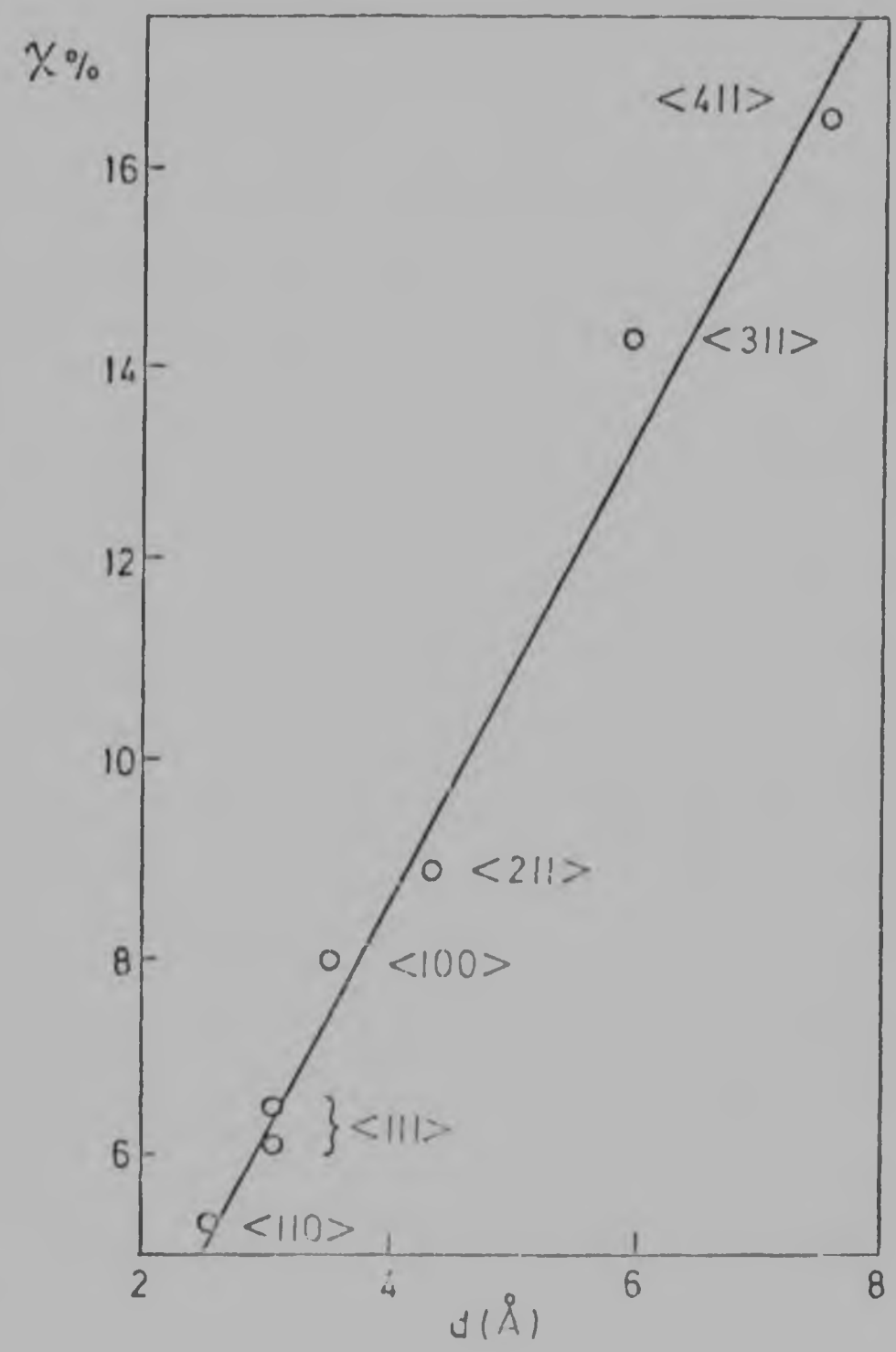

Figure 9.4: Dependence of axial minimum yield on the string spacing. (Di4).

Various modifications to this have been suggested, and are considered later.

For the {111} planes, it was proposed in §7.5.3 that channelling within the narrower of the two spacings is unlikely, and that ions incident therein are probably fed quite rapidly into the random beam. This modifies Eqn 2.9' to read (see Figures 7.31 and 7.32):

$$\chi_{min} = \frac{2\,(\frac{1}{2}d_1 + a_{TF})}{d_2 + 2(\frac{1}{2})d_1}$$

$$= \frac{d_1 + 2a_{TF}}{2d_p}$$

It happens that d_1 (= 0.515 Å) is almost exactly equal to $2a_{TF}$ (= 0.516 Å) giving $\chi_{min} = 2a_{TF}/d_p$ as before. Thus the unequal {111} planar spacing does not reveal itself in the minimum yield in the case of diamond.

Some typical measured values of χ_{min} are compared with $2a_{TF}/d_p$ in Table 9.2; the agreement is reasonable. The dependence on d_p^{-1} is quite accurately followed. It is noteworthy that the measured values are lower than the calculated ones, and not higher as is usually found for other substances (for example, see Dav68).

Morgan and Van Vliet [Mo70] suggested replacing a_{TF} in Eqn 2.9' by a critical approach distance which was to be determined by the procedure outlined in §2.2.1; in Mo71 they included an empirical modifying factor for a vibrating lattice. But as pointed out in §2.2.4, the necessary approximations break down for diamond. Barrett's

TABLE 9.2

Minimum Yields for Diamond Planes

1.0 MeV protons on Di18

Plane	d_p (Å)	$(2a_{TF}/d_p) \times 100$	χ_{min} (%)	$\chi_{min}\, d_p$
{110}	1.261	41	34	43
{111}	1.030	50	41	42
{100}	0.892	59	49	44

Monte Carlo simulations [Bar71] produced a linear dependence of χ_{min} on u_1, with a non-zero intercept, in the planar case. Roosendal et al [Roo74] obtained a good fit to their silicon measurements using

$$\chi_{min} = 2d_p/(u_1 + a_{TF})$$

although they obtained a less accurate fit to the data of Davies et al [Dav68] for Si, W and Au.

The present measurements showed a small dependence on temperature: the total change in χ_{min} between 20°C and 700°C, of ~3 percentage points, was slightly greater than the experimental error. Assuming a relationship of the form

$$\chi_{min} = 2/d_p(Bu_1 + B'a_{TF}) \qquad (9.10)$$

the data were analysed in a similar manner to those for axes (§9.4.^); a linear regression produced the value of B and B' included in Table 9.3, together with those of other workers. (There is an energy dependence, but this is small [Bar71].) The values are in rough agreement but probably depend on the nature of the crystal. It is

TABLE 9.3

Values of B and B' (see Text)

Reference	Crystal	B	B'
This work	C	∿1.0	∿0.6
Roo74	Si	1.0*	1.0
Bar71	W	2.2	0.6

*A greater value produces better agreement with the data of Lav[illegible]

evident that the contribution of thermal vibrations is not negligible, and that Eqn 2.9' is not a very good approximation. The observation that this formula usually underestimates χ_{min} except for diamond, is explained if the apparent trend that B > B', observed in Table 9.3, is true for most substances.

9.4.5 Comparison with Other Measurements

Values for the minimum yield χ_s just behind the surface peak in the <110> axis of diamond have been reported by Piceaux et al [Pic69a] and by Sellschop and Gibson [Se73]. They obtained somewhat different values for different ions and energies, most likely due to statistics or to different surface-peak widths. Their lowest measurements (for 1.0 MeV protons in both cases) are compared with the lowest value typical of the present work in Table 9.4. The theoretical estimates were calculated from Eqn 9.8 using Barrett's values of C and C' ('Theory (1)') and using the values of C and C' obtained in 9.4.2 ('Theory (2)').

TABLE 9.4

Comparison of Diamond Minimum Yields
χ_s Measured by Different Workers

Measured for 1.0 MeV protons in <110>. Values are in %.

This Work	Ref Pic69a	Ref Se73	Theory (1)	Theory (2)
1.9 ± 0.1	4	2.1	3.5	2.2

The second theoretical estimate, the present measurements, and that of Ref Se73, are all in good agreement. The first theoretical value is too high, emphasising the need to use a smaller C'. The measurement of Ref Pic69a is high, typical of a diamond to which the improvement techniques described in Section 5.1 have not been applied (see Table 5.6).

9.5 NATURE OF THE SURFACE

The nature of the diamond surface continues to be a problem; recent reviews are Th75 and Ta75. A simple truncation of the diamond structure at the surface results in 'dangling bonds'; these seem unlikely to exist, and in fact electron spin resonance experiments (for example, Sap68a) show that the density of unpaired electrons on diamond surfaces is very low. There are two obvious possibilities:

i) The surface may reconstruct, involving re-hybridisation of the bonding orbitals of the surface carbon atoms and migration of surface interstitials to produce a self-terminating structure, different from that of the bulk.

ii) The 'dangling bonds' may be satisfied by a layer of foreign atoms.

There is evidence for both mechanisms in LEED studies [Man64, Lan66, Lur76, Lur77], and in the work of Sappok and Boehm [Sap68a, Sap68b]. The latter workers applied a number of chemistry techiques, such as the measurement of heats of hydration, electron spin resonance, infrared spectrometry, qualitative microanalysis, and organic functional group analysis, to fine diamond powders, and were able not only to conclude that clean diamond surfaces can adsorb hydrogen and oxygen (and certain other gases), but also to identify the functional groups formed: chiefly $\rightarrow$CH, $>$CH$_2$, $-$C$=$O, $-$COOH, and $\rightarrow$C$-$O$-$C$\leftarrow$. Other evidence is reviewed in Th75 and Ta75.

The results are not completely consistent, and there are probably

as yet uncontrolled influences, such as surface topography [Lur77]. In this connection it is worth remembering, when experiments have been performed on polished surfaces of, say, nominally {110} or {100} orientation, that micro-facets of {111} orientation may also be present (see below).

The present work was not designed specifically to study diamond surfaces, and lacks the depth resolution of true surface techniques, so that any conclusions on this subject are bound to be less truly surface-specific. However, evidence accumulated during these investigations sheds some light on the problems outlined above.

It appears likely that the 'dangling bonds' can be eliminated either by surface reconstruction or by impurity atoms, the two modes having a certain stability with respect to one another since heating is necessary to promote a transition [Sap a]. Natural diamond surfaces are expected to be terminated by a layer of impurity atoms (the species depending on the environment in which the diamond has resided), and this was seen in the experiments described in §5.3.1. These atoms were found to be difficult to remove, suggestive of chemisorption rather than physisorption; accidentally-introduced silicon, which has the same electronic structure as carbon, was even more tenacious, and must have displaced other species to bond directly to the carbon. On cleaning in stages, the 'earthy' impurities were lost first, then the silicon (Figure 7.3). (The silicon was always associated with three times the number of atoms of oxygen, implying a group containing an SiO_3 grouping.)

Surface impurities could be removed by vigorous chemical action (§5.3.2), but some oxygen always remained as a surface layer (that is, as a peak in the spectrum of backscattered α-particles). The surface density of the oxygen atoms was calculated from the area under the peak, using Eqn 2.15, for a number of {111} surfaces, and compared with the theoretical density assuming one oxygen atom per 'dangling bond': for freshly cleaned surfaces the density corresponded to 1.2±0.1 monolayers. Some beam-stimulated deposition and the lack of a background subtraction would explain the slight excess of this figure over 1.0.

Since the cleaning was carried out in aqueous solution (which was also strongly alkaline), it is speculated that atoms on 'dangling bonds' were replaced by hydroxyl (-OH) groups. Little evidence for such groups was found by Sappok and Boehm [Sap68b], but their surface treatments were not in aqueous media. Hydrogen is not revealed by backscattering, but recent work by Sellschop et al [Sel77] using nuclear reactions, on diamonds cleaned by the same process, has shown a surface concentration of hydrogen, also equivalent to about a monolayer.

Other processes of preparing the surface would be expected to saturate the 'dangling bonds' by different species: for example, single hydrogen atoms (that is, C-H groups) in the case of polishing, which is carried out in oily medium. This was assumed by Lurie and Wilson [Lur76, Lur77] to explain their results on polished samples: LEED patterns characteristic of the bulk, with no impurities detectable by Auger electron spectroscopy (which is blind to hydrogen). On heating, the hydrogen was apparently lost, and the surface reconstructed.

An oxygen layer was also observed by Davidson et al [Das71], after an aqueous cleaning procedure, and identified as a monolayer. However, their calculation is in error by a factor of three, and two-thirds of this oxygen must have been due to beam-induced deposition.

The polishing behaviour of diamond has been successfully explained by experimenters at Oxford University (see for example, Wi72, Cas72, Cas73, Thr76) using a model based on one first put forward by Tolkowsky [To20]. It assumes that polishing proceeds by brittle fracture chiefly along the easy {111} cleavage planes and the tearing off of small particles bounded by irregular {111} faces. This would result in very little damage being propagated into the bulk, and would explain why good channelling was obtained with polished samples (§5.4.3) - in sharp contrast to metals and even the diamond-structure semiconductors such as silicon, in which abrasive polishing is accompanied by considerable plastic flow.

A polished surface would, however, be expected to be intersected by a network of {111}-orientated micro-cracks, representing the incipient stage of the polishing process, and so would be somewhat strained. The improvement of channelling minimum yields which was always observed after polished samples were annealed (§5.4.4) is explained by the healing of these cracks. A network of micro-cracks was also postulated by Vanderkande [Vad73, Vad76] to explain his thermal conductivity results from polished samples.

The channelling observations are also in accord with a

thermally-activated chemical mechanism of diamond polishing, proposed by Seal [Sea58, Sea66]. However, a chemical process ought to leave no damage at all under the surface, and no improvement would be expected on annealing.

Channelled minimum yields at natural diamond surfaces were also improved by annealing (§5.1.1); it is likely that diamonds accumulate mechanical damage during their history. After annealing and cleaning, the size of the surface peak (extrapolated to zero beam-induced deposition) corresponded to an 'effective number of surface layers' (6±1) close to that (5·1) theoretically calculated for a perfect crystal (Section 9.3), indicating that the structure became almost perfect at the surface.

CHAPTER 10

RADIATION DAMAGE

10.1 INTRODUCTION

In the earliest Phase I investigations of diamond with α-particles, radiation damage effects manifested themselves as a progressive increase of the channelled spectrum height with dose. Systematic investigations of radiation damage were therefore undertaken to determine corrections to the channelling data, or to establish whether damage could be made negligible. As some interesting effects appeared, the investigations were pursued somewhat further.

All radiation damage in these studies was induced by 1.0 MeV He^+ ion bombardment, and analysed by channelled α-particles or protons. No systematic investigation of proton damage was undertaken, since no evidence for it was ever seen in the longest runs employed.

A note of warning has rightly been sounded by Quéré [Qu76] against using the channelling effect too naively to extract radiation damage in the form of 'number of displaced atoms' by the method of Bøgh (Section 2.5). Bøgh's analysis was for randomly disordered or amorphous regions of a crystal, whereas in a typical experiment, interstitials, vacancies, voids, dislocation loops, etc might also be formed, all having different dechannelling cross sections and rendering such an

analysis meaningless. At best, it gives a useful indication of the amount of damage, rather than a quantitative measure of the numbe[r] of disordered atoms, unless these are all known to be in amorphous r[e]gions.

In Section 10.2 a simple determination of the relationship between minimum yield and ion dose is described, leading to a limit on the maximum dose tolerable if damage effects were to be negligible. (The influence on critical angle was expected to be less marked, and to occur chiefly via the increased depth of the channelling dip.) Attempts to elucidate the nature of the damage are described in Sections 10.3 (annealing behaviour) and 10.4 (energy dependence), and extractions of the damage profiles are given in Section 10.5. The conclusions are summarised in Section 10.6.

The most remarkable feature of the damage data was its inconsistency. The dechannelling versus dose curves were not accurately repeatable, nor was the annealing behaviour: reverse annealing sometimes occurred. This is regarded as strong evidence for the migration and clustering of point defects (mentioned in Qu76), and for the interaction between them and defects or impurities already present in the crystal in variable amounts. A proper study of light-ion damage in diamond would evidently have to be researched at least as carefully as the channelling studies of undamaged diamond in order to produce consistent results.

Several studies of radiation damage in diamond due to ion bombardment have already been reported; they are reviewed and referenced

in Bou75 (together with neutron and electron irradiation studies). However, all were performed with low-energy heavy ions (for example, 40 keV Ar^+) and the results are not necessarily expected to be closely similar to those of the present work, since a heavy ion on stopping deposits a greater amount of energy into atomic motion, in a smaller volume, than does a 1 MeV He^+ ion. The heavy-ion results could at best be used as a guide, as could similar results for silicon and germanium.

Vavilov and co-workers [Vav74] traced the progress of 40 keV argon-ion damage in diamond using high-energy electron diffraction. Initially, plate-like clusters of displaced atoms were formed; after heavier fluences the crystal broke up into ~1000 Å mosaic blocks and twins orientated parallel to the {111} plane of the specimen, accompanied by some general amorphisation. Finally, complete amorphisation and graphitisation occurred. It may be noted that the fluence ($\sim 10^{15}$ Ar^+ cm^{-2}) was then about two orders of magnitude less than the α-particle fluence needed to render diamond amorphous in the experiments described in Section 10.3. Despite this and the differences in projectile and analysis method, the occurrence of similar processes will be deduced.

The experiments to be described are best regarded as an excursion along an uncompleted line of research. No studies of light ion damage in diamond appear to have been reported hitherto, and this study, although perhaps representative only of particular specimens and conditions, indicates the results which may be anticipated in a fuller investigation.

10.2 EFFECT ON MINIMUM YIELD

10.2.1 Method

To determine the magnitude of damage effects in a typical alpha-channelling experiment, long damage runs were alternated with short analysis runs, both using 1.0 MeV He^+ ions on the same crystal spot. During the analysis runs, <110> channelled spectra were recorded. The damage runs were five times as long as the analysis runs, in either 'random' or <110> orientations.

10.2.2 Results

The minimum yield measured just under the surface (χ_s) is plotted against total alpha-particle fluence D in Figure 10.1, for three different experiments on two stones. It may be noted that the doses involved are heavy: about 3×10^{16} ions cm^{-2} are enough to render the crystal completely amorphous at the end of their range (according to the experiments described in Section 10.4).

A good linear relationship between χ_s and D is revealed (except for an initial region), with the slope for damage in a <110> direction of Di6 being about one-third of that for damage in a random direction on the same stone. This is in agreement with expectations since at these shallow depths the α-beam is well-channelled and little damage would be expected. However, when damaging KT2 in a random direction, the straight line coincides closely with that for Di6 <110> rather than Di6 (random), except for one point (arrowed) which lies on the Di6 (random) line. This one point does not appear to result from error. It may be that there are two different regimes of damage, depending for example on its

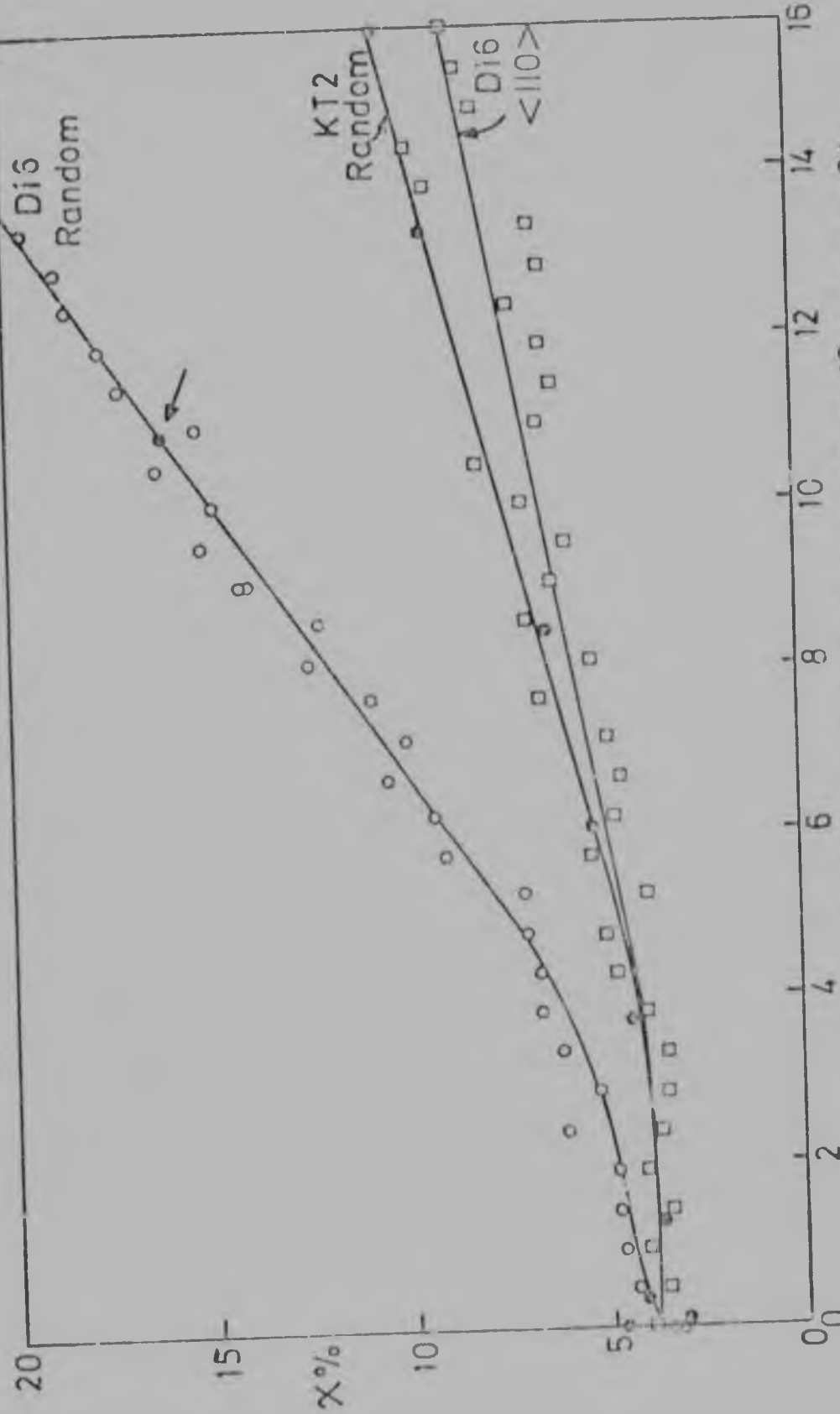

Figure 10.1: Dependence of near-surface minimum yield of scattered 1.0 MeV He^+ ions on ion fluence.

rate of production relative to the rate of migration of interstitials (KT2 had about three times the average beam current density of Di6, but a swept beam was used - see §10.3.2).

The most valuable conclusion from these graphs is that damage effects near the surface only become apparent at a dose of $\sim 3 \times 10^{16}$ ions cm^{-2} (corresponding to the dose for deep amorphisation). It was not difficult to keep below this limit in typical experiments (see Section 6.7).

10.3 ANNEALING

10.3.1 Experimental

The range of 1.0 MeV He^+ ions in carbon is 1.5 μm; the greatest depth from which 1.0 MeV protons can be backscattered out of the crystal is greater, ~2.5 μm, so that by using a proton beam for analysis the entire damaged volume could be investigated at the same energy as was used for the damaging beam. Most of the damage caused by a fast ion is at the end of its range, where nuclear stopping comes into operation, and the alpha-damage shows up in the channelled proton spectra as a peak rising towards the random spectral level, centred on an energy corresponding to a depth of 1.5 μm (Figure 10.2). The peak is due both to dechannelling by disordered regions, and to direct backscattering by atoms not on lattice sites. At greater depths (lower energies) the spectrum does not drop back to the perfect-crystal level owing to the accumulated dechannelling which has already occurred

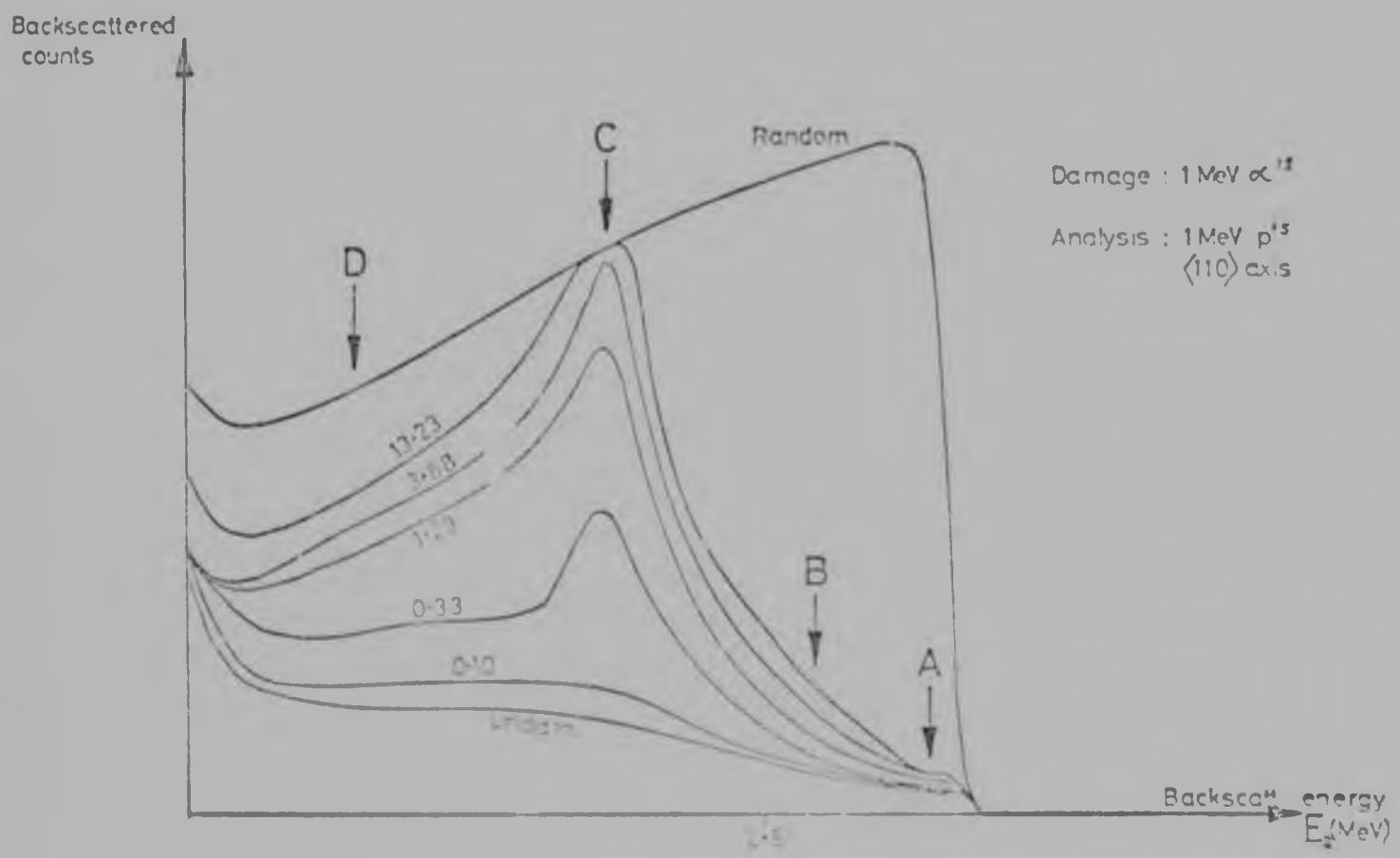

Figure 10.2: Examples of 1.0 MeV proton spectra for <111> incidence on a crystal damaged by 1.0 MeV He^+ ions. Fluences marked in units of 10^{15} ions cm^{-2}. (KT2).

For these experiments, a uniform lateral damage distribution was ensured over an area greater than that of the analysing beam-spot (0.7 mm diameter at normal incidence, spreading to 1.3 mm long at the largest values of θ) by electrostatically scanning the alpha-beam in a raster over the crystal surface, through an oversize collimator (2.0 mm diameter).

Annealing was carried out in (usually isochronal) stages, typically of 20 minutes duration at 100° intervals, up to 700°C, after various total ion bombardments.

10.3.2 Results

The results of annealing were not always consistent, as pointed out in Section 10.1, but some general features could be established.

No annealing of the damage peak was observed after the heaviest bombardments ($\sim 10^{17}$ ions cm^{-2}), even on prolonged heating. After smaller doses ($\sim 10^{15}$ ions cm^{-2}) about a 50% recovery was observed; that is, the peak dropped to midway between the damaged and undamaged levels. The lightly-damaged region between the crystal surface and the damage layer always showed a similar recovery, (50 ± 10) %. Bearing in mind Quéré's warning [Qu76], the reduction in 'disorder' can be taken roughly as ~50%.

It was quite surprising to observe any recovery at all, as the damage was expected to consist of bulk amorphous regions at the end of the range of each ion or knock-on (see Pa65 and references therein) and

these were not annealed to re-crystallize in favour of the prevailing temperature and pressure. One may therefore conclude that about 50% of the displaced atoms are on the fringes of the amorphous zones, surrounded by sufficiently perfect crystal for annealing to be energetically feasible.

This model enables an estimate of the sizes of the zones to be obtained. It will be assumed that they are roughly spherical and that the disorder falls effectively to zero within a few interatomic spacings, say ~10 Å (the length of the carbon-carbon bond in diamond is 1.544 Å). Then for the volume of an amorphous sphere of diameter τ to be equal that of sphere plus semi-damaged halo,

$$\pi/6\tau^3 = \tfrac{1}{2}[\pi/6(\tau + 2\times10)^3]$$

giving approximately,

$$\tau \sim 60 \text{ Å}.$$

This should be an overestimate since it neglects isolated interstitials, and because of the original assumptions.

Another estimate for the size of these zones may be obtained from the failure of the heavily damaged region to anneal at large doses - presumably because the amorphous zones had overlapped to form a single amorphous layer. The critical dose will be taken as $\sim 3\times10^{14}$ ions cm^{-2}, which is also the dose at which the spectral peak was observed to reach the random level. The thickness of the damage layer was determined from the spectra as ~0.6 μm. Then the number of α-particles stopped in unit

volume of the crystal is

$$\frac{3 \times 10^{16}}{1 \times 0.6 \times 10^{-4}} \text{ cm}^3$$

and the volume per damage zone is the reciprocal of this, thus

$$r \sim \sqrt[3]{2 \times 10^{-21}}$$

$$\sim 10 \text{ Å}.$$

This is an underestimate since superinposition of the damage regions has been neglected.

Considering the crudity of the assumptions, the two values agree quite well. This lends confidence in the model of the damage consisting of individual amorphous zones. Amorphous clusters of this size have been observed by transmission electron microscopy in silicon damaged by Ne^+ ions (~50 Å diameter) [Naz68] and germanium damaged by Ar^+ ions (70 - 90 Å diameter) [Pat5].

However, calculations based on the accepted nuclear stopping theories (for example, Lindhard) indicated that α-particles would produce atomic displacements in diamond over a much greater range, ~1000 Å. This implies that aggregation into smaller amorphous clusters must have occurred after damaging, presumably by the motion of interstitials. Similar conclusions were reached by Vandersande [Vad75] from the results of thermal conductivity experiments on diamond after electron irradiation (which produces a different initial distribution of atomic displacements): that the interstitials are mobile and form aggregates of ~100 - 200 Å

diameter at room temperature, or ~55 Å diameter after annealing to 1100°C.

Finally, an estimate of the number of disordered atoms per incident ion may be obtained from the estimated volume of a damage cluster. The number of atoms per unit volume is

$$\frac{\text{density} \times \text{Avagadro's number}}{\text{atomic mass}}$$

and multiplying these two quantities together gives

$$\text{disordered atoms per ion} \sim [2 \times 10^{-21}] \times [3.52 \times 6.023 \times 10^{23}/12.01]$$
$$\sim 3 \times 10^{2}.$$

This agrees with a more accurate estimate which will be obtained subsequently (§10.5.2).

No sharply defined annealing stage was observed: if annealing occurred at all, the spectral height decreased progressively as the temperature was raised (Figure 10.3). Apparent steps are thought to be due to counting statistics or slight crystal misalignments, as they are within experimental error and are not reflected in both the damage and sub-damage regions (defined in §10.4.2). The lack of well-defined annealing thresholds implies that no very specific types of defects, with well-defined activation energies, were annealing out, but that the damage consisted largely of rather general amorphisation and semi-crystalline regions; such damage would also control the rate of annealing by motion of interstitials through the lattice.

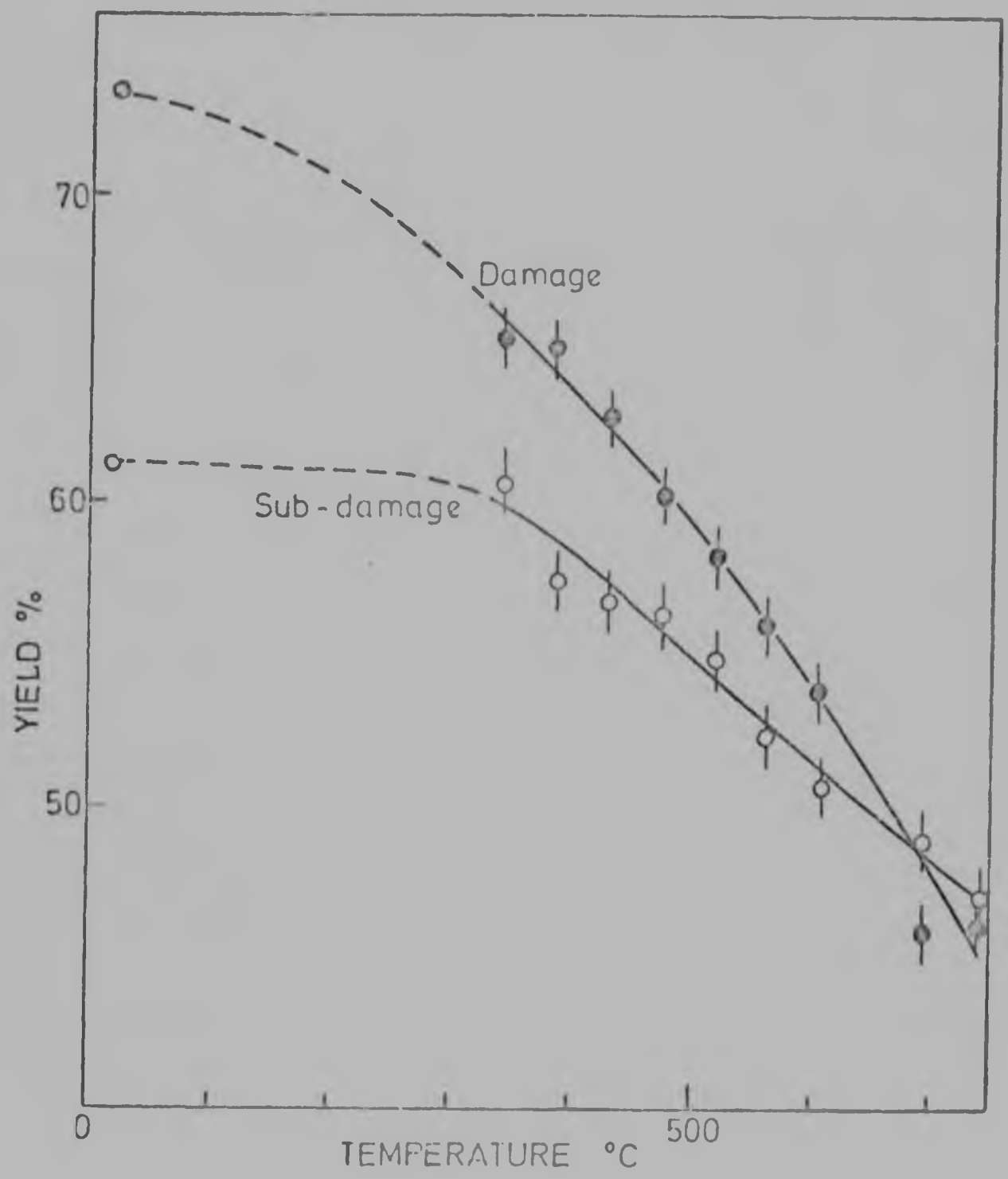

Figure 10.3: Annealing of alpha-damaged diamond monitored by changes in the minimum yield. The damage and sub-damage depths are defined in Table 10.1 with Figure 10.2.

Damage dose = 1.29×10^{16} cm^{-2}

The upper limit of the apparatus for in situ annealing was about 750°C. Annealing to higher temperatures would have been desirable, since complete restoration of crystalline order in ion-bombarded diamond has been reported after annealing at 950°C [Das71].

10.4 ENERGY DEPENDENCE

10.4.1 General

It has been pointed out [Bro73] that the dechannelling cross-sections for small defects (interstitials and clusters) should be proportional to E^{-1}, and for extended defects (such as dislocations) to $E^{-\frac{1}{2}}$ [Qu68a, Qu68b, Moy72]. Energy dependences of $E^{-\frac{1}{2}}$ for proton interstitials [Jou74] and E^{0} for stacking-faults [Moy72] and voids [Ron75] have also been calculated. Proton spectra were therefore obtained at different energies in order to elucidate the nature of the damage.

10.4.2 Experimental

The usable energy range for these experiments was limited by resonances at its lower and upper bounds. Data were taken between 0.75 and 4.50 MeV, using both accelerators. The damage was always by 1.0 MeV He^{+} ions, using a scanned beam, in a random direction near <111>. Light doses were used, up to 1.3×10^{15} ions cm^{-2}.

Channelled minimum yields were plotted logarithmically against energy:

i) for the undamaged crystal, for three different alpha-particle

fluences, and for the subsequently annealed crystal;

ii) for protons channelled down <110>, <111>, and <100> axes;

iii) for four different depths below the surface, including the damage depth: they are indicated on the proton spectra in Figure 10.2 and listed in Table 10.1.

TABLE 10.1

Analysis Depth for Energy Dependence of Dechannelling

Spectrum Region (Figure 10.2)	Referred to as	Depth (μm)
A	Surface	0.0
B	Sub-surface	0.7
C	Damage peak	1.5
D	Sub-damage	2.25

The depth region of greatest interest is the sub-damage region D, in which the dechannelling due to the damage layer manifests itself. For this depth, the 'perfect crystal' yield was subtracted from the 'damaged' yield, and the resulting 'damage dechannelled' yield plotted for conditions (i) and (ii).

The energy E_i at each depth was calculated by the method explained in §2.4.3.

10.4.3 Results

Some of the plots are shown in Figures 10.4 to 10.15. The surface and subsurface yields changed little with the light doses used, and these plots have not been repeated for each damage stage.

Plots for the undamaged crystal, for the four different depth regions, are shown for <110> analysis in Figure 10.4, for <111> in Figure 10.5 and for <100> in Figure 10.6. The surface yield remains nearly constant with energy, as expected from Eqn 2.10, and the other three regions show the energy dependence expected for dechannelling in undamaged diamond due to electron multiple scattering and thermal vibrations [Li65], χ_{min} with $\nu \sim -0.8$.

The curious behaviour of the damage peak and sub-damage regions after α-particle bombardment may be seen in Figures 10.7 to 10.12. At the lower energies ν remains negative as the dose increases, with values between -0.9 and -0.5 (until the yield approaches 100%), but at higher energies the curves for the <110> and the <100> axes curl upward, with ν reaching +1.0 in some cases. The <111> curves maintain substantially their original negative slope throughout. Although only the sub-damage yield is determined purely by dechannelling - the damage peak yield is due to direct backscattering also - the two regions show very similar behaviour. This agrees with a single scattering model of the dechannelling, in which dechannelling and backscattering are

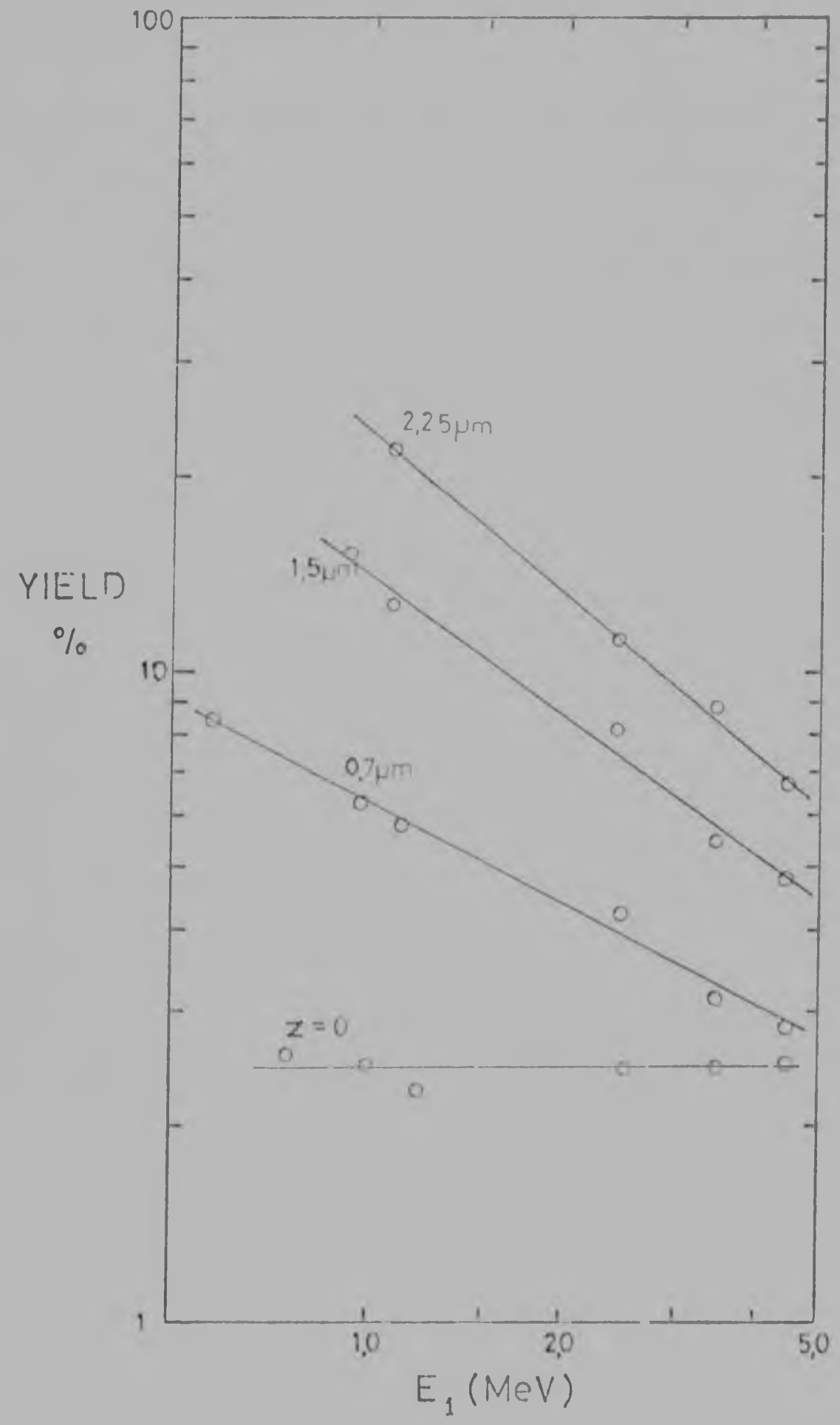

Figure 10.4: Minimum yield versus energy at different depths: undamaged crystal, <110> (KT2).

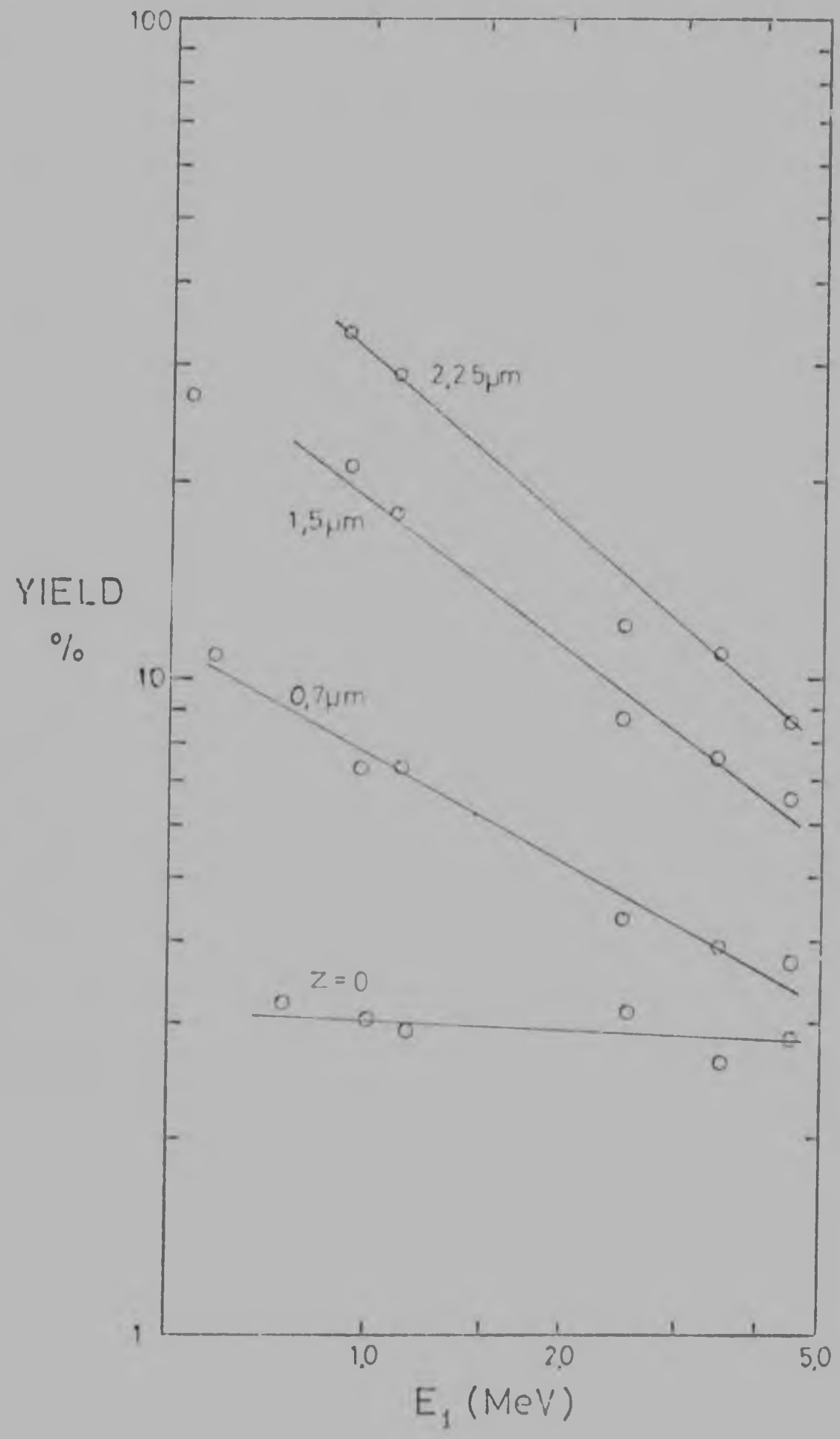

Figure 10.5: Minimum yield versus energy at different depths: undamaged crystal, <111> (KT2).

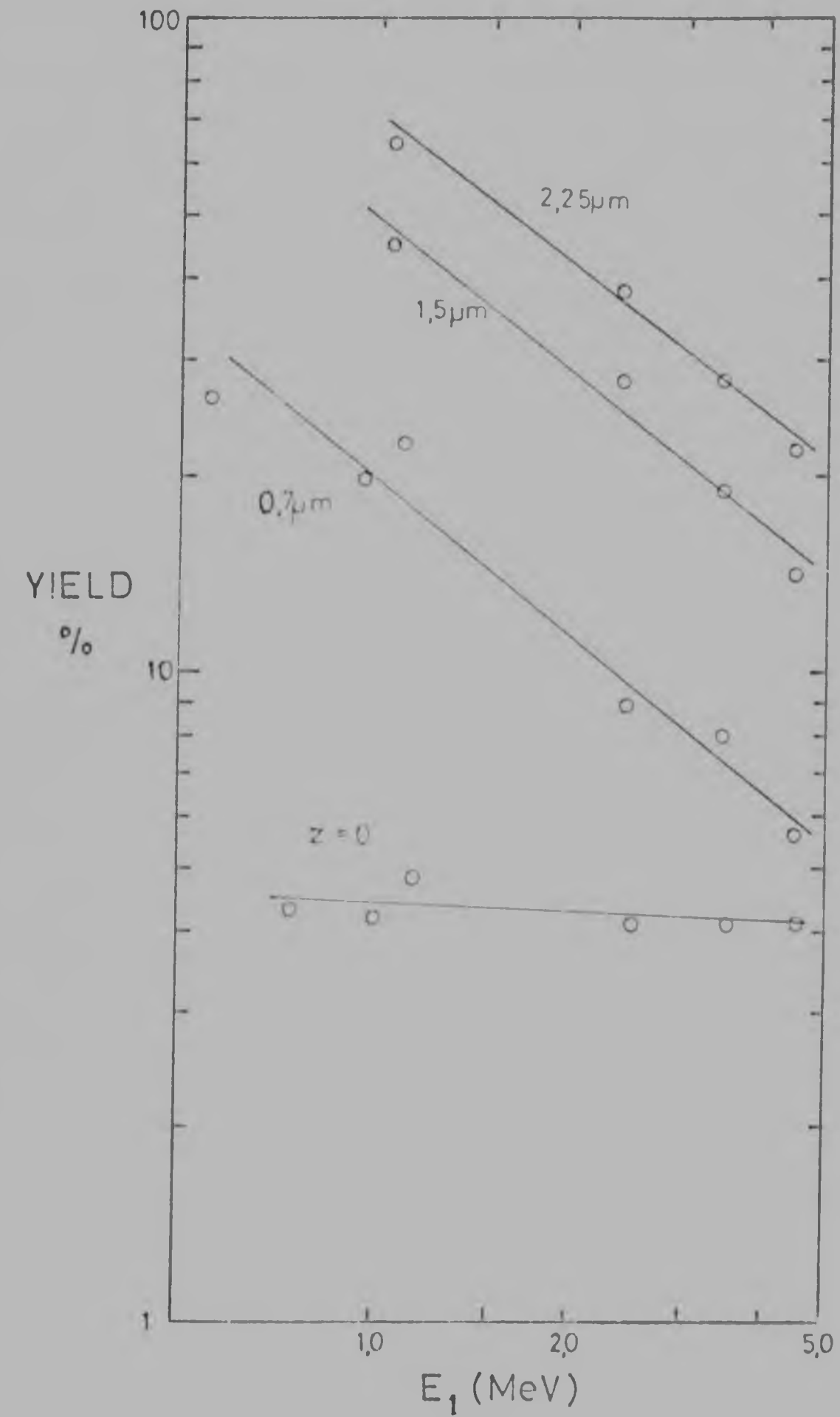

Figure 10.6: Minimum yield versus energy at different depths: undamaged crystal, <100> (KT2).

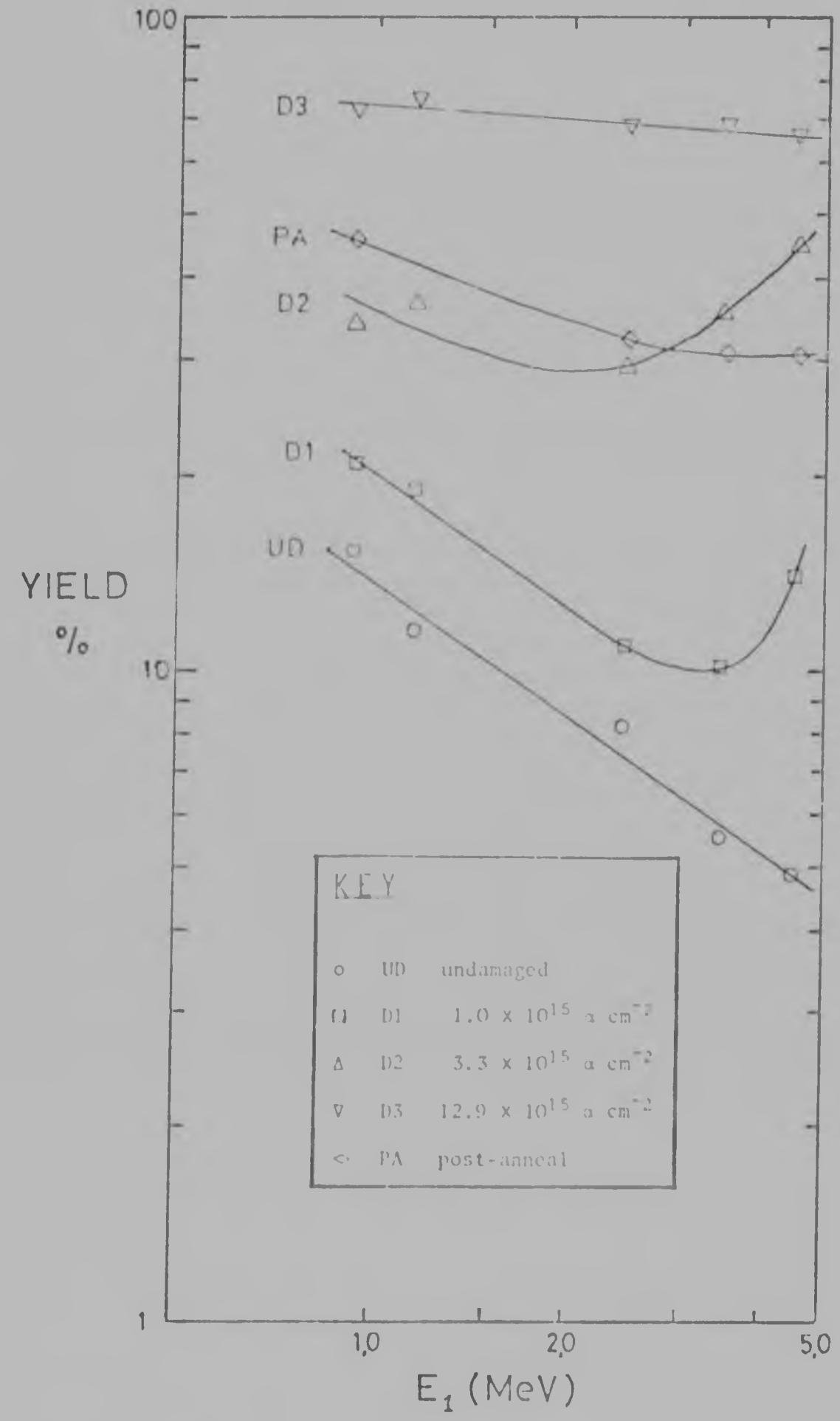

Figure 10.7: Minimum yield versus energy after damage: damage peak depth, ·110 (KT2).

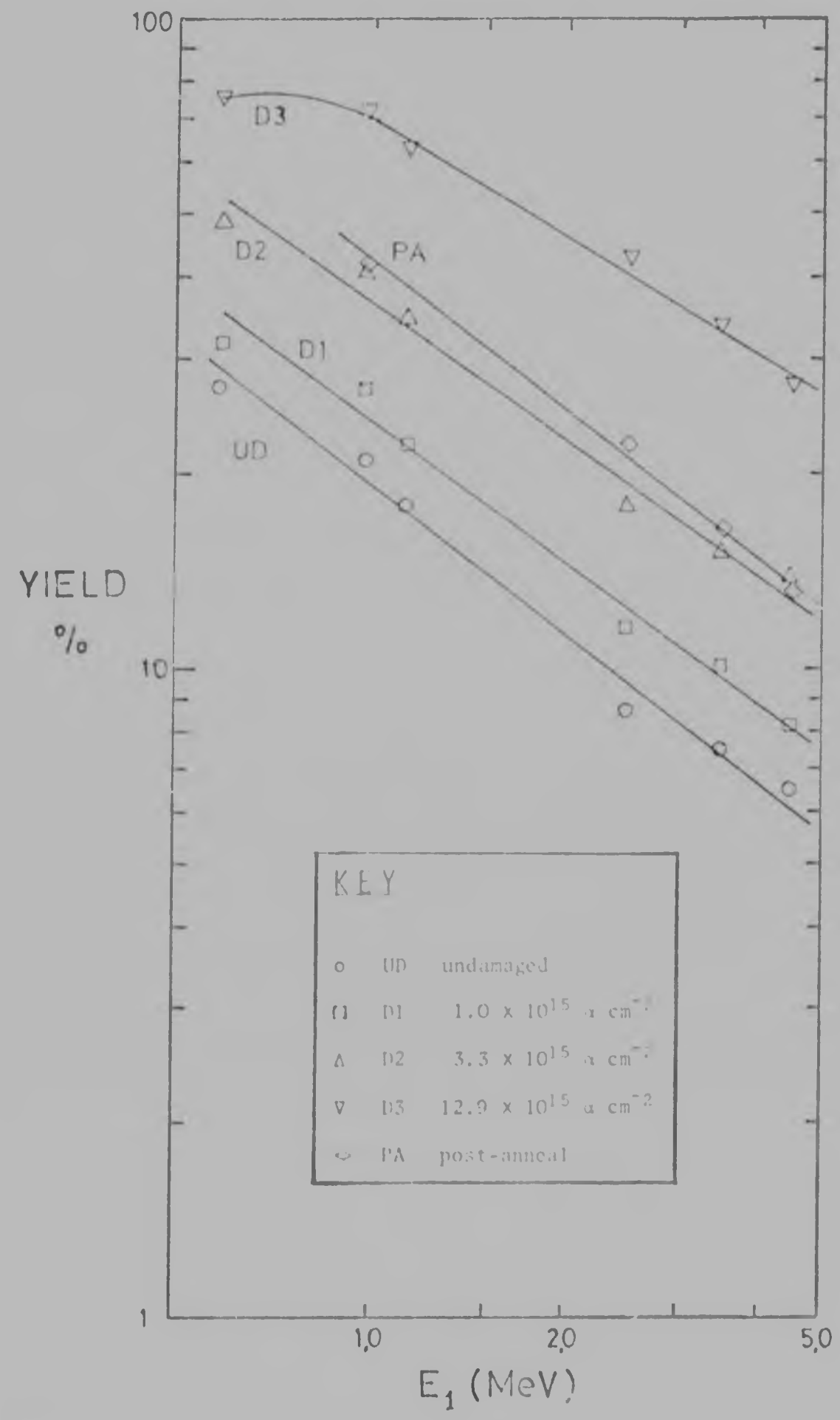

Figure 10.8: Minimum yield versus energy after damage: damage peak depth, ·111 (KT2).

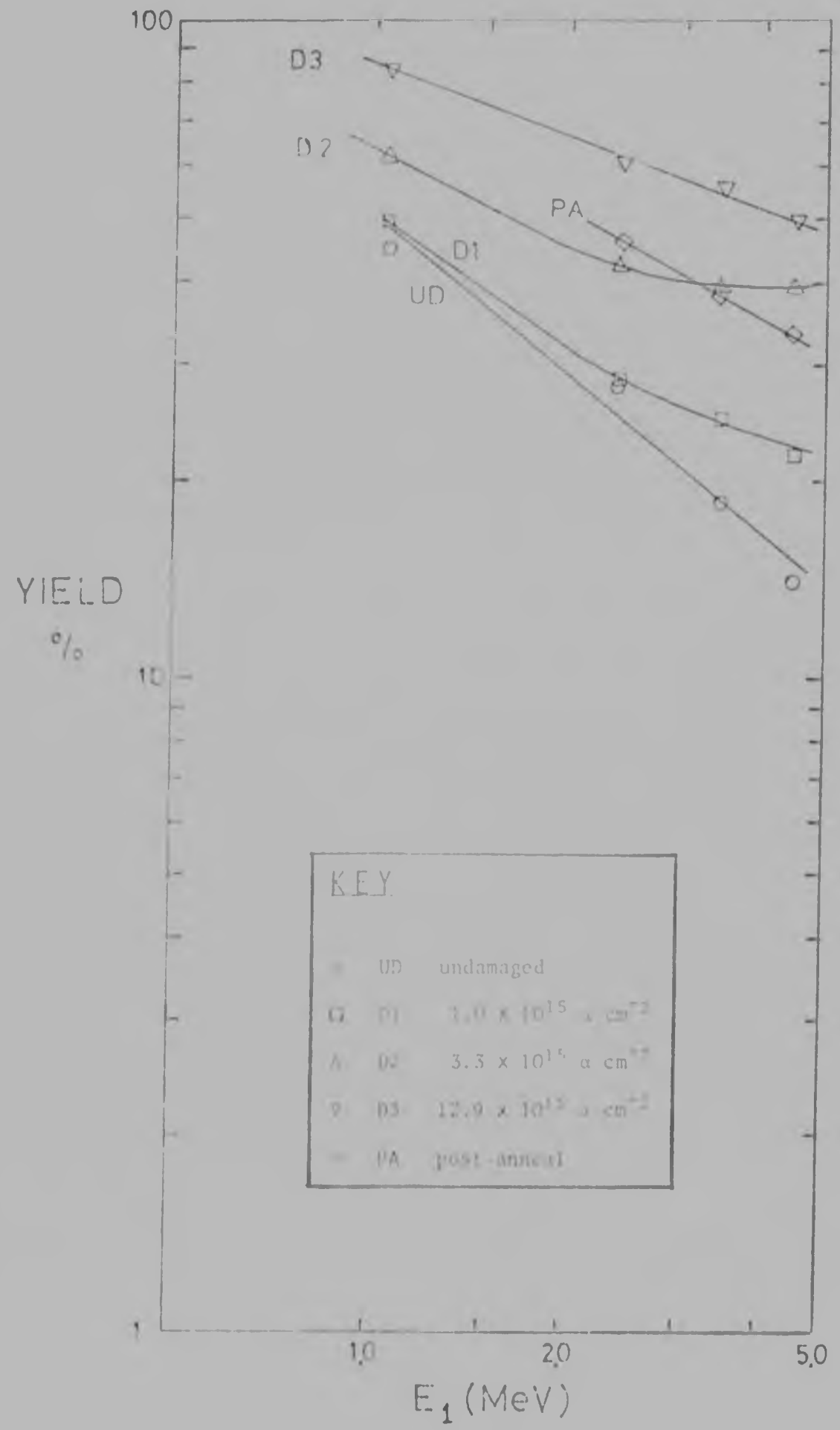

Figure 10.9: Minimum yield versus energy after damage: damage peak depth, 100 (K12).

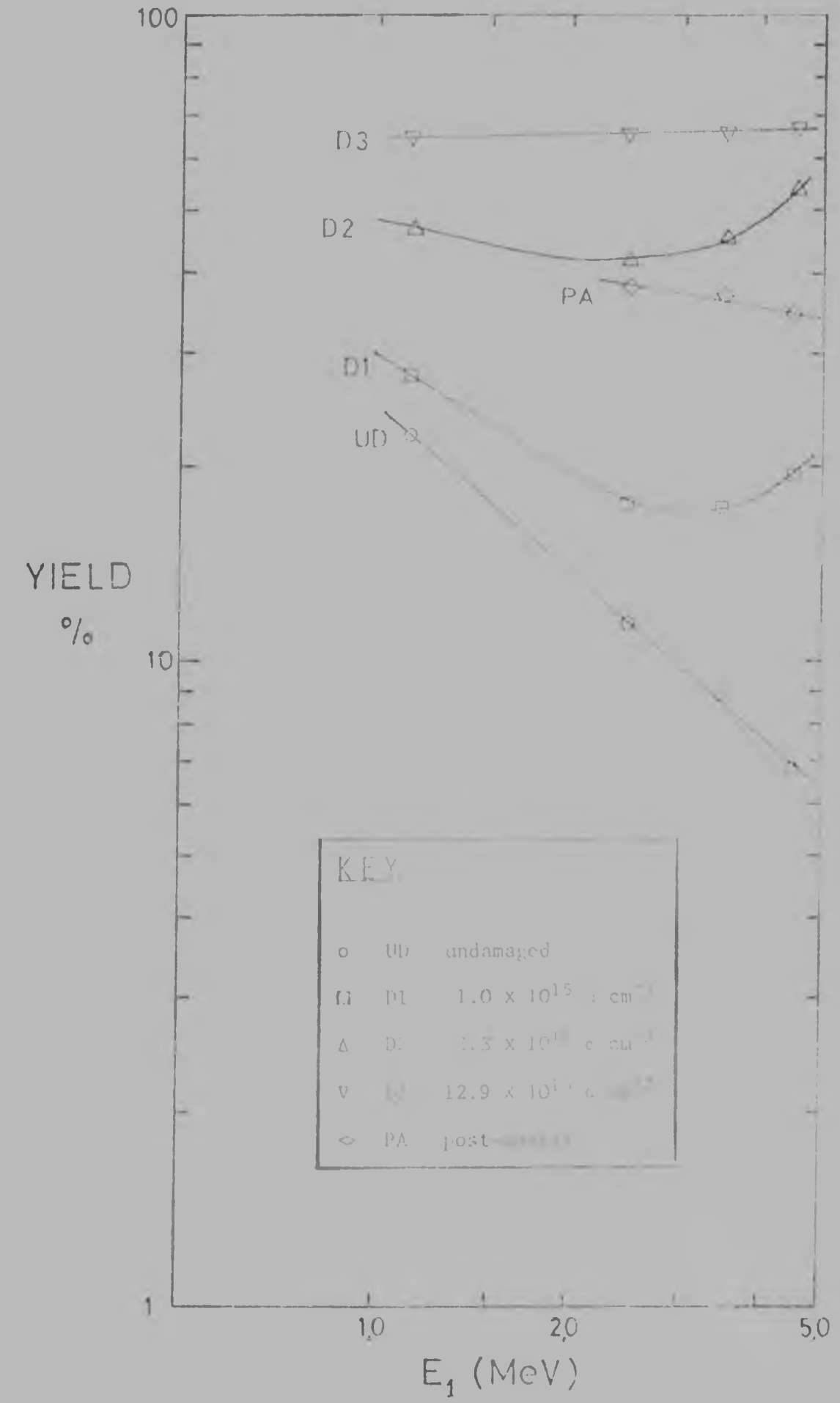

Figure 10.10: Minimum yield [illegible] sub-damage depth, <110> (KT2).

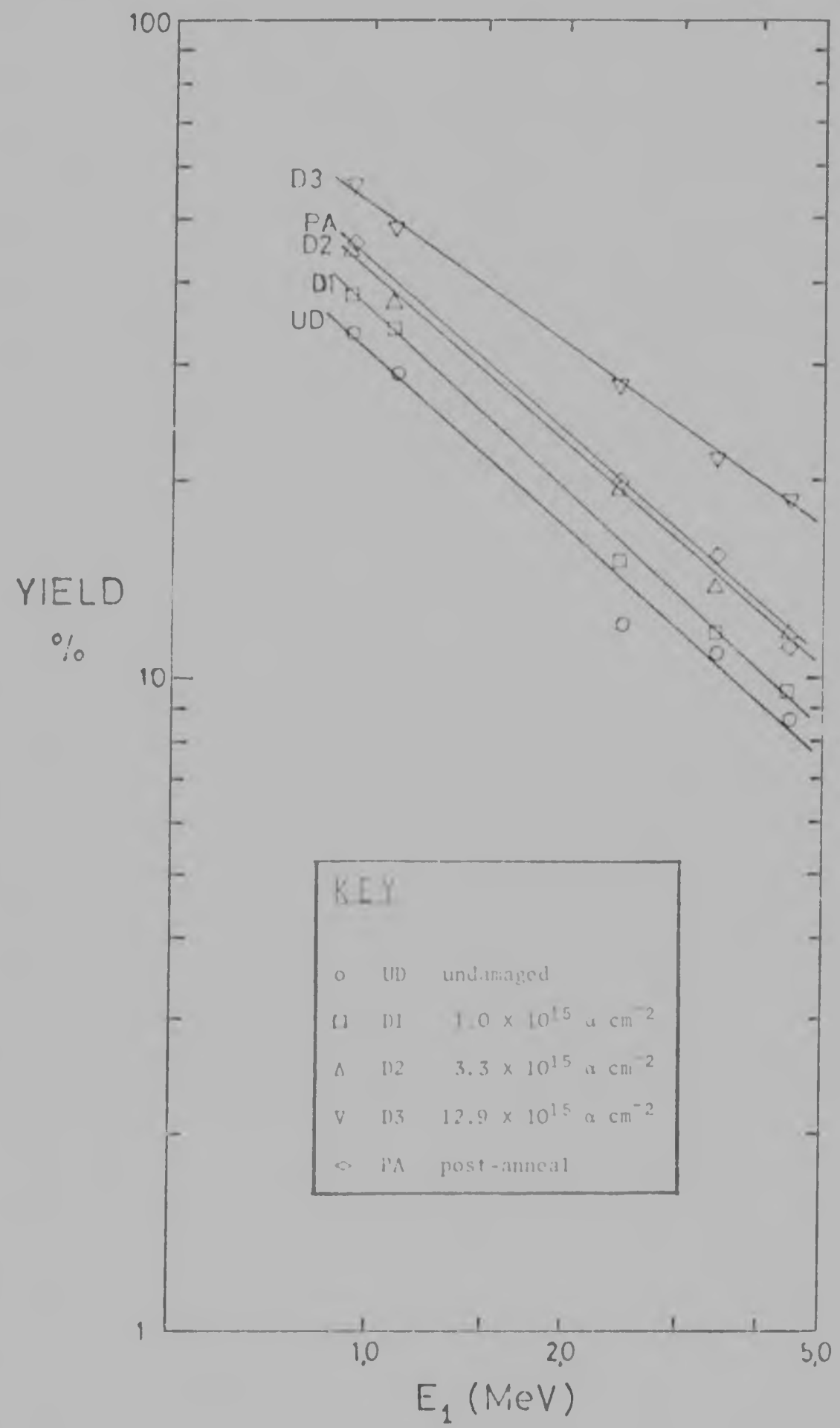

Figure 10.11: Minimum yield versus energy after damage: sub-damage depth, <111> (KT2).

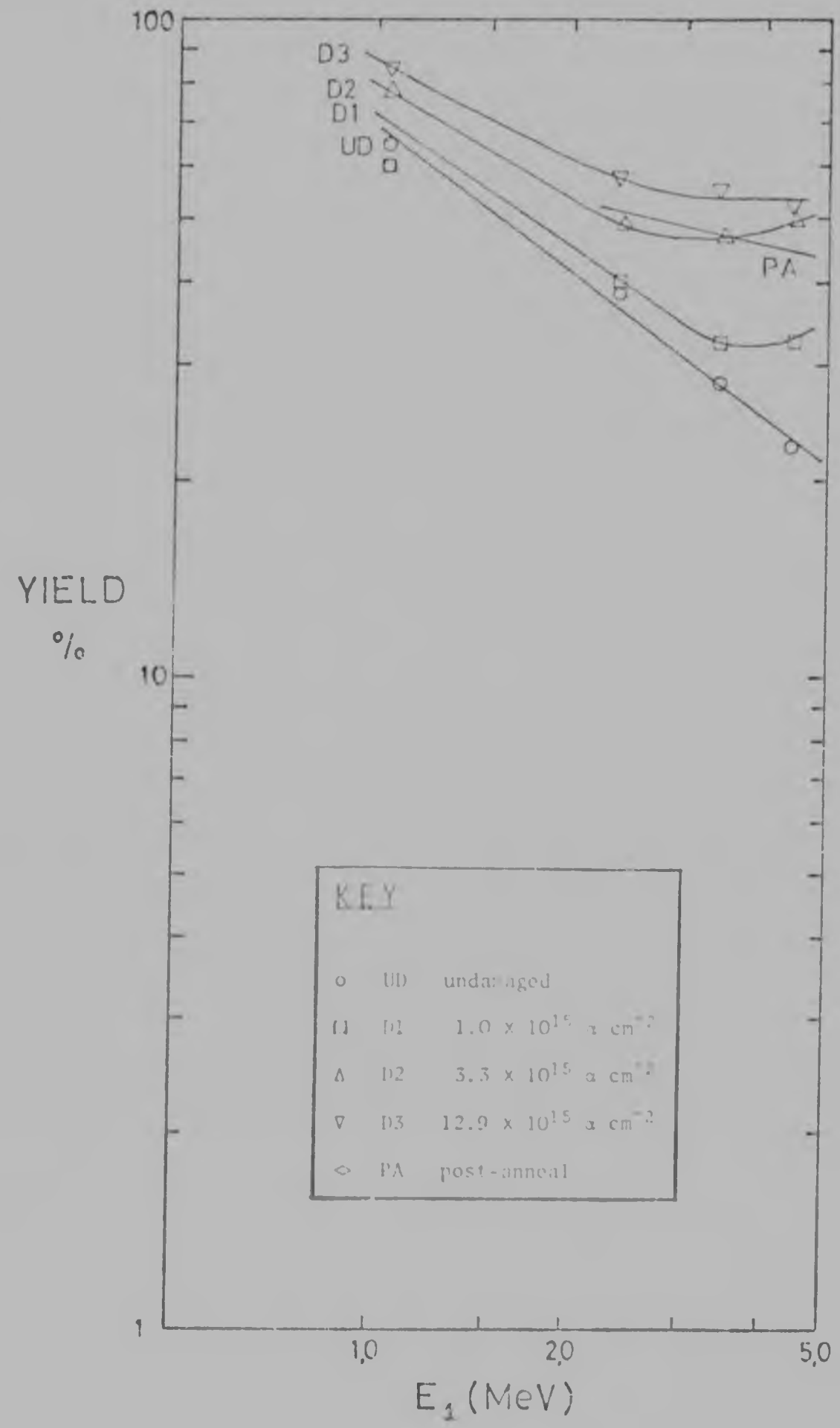

Figure 10.12: Minimum yield versus energy after damage: sub-damage depth, <100> (KT2).

proportional to one another (§2.5.1 and Sc73). The behaviour of the dechannelling due to the damage alone (with the perfect-crystal contribution removed as indicated in the previous section) is illustrated in Figures 10.13 to 10.17. Similar features to the abovementioned ones are seen, except that the low-energy negative slope of the <110> and <100> curves is absent.

It may also be noticed that the amount of dechannelling, and its rate of increase with α-particle fluence, is much greater in <110> than in <111> or <100>. This is illustrated by Figures 10.16 and 10.17, in which yield is plotted against damage dose for two energies, and by Table 10.2, which shows values of the damage dechannelling yield relative

---

TABLE 10.2

Values of "Relative Beam Dechannelling"

Ion dose 1.3×10^{15} [illegible] cm^{-2}

Incident Energy (MeV)	$[\chi_{min}(dam) - \chi_{min}(perf)]/\chi_{min}(rnd)$		
	<110>	<111>	<100>
1.3	2.0	0.7	0.4
4.5	8.7	1.1	1.4

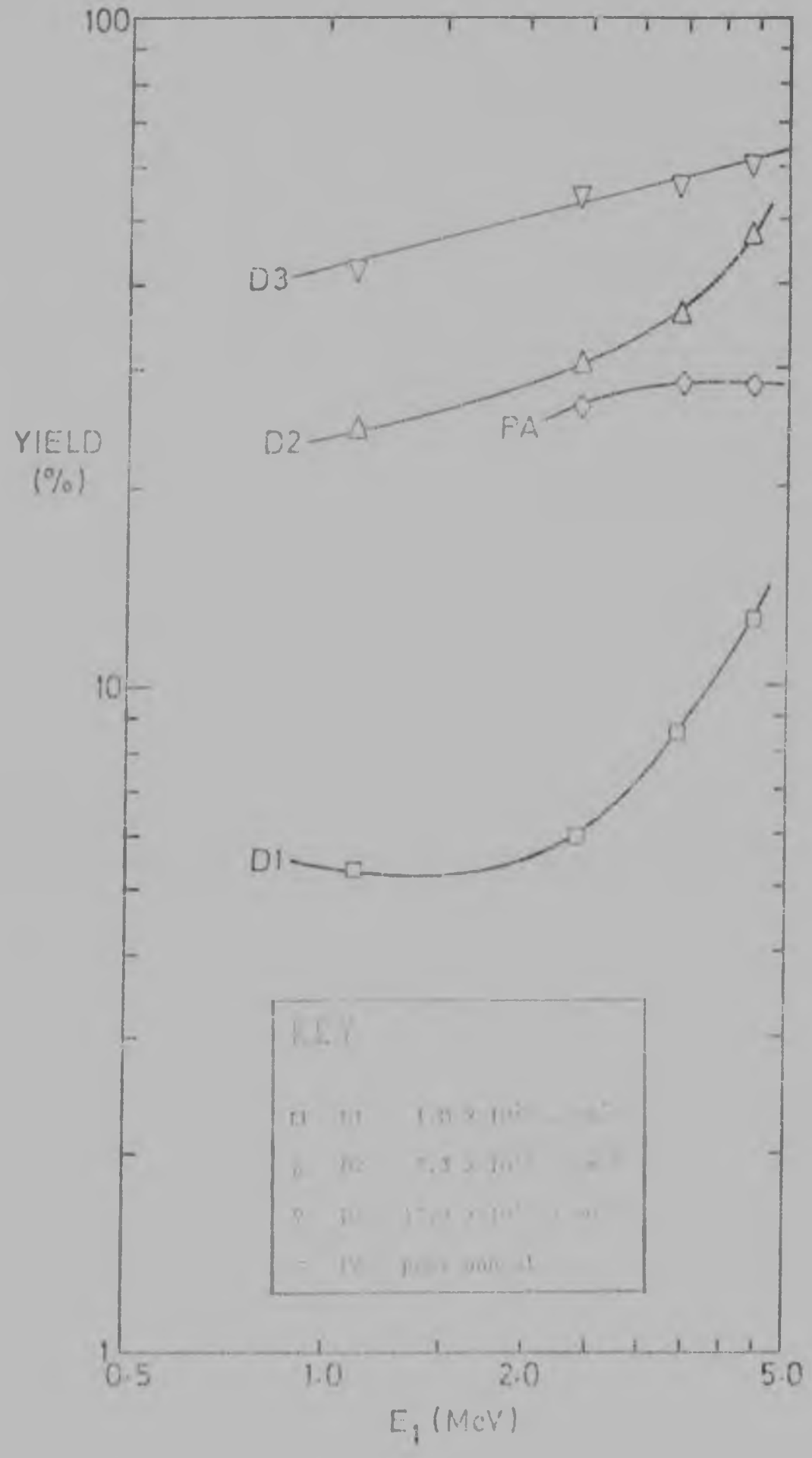

Figure 10.13: Dechannelling component due to damage only, versus energy: <110> (RT).

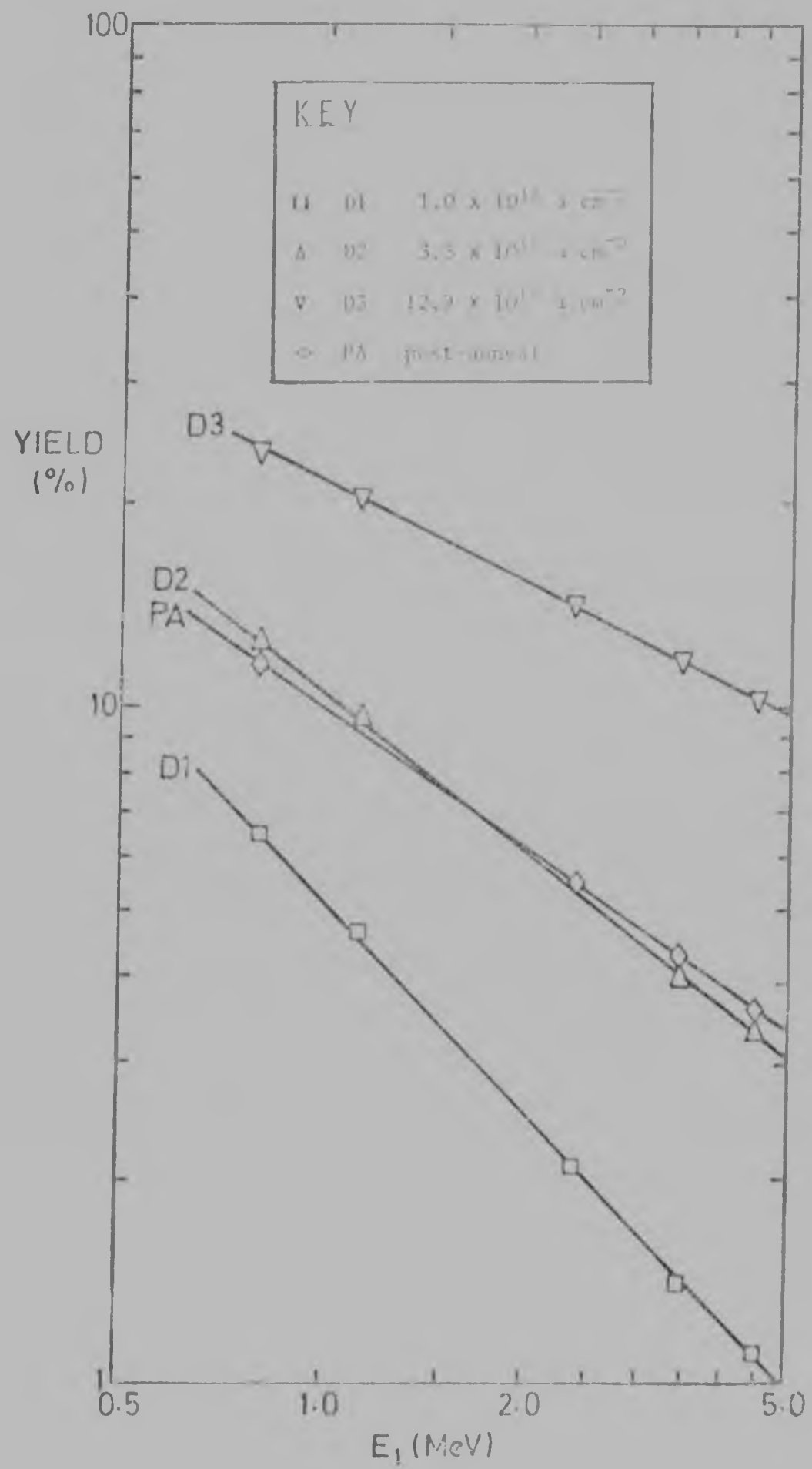

Figure 10.11: Dechannelling component due to damage only, versus energy: <111> (Kr2).

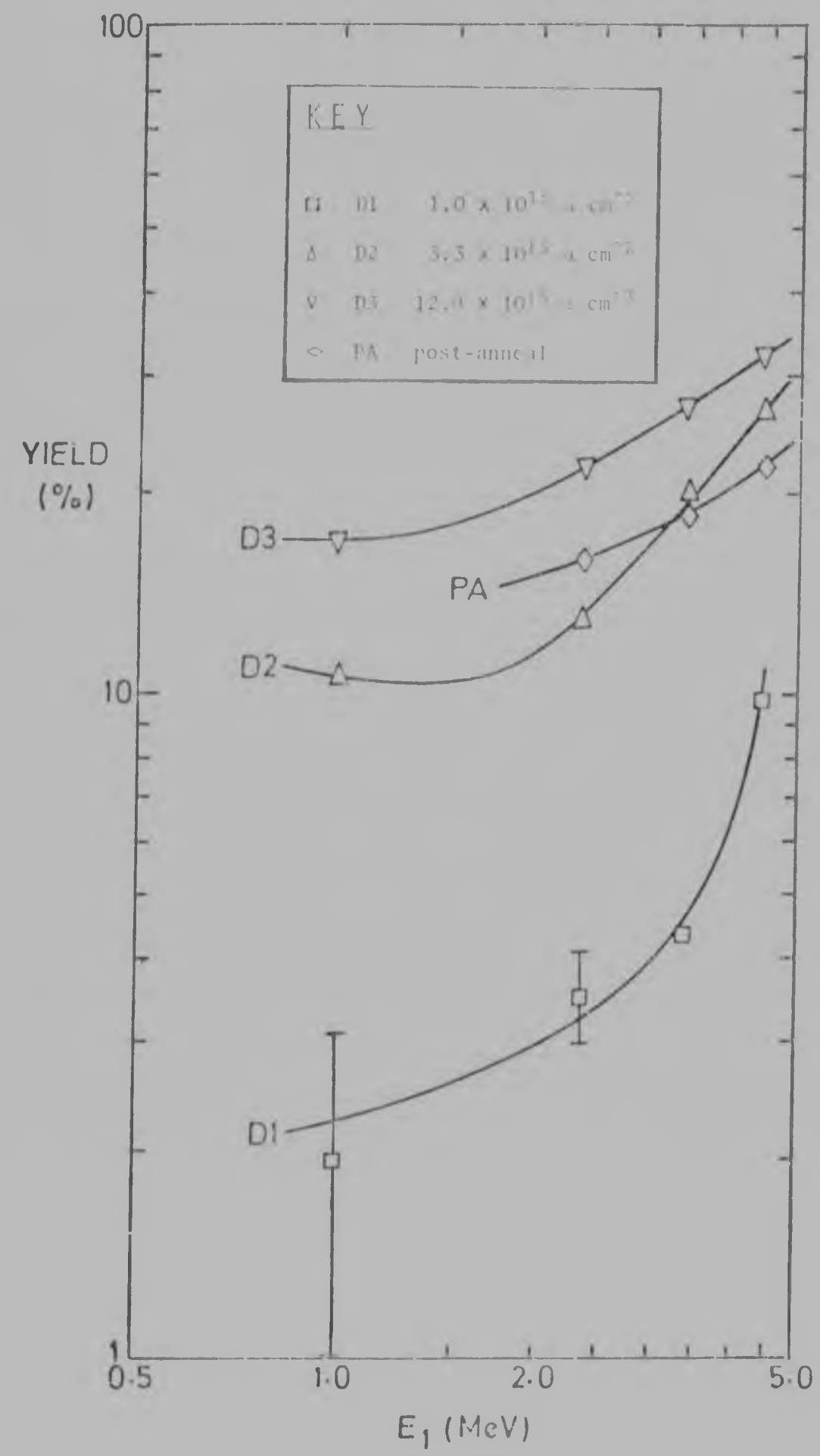

Figure 10.15: Dechannelling component due to damage only, versus energy: ·100· (KT2).

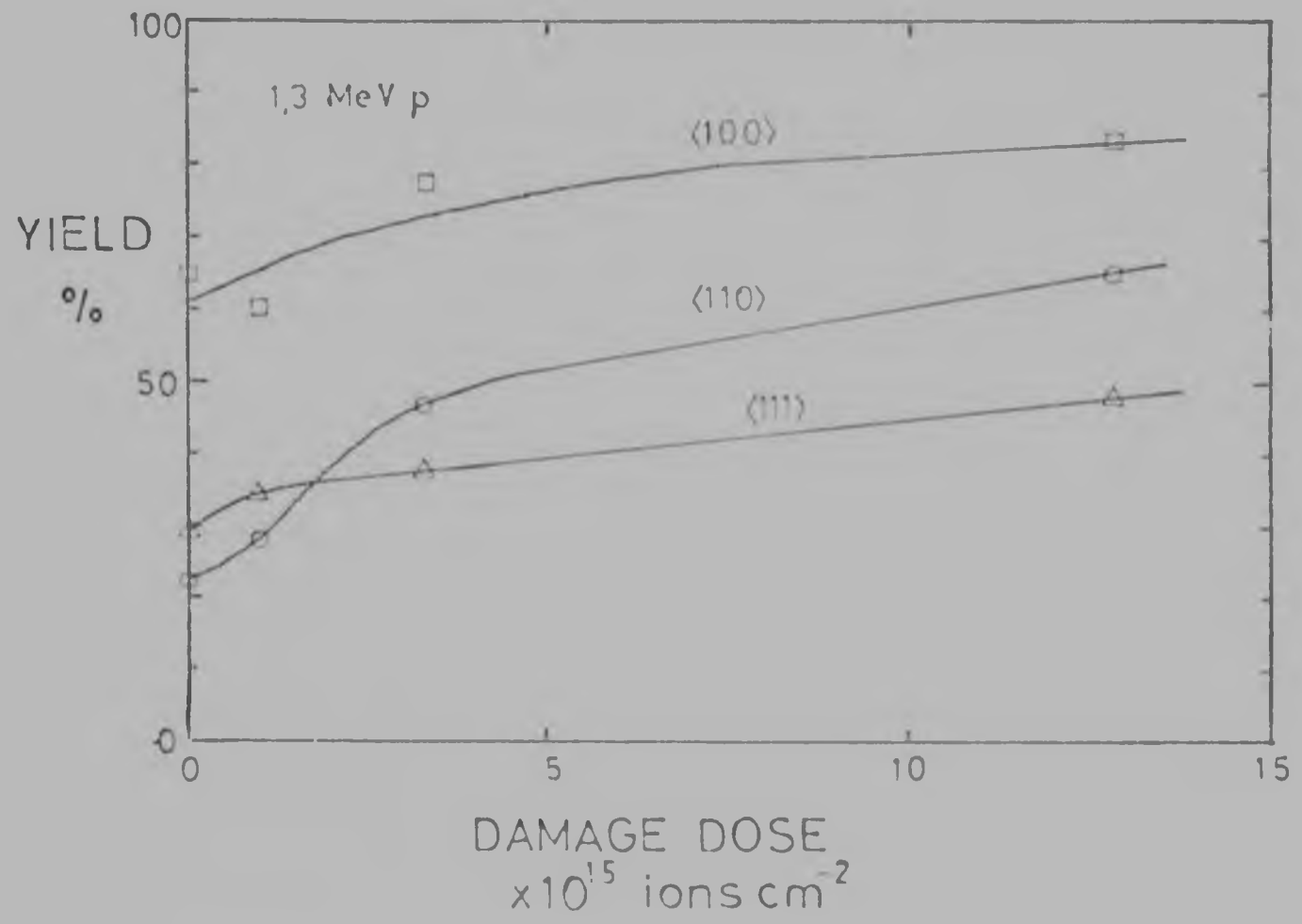

Figure 10.16: Dependence of sub-damage yield on dose, at 1.3 MeV (KT2)
o <110>; Δ <111>; □ <100>

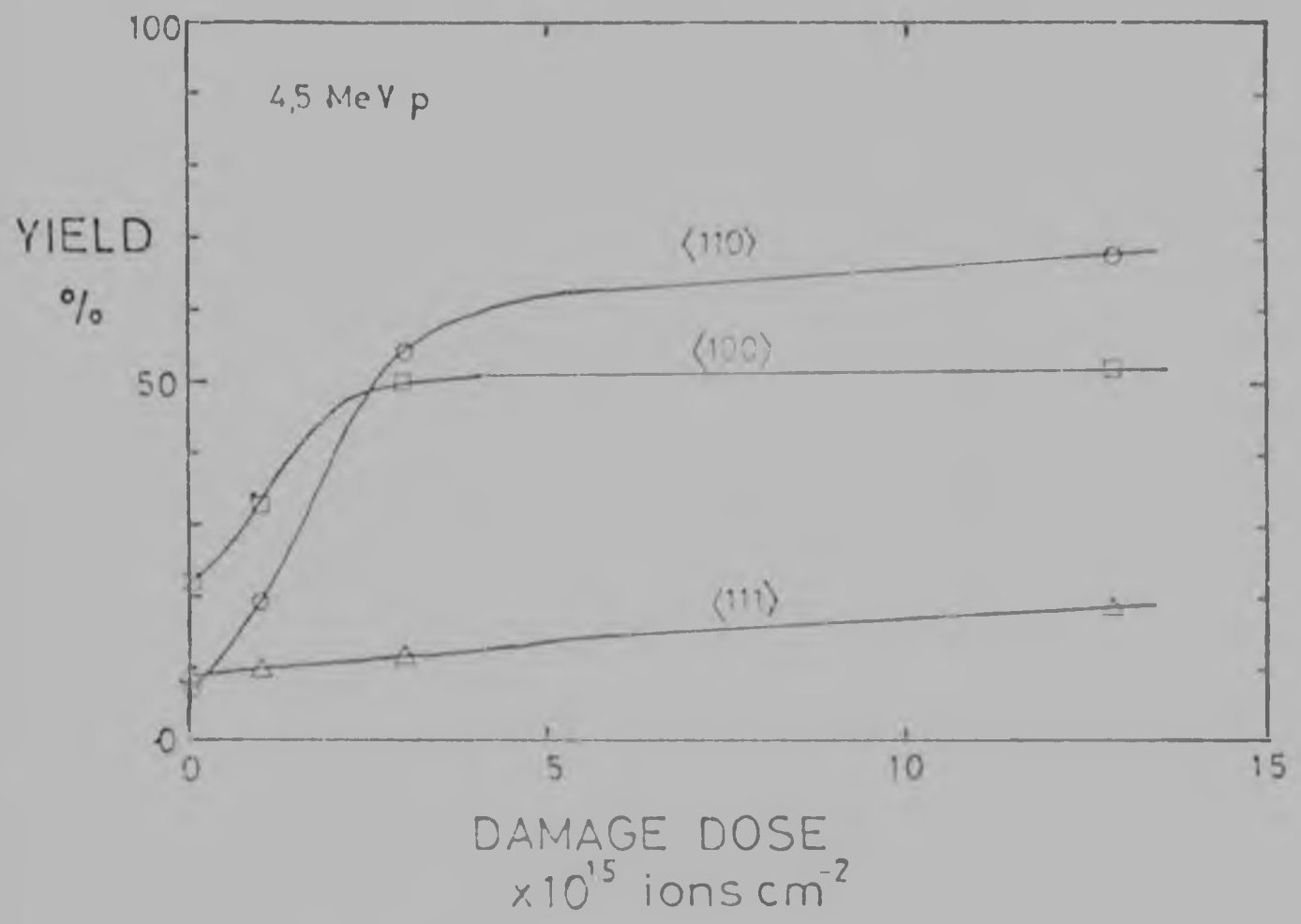

Figure 10.17: Dependence of sub-damage yield on dose, at 4.5 MeV (KT2)
o <110>; Δ <111>; □ <100>.

to that for the perfect crystal, given by

$$[\chi_{min}(dam) - \chi_{min}(perf)]/\chi_{min}(perf).$$

The relative damage dechannelling is similar and small for the <111> and <100> axes, in contrast to the <110> case, and despite the quite different energy dependences of the <111> and <100> yields. The higher <110> dechannelling is evidently the major effect.

10.4.4 Explanations

There appears to be no single explanation for the behaviour just described. It is likely that several types of defect are present, and their influences are seen superimposed in the dechannelling results.

The first possibility which can be dismissed is that the observed curvature of the yield versus energy plots is due to the presence of both small and extended defects, the E^{-1} dependence of the former dominating at lower energies and the $E^{-\frac{1}{2}}$ dependence of the latter taking over at higher energies. Although both types of defects are probably present, the effect of the small defects is strong only in <111> (Figure 10.14), indicating dominance of other damage; moreover at high energies $\nu > 0.5$, in fact $\nu \sim 1.0$.

The most important anomaly to be explained is probably the high <110> damage dechannelling; this could be due to a lattice location of damage interstitials within the regions of nearly perfect crystal. One requires a site which is shielded along the <111> and <100> rows, but not along the <110> rows.

Four sites have been suggested [Wat71, Wei73] for the self-interstitial in diamond; they are illustrated in Figure 10.18. A careful examination of a three-dimensional model reveals that only the tetrahedral site satisfies the above requirements (Figure 10.19). Therefore, the tetrahedral site appears to be the preferred residence of interstitial carbon atoms generated in these experiments, in contrast to calculations [Wat71, Wei73] which have pointed to the 'split-<100> or 'bond-centred' configurations as energetically most favourable.

It remains to be explained why these interstitials do not produce a negative energy exponent for dechannelling in <110> - in fact $v \sim +0.3$ at low energies (Figure 10.13). This could be due to flux-peaking effects: it can be shown [Fea70] that the flux peak at a fixed depth 'sharpens up' as the energy of the ions incident on the crystal surface increases. This would produce an increasing interaction probability between ions and interstitials located near the channel centre as the energy increased.

Many other studies have emphasised the importance of detailed transaxial angular scans in deriving valid lattice-location results, in order to allow for, and take advantage of, flux-peaking effects. Some preliminary scans at 1.0 MeV were undertaken, but no obvious effects of flux-peaking manifested themselves in this mode of analysis. It would be interesting to carry these experiments further.

The strong upward curl of the <110> and <100> curves at the highest energies, to a slope of ~ 1.0, requires an additional explanation.

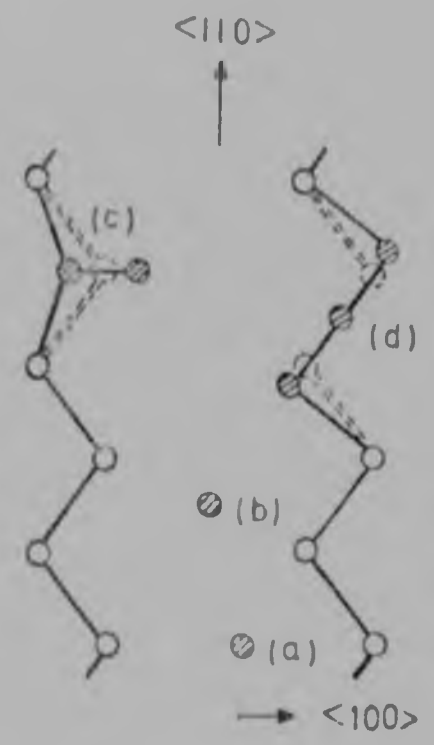

Figure 10.13 Projection of diamond lattice on {110}, showing examples of suggested self-interstitial sites: o lattice atoms; • interstitials, namely: (a) tetrahedral, (b) hexagonal, (c) split-<100>, (d) bond-centred. (After Wat7a).

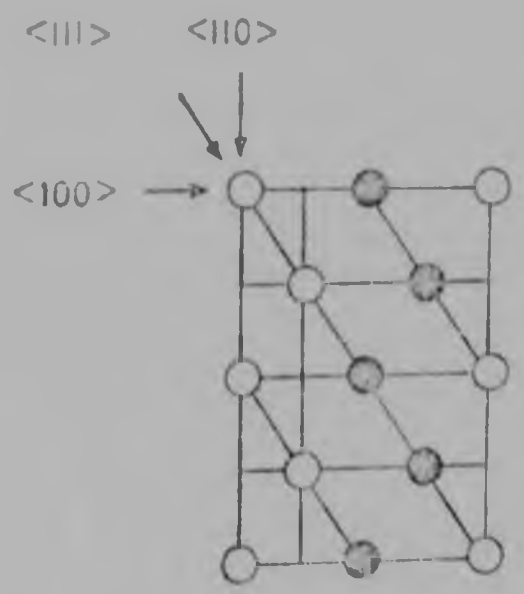

Figure 10.14 Projection of diamond lattice on {110}, showing screening of tetrahedral interstitial sites along <111> and <100>.

o lattice atoms; • tetrahedral sites.

It is suggested that this is due to the breakup of the crystal into slightly misorientated mosaic blocks. Consider channelled ions entering a mosaic block which is misorientated from the original channel axis by a small angle β; their angular spread with respect to that axis will be between $\sim +\psi_{\frac{1}{2}}$ and $\sim -\psi_{\frac{1}{2}}$. Thus if $\beta < \psi_{\frac{1}{2}}$ most of the beam will remain channelled, whereas if $\beta > \psi_{\frac{1}{2}}$ most will be dechannelled. Since $\psi_{\frac{1}{2}}$ depends on energy, a transition between the two regimes will occur as the energy is raised.

The energy dependence of the dechannelling may be obtained by considering the dependence of the yield χ on the incidence angle $(\theta - \beta)$ with respect to the channel axis of a mosaic block. In §7.3.1 it was mentioned that, for $\theta - \beta \gg \psi_{\frac{1}{2}}$, $\chi \propto \theta^{k}$ with $k=4$ for axes at shallow depths (see Eqn 7.1); at the depths now being considered (~2 μm), $k \approx 2$ is found to provide a better fit. The width of the dip scales with $\psi_{\frac{1}{2}}$, so that

$$\chi \propto [(\theta - \beta)/\psi_{\frac{1}{2}}]^2 \qquad (10.1)$$

(neglecting the minimum yield). Either Eqn 2.4 or Eqn 2.7 gives

$$\psi_{\frac{1}{2}} \propto E^{-\frac{1}{2}} \qquad (10.2)$$

and from Eqn 10.2 and Eqn 10.1

$$\chi \propto E^{1} \qquad (10.3)$$

This is the dependence of yield on energy observed for the damage dechannelling at the highest energies, in the <110> and <100> axes. The lack of a similar effect in <111> must be due to all the misorientations

consisting of twists about this <111> axis (the one used was perpendicular to the crystal surface).

It has been implicitly assumed in the derivation above that parallel trajectories were incident on a mosaic block with a well-defined orientation. Of course there is not only a distribution of trajectories as previously mentioned, but also presumably a distribution of β. This does not affect the energy dependence of the overall yield.

An estimate of the mean misorientation of the crystallites may be obtained by considering that the transition from low to high dechannelling occurs when $\chi_{\frac{1}{2}} \sim 1$. For different axes of polar angle θ, one may put $\beta = \gamma \sin\theta$, where γ is the twist of a mosaic block about <111>. The value of γ to be used is that for the energy at which the yield curve begins to curl upward. Then

$$\gamma \sin\theta \sim \chi_{\frac{1}{2}} \qquad (10.4)$$

At this stage it may be noted that the change of slope in the <110> case occurs at about 2 - 3 times the energy of the <100> case (for damage state 2, where the behaviour is clearest, $\sim$ 2.5-3 MeV for <110> (Figure 10.13) and $\sim$ 1-1.5 MeV for <100> (Figure 10.15)). This is in agreement with expectations; either Eqn 2.4 or Eqn 2.7 gives $\chi_{\frac{1}{2}} \propto (Ed)^{-1}$, and if Eqn 10.4 is satisfied, then

$$E_1 \propto (d \sin\theta)^{-1}$$

This gives a calculated value of the ratio E_1<110>/E_1<100> of 2.88.

Inserting the above rough values of Γ_1 into Eqn 10.4 gives

$$\gamma \sim 0.5°$$

for both <110> and <100> data.

Another form of polycrystallinity was considered: microtwinning by 60° rotation about the <111> axis normal to the sample face. (This is the same twin law that produces macles.) It can easily be shown that low-index axes lying in {110} planes (as do all those investigated here) always coincide with low-index axes in the twin; the pairs of axes have indices of the form <h h 1> and <1 1 ℓ> where

$$4h - \ell h - 2\ell - 1 = 0 \qquad (10.5)$$

For <110> and <100> channelling, the corresponding axes presented by twins (<411> and <221>) have smaller critical angles, and enhanced dechannelling would result. A demonstration of this effect in silicon has recently been published [1**].

This mechanism produces an energy independent dechannelling: the ratio between two critical angles depends only on the row spacing, so that the relative narrowing of the channel in the twin does not depend on energy. Dechannelling at the matrix/twin interface is also energy independent as the latter constitutes a stacking-fault or free surface within the crystal.

There is some evidence for an energy-independent component in the dechannelling curves for <110> (Figure 10.13) and <100> (Figure 10.15).

There is no such evidence in the <111> curves (Figure 10.14), as expected, if twinning is by rotation about this axis. Voids also give an energy-independent dechannelling, but would be visible in all axes.

A crucial experiment to test some of the above deductions would be to channel along one of the other <111> axes at 70°32' to the one used. Here the yield versus energy curves would still not be affected by tetrahedral interstitials, but mosaic spread would produce a strong upward trend at high energies, and twinning would contribute an energy-independent component, as according to Eqn 10.5, an axis such as $[11\bar{1}]$ transforms into one of the form <551> in the twin. Unfortunately the maximum angular aperture of the goniometer was 70°, and the experiment was not carried out.

Curves for data taken after annealing to 700°C are also plotted on Figures 10.7 to 10.15. Apart from their lower overall yield values, their most noticeable feature is that at higher energies, for the <110> and <100> axes, they are much flatter than the pre-anneal curves. This implies that the mosaic spread has been reduced. There still seems to be an energy-independent component, implying that the postulated microtwins are stable; and dechannelling in <110> is still greater, although in somewhat smaller proportion relative to that in <111> and <100> than was the case before annealing. One may deduce that not all the tetrahedral interstitials have annealed out at 700°C, although the self-interstitial in diamond is normally mobile below room temperature [Vad75]. This supports the suggestion of §10.3.2 that their motion is here limited by the presence of other forms of disorder which have not yet annealed completely at 700°C.

10.5 DAMAGE PROFILE EXTRACTION

10.5.1 Method

The principle of extracting a quantity representing the 'degree of disorder' of a damaged crystal, as a function of depth, from the depth-dependent channelled minimum yield, was outlined in Section 2.5. A Fortran programme to perform the extraction according to these principles, was written to run as a subroutine of CHANSPEC (§7.2.3).

A 'perfect' (undamaged) spectrum, as well as the 'damaged' spectra and a 'random' spectrum, were required. After depth conversion (§7.2.1) and normalisation (§7.2.2), the value of the disorder parameter $n(z)$ was calculated as a stepwise function of depth, starting at the surface, for each depth increment into which the programme divided the spectra. The dechannelling function $f(z)$ (Eqn 2.19) was required to merge smoothly with the channelled yield $\chi_1(z)$ at depths greater than those of the visible damage peak. The dechannelling parameter κ (Eqn 2.21) was suitably adjusted and the damage extraction re-iterated until this convergence condition was met.

To obtain the initial estimate of κ, κ_0, Schmid [Sc73] showed how to use a straight-line approximation to $f(z)$ under the damage peak. It was found that the particular shapes of the diamond spectra often gave rise to unrealistically large or small values of κ_0 when this method was applied, and the programme became unstable. It was usually better to impose an arbitrary value of κ_0 with $0 < \kappa_0 < 1$, from which the programme was able to converge.

The steps in the calculation were as follows (the notation is that of §2.5.2; i denotes the depth interval number). By Eqns 2.19 and 2.21,

$$f(i) = \chi_p(i) + \kappa \sum_{j=1}^{i-1} g(j)$$

For the first depth interval this became

$$f(1) = \chi_p(1)$$

Then by Eqn 2.18,

$$g(i) = \chi_d(i) - f(i)$$

Finally, by Eqn 2.20,

$$n(i) = g(i)/[1 - f(i)]$$

The programme had to be told approximately where to expect the damage to end (but this could be modified by the programme in the light of the damage actually found). After this point, the sum $\Sigma g(j)$ was no longer accumulated, and the programme began comparing values of f(i) and $\chi_d(i)$. After adjusting κ upward or downward as required, another iteration was performed, until f(i) converged to $\chi_d(i)$ to the stipulated degree of accuracy. The integrated damage (Σ n(i)) and its distribution were then printed out.

10.5.2 Results

An example of a damage profile extraction (traced from the computer output) is shown in Figure 10.20. Extractions were performed

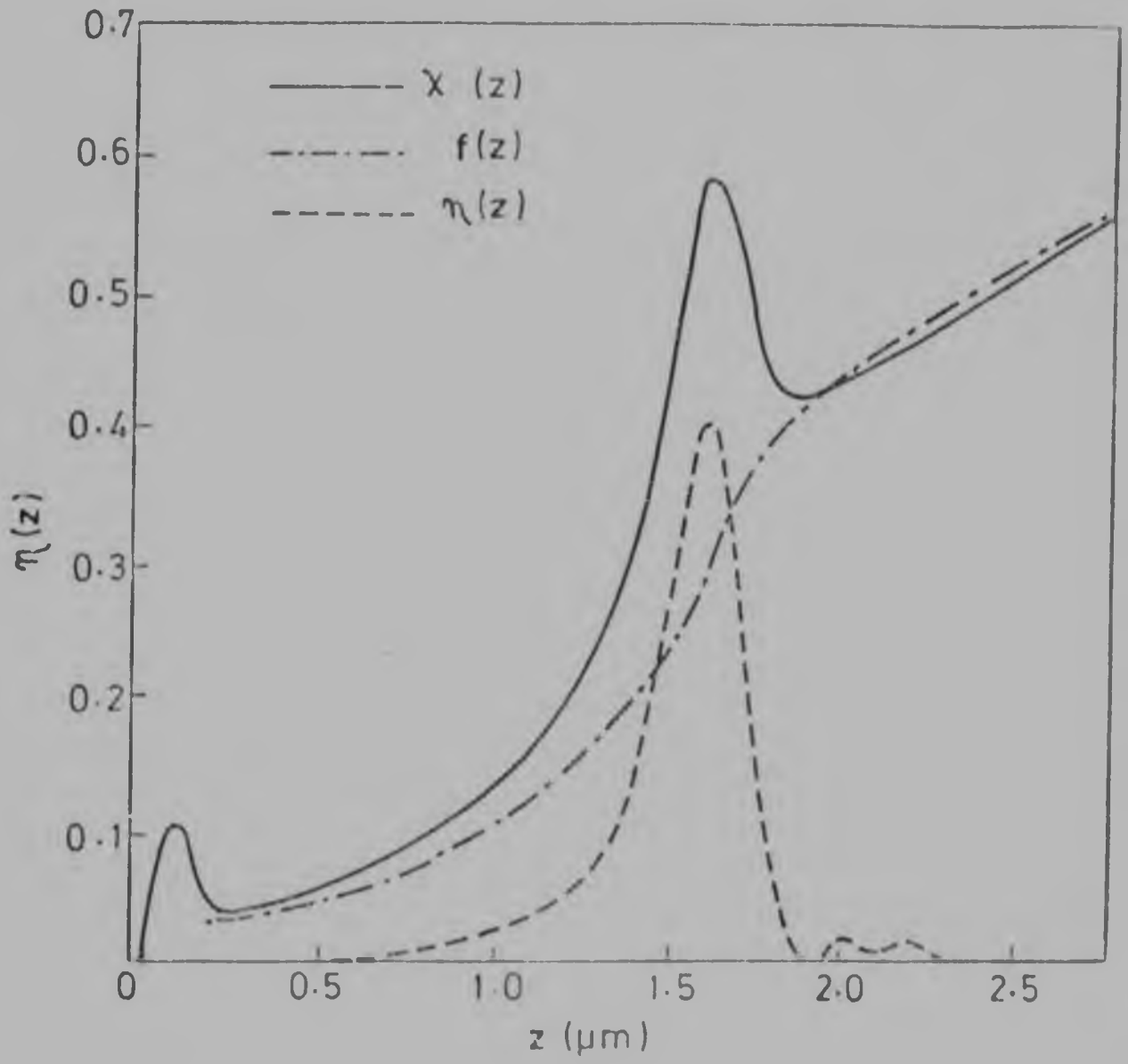

Figure 10.20: Extracted damage profile n(z) with original spectrum χ(z) and fitted dechannelling function f(z) (KT2).

for two of the analysis energies, 1.3 MeV and 4.5 MeV. Approximately the same values of the adjustable parameter κ (which measures the ratio of dechannelling to direct backscattering) were required for different damage stages, but each combination of axis and energy required a different value; they are listed in Table 10.3. It seems possible to fit all the data with a single value of κ using the equivalent of a plural scattering treatment based on the observed dechannelling by amorphous surface layers [Fea75]. Thus the necessity for different

TABLE 10.3

Damage Extraction Parameters

Energy (MeV)	Values of κ			Damage Peak (μm)*	
	<110>	<111>	<100>	Depth	Width
1.3	0.17	0.09	0.11	1.5	0.3
4.5	0.40	0.10	0.20	1.7	0.3

*Errors in these figures are ± 0.05 μm.

values here is probably due to the shortcomings of the single scattering model which is implied in the treatment used (§2.5.2).

Table 10.3 also contains the mean damage depth and the half-width at half-maximum of the extracted peak (after correction for the trajectory angle, these quantities were the same for all three axes). The depth

TABLE 10.4

Integrated Damage as a Function of Damaging Fluence and Analysis Energy

Axis	Damaging Dose D (10^{15} a cm^{-2})	Damage = Σ n(i) x cosθ (10^{18} cm^{-2})	
		1.5 MeV p	4.5 MeV p
<110>	1.0	0.2	0.2
	3.3	0.7	1.2
	12.9	2.8	4.3
	anneal	-	1.5
<111>	1.0	0.2	0.2
	3.3	0.8	0.9
	12.9	2.5	2.5
	anneal	-	1.0
<100>	1.0	0.2	0.3
	3.3	1.0	1.1
	12.9	2.9	2.7
	anneal	-	1.3

increases slightly with energy, the width remaining constant. This may be due to a depth-scale error, but is probably an observation of a phenomenon pointed out by Quéré [Qu76], that defects which obstruct the channels, such as small clusters or stacking-faults, cause most of their dechannelling within a distance $\lambda/4$ beyond the defect, where λ is the channelled trajectory 'wavelength', which increases with energy.

Extracted values of the integrated damage $\Sigma\, n(i)$ are summarised in Table 10.4 and plotted against damaging dose in Figure 10.21. They have been multiplied by cos ψ to eliminate the effect of traversing a greater thickness of damage at larger polar angles. The absolute accuracy of the extraction is approximately independent of dose and is $\sim \pm 0.1 \times 10^{15}$ cm^{-2}.

For <111> and <100> analysis, the integrated damage is independent of axis or energy and increases approximately linearly with α-particle fluence, with some indication of a curvature corresponding to a saturation effect. (It may be noted however that the maximum value of $n(i)$ attained is only 0.4.) For <110>, the relationship is again linear, and similar in magnitude at the lower energy, but more damage is observed at the higher energy. This is in keeping with the suggestions of §10.4.1, that the chief anomaly is that between <110> and the other axes, and that it is due to the presence of tetrahedral interstitials which are only observable in <110> and for which the nuclear encounter probability increases as the energy increases causing the ion flux to peak more sharply at the mid-channel axis [Fea76].

These results provide an experimental example of the problem discussed by Quéré [Qu76]: that unless a damaged region is amorphous,

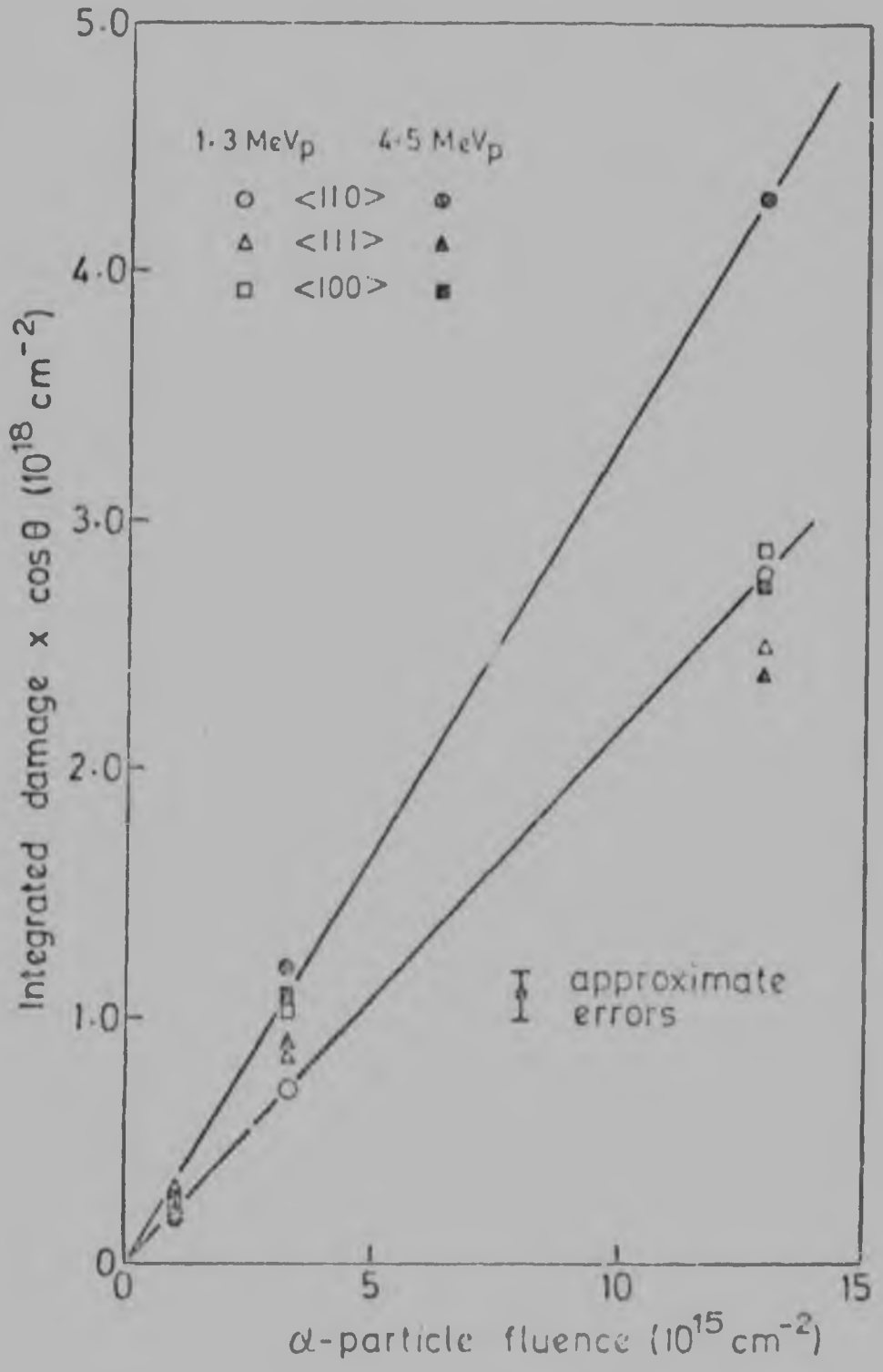

Figure 10.21: Dependence of measured damage on damaging dose (KT2).

the 'amount of damage' found depends on experimental factors and cannot be taken as the 'number of atoms not on lattice sites'.

If despite this the <110> data at 4.5 MeV are taken as giving the best rough estimate of the number of atomic displacements, then the slope of the upper line in Figure 10.21 gives a number of displaced carbon atoms per incident α-particle of 330±20. This agrees with the estimate of ~300 derived from the annealing behaviour (§10.3.2). Inserting it into the Kinchin-Pease relationship in the form

$$N(E_n) = 0.42\ E_n/E_d$$

(where $N(E_n)$ is the number of displaced atoms, E_n is the amount of energy available for nuclear collisions, and E_d is the threshold displacement energy which is equal to 80 eV for diamond when averaged over all directions [Bi⁻4]) gives an estimate for E_n of 60 keV. It would be interesting to compare this value with the result of a comprehensive calculation of Winterbon type [Win⁻2].

10.6 SUMMARY

There was evidence for several different types of damage in α-bombarded diamond, but it was complementary rather than conflicting. In addition to identifiable damage types there were probably more general amorphisation and even graphitisation present.

The annealing behaviour (§10.3.1) implied the existence of clusters with diameters of a few tens of Ångströms (§10.3.2). Although the data were consistent with one cluster per ion track, the size was

smaller than the expected region of heavy damage at the end of the track, and aggregation of interstitials had probably occurred. The clusters may have had amorphous cores which were unable to anneal. The energy dependence of the dechannelling (§10.4.3) pointed to the presence of interstitial carbon atoms in the tetrahedral sites, and mosaic blocks with a spread of ~0.5°; with less direct evidence for microtwinning on {111} plane parallel to the crystal surface (§10.4.4). Dechannelling by extended defects may have been present (there was evidence in the gas-etching results of §5.4.2 for dislocations in bombarded crystal regions) but did not appear to play a major rôle. Extraction of the damage profiles (§10.5.2) supported the deduction of tetrahedral interstitials.

On annealing to ~200°C, the evidence for interstitials and mosaic spread was progressively reduced. The motion of single interstitials, which are normally already mobile at room-temperature, must have been limited by the extent to which other damage had healed.

These results agree quite well with the deductions of Vavilov et al [Vav74] already referred to (Section 10.1), except that those workers observed a sequence of damage types with increasing dose. The ion-beam technique was not sensitive enough to reveal such evidence.

CHAPTER 11

CONCLUSIONS

It has been shown that reproducible, reliable ion channelling data can be obtained for natural diamond, although achieving this is not as straightforward as for many other substances, and special precautions must be taken (Chapters 5 and 6). Results can be very specimen dependent, and careful selection from a moderate number of good stones is necessary in order to obtain specimens representative of intrinsic diamond without appreciable impurity or mechanical damage effects (Section 5.2). Channelled minimum yield measurements provide the best criterion for selecting stones for channelling studies (§5.2.3). Pretreating the diamonds by surface removal or annealing usually produces a significant improvement in crystal quality as monitored by channelling (Section 5.1).

Cleaning, too, can be important, and requires the application of special methods (Section 5.3). Here ion backscattering provides a sensitive means of monitoring surface cleanliness (§5.3.2). Care must be taken to avoid re-contamination from the vacuum environment (Section 6.6), because common contaminants have higher atomic numbers than carbon and can cause significant dechannelling.

Some of the special techniques described in Chapter 6 were evolved to deal with other problems which are more severe with diamond,

such as target charging (Section 6.3) and electronic noise pickup (Section 6.5); in other cases the problems are common to all ion channelling experiments but are not always adequately considered, such as secondary electron suppression (Section 6.2), and the orientation of transaxial scan-planes (Section 6.8). It was shown that the exact choice of axial and planar scans can have a significant effect on the measured values of channelling critical angles (Sections 6.8 and 6.9).

Critical angles $\psi_{\frac{1}{2}}$ have been measured for several low-index axes and planes of diamond, at several energies and for two ion species (Section 7.4). They were reported in Tables 7.3 to 7.8; the channelling dips and their behaviour with depth were plotted in Figures 7.3 to 7.28. The reproducibility of the results between different specimens was good and the errors were $\pm 0.01°$ which is small by ion channelling standards.

With the exceptions noted below, all the results were shown in Section 7.5 to be well described by Barrett's semi-empirical relationships [Bar71], which are rooted in the continuum model of channelling proposed by Lindhard [Lin65]. These relationships are, for axial channelling Eqn 2.7:

$$\psi_{\frac{1}{2}} = k \; F_{RS}\left(\frac{ma_s}{a_{TF}}\right)\left[\frac{2Z_1Z_2e^2}{Ed}\right]^{\frac{1}{2}}$$

with k = 0.83 and m = 1.2, and for planar channelling Eqn 2.8:

$$\psi_{\frac{1}{2}} = k \; F_{PS}\left(\frac{ma}{a_{TF}} \cdot \frac{d_p}{a_{TF}}\right)\left[\frac{2\pi Z_1Z_2e^2a_{TF}N_V d_p}{E}\right]^{\frac{1}{2}}$$

with k = 0.76 and m = 1.6. The other symbols are defined in Chapter 2, and the functions $F_{RS}(\xi)$ and $F_{PS}(\xi,\eta)$ are presented in Bar71 and Ge74. Typical differences between theoretical and experimental values of $\psi_{\frac{1}{2}}$ were $\sim 0.01°$. The values of k and m quoted above were proposed by Barrett as giving the best representation of the variation of $\psi_{\frac{1}{2}}$ with temperature; for the ion and energy dependence he found slightly smaller values of k gave a better fit to his Monte Carlo simulations (see Table 2.1). However, the former set of values gave better agreement with the ion and energy dependence as well as with the temperature dependence in the present case. This may be because Barrett did not extrapolate his values to zero depth, as was done here.

It is remarkable that these expressions apply so well to diamond, which has the lowest values of both $\psi_{\frac{1}{2}}$ and Z_2 for which careful comparisons with experiment have been made, and therefore represents an extreme case.

For higher-order axes (<100>, <211>) a smaller value of k in Eqn 2.7 gave a better fit, namely k = 0.76±0.01; the physical significance of this was not obvious. For an unequally-spaced plane ({111}) Eqn 2.8 gave incorrect values when the mean planar spacing was inserted. However, modifying the equation in terms of the continuum model, to include the effects of the four nearest planes and not just two (Eqn 7.5 with Eqn 7.4) was successful in correctly predicting the measured values of $\psi_{\frac{1}{2}}$ (§7.5.3).

The axial data agreed equally well with values calculated by the method of Varelas and Sizmann [Va.72], based on a consideration of the exactness of transverse energy conservation in the channels as determined

by binary-collision calculations (§7.5.4). The fact that two quite different theoretical approaches can predict experimental results accurately, gives confidence that the channelling phenomenon is well understood. The accuracy of Varelas and Sizmann's treatment does not seem to have been appreciated hitherto, because it produces critical angles ψ_c which should not be compared directly with measured half-angles $\psi_{\frac{1}{2}}$. If Barrett's k is regarded as a conversion factor as in §7.5.4, then the calculated values of $k\psi_c$ are found to agree closely with the measured values of $\psi_{\frac{1}{2}}$.

The empirical approximations of Morgan and Van Vliet [Mo⁻0, Mo⁻1] appear to be out of their range of applicability in the case of diamond.

The dependence of proton critical angles on temperature was also found to be well reproduced by Eqns 2.7 and 2.8 of Barrett, and by the method of Varelas and Sizmann, over the range examined, 20°C to 700°C (Section 8.3). The data were presented in Tables 8.1 and 8.2 and Figures 8.1 to 8.4.

The form of Eqns 2.7 and 2.8 is that obtained in the continuum approximation by putting r_c, the critical approach distance to the strings or planes bounding the channel, equal to mu_1, where u_1 is the RMS thermal vibration amplitude of the atoms in one dimension and $m \sim 1$. The accuracy with which these expressions hold for diamond (§8.3.1) is the most direct confirmation yet obtained that the critical distance parameter for stable channelling is u_1 rather than a_{TF} as suggested by Lindhard [Li65]. In diamond $u_1 \sim 0.17a_{TF}$ whereas in most

solids on which channelling experiments have been performed, the two quantities are comparable.

There was some indication of a stronger temperature dependence than that predicted for axes by Eqn 2.7, as noticed also by others [And72]. It was suggested that this could best be accounted for by a mildly temperature-dependent value of m, that is, by a dependence of ρ_c on u_1 somewhat stronger than linear (§8.3.2).

Studies of the surface peak in the backscatter spectra of axially channelled protons were complicated by the slow deposition of carbon layers from the turbomolecular pump. An extrapolation to zero deposit gave an effective number of surface layers of the crystal itself in near agreement with Barrett's prediction, Eqn 2.12, indicating that the crystal was perfect at the surface with the possible exception of one or two outer layers (Section 9.3).

The surface minimum yield was studied in Section 9.4; data are presented in Tables 9.1 and 9.2. The effect thereon of the surface deposit was small and could be corrected for (§9.4.1). The predicted dependence on row spacing of $\chi_{min} \propto d$ (Eqn 9.8) was well reproduced (§9.4.3; Figure 9.4). The temperature dependence agreed with that proposed by Barrett [Bar71] and embodied in Eqn 2.10:

$$\chi_{min} = N_V d\pi(Cu_2 + C'a_{TT}) \sqrt{1 + \quad} + \chi_3$$

where Barrett's values for C and C' were 3.0±0.2 and 0.2±0.1 respectively, and the other symbols were defined in Chapter 2. (The square-root factor

was always ∿1 in this work, and $\chi_2 \sim 0$.) Barrett suggested that one might generally take C' = 0. The values obtained here were C = 3.2±0.6 and C' = 0.05±0.05 (§9.4.2). Once again, diamond provides a stringent test of theory. The two major terms ($\chi_1 = N_V d\pi C u_1^2$ and $\chi_2 = N_V d\pi C' a_{TF}^2$) are very disparate in most substances, with $\chi_1 \gg \chi_2$ (because $C \gg C'$ and $u_1 \sim a_{TF}$) and the true values of χ_2 and hence of C' are hard to assess; in diamond $\chi_1 \sim \chi_2$ (because $u_1 \ll a_{TF}$) and the value of C' may be examined more closely. The value obtained was distinctly smaller than Barrett's, and supports his suggestion that one may take C' = 0 in practice. In fact, in his analysis, all contributions to χ_{min} were determined by a density-of-trajectories function proportional to u_1^2, and this is vindicated by the present data. In such a model χ_{min} cannot be interpreted geometrically as representing the forbidden area around the strings, as was formerly customary.

Such extensive theoretical predictions for planar minimum yields are not available. It is generally agreed that χ_{min} should be $\propto d_p^{-1}$, and this dependence was well followed by the data (Table 9.2). (By coincidence, the unequal {111} spacing does not produce an anomaly here.) A small temperature dependence was observed, and tentatively fitted by a reasonable function (§9.4.4; Table 9.3).

A by-product of these studies was the shedding of some light on the nature of the diamond surface, which is still an unresolved problem. The ion-beam results agreed with other work which has suggested that the surface 'dangling bonds' can be satisfied either by impurity atoms or by surface reconstruction. The high crystal perfection apparent under

polished surfaces was consistent with a current model of the polishing process as being primarily one of the tearing off of very small blocks by brittle fracture, and also with an alternative mechanism of thermally-activated chemical reaction (Section 9.5).

The radiation damage of diamond by light ions appeared to be a highly complex phenomenon (Chapter 10) as has been observed for other substances and projectiles. It was however possible to keep damage effects negligible while taking channelling data (Section 10.2). From the annealing behaviour (Section 10.3), the energy dependence of the dechannelling (Section 10.4), and the extracted damage profiles (Section 10.5), some deductions could be made about the nature of the damage; they were summarised in Section 10.6. No single type of damage fitted all the observations; there was good evidence for amorphous zones or clusters, self-interstitials preferentially located in the tetrahedral sites, and ballistic spread, and weaker evidence for microtwinning and rather general amorphisation, in general agreement with other studies [Vav74].

Diamond is an easy crystal in which to perform channelling investigations, but a difficult one in which to do them reproducibly. The problem can be overcome by applying careful, logical procedures, and the resulting measurements are of interest in providing some extreme tests of the accepted channelling theories. In most cases theoretical predictions agreed well with the experiments herein described.

A P P E N D I X

A.1 DIAMOND CHANNELLING DATA

All values in Å.

Name	Symbol	Formula	Value
lattice parameter	a	-	3.567
axial spacings	d<110>	a√2/2	2.522
	d<111>	a√3/2	3.089
	d<100>	a	3.567
	d<211>	a√6/2	4.369
planar spacings	$d_p\{110\}$	a√2/4	1.261
	$d_p\{111\}$	a√3/6*	1.030
	$d_p\{100\}$	a/4	0.892
	$d_p\{211\}$	√3/2a/6	0.728
Thomas-Fermi screening distance	$a_{TF}(p)$	Eqn 2.2a	0.258
	$a_{TF}(a)$	Eqn 2.2b	0.21
atoms per unit volume	N_V	$8/a^3$	0.176
thermal vibration amplitude	u_1 (20°C)	Debye	0.044

*But see §7.5.2.

A.2 POCKET CALCULATOR PROGRAMMES

The versions given here are for the Hewlett-Packard HP25. They run with slight modifications on the other HP programmable calculators.

Co-ordinate conventions for both programmes are defined in Figures A.1 and A.2.

The equations used are as follows:

$$\theta = \arccos(\cos\theta_a \cos\psi - \sin\theta_a \sin\psi \cos\phi')$$

$$\phi = \phi_a + \arcsin\frac{\sin\psi \sin\phi'}{\sin\theta}$$

In GCS, the value of ϕ is stepped; in CRAP-2, ϕ' is stepped.

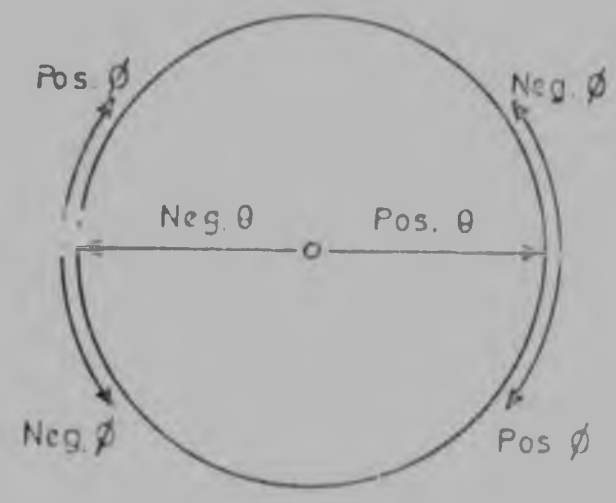

Figure A1: Definition of goniometer coordinates. Ø is positive clockwise.

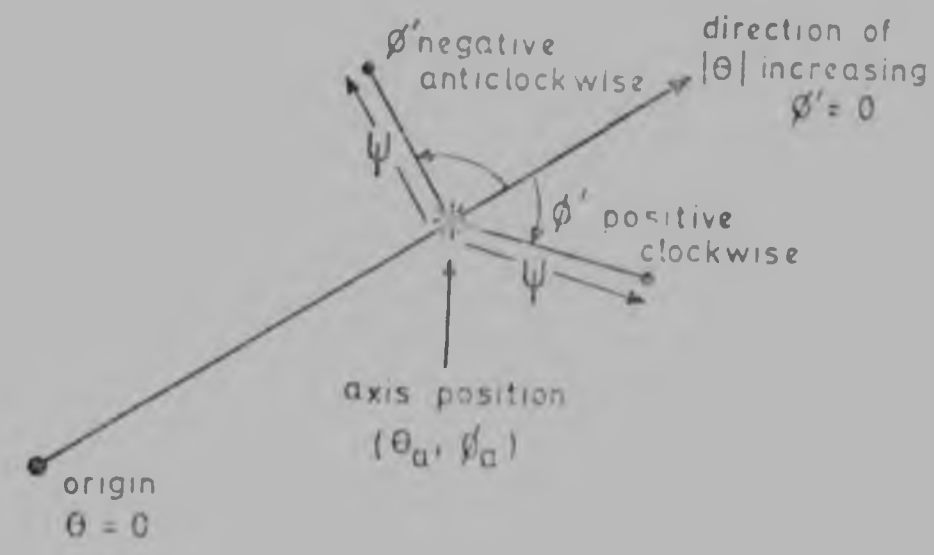

Figure A2: Definition of local coordinates. ψ is always positive. Ø' is positive clockwise.

Great Circle S... (GCS)

Line	Key Entry	Comments
00		
01	RCL 1	
02	f cos	
03	STO 6	Calculation
04	RCL 1	and storage of
05	g ABS	constant
06	f sin	trigonometric
07	RCL 4	functions
08	f cos	
09	x	
10	STO 7	
11	RCL 4	
12	f sin	
13	STO 0	
14	f(CLEAR)STK	
15	RCL 3	
16	f cos	
17	RCL 6	
18	x	
19	RCL 3	θ loop
20	f sin	
21	RCL 7	
22	x	
23	-	
24	g $\cos^{-1}$	

Line	Key Entry	Comments
25	RCL 1	
26	ENTER ↑	
27	g ABS	
28	↓	
29	x	
30	R/S	
31	g ABS	
32	f sin	
33	RCL '	
34	f sin	
35	x ⇄ y	ϕ
36	↑	loop
37	RCL 0	
38	x	
39	g $\sin^{-1}$	
40	RCL 2	
41	+	
42	R/S	
43	RCL 5	Steps scan
44	STO + 3	angle ϕ and
45	GTO 14	goes back to
46		loop start
47		
48		
49		

Registers

R_0	sin ϕ'	R_4	ϕ' (scan plane orientation)
R_1	θ_a (Co ordinates of axis)	R_5	Δϕ (scan angle step)
R_2	ϕ_a (Co-ordinates of axis)	R_6	cos θ_a
R_3	ψ (Insert ... initial s... angle)	R_7	cos ϕ' sin θ_a

Step	Instructions	Input Data/Units	Keys	Output Data/Units
1	Key in programme			
2	Initialize		f PRGM	
3	Store constants	θ_a	STO 1	
		ϕ_a	STO 2	
		ϕ_0	STO 3	
		ϕ'	STO 4	
		Δψ	STO 5	
4	Run		R/S	θ_0
5			R/S	ϕ_0
6			R/S	θ_1
7			R/S	ϕ_1
	Repeat as required			etc
8	To ch... value of ψ used for previous pair of θ and ϕ values		RCL ...	ψ

Constant Radius Azimuthal Procession, Version 2 [CRAP-2]

Line	Key Entry	Comments
00		
01	RCL 1	
02	f cos	
03	RCL 3	
04	f cos	
05	x	Calculation
06	STO 6	and storage
07	RCL 1	of constant
08	g ABS	trigonometric
09	f sin	functions
10	RCL 3	
11	f sin	
12	STO 0	
13	x	
14	STO 7	
15	f(CLEAR)STK	
16	RCL 4	
17	f cos	
18	RCL 7	
19	x	
20	CHS	
21	RCL 6	
22	+	θ loop
23	g $\cos^{-1}$	
24	RCL 1	

Line	Key Entry	Comments
25	ENTER ↑	
26	g ABS	
27	↑	
28	x	
29	R/S	
30	g ABS	
31	f sin	
32	RCL 4	
33	f sin	
34	x ≷ y	
35	↑	φ loop
36	RCL 0	
37	/	
38	g $\sin^{-1}$	
39	RCL 2	
40	+	
41	R/S	
42	RCL 5	Steps azimuth
43	STO + 4	φ' and returns
44	GTO 15	to loop start
45		
46		
47		
48		
49		

Registers

R_0	sin ψ	R_4	φ' (Insert φ', initial azimuth)
R_1	θ_a (Co-ordinates of axis)	R_5	Δφ (Azimuth step)
R_2	ϕ_a (Co-ordinates of axis)	R_6	cos θ_a cos ψ
R_3	ψ (Scan 'radius')	R_7	sin θ_a sin ψ

Step	Instructions	Input Data/Units	Keys	Output Data/Units
1	Key in programme			
2	Initialize		f PRGM	
3	Store constants	θ_a	STO 1	
		ϕ_a	STO 2	
		ψ	STO 3	
		φ'	STO 4	
		Δφ	STO 5	
4	Run		R/S	θ_0
5			R/S	ϕ_0
6			R/S	θ_1
7			R/S	ϕ_1
	Repeat as required			etc
8	To check value of φ' used for previous pair of θ and φ values		RCL 4	φ'

REFERENCES

Ab72 F Abel, G Amsel, M Bruneaux, C Cohen, Phys Lett 42A, 165 (1972).

Ac70 E Acerbi, C Birattari, B Candoni, M Castiglioni, G Dutto, G Fait, C Succi, Nuovo Cimento Lett 3, 569 (1970).

Ah75 M Ahlberg, G Johansson, K Malmqvist, Nucl Instr & Meth 131, 377 (1975).

Ale70 R B Alexander, G Dearnaley, D V Morgan, J M Poate, Phys Lett 32A, 365 (1970).

Alt70 M R Altman, I C Feldman, W M Gibson, Phys Rev Lett 24, 464 (1970).

And67 J U Andersen, K D V S Mat-Fys Medd 36, #7 (1967).

And68 J U Andersen & E Uggerhøj, Can J Phys 46, 517 (1968).

And70 J U Andersen & I C Feldman, Phys Rev B1, 2063 (1970).

And71 J U Andersen, O Andreasen, J A Davies, E Uggerhøj, Radn Eff 7, 25 (1971).

And72 J U Andersen & E Lægsgård, Radn Eff 12, 3 (1972).

And72b J U Andersen, E Lægsgård, I C Feldman, Radn Eff 12, 219 (1972).

Ann76 H J Annegarn, PhD Thesis, University of the Witwatersrand (1976).

Anr65 C J Andreen, R L Hines, W Morris, D Weber, Phys Lett 19, 116 (1965).

Ap65 B R Appleton, C Erginsoy, H E Wegner, W M Gibson, Phys Rev Lett 19, 185 (1965).

As65 G Astner, I Berestrom, B Domeij, I Eriksson, S Person, Phys Lett 14, 308 (1965).

Au71 W M Augustyniak, Private communication (1971).

Bal65 G C Ball & I Brown, Can J Phys 43, 676 (1965).

Bar68 J H Barrett, Phys Rev 164, 219 (1968).

Bar71 J H Barrett, Phys Rev B3, 1527 (1971).

Be65 F Bell & R Sizmann, Phys Lett 19, 171 (1965).

Ber65 "Physical Properties of Diamond", ed. R Berman (Clarendon Press, Oxford, 1965).

Bi74 B R Bibby & I Duncan, Queen's University of Belfast internal report (undated).

Bj68 K Björkqvist, P Domeij, L Eriksson, G Fladda, A Fontell, J W Mayer, Appl Phys Lett 13, 379 (1968).

Bo64 E Bøgh, J A Davies, K O Nielsen, Phys Lett 12, 129 (1964).

Bo65 E Bøgh & E Uggerhøj, Phys Lett 17, 116 (1965).

Bo68 E Bøgh, Can J Phys 46, 653 (1968).

Bo69 E Bøgh, Proc Roy Soc A311, 35 (1969).

Bo72 E Bøgh, Radn Eff 12, 13 (1972).

Bot73 J Böttiger & F H Eisen, Thin Solid Films 19, 239 (1973).

Bou75 J C Bourgoin, Diamond Research 1975, p24 (Published by Industrial Diamond Information Bureau, London).

Bra65 W Brandt, J M Kahn, D L Potter, K D Worley, H P Smith Jr, Phys Rev Lett 14, 42 (1965).

Bra68 W. Brandt, Scientific American, March 1968, p91.

Brn68 F Brown, D A Marsden, R D Werner, Phys Rev Lett 20, 1449 (1968).

Bro73 W L Brown, Radiation Damage and Defects in Semiconductors, Inst Phys Conf Ser #16, 416 (1973).

Bru74 B A Brusilovsky & V A Molchanov, Radn Eff 23, 131 (1974).

Cai68 J A Cairns & R S Nelson, Phys Lett 27A, 14 (1968).

Cam71 S U Campisano, G Foti, F Grasso, E Rimini, Phys Lett 35A, 119 (1971).

Cas72 M Casey & J Wilks, Diamond Research 1972, p6 (Published by Industrial Diamond Information Bureau, London).

Cas73 M Casey & J Wilks, J Phys D: Appl Phys 6, 1772 (1973).

Ch64 D A Channing & J L Whitton, Phys Lett 13, 27 (1964).

C177 C D Clark & I W J Mitchell Inst Phys Conf Ser #31, Chapter 1 (1977).

Co70 J P Coad, H E Bishop, J C Rivière, Surface Sci 21, 253 (1970).

Das69 L A Davidson, J F Gibbons, R L Der, T M Kavanagh, J M Kahn, Appl Phys Lett 14, 295 (1969).

Das71 L A Davidson, S Chou, J F Gibbons, W S Johnson, Radn Eff 7, 35 (1971).

Dat65 S Datz, T S Noggle, C D Moak, Phys Rev Lett 15, 254 (1965).

Dat67 S Datz, C Erginsoy, G Liebfried, H O Lutz, Ann Rev Nucl Sci 17, 129 (1967).

Dat69 S Datz, C D Moak, T S Noggle, B R Appleton, H O Lutz, Phys Rev 179, 315 (1969).

Dav64 J A Davies, G C Ball, F Brown, B Domeij, Can J Phys 42, 1070 (1964).

Dav67 J A Davies, J Denhartog, L Eriksson, J W Mayer, Can J Phys 45, 4053 (1967).

Dav68 J A Davies, J Denhartog, J L Whitton, Phys Rev 165, 345 (1968).

Dea64 G Dearnaley, IEEE Trans Nucl Sci 11, 249 (1964).

Dea68 G Dearnaley, I V Mitchell, R S Nelson, B W Farmery, M W Thompson, Phil Mag 18, 985 (1968).

Der70a T E Derry, 68th Annual Congress of the South African Association for the Advancement of Science, Cape Town 1970 (unpublished).

Der70b T E Derry, 15th Annual Conference of the South African Institute of Physics, Pretoria 1970 (unpublished).

Der71 T E Derry, D W Mingay & J P L Sellschop, 16th Annual Conference of the South African Institute of Physics, Cape Town 1971 (unpublished).

Der74 T E Derry, 72nd Annual Congress of the South African Association for the Advancement of Science, Grahamstown 1974 (unpublished).

Der75a T E Derry, R W Fearick & J P F Sellschop, Abstracts Diamond Conference, Cambridge 1975, paper 1.

Der75b T E Derry, 20th Annual Conference of the South African Institute of Physics, Durban 1975 (unpublished).

Der75c T E Derry, R W Fearick & J P F Sellschop, NPRU Report NPRU 75/13 (1975).

Der76a T E Derry, R W Fearick & J P F Sellschop, Abstracts Diamond Conference, Bristol 1976, paper 2.

Der76b T E Derry, R W Fearick & J P F Sellschop, Abstracts Diamond Conference, Bristol 1976, paper 3.

Der76c T E Derry, R W Fearick & J P F Sellschop, 21st Annual Conference of the South African Institute of Physics, Johannesburg 1976 (unpublished).

Der77a T E Derry, NPRU Report NPRU 77/3 (1977).

Der77b T E Derry, R W Fearick & J P F Sellschop, 22nd Annual Conference of the South African Institute of Physics, Grahamstown 1977 (unpublished).

Der78 T E Derry, R W Fearick & J P F Sellschop, Abstracts Diamond Conference, Oxford 1978, paper 4.

Det75 K Dettmann, Z Physik A272, 227 (1975).

Db73 "Properties of Diamond" (booklet), (De Beers Industrial Diamond Division, London, undated).

Do64 B Domeij, F Brown, J A Davies, G R Piercy, E V Kornelsen, Phys Rev Lett 12, 363 (1964).

Results discussed in C Erginsoy, Phys Rev Lett 12, 366 (1964).

Do65 B Domeij & K Björkqvist, Phys Lett 14, 127 (1965).

Do70 B Domeij, G Fladda, N G E Johansson, Radn Eff 6, 155 (1970).

Ed70 R D Edge & R L Dixon, in Atomic Collision Phenomena in Solids, Ed D W Palmer, M W Thompson and P D Townsend (North-Holland Publ Co 1970) p435.

Erg64 C Erginsoy, H E Wegner, W M Gibson, Phys Rev Lett 13, 530 (1964).

Erg65 C Erginsoy, Phys Rev Lett 15, 360 (1965).

Eri67 L Eriksson, J A Davies, J Denhartog, J W Mayer, O J Marsh, R Markarious, Appl Phys Lett 10, 323 (1967).

Eri69a L Eriksson, G R Bellavance, J A Davies, Radn Eff 1, 71 (1969).

Eri69b L Eriksson, J A Davies, N G E Johansson, J W Mayer, J Appl Phys 40, 842 (1969)

Ev61 T Evans & C Phaal, in Proc 5th Biennial Conf on Carbon (Penn State Univ), 1, 143 (1961).

Ev76 T Evans, Private communication (1976).

Fea75 R W Fearick, Unpublished data (1975).

Fea76 R W Fearick, Unpublished data (1976).

Fea77a R W Fearick, Private communication (1977).

Fea77b R W Fearick, Private communication (1977).

Fea77c R W Fearick, Private communication (1977).

Fea77d R W Fearick, Private communication (1977).

Fea79 R W Fearick, PhD Thesis to be submitted to the University of the Witwatersrand (1979).

Fes73 H W Fesq, D M Bibby, J P F Sellschop, J I W Watterson, J Radioanal Chem 17, 195 (1973).

Fi78 "Physics of Diamonds", ed. J Field (to be published by Academic Press, London, 1978).

Fo70 G Foti, F Grasso, R Quattrocchi, I F Quercia, E Rimini, Nuovo Cimento Lett 1, 707 (1970).

Fo71 G Foti, F Grasso, R Quattrocchi, E Rimini, Phys Rev B3, 2169 (1971).

Fo77 G Foti, L Csepregi, E Kennedy, P Pronko, J W Mayer, Phys Lett 64A, 265 (1977).

Fu69 F Fujimoto, K Komaki, K Ozawa, M Mannami, T Sakurai, Phys Lett 29A, 332 (1969).

Fu70 F Fujimoto, K Komaki, H Nakayama, M Ishii, Phys Lett 33A, 432 (1970).

Ga70 V V Galkin, V V Krasnopevtsev, Y V Mityutin, Fiz Tekh Poluprov 4, 837 (1970).
Translated in Sov Phys - Semicond 4, 709 (1970).

Ge65 D S Gemmell & R E Holland, Phys Rev Lett 14, 945 (1965).

Ge72 D S Gemmell & R C Mikkelson, Phys Rev B6, 1613 (1972).

Ge74 D S Gemmell, Rev Mod Phys 46, #1 (1974).

Gi65 W M Gibson, C Erginsoy, H E Wegner, B R Appleton, Phys Rev Lett 15, 357 (1965).
Results discussed in C Erginsoy, Phys Rev Lett 15, 360 (1965).

Gi70 W M Gibson & K O Nielsen, Phys Rev Lett 24, 114 (1970).

Gi71 W M Gibson, Summer School on the interaction of charged particles with solids, Istanbul (1971).
Published as Brookhaven Nat Lab Report BNL 50336, p331 (1973).

Ha69 R R Hart & O J Marsh, Appl Phys Lett 15, 206 (1969).

Hi77 E H Hirsch, J Phys D : Appl Phys 10, 2069 (1977).

Hor75 S M Horszowski, Private communication (1975).

How71 L M Howe & S Schmid, Can J Phys 49, 2321 (1971).

In62 C N Inskeep, W W Eidson, R A La Salle, IRE Trans Nucl Sci NS9, 167 (1962).

Ja75 F James & M Roos, Computer Physics Communications 10, 343 (1975).

Jo69 A Johansen, J S Olsen, S Steenstrup, J Koch, Radn Eff 2, 19 (1969).

Jou74 J C Jousset, J Morv, J J Quillico, J Physique (lettres) 35, L229 (1974).

Kau75 E N Kaufmann, P Raghavan, R S Raghavan, E J Ansaldo, R A Naumann, Phys Rev Lett 34, 1558 (1975).

Kay57 G W C Kaye & T H Laby, "Tables of Physical and Chemical Constants", 11th Edition (Longmans, Green & Co, London, 1957).

Kb73 Y Kubota & Y H Ohtsuki, Phys Lett 45A, 521 (1973).

Ki74 R E Kirby & D Lichtman (I), Surface Sci 41, 447 (1974).

Kl62 D L Klein & D J D'Stefan, J Electrochem Soc 109, 37 (1962).

Kom69 K Komaki & F Fujimoto, Phys Lett 29A, 544 (1969).

Kom71 K Komaki, F Fujimoto, M Ishii, H Nakayama, Phys Lett 37A, 271 (1971).

Kor64 E V Kornelson, F Brown, J A Davies, B Domeij, G R Piercy, Phys Rev 136, A849 (1964).

Ku70a M A Kumakhov, Phys Lett 32A, 538 (1970).

Ku70b M A Kumakhov, Phys Lett 33A, 133 (1970).

Lae68a E Laegsgaard, F W Martin, W M Gibson, Nucl Instr & Meth 60, 24 (1968).

Lae68b E Laegsgaard, F W Martin, W M Gibson, IEEE Trans Nucl Sci NS-15, 239 (1968).

Lam73 R M Lambert & C M Comrie, Surface Sci 38, 197 (1973).

Lan66 J J Lander & J Morrison, Surface Sci 4, 241 (1966).

Lau52 M T F von Laue, International Tables for X-ray Crystallography, 1, 1 (Historical introduction) (1952 ff).

Li64 J Lindhard, Phys Lett 12, 126 (1964).

Li65 J Lindhard, K D V S Mat-Fys Medd 34, #14 (1965).

Li68 J Lindhard, V Nielsen, M Scharff, K D V S Mat-Fys Medd 36, #10 (1968).

Lon48 K Lonsdale, Acta Cryst 1, 142 (1948).

Lov69 L Lovelace, J Oral Biology 69, 69 (1969).

Lut63 H O Lutz & R Sizmann, Phys Lett 5, 113 (1963).

Lut64 H O Lutz, R Sizmann, Z Naturforsch 19a, 1079 (1964).

Lut66 H O Lutz, S Datz, C D Moak, T S Noggle, Phys Rev Lett 17, 285 (1966).

Lur76 P G Lurie & J M Wilson, Diamond Research 1976, p26 (Published by Industrial Diamond Information Bureau, London).

Lur77 P G Lurie & J M Wilson, Surface Sci 65, 453 (1977).

Ma64 T C Madden, W M Gibson, IEEE Trans Nucl Sci 11, 254 (1964).

Ma70 T C Madden, Private communication (1970).

Mah64 J B Marsh & H E Farnsworth, Surface Sci 1, 3 (1964).

Mar69 M Maruyama, K Tsukada, K Ozawa, F Fujimoto, K Komaki, M Mannami, T Sakurai, Phys Lett 29B, 111 (1969).

Mas70 D H Mash, G D Henshall, B A Bales, J Phys D : Appl Phys 3, 1199 (1970).

Mat67 H Matzke & J A Davies, J Appl Phys 38, 805 (1967).

Matt76 S Matteson, E K L Chau, D Powers, Phys Rev A14, 169 (1976).

May67 J W Mayer, J A Davies, L Eriksson, Appl Phys Lett 11, 365 (1967).

May68 J W Mayer, L Eriksson, S T Picraux, J A Davies, Can J Phys 46, 663 (1968).

Maz68 D J Mazey, R S Nelson, R S Barnes, Phil Mag 17, 1145 (1968).

Me74 M J Mendelssohn, H J Milledge, I Nave, D A Woods, Abstracts Diamond Conference, Oxford 1974, Paper 34.

Mey67 O Meyer & G Hauschahn, Nucl Instr & Meth 56, 177 (1967).

Mey70 O Meyer, J Gyulai, J W Mayer, Surface Sci 22, 263 (1970).

Mo70 D V Morgan & D Van Vliet, Radn Eff 5, 157 (1970).

Mo71 D V Morgan & D Van Vliet, Radn Eff 8, 51 (1971).

Mo72 D V Morgan & D Van Vliet, Radn Eff 12, 203 (1972).

Mo73 "Channelling: Theory, Observation, and Applications", ed. D V Morgan (Wiley, London, 1973).

Mol47 G Molière, Z Naturforsch A2, 133 (1947).

Mor70a K Morita & N Itoh, Phys Lett 31A, 283 (1970).

Mor70b K Morita, K Tachibana, N Itoh, Phys Let 33A, 257 (1970).

Mor71 K Morita & N Itoh, Phys Lett 34A, 359 (1971).

Moy72 J Mory & Y Quéré, Radn Eff 13, 57 (1972).

Ne62 R S Nelson & M W Thompson, Phys Lett 2, 124 (1962).

Ne63 R S Nelson & M W Thompson, Phil Mag 8, 1677 (1963).
For a numerical correction to this work, see M W Thompson, Phil Mag 9, 1069 (1964).

Ne69 R S Nelson, Radn Eff 2, 47 (1969).

Oe62 (i) O S Oen, M T Robinson, D K Holmes
(ii) M T Robinson, D K Holmes, O S Oen
Bull Am Phys Soc 7, 171 (1962).

Oe65 O S Oen, Phys Lett 19, 358 (1965).

Og59 G J Ogilvie, J Phys Chem Solids 10, 222 (1959).

Pa65 J R Parsons, Phil Mag 12, 1159 (1965).

Ph62a C Phaal, PhD Thesis, Reading University (1962).

Ph62b C Phaal, Industrial Diamond Review (1962) (Published by the Industrial Diamond Information Bureau, London).

Pic69a S T Picraux, J A Davies, L Eriksson, N G E Johansson, J W Mayer, Phys Rev 180, 873 (1969).

Pic69b S T Picraux, J E Westmoreland, J W Mayer, R R Hart, O J Marsh, Appl Phys Lett 11, 7 (1969).

Pic69c S T Picraux & J U Andersen, Phys Rev 186, 267 (1969).

Pie63 G R Piercy, F Brown, J A Davies, M McCargo, Phys Rev Lett 10, 399 (1963).

Pie64 G R Piercy, M McCargo, F Brown, J A Davies, Can J Phys 42, 1116 (1964).

Po71 J-C Poizat & J Remillieux, Phys Rev Lett 27, 6 (1971).

Pow54 B D Power & D J Crawley, Vacuum 4, 415 (1954).

Qu68a Y Quéré, Phys Lett 26A, 578 (1968).

Qu68b Y Quéré, Phys Stat Sol 30, 713 (1968).

Qu76 Y Quéré, Radn Eff 28, 253 (1976).

Rei67 C H Reinsch, Numerische Mathematik 10, 177 (1967).

Ren72 M J Renan, PhD Thesis, University of the Witwatersrand (1972).

Ro63a M T Robinson & O S Oen, Appl Phys Lett 2, 30 (1963).

Ro63b M T Robinson & O S Oen, Phys Rev 132, 2385 (1963).

Ro69 M T Robinson, Phys Rev 179, 327 (1969).

Ron75 D Ronikier-Polonsky, G Désarmot, N Housseau, Y Quéré, Radn Eff 27, 81 (1975).

Roo74 H E Roosdendaal, W H Kool, W F van der Weg, J B Sanders, Radn Eff 22, 89 (1974).

Sap68a R Sappok & H P Boehm, Carbon 6, 283 (1968).

Sap68b R Sappok & H P Boehm, Carbon 6, 573 (1968).

Sat65 A R Sattler & G Dearnaley, Phys Rev Lett 15, 59 (1965).

Sc73 K Schmid, Radn Eff 17, 201 (1973).

Sc73 J P F Sellschop & W M Gibson, Diamond Research 1973, p32 (Published by Industrial Diamond Information Bureau, London).

Sc77 J P F Sellschop, H J Annegarn, R J Keddy, C C P Madiba, M J Renan, Abstracts Diamond Conference, Reading 1977, paper 9.

Sea58 M Seal, Proc Roy Soc A248, 379 (1958).

Sea66 M Seal, in "Science and Technology of Industrial Diamonds", ed. J Burls (Published by Industrial Diamond Information Bureau, London, 1966) 1, p115.

Sof61 S D Softky, Phys Rev 123, 1685 (1961).

Son72 K Sone & F Fukuzawa, Phys Lett 40A, 11 (1972).

Sta12 J Stark, Phys Z 13, 973 (1912).
Also see J Stark, G Wendt: Ann der Phys 38, 921 (1912), and Ann der Phys 38, 941 (1912).

Ste57 E J Sternglass, Phys Rev 108, 1 (1957).

Ta75 D Tabor, Diamond Research 1975, p9 (Published by Industrial Diamond Information Bureau, London).

Th75 J M Thomas & E L Evans, Diamond Research 1975, p2 (Published by Industrial Diamond Information Bureau, London).

Thm64 M W Thompson, Phys Rev Lett 13, 756 (1964).

Thm68 M W Thompson, Contem Phys 9, 375 (1968).

Thr76 A G Thornton & J Wilks, J Phys D : Appl Phys 9, 27 (1976).

To?0 M Tolkowsky, DSc Thesis, London University (1920).

Tu65a A F Tulinov, Dokl Akad Nauk SSSP 162, 546 (1965).
Translated in Soviet Physics - Doklady 10, 463 (1965).

Tu65b A F Tulinov, B G Akhmetova, A A Puzanov, A A Bednyakov, ZLETF Pis Red 2, 48 (1965).
Translated in JETP Lett 2, 30 (1965).

Tu65c A F Tulinov, V S Kulilauskas, M M Malov, Phys Lett 18, 304 (1965).

Vad73 J W Vandersande, Diamond Research 1973, p21 (Published by Industrial Diamond Information Bureau, London).

Vad75 J W Vandersande, Inst Phys Conf Ser #23, Chap 4, 308 (1975).

Vad76 J W Vandersande, Phys Rev B13, 4560 (1976).

Vae73 W F van der Weg, H E Roosendaal, W H Kool, Radn Eff 17, 91 (1973).

Vai71 D Van Vliet, Radn Eff 10, 137 (1971).

Var72 C Varelas & R Sizmann, Radn Eff 16, 211 (1972).

Vav74 V S Vavilov, V V Krasnopevtsev, Y V Miljutin, A E Gorodetsky, A P Zakharov, Radn Eff 22, 141 (1974).

Vic62 A C Victor, J Chem Phys 36, 1903 (1962).

Vo73 J D M Vorster, Private communication (1973).

Wal77 R S Walker, D A Thompson, S W Pochlman, Radn Eff 34, 157 (1977).

Wat71 G D Watkins, R P Messmer, C Weigel, D Peak, J W Corbett, Phys Rev Lett 27, 1573 (1971).

Wei73 C Weigel, D Peak, J W Corbett, G D Watkins, R P Messmer, Phys Rev B8, 2906 (1973).

Wes69 J E Westmoreland, J W Mayer, F H Eisen, B Welch, Appl Phys Lett 15, 308 (1969).

Wh65 J L Whitton, J Appl Phys 36, 3917 (1965).

Wh69 J L Whitton, Proc Roy Soc A311, 63 (1969).

Wi71 E M Wilks & J Wilks, Industrial Diamond Review, June 1971, p238 (Published by Industrial Diamond Information Bureau, London).

Wi72 E M Wilks & J Wilks, J Phys D : Appl Phys 5, 1902 (1972).

Wi76 E M Wilks, Nature 262, 570 (1976).

Win72 K B Winterbon, Radn Eff 13, 215 (1972).

Za74 C S Zaidins, Nucl Instr & Meth 120, 125 (1974).

Zi72a J F Ziegler, J Appl Phys 43, 2973 (1972).

Zi72b J F Ziegler & B L Crowder, Appl Phys Lett 20, 178 (1972).